EXPERIMENTAL ANALYSIS, MATHEMATICAL MODELING AND CONTROL OF PARTICLE SIZE DISTRIBUTION IN SEMI-BATCH EMULSION POLYMERIZATION

by

Charles David Immanuel

A dissertation submitted to the Faculty of the University of Delaware in partial fulfillment of the requirements for the degree of Doctor of Philosophy in Chemical Engineering

Fall 2002

EXPERIMENTAL ANALYSIS, MATHEMATICAL MODELING AND CONTROL OF PARTICLE SIZE DISTRIBUTION IN SEMI-BATCH EMULSION POLYMERIZATION

by

Charles David Immanuel

Approved: _____

Mark A. Barteau, Ph.D.
Chair of the Department of Chemical Engineering

Approved: _____

Eric W. Kaler, Ph.D.
Dean of the College of Engineering

Approved: _____

Conrado M. Gempesaw II, Ph.D.
Vice Provost for Academic Programs and Planning

I certify that I have read this dissertation and that in my opinion it meets the academic and professional standard required by the University as a dissertation for the degree of Doctor of Philosophy.

Signed: _____

Francis J. Doyle, III, Ph.D.
Professor in charge of dissertation

I certify that I have read this dissertation and that in my opinion it meets the academic and professional standard required by the University as a dissertation for the degree of Doctor of Philosophy.

Signed: _____

Eric W. Kaler, Ph.D.
Member of dissertation committee

I certify that I have read this dissertation and that in my opinion it meets the academic and professional standard required by the University as a dissertation for the degree of Doctor of Philosophy.

Signed: _____

Norman J. Wagner, Ph.D
Member of dissertation committee

I certify that I have read this dissertation and that in my opinion it meets the academic and professional standard required by the University as a dissertation for the degree of Doctor of Philosophy.

Signed: _____

Cajetan F. Cordeiro, Ph.D.
Member of dissertation committee

"Drones make a great deal more noise, fly about much more quickly than other bees, but they only make wax, not honey;..."

"...when your business is such that, to do it well, you must give it your whole attention, you should look at Him now and then; doing as mariners do; for when they want to reach some country, they look up to the sky, not down to the waves they are sailing over. In this manner, God will work for you, with you, in you, and when your work is done will comfort you."

Saint Francis de Sales

"It is upon heaven that everything hinges... Everything is Grace."

Saint Therese of Lisieux, the Little Flower

He Who is Mighty has done great things...
And His Mercy is on those who fear Him from generation to generation.
He has ... exalted those of low degree...

The Canticle of Mary Luke 1:49-50,52

ACKNOWLEDGMENTS

First and foremost, I express my profound thanks to my advisor Prof. Francis J. Doyle, III. He was a great source of help, encouragement and support throughout the duration of my grad school. The enthusiasm and agility that he brings into every aspect of the work is strongly contagious. He opened up several opportunities to project the study, and his extremely accommodative nature greatly facilitated working in the project. He granted all concessions ever requested for, including conference attendance, journal choices for our publications, and more importantly my long vacations home.

The strong collaboration with Air Products and Chemicals Inc. shaped this project to be of relevance to actual practice while simultaneously addressing some of the theoretical issues. The interaction with several engineers at Air Products, including Drs. Cajetan F. Cordeiro, Sekhar Sundaram, Cory Schlags, Denis Nagy and Frank Petrocelli is very gratefully acknowledged. Cajee showed great interest, sparing time in the midst of his very busy schedule to bring his knowledge and expertise into the project. He also served in my dissertation committee, besides co-authoring papers. In addition, we received much chemicals to be used in our experiments at Delaware. Sekhar was kind enough to share some of the model parameters developed in his studies at Air Products.

I thank my former and current group mates, including Jorge Castro, Darrin Feather, Kapil Gadkar, Ed Gatzke, Nick Hernjak, Toby Junker, Krishna Mahadevan, Kapil Mayawala, Camelia Owens, Bob Parker, Luis Puig, Dan Saffer, Raj Vadigepalli, Ping Xu and Dan Zak, and the post docs Selwa Ben Amor, Sharad

Bhartiya, Tim Crowley, Pascal Dufour and Scott Meadows. Very special thanks are due to Tim and Scott for their thorough mentoring during my early days in the project, and for the strong collaboration in setting up the experimental facility.

I thank all my teachers at the University of Delaware, whose courses helped in developing a new 'Delaware-flavour', besides enhancing my knowledge in the various subjects. Very special thanks to Dean Kaler and Prof. Wagner for serving in the dissertation committee, and to Prof. Ogunnaike for his insightful comments and suggestions on the work. Dean Kaler's course on 'Colloidal Phenomena' and his inputs outside of the course were very helpful in our coagulation modeling efforts, as were the course on the Numerical Methods offered by Prof. Beris and the discussions with him. I thank my TA advisors, particularly Profs. Doyle and Dhurjati, for their guidance and also for providing a chance to hone my teaching skills. I also thank several people in the department who were of tremendous help in setting up the emulsion laboratory, managing the procurements and general management. I am grateful to the procurement crew, including Nancy Levely, Lucille Wilson and Kim Correll for being patient with me through all the delays and confusions which accompanied every purchase!

I acknowledge funding from the University of Delaware in different forms, during the period of my graduate studies. Funding from the Office of Naval Research (Grant No. N000-14-96-1-0695) for the laboratory equipment and the Process Control and Monitoring Consortium for the laboratory operation and maintanence is also gratefully acknowledged.

I fondly remember all the good people whom I met during my stay in Delaware, who made life interesting. It is a great delight to know Prof. Doyle's marvelous family, his three wonderful children and his unassuming and friendly wife. My elderly neighbour was an excellant gentleman, the conversations with whom I enjoyed immensely. He never lost an opportunity to chide me for working too late and being up

early again... if only he knew the truth! I am thankful to the Saint Thomas Moore Oratory, which was a place to share my joys and sorrows, and to spend quiet times with the Almighty. The *lively* study space, filled with enthusiastic young students, was a blessing for me to brush away any loneliness and be motivated to work more. It is a special joy to have known Fr. Szupper at the Oratory. I am very pleased to have had the opportunity to meet several people at the Oratory and at the Saint John's Church over the four years. I thank God for having given this opportunity to live among such good people. I will for ever remember the Rosary group that met weekly to reflect on the Greatness of God and the Mystery of His Saving Power. It is a special joy that my dissertation defense took place on the Feast of Our Lady of the Rosary.

I take this opportunity to thank my parents and my brother John Christopher. My parents continue to be very patient through all my gimmicks. I thank my beloved brother John for his unconditional love.

TABLE OF CONTENTS

LIST OF FIGURES

LIST OF TABLES

ABSTRACT

The control of particle size distribution (PSD) in emulsion polymerization is motivated by the crucial role played by the PSD in determining the properties of the latex, including adhesion, rheological properties, and drying characteristics, among other things. Thus, the control of the entire multi-modal distribution leads to a better quality product. This dissertation demonstrates the control of PSD in semi-batch emulsion polymerization. The system investigated is vinyl acetate-butyl acrylate co-polymerization with non-ionic surfactants. The evolution of PSD is determined by the interplay of the phenomena of particle formation, particle growth and coagulation/aggregation. The main aspects of the project can be broadly summarized as follows:

- Performance of detailed process analyses to elucidate the mechanisms, understand the controllability, and identify control strategies.
- Development of detailed population balance models and development of efficient numerical methods.
- Development of control algorithms and strategies to produce better quality products.

Elaborating on the above aspects, an experimental study of the feasibility and methods of producing multi-modal distributions was performed, and the best control strategy was identified. Also, the types of distributions that can be produced, and their sensitivity to uncertainties in the model and the process were examined. Such a study is necessary for successful control of any process.

The next aspect of the research was to develop a detailed first principle model for the process of the evolution of the PSD in semi-batch emulsion co-polymerization. The model is cast in a population balance framework, accounting for the nucleation, growth and coagulation phenomena. The population balance equations – which are hyperbolic partial differential equations – and the associated complete model equations can be solved using standard techniques, as was demonstrated in our study. However, besides being high-dimensional, the system is also characterized by a large stiffness due to the wide difference in the time constants that characterize the nucleation, growth and coagulation processes, rendering the solution computationally very expensive and time consuming. This served as an impetus to develop better numerical solution techniques for the model. An efficient solution technique has been developed, that employs process understanding to re-cast the solution in a hierarchical framework, with the nucleation, growth and coagulation phenomena considered individually to update the PSD. The improved solution technique brings on-line feedback control within the feasibility realm.

The final aspect of the research was to perform optimization and control studies on the PSD. Optimization studies were performed, to design recipe for semi-batch operation that attain target PSDs in the latex. The discontinuities in the process preclude the application of traditional gradient-based optimization techniques to this problem. Thus, direct optimization techniques such as a genetic algorithm were employed to solve this optimization problem. The tracking of a trajectory of PSD was transformed into a multi-objective optimization problem, again in a hierarchical framework in terms of the nucleation and growth rates, and this was solved using a multi-objective extension of genetic algorithm (Non-dominated Sorting Genetic Algorithm). The ability to account for model-mismatch using the on-line measurements was examined using different estimation techniques. Also (off-line) feedback studies were performed which provide encouraging results about the optimization

and control of the PSD in semi-batch emulsion polymerization. The studies reveal the potential for different methodologies of feedback control, specifically in-batch (on-line) feedback control and batch-to-batch feedback control.

Chapter 1

INTRODUCTION

1.1 Distributed Parameter Systems

Most processes are distributed with respect to one or more of their internal characteristics. A classic example is the residence time of the components in a continuous stirred tank reactor (CSTR). More subtle, but well-known examples of the distributed nature of processes are the size distribution of crystals, emulsion polymers and granules, and the age distribution of microbial cell populations. These processes are categorized as distributed parameter systems (DPS). In addition to the above mentioned examples which constitute the so-called population balance systems, other examples of DPS include flow systems characterized by a velocity distribution, general reactor and separator systems characterized by a residence time distribution, and sheet and film-forming processes characterized by thickness profiles. Researchers in the past were obligated to treat these processes as lumped processes because of the following reasons:

- lack of instrumentation to discern these distributed attributes of the processes
- lack of computational tools to deal with the increased complexity
- lack of understanding of the underlying mechanisms that form distributions.

Analogous to the loss of performance associated with the design of ideal CSTRs, there is a loss of value in neglecting the distribution in size/age of crystals, polymer particles and cell populations. There is a recognition in the industries of a

need to reduce the fluctuations in product qualities by dealing with entire distributions (Congalidis and Richards, 1998). Furthermore, there is a growing recognition among researchers of the substantial improvement in product quality by acknowledging the distributed attributes of the processes (Doyle III et al., 2001; Christofides, 2002; Braatz and Hasebe, 2001; Daoutidis and Henson, 2001). Such improvements are obtained by tailoring the distributions to suit specific end-use applications. This idea is promoted by the recent advances in instrumentation technology and in computing technology. Most processes of interest in this regard are characterized by distributions in the sub-micron and nano scales. The advances in instrumentation facilitate the monitoring or inferring of the sub-micron and nano states of the system, thereby bridging the gap between the molecular scale and the macro scale. However, dealing with the nanoscale of the processes and with distributions necessitates development of knowledge and theories, leading to a multi-disciplinary research. This new rigorous approach, while benefiting from existing theories, also indicates the erroneous conclusions drawn when treating processes through lumped parameters. The rectification of such anomalies is an additional factor that leads to improvements in the processes, and in the product qualities.

1.2 PSD in Emulsion Polymerization

Emulsion polymerization, in which the polymer is primarily produced as a colloidal dispersion of particles in the aqueous phase, has several advantages over other types of polymerization processes such as bulk and solution polymerization. The compartmentalized (heterogeneous) arrangement of the reaction mixture enables producing high molecular weight products. Also, the overall Trommsdorff (gel) effect, being restricted to the particle phase, is much subdued in emulsion polymerization unlike in bulk polymerization. In addition, no organic solvents are employed in the formulation, alleviating environmental concerns. The particle size distribution (PSD) of the emulsion latex is strongly correlated with the end-product properties

of the emulsion. The PSD influences the rheological properties, adhesion, drying characteristics, optical properties, mechanical strength, and film-forming properties of the final products, which include adhesives, coatings, paints, *etc.* For example, the particle size distribution determines the achievable solids content, which in turn is critical for film-forming applications and mechanical strength. Similarly, paint-based applications require particular shear-thinning behavior – high viscosity at low shear rates and vice versa. Such properties are provided by multi-modal distributions, thereby motivating the need to produce multi-modal particle size distributions in the emulsions. The multi-modal PSDs of interest are not represented adequately by lumped properties such as average particle size or even with a small number of higher moments of the distribution. Hence, the problem of the control of the full distribution in emulsion polymerization becomes a classical example of nanoscale distribution control problems that lead to substantial quality improvements.

1.2.1 Mechanism of Evolution of Distributions

As illustrated in the foregoing discussion, emulsion polymerization is a multi-phase reaction system wherein the main locus of polymerization lies within organic particles (in the size range of about 2 nm to 1 μ), which are dispersed in the aqueous phase. The polymerization is primarily initiated in the aqueous phase, and results in aqueous phase oligomers. However, both the monomers and polymers have a limited solubility in the aqueous phase, thereby limiting the extent of polymerization in this continuous phase. The particle phase is formed by two major mechanisms involving the aqueous phase oligomers. The primary mechanism of particle formation is micellar nucleation, which is effected by the entry of an oligomer from the aqueous phase into a micellar aggregate of amphiphilic surfactants. These micelles are formed under high concentration of surfactant molecules in the aqueous phase, exceeding the critical micelle concentration (cmc) threshold. The second mechanism of particle formation does not explicitly involve the heterogenous surfactant molecules, and is

termed homogenous nucleation. This occurs by the precipitation of these oligomers into separate particles upon attainment of their critical chain lengths (corresponding to their solubility limits). The polymer chains inside the particles propagate at very high rates compared to that in the aqueous phase, causing the particles to grow in size. The growth dynamics depend on the number of polymer chains within the particles. This in turn depends upon the rate of entry of oligomers from the aqueous phase into the particles, the rate of desorption of chains formed by chain transfer within the particles back into the aqueous phase, and the rate of mutual termination of chains within the particles. Particles can also increase in size by coalescence with other particles, either due to insufficient stabilization by surfactants or due to the shear stress imparted on the particles by the mixing in the reactor. Thus, the particle size distribution (PSD) is determined by the interplay of three major processes – nucleation, growth and coagulation. See (Gilbert, 1995; Asua, 1996) for a good introduction to emulsion polymerization.

Although emulsion polymerization has the operational advantage of a subdued gel effect compared to bulk polymerization, the stabilization of the dispersed phase is critical, and leads to concerns with instrumentation and operation. The stabilization is achieved by the use of surfactants to counter the universal van der Waals' forces. These amphiphilic and surface-active surfactants adsorb onto the particles with their hydrophobic end-groups, while the hydrophilic end-groups extend into the aqueous phase. Different surfactants effect stabilization by different mechanisms. The two major types of surfactants are ionic and non-ionic. Ionic surfactants stabilize the particles by electrostatic repulsion caused by the charge attached to their hydrophilic ends. On the other hand, the non-ionic surfactants cause the stabilization by many different, relatively less understood processes. The major process among these is steric stabilization, caused by the bulkiness of the surfactant chains. In addition to the surfactant-induced stabilization, the shear effects due to

mixing play a strong role in determining particle (in)stability.

In addition to particle stabilization, surfactants play a major role in the micellar nucleation phenomenon by forming micelles which serve as precursors to particles (new reaction sites). This role is uncomplicated in the case of the ionic surfactants which restrict themselves to the aqueous phase and its interface with the dispersed phases. The micelles are formed when the concentration of the surfactants in the aqueous phase exceeds the cmc value. On the other hand, the non-ionic surfactants partition into the dispersed phases leading to profound alterations to the nucleation pattern. However, the non-ionic surfactants are preferred over their ionic counterparts, as the ionic surfactants adversely affect the water-resistance characteristics of the emulsion polymer.

1.3 Issues in the Control of Distributions

To attain the goal of the control of the full distributions, one has to start from scratch on several counts, including process analysis and controllability studies, process modeling, optimization and control. The focus on the sub-micron regime would require the knowledge of aspects that were not critical or essential when dealing with the macro scale. A good understanding of the intricate behavior of the distributions are required. The modeling studies assume special considerations with regard to the underlying concepts, and the computational complexity. Optimization and control might necessitate the development of newer tools and algorithms, assuming newer dimensions. These aspects are outlined below.

1.3.1 Instrumentation and Monitoring

The success of the studies on the control of PSD depends upon several factors, the primary factor being the availability of good instrumentation. Feedback control necessitates the measurement of PSD on-line, at a sufficiently rapid frequency. One

also needs a good understanding of the mechanism of the evolution of the PSD, and the sensitivities in the process.

Monitoring emulsion polymerization is easier as compared to bulk polymerization, and a considerable literature exists on this topic, particularly for macroscopic and lumped properties such as the conversion and copolymer composition. However, an issue to be reckoned with is the coagulation of the mass in the sampling loop. Recent improvements enable the monitoring of the process at the sub-micron level, and at sufficiently rapid frequency to enable on-line control. Instruments for monitoring the PSD include light scattering equipment, and more recent hydrodynamic equipment. Kammona *et al.* (1999) provide an excellent review on the instrumentation applied to emulsion polymerization. To cite a few relevant studies, Noel *et al.* (1995) investigated the use of on-line gas chromatography and densimetry to obtain the conversions of the individual monomers in a two-monomer system. Siani *et al.* (1999) also investigated the inference of monomer conversion for multi-monomer systems using ultrasonic sensors. The use of calorimetry to monitor conversion in emulsion polymerization via the direct measurement of the polymerization rate, was demonstrated by several authors (McKenna et al., 1996; Ozdeger et al., 1997b; de la Rosa, 1996). Liotta (1996) constructed a model emulsion polymerization system incorporating instrumentation for on-line measurement of conversion and PSD, as part of a study on the control of the diameter ratio of bi-disperse populations.

Several studies addressed the evolution of the distribution in semi-batch emulsion polymerization, by focusing on individual aspects of the evolution. Chern *et al.* (1997) studied the effect of mixtures of anionic and non-ionic surfactants on the coagulation phenomenon, and found that the system considerably deviates from Smith-Ewart kinetics. Piirma & Chang (1982) studied the alterations to the nucleation pattern introduced by non-ionic surfactants, attributed to their tendency to

be absorbed into the dispersed phases. Similar observations were made by Ozdegar *et al.* (1997a; 1997b) in the batch emulsion polymerization of styrene and n-butyl acrylate using non-ionic surfactants. Low and high initial surfactant concentrations resulted in unimodal distributions, while intermediate concentrations resulted in bimodal distributions in batch polymerization. The unimodal distributions produced at low initial surfactant concentrations were attributed to homogenous nucleation and those at high initial surfactant concentrations were attributed to micellar nucleation. The bimodal distributions produced in the intermediate case were attributed to a primary homogenous nucleation followed by a secondary micellar nucleation. Sajjadi & Brooks (2000) observed the evolution of bimodal distributions in semi-batch recipes that do not contain any emulsifier in the initial batch. The primary nucleation event was attributed to the homogenous nucleation mechanism, and the secondary nucleation was attributed to either homogenous or micellar nucleation. However, detailed modeling studies undertaken in this dissertation have indicated that even for a highly water-soluble monomer such as vinyl acetate, homogenous nucleation rate fails to compete with radical entry into existent particles/micelles. This clearly attributes the secondary nucleation event seen in the study of Sajjadi & Brooks on butyl acrylate emulsion polymerization to a micellar phenomenon. The work of Sajjadi & Brooks serves as an experimental demonstration of the feasibility of effecting secondary particle nucleation and producing bimodal distributions by semi-batch operation, particularly with surfactant feed. This aspect was demonstrated via detailed mathematical modeling by other authors (Crowley et al., 2000; Meadows et al., 2002).

1.3.2 Sensitivity Studies, Process Potentials and Limitations

Effective control of any process depends upon two pre-requisites – the identification of the sensitivities in the process on the one hand and its potentials and

limitations on the other. The first step enables developing efficient and effective control strategies. While this analysis is obvious and intuitive in most systems when viewed through lumped parameters, in the case of new and emerging processes, particularly when characterized by distributions and profiles, any intuition that may be available is negated in a number of situations. The few studies reported in the literature on the control of distributions have defaulted on surfactant feed, in some cases along with initiator feed, as the manipulated variable. For certain specific applications (to control the growth of seeded particles), researchers have employed monomer feed as the manipulated variable. However, the mechanism of formation of distributions and profiles are intricate and are influenced in complex and in some cases non-intuitive ways by the inputs available in the process, as would be clear from the mechanism presented previously. It is of interest to identify the most suitable control configurations for all possible scenarios. Hence the need for the sensitivity analysis.

The second pre-requisite for efficient design and control is the identification of the reachable regions of the outputs — this aspect also being tied to the potentials and limitations in the system. Again, while it is easier to ascertain the controllability of lumped parameter systems, it is not so in the case of the distributed parameter systems (which are modeled through partial differential equations). Distributions constitute an infinite-dimensional system with respect to the outputs, while the dimension of the inputs is small (depending upon the parameterization chosen). Thus, the achievable distributions are limited. Also, in the case of multi-variate systems, the attainable regions of the different variables are usually correlated, and hence the reachability analysis assumes a further dimension. This is the case for the control of distributions, and thus the shape of the achievable distributions are limited. These aspects need to be understood to formulate meaningful control objectives for the process. Semino & Ray (1995a) addressed the controllability of population

balance systems. They found in their study that employing the feed concentration of surfactant, initiator and inhibitor as manipulated variables ensures the controllability of the distributions for the unconstrained case. Liotta, Georgakis, Sudol & El-Aasser (1997) performed simulation-based controllability studies to determine the reachable region for the control of the diameter ratio of a bi-disperse population. They identified the reachable regions of diameter ratio, and examined its sensitivity to the initial conditions. They used the monomer concentration within the particles as the manipulated variable, which in turn can be controlled by manipulating the monomer feed rate. The upper and the practical lower limits on the monomer concentration within the particles were used to identify the reachable regions. These aspects need to be elaborated upon under more general conditions, and the controllability under constrained conditions needs to be studied.

1.3.3 Process Modeling and Computational Methods

As in the case of the sensitivity and controllability analyses, the new outlook to the process requires a paradigm shift in the modeling approach too. There is a rich literature on lumped parameter models for emulsion polymerization processes, starting with the conventional Smith-Ewart model which identified three regimes in terms of the relative importance of the rates of entry, desorption and termination (Gilbert, 1995), and derived expressions for the average number of radicals per particle $\bar{n}$ for each regime. The lumped parameter models approximate complete PSD or molecular weight distribution (MWD) information by a few moments. These models enable calculation of monomer conversion and average co-polymer composition. The average number of radicals per particle $\bar{n}$ is modeled using the expression of Smith & Ewart (corresponding to one of the three regimes) or the Stockmayer & O'Toole modifications (O'Toole, 1965). Such lumped parameter models include the works of Nomura *et al.* (1982), Dimitratos *et al.* (1989; 1991) and Urretabizkaia *et al.* (1992). Penlidis *et al.* (1985) provide a review of the lumped parameter models in

emulsion polymerization. Forcade & Asua (1990) modeled three populations of particles – characterized by the number of radicals in them. DeGraff & Poehlein (1971), Kiparissides *et al.* (1979) and Mead & Poehlein (1988) studied continuous emulsion polymerization reactors. Richards *et al.* (1989) lumped all particles above a cut-off size into a single entity in their model, although they account for the size distribution of the particles at the smaller size end.

Min & Ray (1974) were among the first to introduce a paradigm shift in the modeling of PSD, by employing the population balance approach to model the entire PSD. In this approach, the particles are characterized by a population density function such as $F_n(x,t)$ – a measure of the concentration of particles having n growing radicals, where x is some measure of the particle size, say mass, volume, radius, life time, etc. Rawlings & Ray (1988a; 1988b) generalized this model and performed parametric sensitivity studies. Storti *et al.* (1989) proposed the pseudo-homopolymerization approach, as an extension of the model to copolymer systems. Saldivar *et al.* (1998) developed a comprehensive and generalized model for PSD and MWD for multi-monomer systems, employing the pseudo-homopolymerization approximation. Melis *et al.* (2000) addressed the modeling of the coagulation phenomenon in a population balance framework. Another class of distributed parameter population balance modeling is the zero-one model. This model assumes that the particles have either one radical or none at all, based on assumptions on the rates of entry, termination and desorption. Chen & Wu (1988) modeled a copolymer system using the zero-one model. Other studies based on the zero-one approach include the works of Coen *et al.* (1998), Crowley *et al.* (2000) and Araujo *et al.* (2001).

In general, population balances account for the modeling of systems characterized by nucleation (birth), growth (aging), and coagulation/breakage (aging and loss). These so-called population balance systems are represented by some quantity

of interest that is distributed along a certain coordinate of property, *e.g.,* the population of the world, which is distributed with respect to the age of the members. Although the birth and loss of members can be accounted for by the conventional material and energy balances, the drift of the population from one age group to another (the aging process), which is internal to the system, requires a new modeling framework. The population balance modeling principle accounts for these internal realignment processes. The population balance concept has been employed in solving chemical engineering problems since the early 1960's, covering a wide range of systems which fall under the broad class of distributed parameter systems. The systems considered range from crystallization (Randolph and Larson, 1962), microbial cell population (Fredrickson and Tsuchiya, 1963), and residence time distribution or catalyst activity distribution in fluidized bed reactors (Behnken et al., 1963; Randolph, 1964). The text by Ramkrishna (2000) provides a very good introduction to population balances.

The general population balance equation is given by:

$$\frac{\partial}{\partial t}\zeta(\eta,t) + \frac{\partial}{\partial \eta}(\zeta(\eta,t)\frac{d\eta}{dt}) = \Re_{nuc}(\eta,t) + \Re_{internal}(\eta,t) \tag{1.1}$$

where $\zeta(\eta,t)$ is the population density function, defined such that $\zeta(\eta,t)d\eta$ is the concentration or value of the quantity whose internal property value lies within a small interval $d\eta$ of η. $\Re_{nuc}(\eta,t)$ accounts for the 'birth' of the quantity in the various parameters range. For example, in human population balance, birth is restricted to the smallest age group, and $\Re_{nuc}(\eta,t) = 0$ for $\eta > \eta_{min}$. The terms $\frac{\partial}{\partial \eta}(\zeta(\eta,t)\frac{d\eta}{dt})$ and $\Re_{internal}(\eta,t)$ are the two terms which account for the internal realignment processes. The partial derivative term accounts for a continuous growth process, *e.g.,* the aging process in human populations, in which case the term $\frac{d\eta}{dt} = 1$ (as in the case of all systems where age is the internal coordinate). Similarly, in polymerization processes, the entities increase in size/length due to the polymerization reactions, in which case $\frac{d\eta}{dt}$ is related to the polymerization rate. $\frac{d\eta}{dt}$ can also take negative values, as in

the case of the dissolution process. While this first realignment term accounts for a relatively gradual process, the other realignment term ($\Re_{internal}(\eta, t)$) accounts for more discrete processes. These include the coagulation (aggregation) and breakage processes. Coagulation accounts for the merging of two components with particular values of the internal quantity to form a third component with a different value of the internal quantity. For example, in granulation, two particles of sizes r_1 and r_2 combine to form a single particle of a larger size r_3. Breakage accounts for the converse effect, of one particle breaking into two (or more) smaller particles. The internal coordinate η can also assume discrete values – for example, the number of active radicals and inactive polymer chains inside the particles in emulsion polymerization. As mentioned earlier, systems characterized by population balance cover a wide gamut, ranging from crystallization, precipitation, granulation, cell population and viral population in biochemical and biomedical applications, mineral processing (dissolution), comminution processes, and a variety of polymerization systems (both homogeneous and heterogeneous).

One important issue in population balance modeling is the computational solution of the resultant partial differential equations or integro-partial differential equations (the integrals arising in the $\Re_{internal}(\eta, t)$ term). While this issue has limited the type of applications amenable to population balance considerations, the recent advances in computing have greatly facilitated the application of population balances to many complicated systems. The recent applications of population balance principles include, besides emulsion polymerization, crystallization (Braatz and Hasebe, 2001; Gerstlauer et al., 2001), precipitation (Falk and Schaer, 2001; Mahoney and Ramkrishna, 2002), cell populations (Daoutidis and Henson, 2001), dissolution processes (Giona et al., 2002), polyolefins (Prasetya et al., 1999; Yiannoulakis et al., 2001), and micro-emulsion applications (Bandyopadhyaya et al., 1997; Ramkrishna and Mahoney, 2002).

1.3.4 Optimization and Control

In contrast to the relative dearth of literature on the control of the full PSD, there is a considerable literature on the control of lumped properties. These include the studies addressing the issue of state estimation for semi-batch emulsion polymerization. These state estimation studies become important for feedback purposes, either due to the lack of instrumentation to measure several important properties, or due to infrequent measurements. Such state estimation studies include the works of Dimitratos *et al.* (1989; 1991), Kozub & MacGregor (1992b), Liotta, Georgakis & El-Aasser (1997) and Astorga *et al.* (2002). These studies used an extended Kalman filter with parameter augmentation of the states, and a receding-horizon framework in the estimator. Kozub & MacGregor (1992b) suggested the need to update the initial conditions in addition to the parameters (reiterative extended Kalman filter), along the lines of the proposition in Jazwinski (1970). They suggest a full non-linear optimization strategy utilizing all the data points (available up to the current time), to determine the initial conditions. However, all these studies deal with lumped parameter models, and there are no state estimation studies reported, that deal with the full PSD in emulsion polymerization.

On the optimization and control of semi-batch emulsion polymerization, Kozub & MacGregor (1992a) applied the idea of a two-tier control strategy – open-loop feed-forward design of an optimal recipe, which is then re-computed on-line based on feedback from process measurements – for the multi-variable control of composition and average molecular weight. They utilized the idea of the control of instantaneous properties. A similar strategy was employed by Urretabizkaia *et al.* (1994) for the open-loop control of ter-polymer composition. Saldivar & Ray (1997) studied the control of copolymer composition and average molecular weight for semi-continuous emulsion polymerization, employing open-loop recipe design coupled with on-line re-computation based on measurements – the so-called

two-tier approach. This work was the first experimental application of multi-variable control in emulsion polymerization. Semino & Ray (1995b) demonstrated the control of PSD, based on their controllability studies on the system. Liotta, Georgakis & El-Aasser (1997) configured a linear MPC with state estimation for the control of the diameter ratio of a bi-disperse (two mono-disperse) population. Liotta, Georgakis, Sudol & El-Aasser (1997) studied the possibility of exploiting the gel-effects for manipulating competitive particle growth on a styrene system. Clarke-Pringle & MacGregor (1998) presented a batch-to-batch adjustment strategy for the control of molecular weight distribution (MWD), to re-optimize the inputs for the subsequent batch based on end-point measurement of the MWD. Crowley *et al.* (2000) were among the first researchers to address the optimal control of the full particle size distribution. They used a detailed population balance model for styrene emulsion polymerization to design open-loop optimal recipes for semi-batch emulsion polymerization, to achieve a target PSD. They considered different objective norms, with both surfactant feed rate and free surfactant concentration as possible manipulated variables. In a subsequent study, Crowley *et al.* (2001) used a hybrid modeling strategy in batch-to-batch optimization for PSD control. They augmented their first-principles model with a Partial Least Squares (PLS) correction to account for model discrepancies. This PLS correlation was updated after each batch, and the combined model used to re-optimize the feed profile. Recently, Flores-Cerrillo & MacGregor (2002) developed a feedback control strategy for the control of PSD, in which they employ a mid-course correction to the open-loop optimal recipe based on the PSD measurement available by that time. They addressed the control of both absolute and relative distributions in their study.

1.4 Outline of the Dissertation

The objective of this dissertation is to address the different challenges and issues involved in the control of distributions that were highlighted above. The test

bed chosen for the study is the control of PSD in emulsion polymerization. The specific system chosen is vinyl acetate (VAc) - butyl acrylate (BuA) co-polymerization with non-ionic poly-ethylene oxide surfactants. A redox initiator pair of t-butyl hydrogen peroxide (tBHP) and sodium formaldehyde sulphoxylate (SFS) is employed, with ferrous ammonium sulphate as the co-ordination agent. In addition to addressing the specific problem of the control of PSD in emulsion polymerization, the study also serves as a guide to general population balance systems. The dissertation is organized as follows: chapter 2 presents the experimental system and defines instrumentation considerations. It also studies the evolution of PSD in semi-batch operation, examines the overall feasibility of producing multi-modal distributions, and presents different methods of producing these multi-modal distributions. Chapter 3 presents a detailed population balance model, with parametric sensitivity studies on the model. Validation of the model against experimental data is also discussed. Chapter 4 presents an efficient numerical computation technique for population balance models. Chapter 5 presents experimentally-observed sensitivities aimed at identifying suitable manipulated variables and control configurations. It also presents simulation-based reachability studies that identify potentially-reachable distributions, and the effect of disturbances and uncertainties on the reachable distributions. Chapter 6 presents open-loop optimization studies to attain target end-point PSDs and track target PSD trajectories. The chapter also presents feedback considerations of state estimation and receding horizon re-optimization of the recipe. Chapter 7 presents conclusions with indications to future work.

Chapter 2

EXPERIMENTAL STUDY OF THE EVOLUTION OF MULTI-MODAL PARTICLE SIZE DISTRIBUTIONS

2.1 Introduction

The success of the open-loop and feedback studies aimed at the control of the PSD depends upon several factors including accurate instrumentation, a solid understanding of the mechanism of the evolution of the PSD, and some knowledge of the sensitivities in the process.

Experimental and theoretical studies in emulsion polymerization have covered a wide range of topics, from kinetic studies, to analysis of particle formation and growth, to instrumentation and calibration procedures. This chapter addresses most of these issues in a consistent framework. In particular, the aim of the chapter is to

- present an overall emulsion polymerization system, equipped with state-of-the-art sensors for both on-line and off-line measurements, and adapted for both semi-batch and batch emulsion polymerization
- describe procedures for interpretation of sensor measurements (first principle-based calibration)
- study the mechanism of evolution of PSD and demonstrate the evolution of multi-modal distributions in semi-batch emulsion polymerization.

2.2 Experimental System

Figure 2.1 shows the schematic of the experimental facility employed in the study. This facility is based on a similar facility at the Emulsion Polymerization Institute at the Lehigh University, Pennsylvania (Liotta, 1996). It includes a 3 liter borosilicate reactor (Chemglass), equipped with four vertical baffles, and implemented with an agitator from Parr Instruments. The agitator shaft is provided with three 45^0 teflon impeller blades of $2\frac{1}{2}''$ diameter, attached about 1 cm apart, and is about 2 cm from the bottom of the reactor. The top of the reactor is covered with a Stainless Steel plate, and sealed using gaskets and a Stainless Steel latch. The reactor is provided with a jacket, which serves as one means of heat transfer. The temperature of the reactor is controlled through a Lauda circulator, which is equipped with a temperature bath. The bath could be used for both heating and cooling, via automatic control through a solenoid valve attached to a cooling water loop. The other means of heat transfer from the reactor is through an overhead condenser (Lauda) (connected to the shell side of a chiller), attached to the top of the reactor. The reactor headspace is continuously purged with nitrogen gas to maintain an inert (oxygen-free) environment in the reactor. This exit purge gas, with the vapors of the monomers and water, passes through the overhead condenser, and gets condensed back to the reactor. The uncondensed purge gas is then bubbled through cold water in a dip-tube, to condense out any remaining monomer before release into the fume hood.

The top plate of the reactor has openings for the feed streams – the monomers, surfactants, and initiators. These openings are connected through Swagelok fittings to $\frac{1}{8}''$ teflon tubings, that emanate from the feed pumps. Reciprocating pumps are used to feed the reagents from the burette to the reactor, through these $\frac{1}{8}''$ tubing. The feed pumps (Fluid Metering Inc.) are equipped with Hall effect flow sensors,

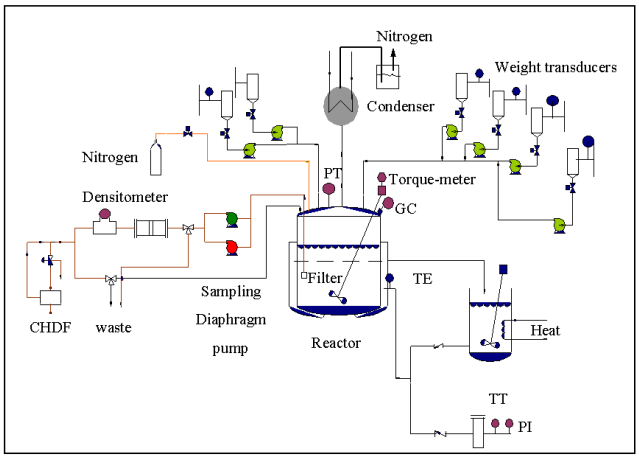

Figure 2.1: Schematic of the experimental emulsion polymerization system.

which measure the feed rates based on the speed of rotation of the pumps. An alternative, more robust measurement of feed rate is through weight or force transducers (Load cells) from Interface Inc., from which the feed burette are suspended. These load cells record the weight of the burette, from which data the mass of reagent fed and their mass feed rate can be calculated. The top plate of the reactor is also provided with openings for a Pressure Transducer (Cole Parmer), and a Resistance Temperature Detector (RTD) (Omega Engineering) for temperature measurement. For the latex sampling, a $\frac{1}{4}''$ Stainless Steel dip tube from the latex is attached to another opening in the top plate, which is connected through Swagelok fittings to $\frac{1}{4}''$ teflon tubing leading to a diaphragm pump (Cole Parmer). The diaphragm pump outlet passes through the tube side of a shell-and-tube heat exchanger, into an on-line Anton Parr densitometer. This unit measures the density of the latex by measuring the frequency of vibration of the glass U-tube through which the latex passes. A slip stream is taken from the outlet of the densitometer to a MATEC Capillary Hydro-Dynamic Fractionator (CHDF) for measurement of Particle Size

Distribution (PSD), while the rest is returned to the reactor, through another opening in the top plate.

The CHDF is chosen over the light scattering equipment due to ease of adaptation for on-line purposes, and the better resolution over a wider particle range, in spite of a longer measurement time. In particular, the CHDF resolves the distribution every 4 nm from 8 nm to 500 nm, and every 5-6 nm up to 1100 nm. The instrument fractionates the particles based on their size using the concept of hydrodynamic segregation. The latex is diluted and carried through a long capillary column by the eluant stream at a fixed flow rate. The particles are segregated in this laminar flow regime based on size, with the largest particle eluting first and the smallest eluting last. The particle size is obtained from the elution time via calibration for a particular flow rate of the eluant. The particle size is estimated based on reference particles, using the retention factor values. The relative particle concentration in the various size ranges is determined through UV absorbance. See DosRamos and Silebi (1993) for more details on the instrument. The analysis of each sample takes approximately 11 minutes, as the sample is eluted through the capillary. The CHDF is augmented with a LabPRO autosampler for on-line PSD analysis. Figure 2.2 shows a schematic of the sampling process. The slip stream from the sampling loop (densitometer outlet) is diluted with an eluant stream from the CHDF itself (through a T-connection), and circulated through a sampling loop (25 μl capacity) to the waste. The marker (sodium benzoate) reference fluid is also circulated through another sampling loop of 20 μl capacity ($\frac{1}{16}''$ tubing employed for these flow streams). Once a sample has been analyzed, and after the specified wait period, the 10-way vial of the autosampler is switched to position 1 (see Figure 2.2(b)). At this time, a new sample is injected into the CHDF for analysis. One minute after injecting the sample, the autosampler switches to position 2 (Figure 2.2(c)), during which time the reference is injected into the capillary. The

autosampler then returns to its normal position. Thus, on-line PSD measurements are obtained once every 11 minutes.

A Honeywell distributed control system (DCS), Plantscape, is employed for both the data acquisition and for the operation of the process. The DCS system is provided with the hybrid control module and the control and monitoring softwares. The hybrid control module is the I/O card that interfaces the process with the computer. It receives 4-20 mA signals from the process (or 0-5 V as appropriate), relaying it to the computer in suitable digitized format, and also conveys control moves back to the process as 4-20 mA signals through D/A converters. The control software can be used to build PID (proportional-integral-derivative)-type controllers, and also sequential logic controllers. The monitoring software provides a user interface to monitor plant operation, make set-point changes, and to historize process data. The Anton Parr densitometer is provided with an evaluator unit to convert the vibration frequency measurements to density information. This unit produces a 4-20 mA analog output signal which is conveyed to the hybrid controller (through wiring). Similarly, the load cells are attached to transducers that produce 4-20 mA signals. The flow meters in the feed pumps are attached to frequency-to-analog transducers, to produce the appropriate current signals. The hybrid controller is adaptable with the resistance signals from the RTD used for the temperature measurement. Each of these measurements are calibrated in the software, to convert the signals to appropriate engineering units (using a linear scaling). In the case of the PSD measurements from the CHDF, they are processed in a dedicated PC through the MATEC software, to produce PSD information. This information is then conveyed to the Honeywell PC through data-transfer protocol, from where the Plantscape software reads the data into it as points. Advanced control requires application program interfacing between a FORTRAN or C application and the Plantscape software. The software is set to historize the data once every

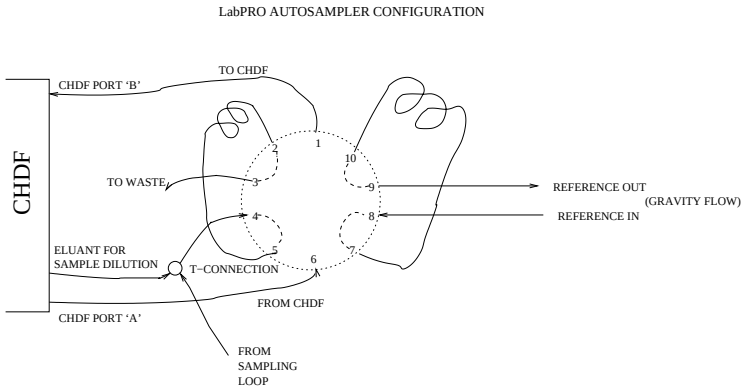

(a) rest position of the on-line autosampler

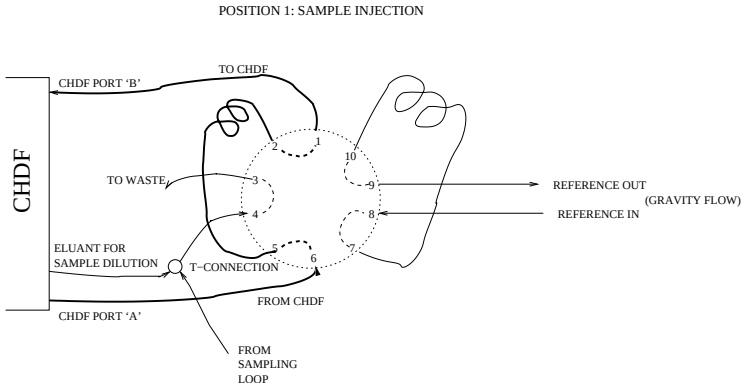

(b) sample injection position of the on-line autosampler

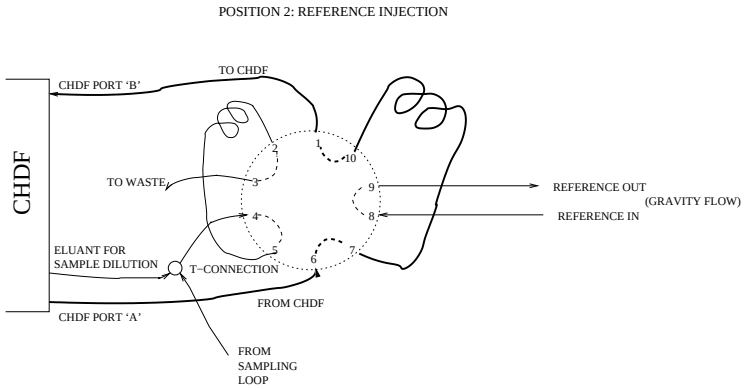

(c) reference injection position of the on-line autosampler

Figure 2.2: LabPRO autosampler 10-way valve configuration for on-line sampling of the latex from the sampling loop.

minute for all important process information such as feed rates, load cell readings, density measurements, reactor temperature and agitator speed. The feed pumps are operated through FMI stroke rate controllers, which are amenable to both remote and manual modes of operation. Remote operation is through 4-20 mA signals, emanating from the Plantscape DCS system and conveyed through the hybrid controller block.

2.3 Experimental Procedure and Typical Results

The monomers of interest in our study are vinyl acetate (VAc) and n-butyl acrylate (BuA). The emulsifiers employed are non-ionic poly-ethylene oxide surfactants in most cases, although anionic surfactants have also been considered. Figure 2.3 shows the chemical structure of the various surfactants employed in the study. The initiator employed is a redox pair, t-butyl hydrogen peroxide (t-BHP) and sodium formaldehyde sulphoxylate (SFS), with ferrous ammonium sulphate as the coordination agent. The monomer pair has a large reactivity ratio (with BuA being the more reactive monomer), and wide differences in saturation limits and solubilities in the particles and the aqueous phase (VAc has about 2% solubility in water while BuA has a trace solubility). The non-ionic surfactants add to the richness of the process by alterations in the nucleation pattern, attributed to their tendency to partition into the particles and monomer droplets. The redox initiation mechanism in itself is quite complicated and not well-understood. The reducer in the redox pair, SFS can itself act as an initiator under certain conditions (Wang et al., 2000). In addition, the oxidant t-BHP tends to participate in the partitioning phenomenon, like the monomers and the surfactants. The redox mechanism however, has more flexibility than the thermal initiation, and is also conducive to low temperature operations. However, too low temperature operation may not be desirable due to cloud point considerations with the surfactants. The normal operating temperature is 60^0C in these experiments.

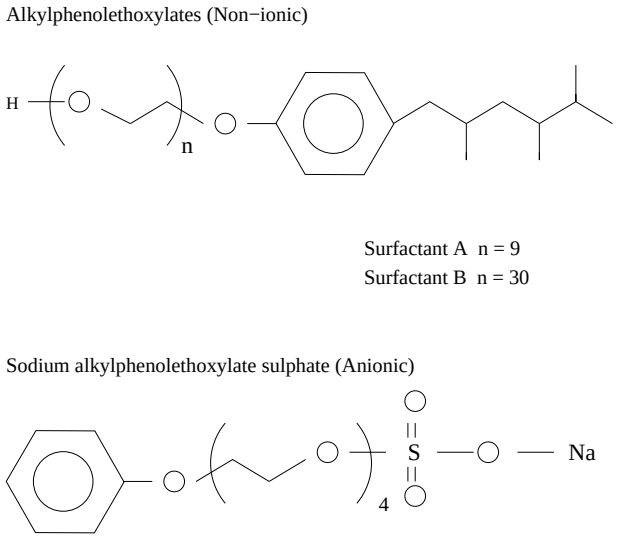

Figure 2.3: Chemical structure of the surfactants employed in the study.

The experiments involved elaborate pre- and post-operations. The pre-experimental operations involve preparing the reagents and the initial mixture. The reagents are added to the burette, and the initial mixture to the reactor. The reactor is mounted on a stand and sealed air-tight to ensure that the purge gas exits through the overhead condenser and bubbler. (Typically, the experiments are performed close to atmospheric pressure). The purging of the reactor with nitrogen gas is started, and the mixing of the reactor contents is initiated. The heating of the reactor through the circulator is begun 20-30 minutes after the start of the purging. The sampling pump is started, and maintained at a constant circulation of about 25-30 ml/min. After the contents are raised to the reaction temperature and maintained, the monomer in the initial recipe is added, and the temperature is controlled to the set-point value.

The process itself is carried out in an automated fashion, using the sequential control option available in the Plantscape control software. The software is preprogrammed to implement the recipe. This sequential controller writes the set-point values for the reagents, making the necessary changes in the feed rates at the appropriate times, and returns control to the operator (to make changes to the

recipe on-line, if needed). For future control experiments, an application program will write set-points to these PI(D) controllers (over-riding the open-loop sequential controllers). Each of these feed rates are then maintained by the corresponding PI controllers, by varying the pump speeds. The temperature is maintained at the set-point value through a PID controller, that provides a set-point value for the bath temperature (cascaded control).

Figure 2.4 shows the feed profiles for a typical semi-batch emulsion polymerization experiment. The monomer feeds (VAc and BuA) are pure components, while the surfactant and initiator feeds are aqueous solutions. The surfactant employed in this recipe (surfactant A) has a low carbon chain length (9 ethylene oxide linkages, molecular weight 616), a relatively low cmc value (5×10^{-5} mol/liter at room temperature), and a tendency to partition into the dispersed organic phases (partition co-efficient value at room temperature of 15.5 into the monomer droplets, with a hydrophilic-lyophilic balance of 13.0), besides being adsorbed onto the interfaces (adsorption isotherm characterized by an adsorption equilibrium constant of $K_{ad} = 1 \times 10^6$ liter/mol, and a maximum surface coverage of $\Gamma_\infty = 4.5 \times 10^{-6}$ mol/sq.m). The surfactant solution has a weight % concentration of 22.8, while the redox pair t-BHP and SFS have weight % concentrations of 3.33 and 3.41, respectively. The recipe is programmed in the sequential controller and implemented in an automated fashion. Figure 2.5 shows the latex density over the course of the batch spanning two hours. The data shows two periods of increasing rates – one around 10 minutes and the other around 45 minutes, with a period of near-constant rate in between (after a slight slump). The rates begin to fall after the monomer feeds are completed, and the density value stagnates after about 90 minutes, in spite of an increase in the initiator feed rates at this time. For most part of the batch, the temperature was within +/- 2^0C of the set-point value of 60^0C. Thus, the batch is assumed to be isothermal in treating the density data, as per the sensitivity result

present by Rawlings and Ray (1988a).

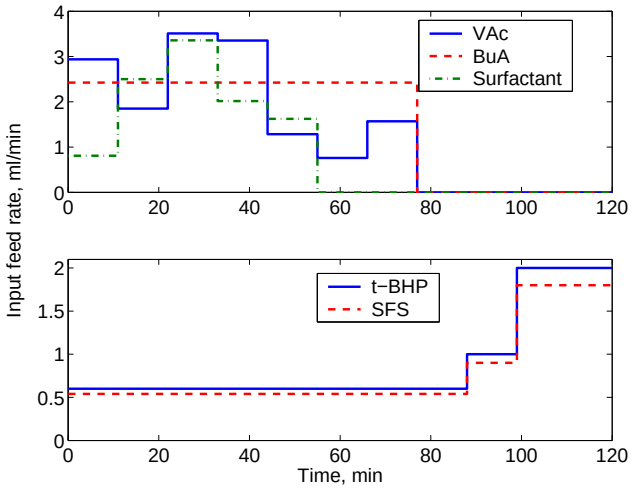

Figure 2.4: Nominal feed profile for semi-batch emulsion polymerization.

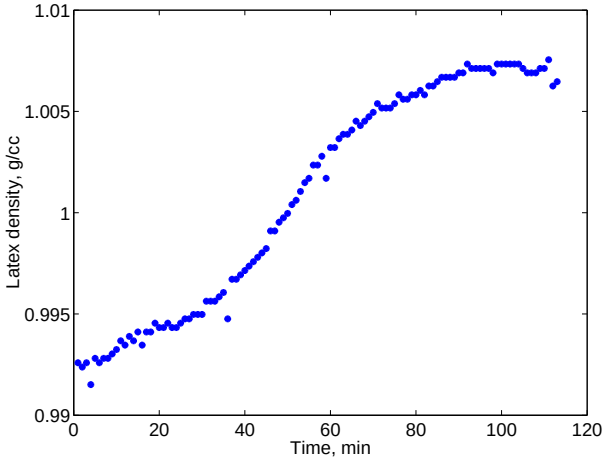

Figure 2.5: Evolution of the latex density during the semi-batch experiment.

2.3.1 Analysis of latex density data

The information of the density of the latex along with the feed rates of the various reagents can be utilized to calculate conversion values, solids content, and the co-polymer composition. This can be done by calibrating the densitometer, or

by employing process calculations. The former approach is discouraged mainly due to the fact that a number of factors influence the underlying calibration. The calibration would be limited to one set of conditions, and a separate calibration would be needed for every possible condition. Also, a separate calibration would be necessary for every system. These aspects advocate the use of simple first principle-based process calculations in interpreting the data. Another advantage with this model-based approach is that it enables the calculation of the partial conversion of both the monomers from the densitometer measurements (along with the information of the feed rates and total masses that are available from the measurements of the flow meters or the load cells). While this calculation is straightforward in the case of hompolymerization, a copolymerization system is more involved, necessitating reactivity ratios and the partitioning calculations. This is done as follows: the total mass of the various reagents in the latex (monomers, surfactants, water, initiator components) at any given time is calculated from the load cell readings, and the total mass of the latex is computed. From the value of the density of the latex at the current time instant and the total mass of the latex, the volume of the latex is calculated. At this stage, the assumption of the ideality of the latex is invoked. Although the polymeric solution is far from ideal, the ideality assumption is quite common in the calibration of instruments (Siani et al., 1999). Thus,

$$V_{m1} + V_{m2} + V_p + V_w + V_{surf} = V_T = \frac{m_T}{\rho_{latex}} \tag{2.1}$$

where V_{mi} is the volume of unreacted monomer 'i' in the latex, V_p is the volume of the polymer in the latex, V_w is the volume of water, V_{surf} is the volume of the surfactants, V_T is the total volume of the latex, m_T is the total mass of the latex (from load cell measurements) and ρ_{latex} is the density of the latex (from the densitometer). V_w and V_{surf} are known from the mass of these reagents in the latex, and known density values. Although volume additivity is invoked, a provision does exist to account for non-ideality in an approximate manner. At the initial time

(before the start of polymerization) the volume change on mixing can be computed as

$$\Delta V_{mix} = V_T - V_{m1} - V_{m2} - V_w - V_{surf} \tag{2.2}$$

This change can be assumed constant throughout the batch. Although this accounts for the non-ideality in the initial colloidal dispersion, the non-ideality could increase with the formation of polymer in the latex.

The total mass balance on the components is:

$$V_{m1}\rho_{m1} + V_{m2}\rho_{m2} + V_p\rho_p = m_{m1}^T + m_{m2}^T \tag{2.3}$$

where m_{mi}^T is the total mass of the monomer 'i' added to the latex up to the current time instant. The ratio of the conversion of the two individual monomers is computed as:

$$\frac{(V_{m1}^T - V_{m1})\rho_{m1}}{MW_{m1}} = \Re\frac{(V_{m2}^T - V_{m2})\rho_{m2}}{MW_{m2}} \tag{2.4}$$

where V_{mi}^T is the total volume of monomer 'i' fed to the reactor up to the current time instant, MW_{mi} is the molecular weight of monomer 'i', and $\Re$ is the ratio of the reaction rate of monomer 1 to that of monomer 2. This can be calculated as $\Re = \frac{k_{p11}p_1[M_1]_p + k_{p21}p_2[M_1]_p}{k_{p12}p_1[M_2]_p + k_{p22}p_2[M_2]_p}$, where p_i $(i = 1, 2)$ is the pseudo-homopolymer probability (fraction of polymer radicals of type 'i') (defined in Chapter 3), $[M_i]_p$ is the concentration of monomer 'i' in the particle phase, k_{pij} is the propagation rate constant for polymer of type 'i' with monomer 'j', . The pseudo-homopolymer probability is calculated as $p_1 = \frac{k_{p21}[M_1]_p}{k_{p21}[M_1]_p + k_{p12}[M_2]_p}$, and $p_2 = 1 - p_1$, neglecting the chain transfer events (Storti et al., 1989). Thus, the ratio of the reaction rates becomes $\Re = \frac{k_{p21}(k_{p11}[M_1]_p + k_{p12}[M_2]_p)[M_1]_p}{k_{p12}(k_{p21}[M_1]_p + k_{p22}[M_2]_p)[M_2]_p}$.

In the above equation, the instantaneous reactivity ratio is applied for the entire duration from the start of the batch to the current time instant. One could instead recast it to account only for the current time instant as:

$$\frac{(V_{m1}^{p}+V_{m1}^{a}-V_{m1})\rho_{m1}}{MW_{m1}} = \Re\frac{(V_{m2}^{p}+V_{m2}^{a}-V_{m2})\rho_{m2}}{MW_{m2}} \tag{2.5}$$

where V_{mi}^{p} is the volume of unreacted monomer 'i' at the previous time instant, and V_{mi}^{a} is the volume of monomer 'i' added during the current time instant. The concentration of the monomers in the particle phase, $[M_j]_p$, are obtained from partitioning calculations as:

$$[M_i]_p V_p^s + \frac{[M_i]_p}{K_{pi}} V_w + \frac{[M_i]_p}{K_{di}} V_d = \frac{V_{mi}\rho_{mi}}{MW_{mi}} \tag{2.6}$$

for each monomer ($i = 1, 2$), where V_p^s is the swollen volume of the particles, related to the total polymer volume V_p as $V_p^s = \frac{V_p}{1-\frac{[M_1]_p MW_{m1}}{\rho_{m1}} - \frac{[M_2]_p MW_{m2}}{\rho_{m2}}}$, and V_d is the volume of monomer droplets. One can define an equation for the calculation of the volume of droplets in terms of the monomer concentrations in the particle phases and the partition co-efficients as $\Sigma_{i=1}^{2} \frac{[M_i]_p K_{di} MW_i}{K_{pi}\rho_i} = 1$ (balance of the volume of droplets) , to constitute the sixth equation of the set. However, in the present case, the droplets were assumed to be absent in performing the partitioning calculations. Thus, the equations (Equation (2.1), (2.3), (2.4) or (2.5), and (2.6)) constitute a complete system of equations in the unknowns V_{mi} and $[M_i]_p$, for $i = 1, 2$ and V_p, which can be solved for using any suitable method. Once these quantities are known, they can be utilized to compute the individual and overall conversions, the solids content, and the copolymer composition.

Figures 2.6 shows the solids content, the overall conversion values (instantaneous and cumulative), and the copolymer composition. The value of the polymer density ρ_P was adjusted for one particular experiment to provide a good fit between the solids content predicted by the above approach with that obtained from gravimetric analysis. Although the polymer density might vary with composition, this

same value was used for all subsequent experiments (including the current one). As can be seen from Figure 2.6(a), there is a good correspondence between the gravimetric and densimetric estimates, in spite of the assumptions of ideality, uniform polymer density and isothermal operation. The conversion profiles capture the initial increasing rate period, an intermediate seemingly constant rate period and a falling rate period towards the end of the batch. For this experiment, in which the copolymer composition was not controlled, the composition shows a drift before settling at about 52% VAc polymer.

2.3.2 Analysis of Particle Size Distribution Measurements

Figure 2.7(a) shows the fractogram for a typical PSD sample. The peak at 520 s pertains to the reference particles. The peak starting at approximately 400 s corresponds to the surfactant species, and the peak centered at 350 s corresponds to the polymer particles. This chromatogram of UV absorbance versus elution time is converted by the MATEC software to relative PSD information based on the calibration data. Figure 2.7(b) shows the relative weight-averaged PSD corresponding to the fractogram shown in Figures 2.7(a). As seen in this plot, the CHDF measures the relative concentration of the particles in the various size ranges, and produces a distribution with the largest peak assigned a value of 100. The actual weighted distribution is inferred from the data as follows: the distribution produced by the CHDF, $N(r)$, is related to the actual weighted distribution $W(r)$ as $N(r) = \frac{100}{W_{max}} W(r)$, where W_{max} is the highest value of the weight averaged distribution over the entire particle size range (largest peak in the distribution). The actual weighted distribution satisfies the particle probability density function condition $\Sigma_j W_j = 1$, where W_j is the weight-averaged distribution at discrete points of size r_j. Using this condition in the above relation results in $W_{max} = \frac{100}{\Sigma_j N_j}$, and the probability density function is retrieved from the data produced by the CHDF using the formula, $W(r) = \frac{W_{max}}{100} N(r)$. Thus, the actual weighted distribution can

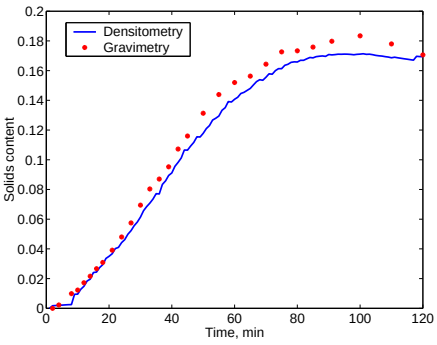

(a) profile of solids content from densimetric and gravimetric estimates

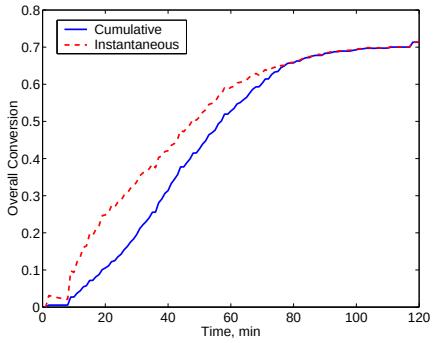

(b) profiles of conversion from densimetry

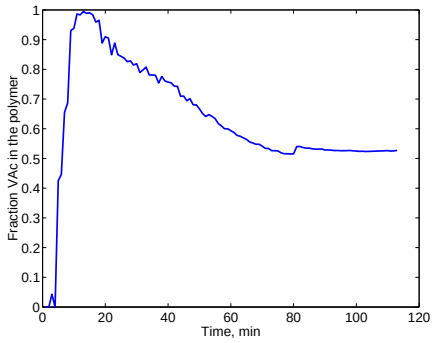

(c) profile of co-polymer composition from densimetry

Figure 2.6: Estimates of process variables based on the densitometer and load cell information.

be inferred from the data produced by the CHDF. Figures 2.8 and 2.9 show the evolution of the weight- and number-averaged PSD over the course of the batch. These show the emergence of a clear bimodal distribution, with a comparable number of particles in both the modes (Figure 2.9), but a higher mass of particles in the larger mode (Figure 2.8), in a relative sense.

The above weighted distribution data can be combined with the data on the solids content to extract the absolute distribution information. The absolute PSD $F(r)$ is related to the weight-averaged distribution (particle probability density function) $W(r)$ as $W_j = \frac{r_j^3 F_j}{\Sigma_j r_j^3 F_j}$, where F_j is the value of $F(r)$ at the discrete point of size r_j. The absolute distribution can be derived from this relation, using the volume of the polymer available from the densitometer calculations (or gravimetric calculations), as $F_i = \frac{V_p}{N_A}\frac{W_i}{v_i}$, where v_i is the volume of a particle at the discrete point of size r_i ($v_i = \frac{4\pi}{3} r_i^3$). From the absolute distribution, the total particles can be computed as $N_p = N_A \Sigma_i F_i$. One can also obtain the total particle surface area, and perform surfactant partitioning calculations using these information, if required.

Figure 2.10(a) shows a plot of the evolution of the absolute PSD along the course of the batch, and Figure 2.10(b) shows the corresponding profile of the total particles. This shows a relatively constant number of particles initially (up to about 40 minutes), followed by a prolonged secondary nucleation event resulting in almost three times the number of particles at the end of the batch. The emergence of a bimodal distribution after 40 minutes coincides with the decrease in the VAc feed rate at this time, and occurs despite a drop in the feed rate of the surfactant. This is due to the depletion of the monomer droplets from the system and the associated release of the surfactants accumulated within them back into the aqueous phase, causing a crossing of the cmc-barrier to micelle formation and nucleation, and resulting in a secondary micellar nucleation event. This is similar to the study in batch reactors, in which the disappearance of the monomer droplet phase resulted

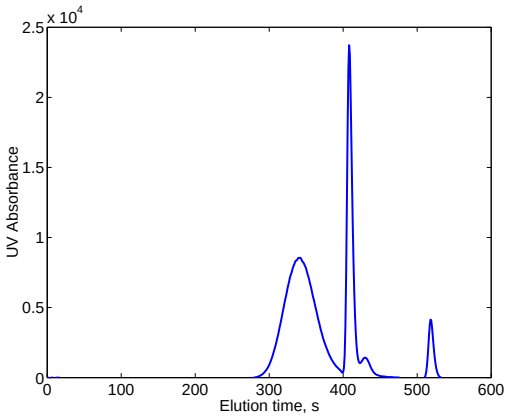

(a) typical fractogram observed in the capillary hydro-dynamic fractionator

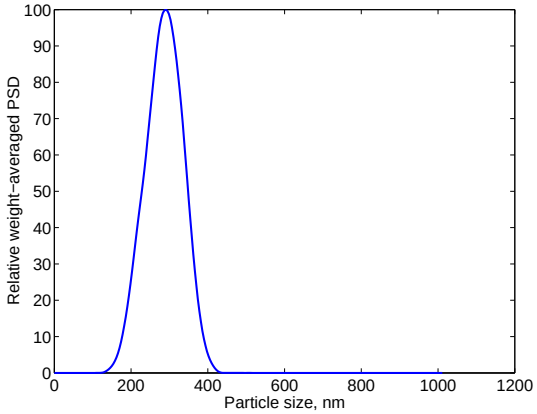

(b) relative weight-averaged distribution as re-convoluted by the MATEC software

Figure 2.7: Measurement of the PSD by the Capillary Hydro-Dynamic Fractionator (CHDF).

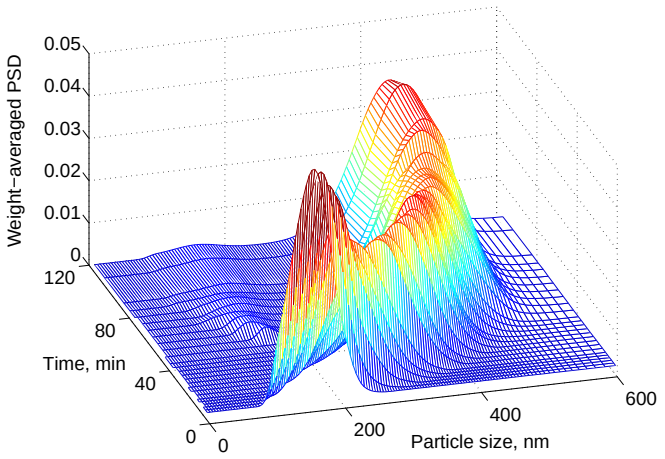

Figure 2.8: Evolution of the weight-averaged PSD.

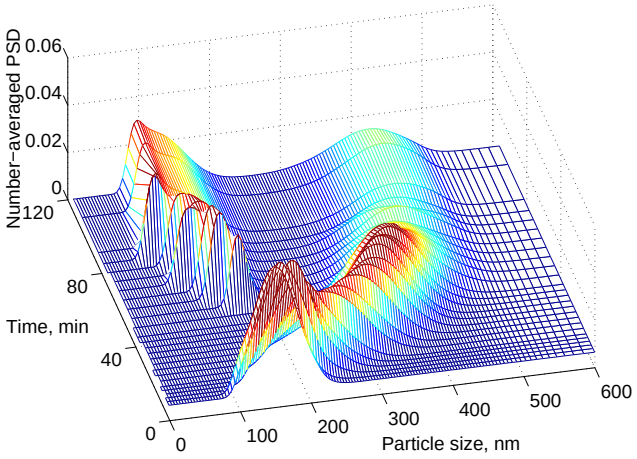

Figure 2.9: Evolution of the number-averaged PSD.

in the secondary nucleation event caused by the release of the absorbed surfactants (Ozdeger et al., 1997b). (Note that the higher feed rates of the surfactant employed at earlier times is not sufficient to cause a secondary nucleation as a portion of it is lost into the monomer droplets). Figure 2.11 depicts the evolution of the PSD against the cumulative overall conversion. It can be seen from this Figure that the secondary nucleation event begins at about 40 % overall cumulative conversion, which corresponds to about 50 % instantaneous conversion (Figure 2.6(b)). Figure 2.12(a) shows the evolution of the PSD against the mass of SFS added to the reactor, while Figure 2.12(b) gives a plot of the total mass of t-BHP against the total mass of SFS.

The previously detailed results clearly elucidates the potential to produce multi-modal distributions in semi-batch emulsion polymerization. However, the process is more complicated than in the case of ionic surfactants mainly due to the absorption of the surfactants into the like monomer droplets. This aspect is further illustrated in the results presented next, in which the distributions produced by two different surfactants with different partitioning characteristics are compared under the same operating conditions. Thus, one might have to manipulate the feed of the monomer in the semi-batch mode in addition to the feed of the surfactant.

2.3.3 Reproducibility Considerations

Before presenting the sensitivity results pertaining to different surfactants, it is important to confirm that the measurements produced by the major equipment are reproducible, and to document noise levels in these measurements. Figures 2.13(a) and 2.13(b) show repeated measurements of two samples in the CHDF equipment. Figure 2.13(a) shows that most of the distributions overlay on each other indicating very good reproducibility. Figure 2.13(b) depicts the lowest reproducibility of 70% observed in the equipment. The reproducibility is also evident in the evolution plots of the distribution that were presented earlier (Figure 2.10(a), for example),

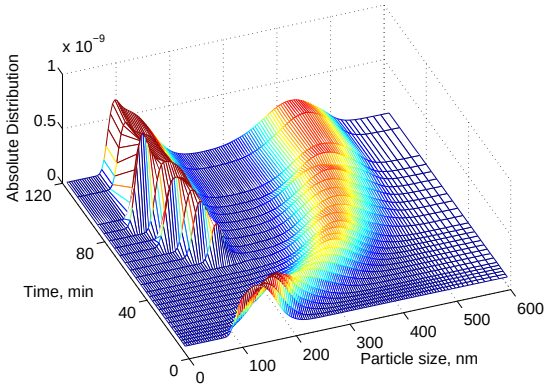

(a) evolution of the absolute PSD

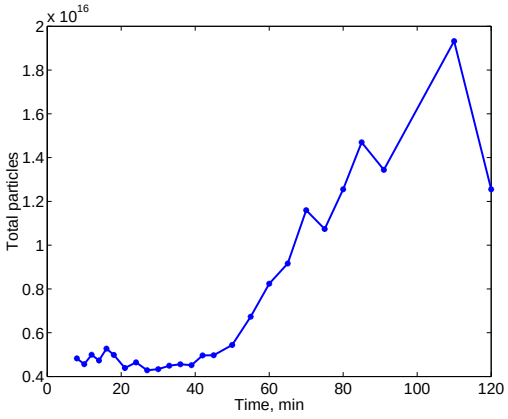

(b) profile of total particles

Figure 2.10: Estimation of the absolute distribution from the measurements of the CHDF and the densitometer.

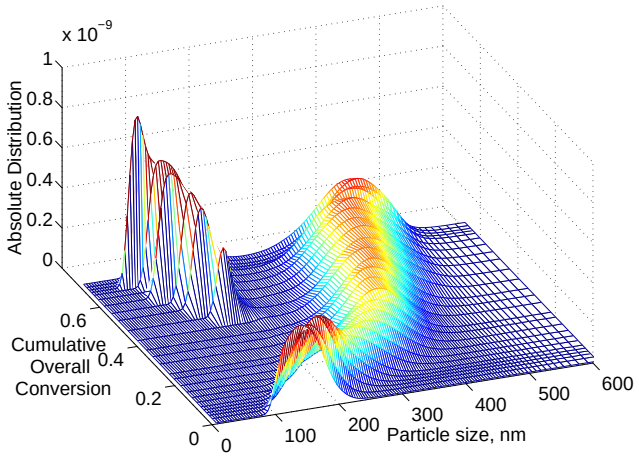

Figure 2.11: Evolution of the absolute distribution versus the overall conversion of the monomers.

in which the instrument captures the smooth and evolving distribution rather well. However, the CHDF does not detect the particles until a solids content of about 0.5% is reached. So, in *ab initio* experiments, the first successful PSD measurement is not available until about 6-10 minutes, typically.

The profile of the latex density shown in Figure 2.5 again indicates a good reproducibility in the density measurements, in that it captures the evolution of the latex density with only a few evident outliers. The whole experiment was repeated to study the overall reproducibility of the experiment in the face of unavoidable initial condition errors. Figure 2.14 compares the density measurements over the course of the two batches, showing good qualitative and quantitative matches. Figures 2.15 and 2.16 compare estimates of the solids content by densimetric calculations and by gravimetry, respectively, and show errors of about 5% or less. On the other hand, Figure 2.17 compares the overall evolution of the PSD in the two batches, and Figure 2.18 compares the individual PSD data at different times in the batch. The evolution of the distribution is more intricate than the lumped solids content, and is also subjected to the cascaded errors of disturbances. Even though the

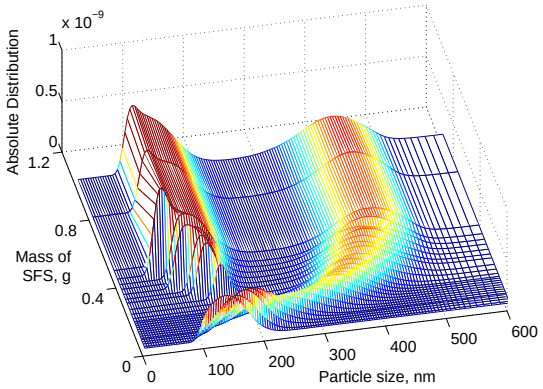

(a) evolution of the absolute PSD against the mass of the reducer (sodium formaldehyde sulphoxylate) in the redox pair

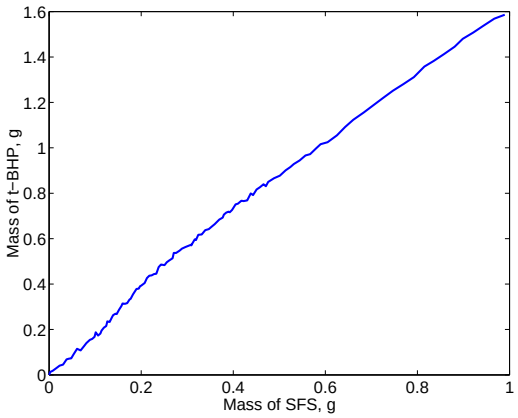

(b) mass of the oxidant (t-butyl hydrogen peroxide) against the mass of the reducer (sodium formaldehyde sulphoxylate)

Figure 2.12: Plot of the absolute distribution against the mass of the initiator components.

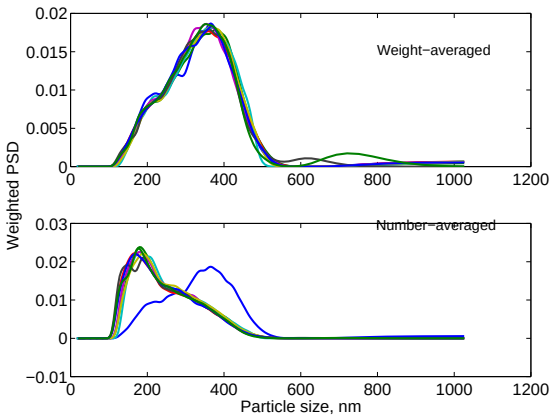

(a) repeated measurements of a particular sample in the CHDF

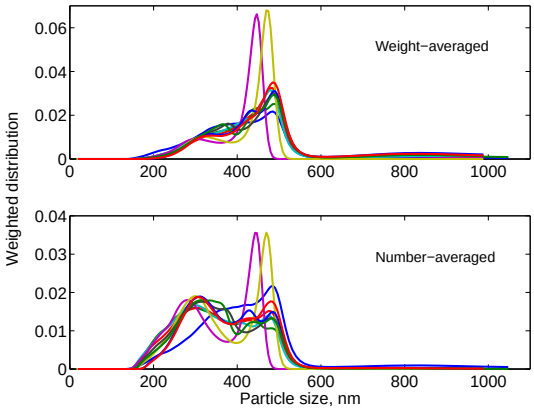

(b) repeated measurements of a particular sample in the CHDF - the lowest reproducibility observed in the instrument

Figure 2.13: Reproducibility of PSD measurements in the CHDF.

reproducibility is not as good as in the case of the lumped solids content data, there is an overall qualitative and reasonably quantitative reproducibility that is evident in the plots.

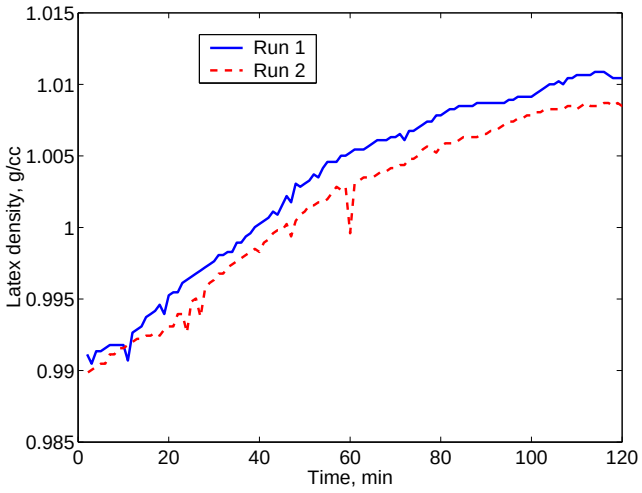

Figure 2.14: Overall reproducibility on a run-to-run basis - density measurements.

2.3.4 Influence of surfactants on the evolution of PSD

Figures 2.20 and 2.21 compare results corresponding to the same semi-batch emulsion polymerization recipe shown in Figure 2.19, but with different non-ionic surfactants. While surfactant A is the same non-ionic poly ethylene oxide surfactant whose properties were described previously, surfactant B is also a poly ethylene oxide surfactant with 30 ethylene oxide linkages, and a hydrophobic-lyophobic balance of 17.2. It has a much lower partition co-efficient into the monomer droplets of 0.035. Thus, this surfactant resides predominantly in the aqueous phase and the interface, unlike surfactant A which partitions appreciably into the monomer droplets and into the particles. The cmc value of surfactant B is 1.8×10^{-4}, almost four times higher than that of surfactant A, while its adsorption isotherm is characterized by an adsorption equilibrium constant of $K_{ad} = 3 \times 10^{6}$ liter/mol and maximum surface coverage $\Gamma_{\infty} = 1.1 \times 10^{-6}$ mol/sq.m. The difference in the results

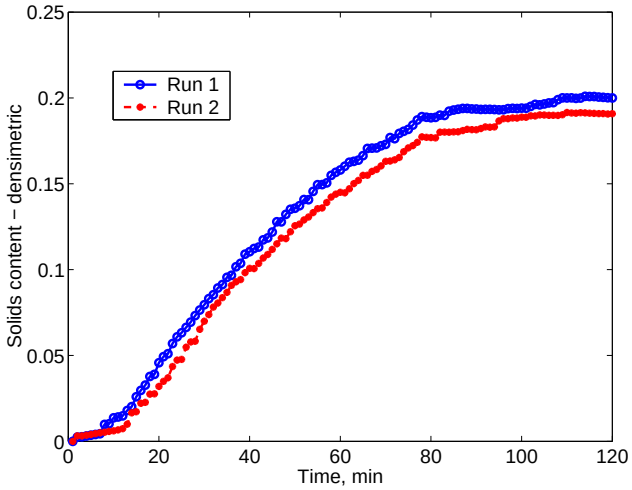

Figure 2.15: Overall reproducibility on a run-to-run basis - solids content estimates by densimetry.

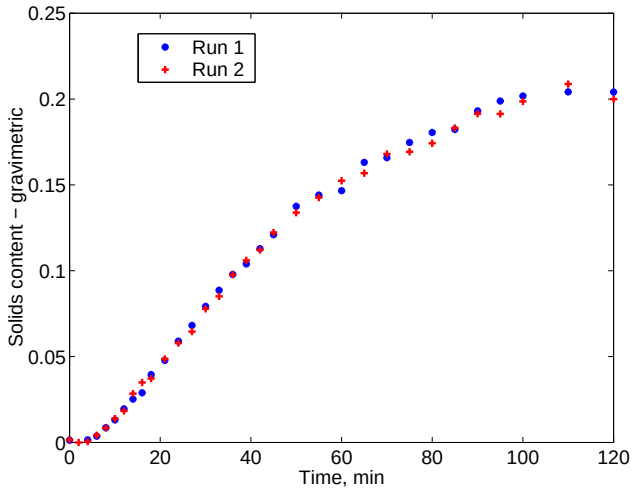

Figure 2.16: Overall reproducibility on a run-to-run basis - solids content estimates by gravimetry.

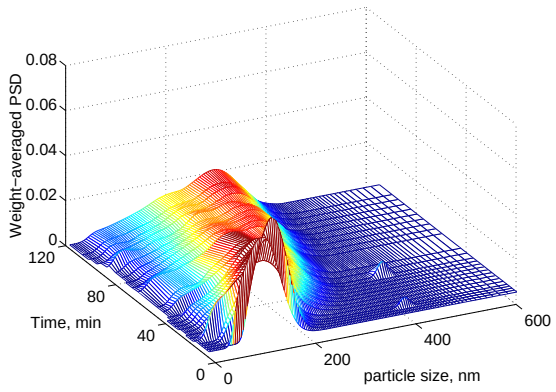

(a) evolution of PSD in run 1

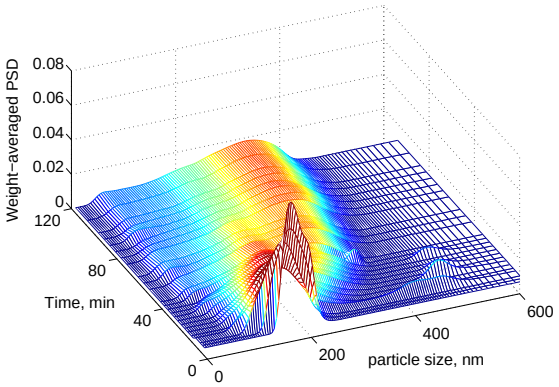

(b) evolution of PSD in run 2

Figure 2.17: Overall reproducibility on a run-to-run basis - evolution of the PSD.

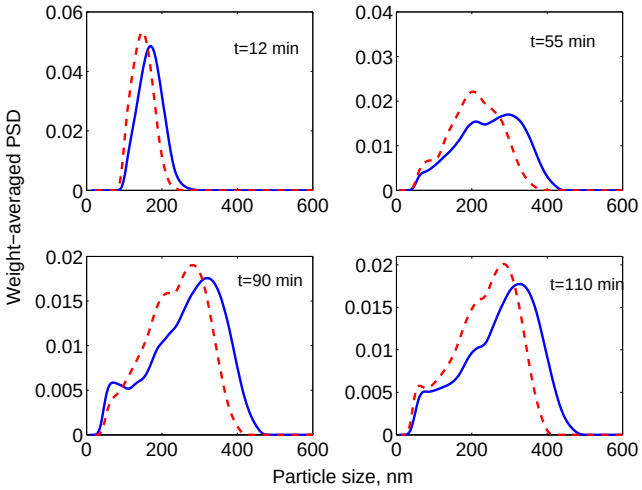

Figure 2.18: Overall reproducibility on a run-to-run basis - comparison of the PSD at select time instances.

produced by the two surfactants can be analyzed in terms of the nucleation, growth and coagulation events which determine the PSD. For the same feed rates of the surfactants, monomers and the initiator components, surfactant B results in a much larger nucleation rate in spite of its higher cmc value compared to surfactant A, due to the profound difference in the partitioning tendency of the two surfactants. Nucleation continues in both the cases until about 70 minutes, at which time the feed of the surfactant is completed. On the growth front, the larger number of particles in the case of surfactant B results in reduced concentrations of the monomers and the polymer radicals inside the particles, resulting in reduced growth rates. On the coagulation front, surfactant A is more prone to coagulation than surfactant B (due to its lower value of adsorption equilibrium constant). Thus, as seen in Figure 2.20, surfactant A results in a broader PSD at the end of the batch compared to surfactant B. Although the solids content in surfactant B is higher at early times due to the large number of particles nucleated, it drops at later times due to reduced growth rates. These results are further illustrations of the complications in the nucleation pattern that is introduced by the tendency of certain surfactants to partition into

the monomer droplets, and of the need to employ both monomer and surfactant in semi-batch mode to produce the desired PSD.

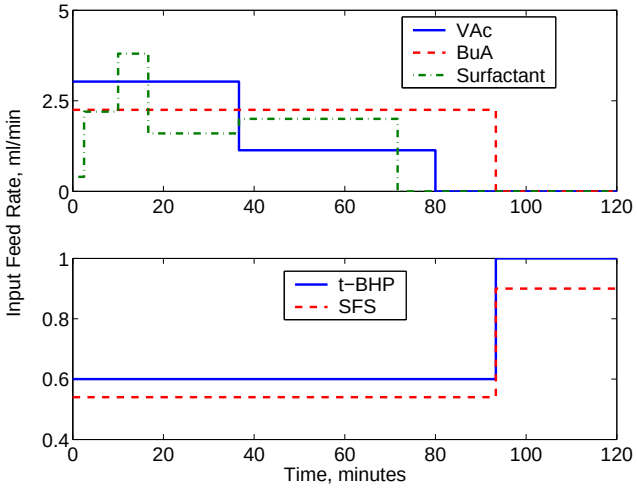

Figure 2.19: Feed profile of the various reagents including the surfactant solution, for the study on the sensitivity to the properties of different surfactants.

2.3.5 Coagulation-induced bimodal distribution

The experiments described in this section show that multi-modal distributions can be produced by exploiting the undesirable coagulation events. The first of these experiments is a VAc-BuA copolymerization experiment with mixed surfactants, and the next is a VAc homopolymerization experiment with a single non-ionic surfactant.

2.3.5.1 Higher solids - mixed surfactant system

The recipe described next is designed to achieve a higher solids content. It is a VAc-BuA co-polymerization experiment with a mixture of non-ionic surfactants (poly ethylene oxides) (about 4.4% by weight of the total monomer used in the batch) and anionic surfactants (sodium alkylphenolethoxylate sulphate) (about 0.7% by weight of the total monomer) as emulsifiers. All the surfactants are added into

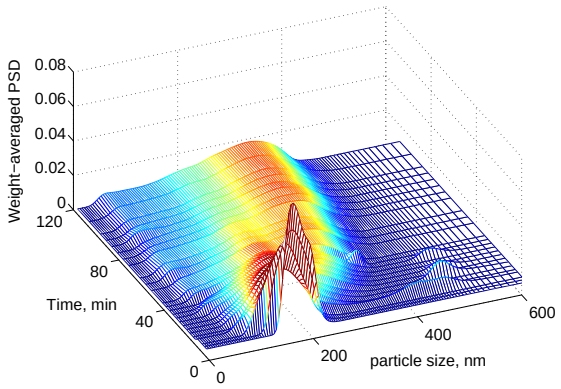

(a) evolution of PSD in the case of Surfactant A

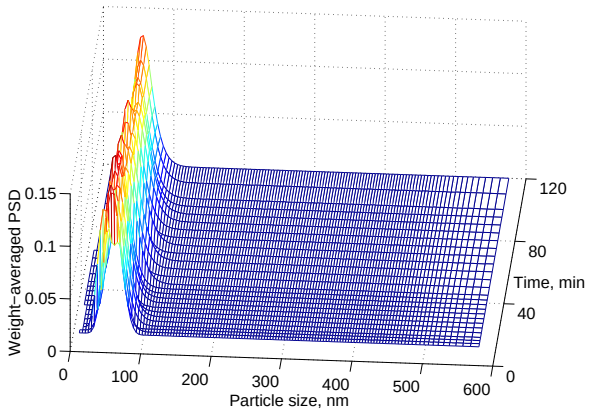

(b) evolution of PSD in the case of Surfactant B

Figure 2.20: Comparison of the experimental results with two different surfactants, for similar operating conditions and feed rates.

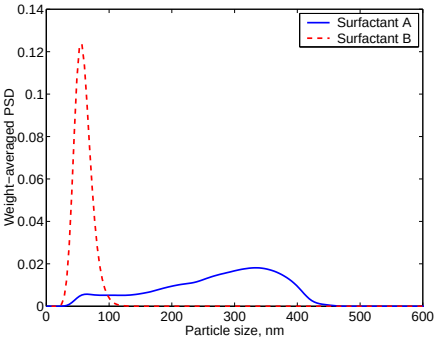

(a) comparison of the end-point PSD produced by the two surfactants

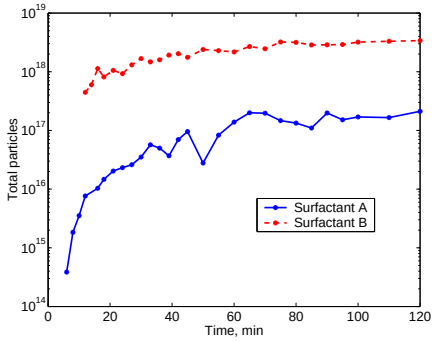

(b) comparison of the profile of total particles

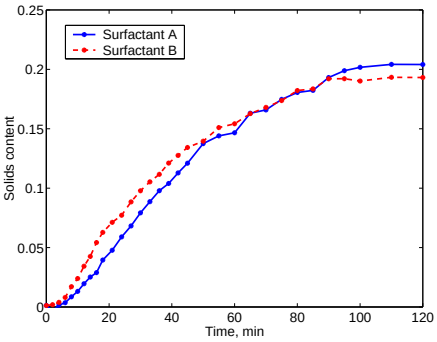

(c) comparison of the profile of solids content

Figure 2.21: Comparison of the experimental results with two different surfactants, for similar operating conditions and feed rates.

the initial mixture, which comprises of DI water and ferrous ammonium sulphate. The monomers were used as a 86% VAc and 14% BuA mixture. t-BHP and SFS were 2.2% and 1.7% by weight aqueous solutions, respectively. The reactor contents were agitated at approximately 120 rpm, and maintained at 65^0C. 8.5% of the total monomer mixture was added into the initial batch, and the feed of the SFS solution was started at 0.2 ml/min. The feeding of the other components was delayed, to cause the nucleation. Once initiation and nucleation were observed (as evident primarily by a color change due to light scattering by the nucleated particles, with the solution turning light blue at first and then white – one could also deduce nucleation by noticing an increase in the reactor temperature), the monomer mixture feed was started at 5 ml/min and the t-BHP solution feed at 0.26 ml/min. The monomer and t-BHP feeds were maintained for 180 minutes, and the SFS feed for 240 minutes.

Figure 2.22 shows on-line PSD measurements from the batch. As stated earlier, a sample analysis through the CHDF takes approximately 12-14 minutes, and there was a wait period of 10 minutes between the samples. The measured distributions are relatively narrow and unimodal until the sample at 129 minutes. Subsequently, the sample at 153 minutes (Figure 2.22(b)) shows a bimodal distribution, and the bimodality carries through the rest of the batch. This bimodality is caused by a coagulation event after 129 minutes, resulting in the second larger mode. In some cases, this coagulation event leads to the release of some *adsorbed* surfactants (due to a decrease in the total surface area) so as to cause a nucleation event. The solids content at the end of the batch is about 37%, with approximately 2×10^{18} particles.

2.3.5.2 Vinyl acetate homopolymerization

Figure 2.23 shows plots of the total mass of the various reagents in the reactor at various times, for a VAc-homopolymerization experiment with a single non-ionic

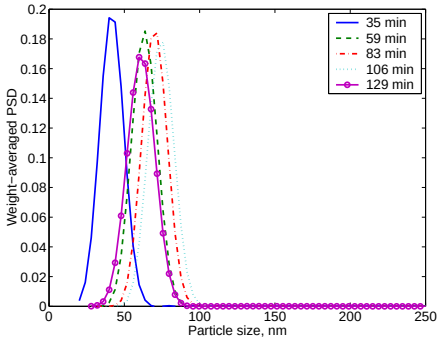

(a) PSD at the early times of the batch

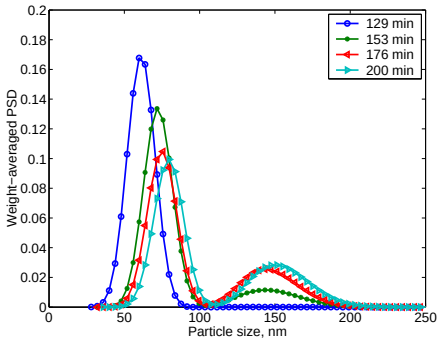

(b) PSD at the intermediate times - emergence of a bimodal distribution

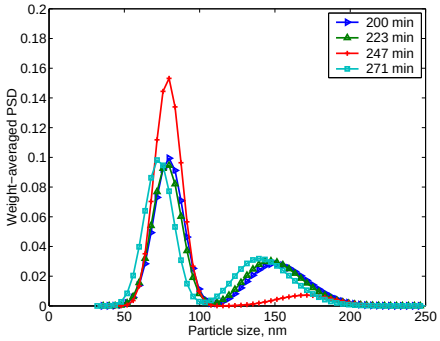

(c) PSD at the later times of the batch - retaining the bimodality

Figure 2.22: Evolution of PSD in high solids content emulsion co-polymerization of vinyl acetate and butyl acrylate with mixed non-ionic and anionic surfactants.

surfactant (surfactant A) as the emulsifier. Figure 2.24 shows the evolution of the distribution (off-line analysis). The plots show a probable coagulation event between 12 and 15 minutes, that results in a bimodal distribution. The bimodality becomes more prominent at later times with more nucleation, growth and coagulation, resulting in a broad distribution at the end of the batch (100 min sample). The solids content at the end time is approximately 17%.

Thus, semi-batch surfactant addition policy can be utilized to engineer a coagulation event mid-course, and thereby produce a bimodal distribution. One has to have recourse to a detailed model incorporating the coagulation event, to predict the surfactant concentration to be employed through the batch in causing the desired coagulation event.

2.3.6 Delayed surfactant addition

Sajjadi and Brooks (2000) observed that in a recipe that does not contain any surfactant in the initial mixture, there is a primary homogenous nucleation. This can be followed by a secondary nucleation event later in the batch, to produce a bimodal distribution. The result presented here provides a similar case. Figure 2.25 shows the feed profiles for the two monomers (VAc and BuA), the surfactant solution (surfactant A), and the initiator solutions. The solution concentrations are the same as in the first case presented here. The initial mixture contains 1 liter DI water, 52 g VAc monomer, and 0.1 g ferrous ammonium sulphate. The feed of the monomers and the surfactant solution is delayed by approximately 20 minutes compared to that of the initiator solutions. Polymerization of the monomer in the initial mixture is initiated once the feed of the redox pair is started. Particles are nucleated by the homogenous nucleation mechanism. The particles exhibit some instability due to the absence of any external surfactant at this point, as seen in the plot of the total particles in Figure 2.27 (stabilization is probably through *in situ* generated surfactants). Once the feed of the surfactant and the monomers

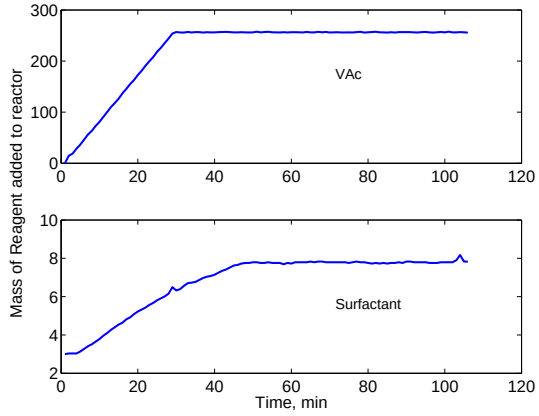

(a) mass of monomer and surfactant

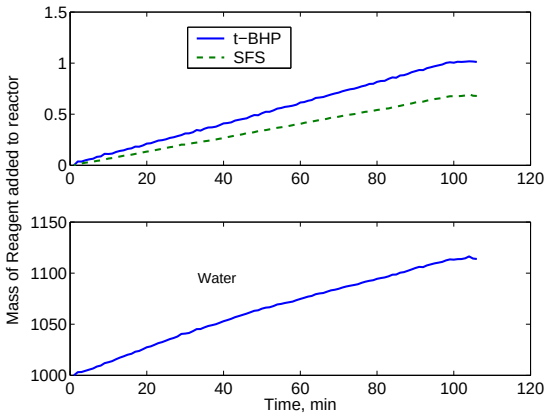

(b) mass of initiator components and water

Figure 2.23: Profiles of the total mass of the various reagents, in vinyl acetate homopolymerization.

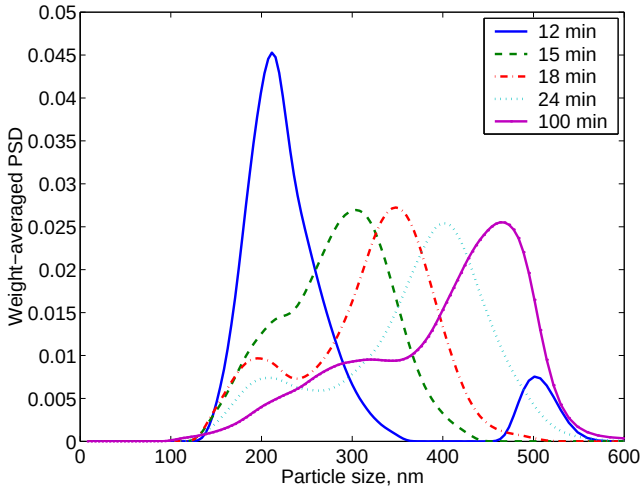

Figure 2.24: Emergence of a bimodal distribution in a vinyl acetate homopolymerization experiment, caused by coagulation events.

are commenced, particle nucleation occurs by the micellar mechanism, resulting in a clearly separated bimodal distribution in the final latex, as seen in Figure 2.26. Hence, this is an alternate method for producing a bimodal distribution, although partitioning considerations and their effect on the nucleation phenomenon are still to be accounted for in causing the secondary micellar nucleation.

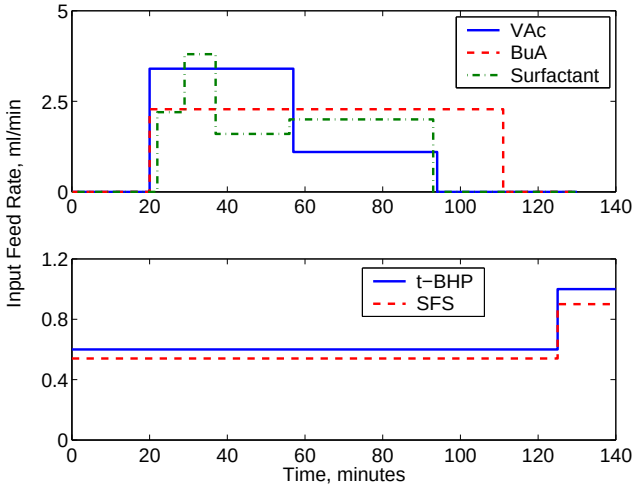

Figure 2.25: Feed profile of the reagents with delayed feed of surfactant.

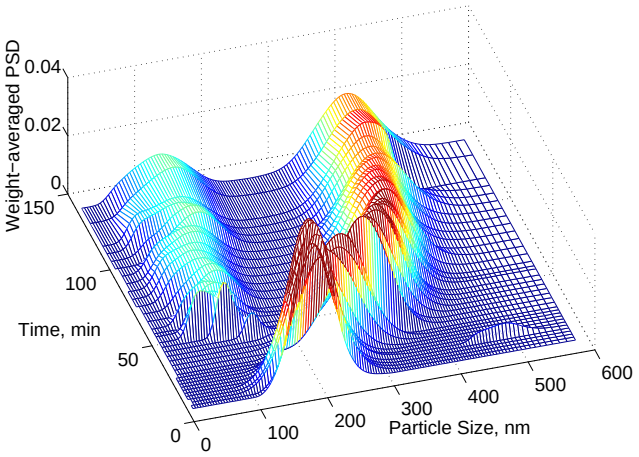

Figure 2.26: Evolution of the bimodal distribution, the primary mode attributed to homogenous nucleation and the secondary mode to micellar nucleation.

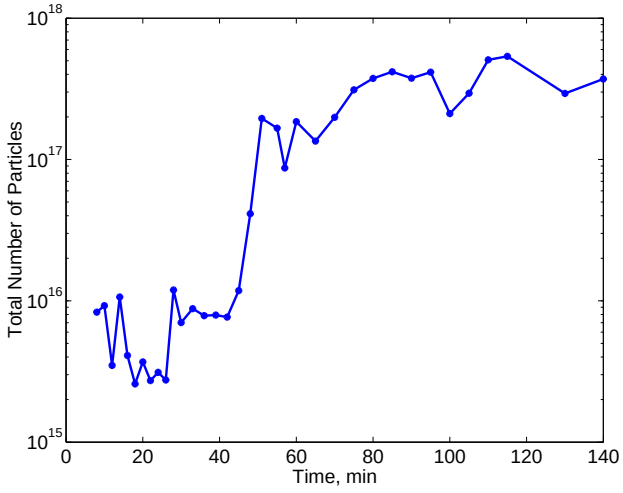

Figure 2.27: Total particles profile over the course of the batch.

2.4 Summary

A complete experimental facility for semi-batch emulsion polymerization, equipped with state-of-the-art instruments for measurement and estimation of PSD, monomer conversions and co-polymer composition was presented. Detailed procedures for the inference of important process variables from the measurements available were described. The calculation procedure, based on a simple steady state first principle model, enables the inference of the partial conversion of both the monomers and the co-polymer composition with the measurement of the latex density alone. The reproducibility characteristics of the individual equipment and the overall process (sensitivity to the initial conditions and to operational uncertainty) were examined. The equipment showed very good reproducibility. While the lumped variables such as the solids content showed good reproducibility on a run-to-run basis, the more detailed PSD measurements showed a reproducibility greater than 75%. The instrumentation demonstrate the ability to employ on-line feedback control of the process.

Semi-batch experiments were described for vinyl acetate-butyl acrylate emulsion polymerization, showing the evolution of multi-modal distributions. Different methods of producing multi-modal distributions were examined. A semi-batch mode of operation can be used in producing multi-modal distributions with given mean and variance of each mode, by causing multiple nucleation events at predetermined points in the batch. However, in recipes employing non-ionic surfactants, one needs to recruit the feed rates of both the surfactants and the monomers to engineer secondary nucleation events at the desired times, and thereby produce the desired distributions. Alternatively, multi-modal distributions can be engineered by causing a strong coagulation event, which splits a given mode of particles to form a larger mode of particles. However, this is complicated by shear considerations, and one needs to employ a detailed first principle model to design a suitable recipe. A

third, rather interesting method of producing bimodal distributions is by causing an initial homogenous nucleation (in the absence of surfactants), and nucleating another mode at a later time in the batch by the micellar mechanism. This approach, though straightforward, is still beset with all the factors that attend the first approach. This study illustrates the ability to design recipes for the attainment of multi-modal distributions, while the strong sensitivity in the process shows the need for careful control.

Chapter 3

POPULATION-BALANCE MODEL FOR PARTICLE SIZE DISTRIBUTION

3.1 Introduction

One of the major challenges in the control of PSD is obtaining on-line measurements. The acquisition of PSD data at a reasonable frequency is required to facilitate corrective action. This challenge was addressed in the previous chapter. On the other hand, corrective action is not possible in many cases and an error, once committed, will carry through the entire batch. This motivates the development of a model with good predictive ability for use in optimization studies and in model-based control. In this chapter, a model is presented for a vinyl acetate(VAc) - butyl acrylate(BuA) co-polymer system, using non-ionic surfactants. The general structure of the pseudo-homopolymer model of Saldivar *et al.* (1998) is adopted, with considerable influence from other works (Coen et al., 1998; Crowley et al., 2000). However, a number of significant changes are introduced. The pseudo-homopolymerization model necessitates an equation describing the average number of radicals/particle. This is modeled with equations derived from first principles, unlike the simplifications employed in the earlier models. The non-ionic surfactants tend to partition into the organic phases, thereby drastically altering the evolution of particles and the final PSD, as was demonstrated experimentally. This aspect is also incorporated into the model.

In the next section, the features of the coagulation-free model will be described, highlighting the novelties and the hybrid adaptations. This will be followed by the description of the general solution technique employed. The next three sections will discuss some simulation results, comparison of the simulation results with the experimental results, and the sensitivity of the results to the model parameters, respectively. The coagulation-inclusive model will be presented in the subsequent sections, along with the simulation results and experimental validation.

3.2 Model Formulation

The kinetic scheme for the process is detailed in Table 3.1.

3.2.1 Initiation

As can be seen from Table 3.1, polymerization is initiated in the aqueous phase. The oxidant t-butyl hydrogen peroxide (tBHP) (I_w), reacts with the catalyst (Y_1^r) (ferrous ion), and forms the initiator radical (R_w) ($(CH_3)_3C - O^{\cdot -}$). The material balances for the oxidizer $[I]_w$ is given as follows:

$$\frac{d([I]_w V_{aq})}{dt} = -k_{d1}[I]_w[Y_1^r] + \upsilon_I \tag{3.1}$$

In the process, the ferrous ion is oxidized to ferric ion (Y_1^o). The ferrous ion is regenerated from the ferric ion by the reductant sodium formaldehyde sulphoxylate, (SFS) (Y_2). The material balances for the reducer $[Y_2]$ is given as follows:

$$\frac{d([Y_2]V_{aq})}{dt} = -r_I k_{d1}[I]_w[Y_1^r] + \upsilon_{Y_2} \tag{3.2}$$

Employing the pseudo steady state assumption for the intermediate iron radicals, the concentration of the catalyst in the reduced form, in terms of the total moles of the catalyst (both oxidized and reduced) in the system $[Y_1]$, is given by:

$$[Y_1^r] = \frac{k_{d2}[Y_2]}{k_{d1}[I]_w + k_{d2}[Y_2]}[Y_1] \tag{3.3}$$

In the above equations, k_{d1} and k_{d2} are the kinetic constants for the oxidation and reduction steps respectively, r_I is the stoichiometric ratio between the oxidizer and the reducer, υ_i is the molar feed rate of component i, and V_{aq} is the volume of the aqueous phase.

The initiator radical R_w reacts with the sparingly soluble monomer in the aqueous phase and initiates the polymerization. The material balance for $[R_w]$ is given by:

$$\frac{d([R_w]V_{aq})}{dt} = k_{d1}[I]_w[Y_1^r] - V_{aq}\sum_{i=1}^{2} k_{ri}[R_w][M_{iw}] - V_{aq}k_{tav}^w[R_w](\sum_{l=0}^{j_{cr}-1}[P_w]^l + [R_w]) \tag{3.4}$$

where $[P_w]^l$ is the concentration of aqueous phase oligomers of chain length l, j_{cr} is the critical chain length, $k_{tav}^w = \sum_{i=1}^{2}\sum_{i=1}^{2} k_{tij}^w p_{iw} p_{jw}$ is the pseudo-homopolymer rate constant for termination in the aqueous phase (k_{tij}^w being the termination rate constant for a polymer chain of type i with a polymer chain of type j) and $[M_i]_w$ is the concentration of monomer i in the aqueous phase.

3.2.2 Pseudo-homopolymerization approximation

In this two-monomer system (VAc and BuA), the polymer chains are of two types – one in which the free-radical endgroup is derived from VAc and the other in which it is derived from BuA. To simplify the model, the two chain types are lumped into a single type, yielding the so-called pseudo-homopolymerization model (Storti et al., 1989; Saldivar et al., 1998). The model assigns the polymer chains to one type or the other based on a pseudo-homopolymer probability. This is derived by accounting for the interchanging of the polymer chains between the two types by cross-propagation and cross-chain transfer. This factor for the aqueous phase is given by:

$$p_{w1} = \frac{(k_{p21}^w + k_{tr21}^w)[M_1]_w}{(k_{p21}^w + k_{tr21}^w)[M_1]_w + (k_{p12}^w + k_{tr12}^w)[M_2]_w} \tag{3.5}$$

where k^w_{pij} and k^w_{trij} are the propagation and chain transfer constants for chains of type i with monomer j in the aqueous phase. p_{w1} defined above is the fraction of the aqueous phase oligomers that are of type 1, *i.e.,* have a VAc end group.

3.2.3 Aqueous phase oligomers

The initiator radical $[R_w]$ reacts with the sparing amount of monomer dissolved in the aqueous phase and forms an oligomer of chain length 1. This can further propagate until the critical chain length j_{cr} is attained. The material balances for these oligomers are given by

$$\begin{aligned}\frac{d([P_w]^1 V_{aq})}{dt} = V_{aq}\sum_{i=1}^{2} k_{ri}[R_w][M_{iw}] - V_{aq}k^w_{tav}[P_w]^1(\sum_{l=0}^{j_{cr}-1}[P_w]^l + [R_w]) - \\ (k^w_{pav} + k^w_{trav})[P_w]^1 V_{aq} + k^w_{pav}[P_w]^0 V_{aq} - \sum_{i=1}^{2} e^1_{i,micelle} p_{wi}[P_w]^1 C_{micelle} V_{aq} \\ - \int_{r=r_{nuc}}^{r_{max}} \sum_{i=1}^{2} e^1_i(r) p_{wi}[P_w]^1 F(r,t)dr\end{aligned} \tag{3.6}$$

$$\begin{aligned}\frac{d([P_w]^n V_{aq})}{dt} = k^w_{pav}([P_w]^{n-1} - [P_w]^n)V_{aq} - \sum_{i=1}^{2} e^n_{i,micelle} p_{wi}[P_w]^n C_{micelle} V_{aq} \\ -k^w_{trav}[P_w]^n V_{aq} - \int_{r=r_{nuc}}^{r_{max}} \sum_{i=1}^{2} e^n_i(r) p_{wi}[P_w]^n F(r,t)dr - \\ k^w_{tav}[P_w]^n(\sum_{l=0}^{j_{cr}-1}[P_w]^l + [R_w])V_{aq} \quad n = 2, 3 ... j_{cr} - 1\end{aligned} \tag{3.7}$$

$$\begin{aligned}\frac{d([P_w]^0 V_{aq})}{dt} = k^w_{trav}\sum_{l=1}^{j_{cr}-1}[P_w]^l V_{aq} + \sum_{i=1}^{2}\sum_{j=1}^{2} k_{trij} p_{wi} \int_{r_{nuc}}^{r_{max}} \frac{\bar{n}(r,t)F(r,t)k_{dMj}(r)[M_j]_p dr}{k_{dMj}(r) + \sum_{l=1}^{2} k_{pjl}[M_l]_p} \\ -k^w_{pav}[P_w]^0 V_{aq} - k^w_{tav}[P_w]^0(\sum_{l=0}^{j_{cr}-1}[P_w]^l + [R_w])V_{aq} - \sum_{i=1}^{2} e^0_{i,micelle} p_{wi}[P_w]^0 C_{micelle} V_{aq} \\ - \int_{r_{nuc}}^{r_{max}} \sum_{i=1}^{2} e^0_i(r) p_{wi}[P_w]^0 F(r,t)dr\end{aligned} \tag{3.8}$$

where the pseudo-homopolymer rate constants are given by $k^w_{pav} = \sum_{i=1}^{2}\sum_{j=1}^{2} k^w_{pij} p_{wi}[M_j]_w$, $k^w_{trav} = \sum_{i=1}^{2}\sum_{j=1}^{2} k^w_{trij} p_{wi}[M_j]_w$ and $k^w_{tav} = \sum_{i=1}^{2}\sum_{j=1}^{2} k^w_{tij} p_{wi} p_{wj}$.

These equations account for the propagation, chain transfer, and termination reactions that occur in the aqueous phase, and for the loss/gain of radicals to/from the dispersed phases – micelles and particles. No distinction is made between the initiator-derived polymer chains and those that result from chain transfer to the monomers.

3.2.4 Nucleation

Nucleation is the process of formation of polymer particles. It can occur by two methods, namely, micellar nucleation and homogenous nucleation. Micellar nucleation occurs when the free surfactant concentration in the aqueous phase, S_w, exceeds a certain equilibrium solubility called the critical micelle concentration (cmc). Above the cmc, the excess surfactant molecules aggregate in the aqueous phase and form entities called micelles. The concentration of these micelles is determined as follows:

$$C_{micelle} = \frac{(S_w - cmc)\alpha_{m,s}}{4\pi r_{micelle}^2} \tag{3.9}$$

where $\alpha_{m,s}$ is the area occupied by one surfactant molecule and $r_{micelle}$ is the radius of a micelle. The oligomer radicals in the aqueous phase, upon encountering the micelles, enter into them, converting the micelles into polymer particles. This phenomenon is called micellar nucleation.

The rate of micellar nucleation is given by

$$\Re_{micellar} = \sum_{l=0}^{j_{cr}-1} \sum_{i=1}^{2} e_{i,micelle}^{l} p_{wi} [P_w]^l C_{micelle} V_{aq} \tag{3.10}$$

where the entry rate constant $e_{i,micelle}^{l}$ for oligomers of type i and chain length l is given by

$$e_{i,micelle}^{l} = 4\pi r_{micelle}^{n} N_A D_{wi}, \quad l = 0, 1 \tag{3.11}$$

$$e_{i,micelle}^{l} = 4\pi r_{micelle}^{n} N_A D_{wi} / \sqrt{l-1}, \quad l = 2, 3 ... j_{cr} - 1 \tag{3.12}$$

D_{wi} is interpreted as related to the diffusion coefficient of species i radical when $n = 1$, and as related to the mass transfer coefficient when $n = 2$.

Upon reaching the critical chain length j_{cr}, the oligomers in the aqueous phase are rendered totally hydrophobic. Thereby, the oligomers precipitate out of the aqueous phase, aggregate surfactant molecules around them and form a new particle. This phenomenon is called homogenous nucleation. The rate of homogenous nucleation is defined as:

$$\Re_{homogenous} = k_{pav}^{w}[P_{w}^{j_{cr}-1}]V_{aq} \tag{3.13}$$

Thus, the combined nucleation rate is given by

$$\Re_{nuc} = \Re_{micellar} + \Re_{homogenous} \tag{3.14}$$

3.2.5 Polymer particles

The polymer particles are characterized by a population density. The particle density $F(r,t)dr$ is defined as the moles of particles of unswollen size between r and $r + dr$ at time t. The particle density is described by a population balance equation (PBE), which accounts for the nucleation of new particles, and their growth – both by polymerization and in discrete leaps by coagulation with other particles. Thus the particle population is described by

$$\frac{\partial}{\partial t}F(r,t) + \frac{\partial}{\partial r}(F(r,t)\frac{dr}{dt}) = \Re_{nuc}\delta(r - r_{nuc}) + \Re_{coag} \tag{3.15}$$

$\Re_{nuc}$ is the rate of nucleation and $\delta(r-r_{nuc})$ is the Dirac delta function which is unity at $r = r_{nuc}$ and zero elsewhere. This assumes that the nucleation occurs at a fixed minimum size r_{nuc}. It is also assumed that $r_{nuc} = r_{micelle}$, the radius of a micelle, for both homogenous and micellar nucleation. $\Re_{coag}$ incorporates terms accounting for the loss and gain of particles of size between r and $r + dr$ due to coagulation. The case corresponding to no coagulation ($\Re_{coag} = 0$) is presented first, to study its

validity under low solids content emulsion polymerization. This is then compared with the coagulation-inclusive case.

The total number of particles in the system is calculated as $N_p = N_A \int_{r_{nuc}}^{r_{max}} F(r,t)dr$, where N_A is the Avogadro number and r_{nuc} and r_{max} are the minimum and maximum size of the unswollen particles, respectively.

3.2.6 Average number of radicals/particle

An average number of active polymer chains (of both types combined) inside particles of a given size can also be modeled by a population balance as below:

$$\frac{\partial}{\partial t}(\bar{n}(r,t)F(r,t)) + \frac{\partial}{\partial r}(\bar{n}(r,t)F(r,t)\frac{dr}{dt}) = \Re_{entry}(r) + \Re_{desorption}(r) + \Re_{termination}(r) + \Re_{coagulation}(r) \tag{3.16}$$

where $\bar{n}(r,t)$ is the average number of growing polymer chains/particle in particles of size r at time t, $\Re_{entry}$ accounts for the entry into all particles of size between r and $r+dr$, $\Re_{desorption}$ accounts for the desorption from all particles of size between r and $r+dr$, $\Re_{termination}$ accounts for the termination within all particles of size between r and $r+dr$, and $\Re_{coagulation}$ accounts for the coagulation effects. The pseudo-homopolymerization approach is employed to distinguish between the two types of polymer chains. Analogous to that in the aqueous phase, the pseudo-homopolymer probability in the particle phase is defined as

$$p_1 = \frac{(k_{p21} + k_{tr21})[M_1]_p}{(k_{p21} + k_{tr21})[M_1]_p + (k_{p12} + k_{tr12})[M_2]_p} \tag{3.17}$$

Alternatively, fixing the attention on a single particle, and making a balance between the rates of entry, desorption and termination of radicals, and neglecting coagulation, one obtains

$$\frac{\partial}{\partial t}(\bar{n}(r,t)) = \Re'_{entry}(r) - \Re'_{desorption}(r) - 2\Re'_{termination}(r) \tag{3.18}$$

where $\Re'_{entry}$ is the total rate of entry into a single particle of size between r and $r+dr$, $\Re'_{desorption}$ is the total rate of desorption from a single particle of size between r and $r+dr$, $\Re'_{termination}$ is the total rate of termination within a single particle of size between r and $r+dr$. These terms are described in detail later. For the smallest size particles ($r = r_{nuc}$), a $\bar{n}$ value of unity is assumed. One could also assume a pseudo-steady state in Equation (3.18) and obtain

$$\Re'_{entry}(r) - \Re'_{desorption}(r) - 2\Re'_{termination}(r) = 0 \tag{3.19}$$

This yields a quadratic equation for $\bar{n}(r,t)$. A global average can be derived from $\bar{n}(r,t)$ as

$$n_{ave}(t) = \frac{\int_{r_{nuc}}^{r_{max}} \bar{n}(r,t)F(r,t)dr}{\int_{r_{nuc}}^{r_{max}} F(r,t)dr} \tag{3.20}$$

3.2.7 Growth

The second term on the left hand side of Equation (3.15) accounts for the growth of the particles by polymerization. A polymer chain inside the particles propagates at a rapid rate due to the high concentrations of the monomers within, thereby increasing the mass and the size of the particles. The growth kernel, which is the rate of increase in size, is given by:

$$\frac{dr}{dt} = \frac{1}{4\pi r^2 \rho_p} \sum_{i=1}^{2} \sum_{j=1}^{2} k_{pij} p_i \frac{\bar{n}(r,t)}{N_A} [M_j]_p MW_j \tag{3.21}$$

where $[M_j]_p$ is the concentration of monomer j in the particles, MW_j is the molecular weight of monomer j, ρ_p is the density of the polymer, and k_{pij} is the propagation rate constant for polymer of type i with monomer j in the particle phase.

3.2.8 Monomer balances

In a semi-batch reactor system, with continuous feed of the monomers, the material balance for the monomers is given by:

$$\begin{aligned}\frac{dM_j}{dt} = \upsilon_{M_j} - \sum_{i=1}^{2}(k_{pij}^w + k_{trij}^w)p_{wi}[Oligomer][M_j]_w V_{aq} \\ - \sum_{i=1}^{2}(k_{pij} + k_{trij})p_i[M_j]_p \int_{r=r_{nuc}}^{r_{max}} \bar{n}(r,t)F(r,t)dr\end{aligned} \tag{3.22}$$

where υ_{M_j} is the molar feed rate of monomer j, $[M_j]_w$ is the concentration of monomer j in the aqueous phase, k_{pij}/k_{pij}^w and k_{trij}/k_{trij}^w are the rate constants in the particle/aqueous phases for propagation and chain transfer to monomer respectively, for a polymer of type i with monomer j, and $[Oligomers] = \sum_{n=0}^{j_{cr}-1}[P_w]^n$.

The monomers reside essentially in the dispersed phases due to their sparing solubility in the aqueous phase. If the system is saturated with the monomers, such that their concentrations in the aqueous phase and polymer phase is at the equilibrium solubility, then a separate droplet phase comprising the monomers is formed. The partitioning of the monomers among the dispersed and continuous phases is modeled using partition coefficients. This involves solving the set of algebraic equations described below, similar to the approach of Urretabizkaia *et al.* (1994).

$$\begin{aligned} V_{1,p} + V_{2,p} + V_p &= V_p^s && \textit{Particle-phase balance} \\ V_{1,w} + V_{2,w} + V_w &= V_w^T && \textit{Aqueous-phase balance} \\ V_{1,d} + V_{2,d} &= V^d && \textit{Droplet-phase balance} \\ V_{i,p} + V_{i,d} + V_{i,w} &= \frac{M_i MW_i}{\rho_{M_i}}; i = 1,2 && \textit{Total monomer balance} \end{aligned}$$

where $V_{i,p}$, $V_{i,w}$ and $V_{i,d}$ are the volume of monomer i in the particles, aqueous phase and monomer droplets respectively, and V_p^s, V_w^T and V^d are the total volume of the swollen polymer, the aqueous phase and the droplets, respectively. These quantities are related via partition coefficients as $\frac{V_{i,p}}{V_p^s} = K_{pi}\frac{V_{i,w}}{V_w^T}$ and $\frac{V_{i,d}}{V^d} = \frac{K_{di}}{K_{pi}}\frac{V_{i,p}}{V_p^s}$.

The total volume of the particles is given by $V_p = N_A \int_{r_{nuc}}^{r_{max}} \frac{4}{3}\pi r^3 F(r,t)dr$, where r is the radius of the unswollen particles. The swollen and unswollen radii are related as $r_s^3 = \frac{r^3}{(1-\frac{MW_1[M_1]p}{\rho_{M_1}}-\frac{MW_2[M_2]p}{\rho_{M_2}})}$, where ρ_{M_i} is the density of monomer i.

3.2.9 Surfactant balances

One of the main roles of surfactants is to stabilize the polymer particles in the continuous aqueous phase. They adsorb on the surface of the dispersed phases (polymer particles and monomer droplets), with their lyophilic end groups facing inwards and their hydrophilic ends directed outwards. The adsorption of surfactant onto the particles and droplets is modeled as a Langmuir mono-layer adsorption. Non-ionic surfactants, besides adsorbing onto the particles, also tend to partition into the organic phases. This phenomenon is also modeled as an equilibrium phenomenon, using partition coefficients.

Thus, the surfactant balance is given by:

$$V_w S_w + K_s S_w V_p^s + K_s^d S_w V^d + \frac{\Gamma_\infty K_{ad} S_w A_p^s}{1 + K_{ad} S_w} = S_T \tag{3.23}$$

where V_w is the volume of the aqueous phase, S_w is the concentration of surfactant in the aqueous phase, and S_T is the total moles of surfactant in the reactor. $K_s S_w V_p^s$ and $K_s^d S_w V^d$ account for the moles of surfactant absorbed into particles and droplets, respectively. Here, K_s and K_s^d are the partition coefficient for surfactant between the particles and the aqueous phase, and between the droplets and the aqueous phase, and V_p^s is the total swollen particle volume. The term $\frac{\Gamma_\infty K_{ad} S_w}{1+K_{ad} S_w} A_p^s$ is the Langmuir isotherm, which accounts for the moles of surfactant adsorbed onto the particles, in equilibrium with that in the aqueous phase. Here, A_p^s is the total surface area of the swollen particles defines as $A_p^s = \int_{r_{nuc}}^{r_{max}} 4\pi r_s^2 N_A F(r,t)dr$ (where r_s is the swollen radius defined earlier), and Γ_∞ and K_{ad} are Langmuir adsorption constants. The quadratic equation (3.23) can be solved for the aqueous phase surfactant concentration S_w.

3.2.10 Entry into particles

The oligomers in the aqueous phase, besides entering into micelles and thereby nucleating particles, can also enter into existent polymer particles. This phenomenon will influence the average number of radicals/particle, as is evident from Equation (3.18).

Analogous to the entry rate coefficients for radicals into micelles, the entry rate coefficients for radicals of type i, $(i = 1, 2)$ and chain length l, $(l = 0, 1, ...j_{cr} - 1)$ into particles of size r is modeled as

$$e_i^l(r) = 4\pi r^n N_A D_{wi}, \quad l = 0, 1 \tag{3.24}$$

$$e_i^l(r) = 4\pi r^n N_A D_{wi}/\sqrt{l-1}, \quad l = 2, 3...j_{cr} - 1 \tag{3.25}$$

where $n = 1$ corresponds to the Fickian diffusion model, and $n = 2$ corresponds to the collision model.

As in the approach of Saldivar *et al.* (1998), no cut-off chain length is fixed for the oligomers to enter into particles or micelles, and oligomers of all length $l = 0, 1, ...j_{cr} - 1$ are allowed entry. Thus, the total rate of entry into a single particle of size r is given by

$$\Re'_{entry}(r) = \sum_{l=0}^{j_{cr}-1} \sum_{i=1}^{2} e_i^l(r) p_{wi} [P_w]^l. \tag{3.26}$$

3.2.11 Desorption from particles

As shown in Table 3.1, the polymer chains inside the particles undergo chain transfer to the monomers. The resultant radicals can either propagate within the particles or desorb out of it into the aqueous phase (but once propagated, they can not desorb any more). The desorption rate is derived, extending the approach of Coen *et al.* (1998) to copolymer systems, as follows:

A balance for L_j^0 (Table 3.1 - particle phase) gives

$$\frac{d[L_j^0]}{dt} = \sum_{i=1}^{2} k_{trij}[L_i][M_j]_p - \sum_{i=1}^{2} k_{pji}[L_j^0][M_i]_p - k_{dMj}[L_j^0] \tag{3.27}$$

where the desorption rate coefficient $k_{dMj}(r)$ is given by $k_{dMj} = \frac{3\bar{D}_{wj}}{r^2}$, with $\bar{D}_{wj}$ being the diffusion coefficient of monomer j in the aqueous phase. Assuming a pseudo steady state,

$$[L_j^0] = \frac{\sum_{i=1}^{2} k_{trij}[L_i][M_j]_p}{k_{dMj} + \sum_{i=1}^{2} k_{pji}[M_i]_p} \tag{3.28}$$

Thus, the total rate of desorption of monomeric radicals from particles of size r is given by

$$\Re'_{desorption}(r) = \sum_{j=1}^{2} k_{dMj}(r) \frac{\sum_{i=1}^{2} k_{trij} p_i \bar{n}(r,t)[M_j]_p}{k_{dMj}(r) + \sum_{l=1}^{2} k_{pjl}[M_l]_p} \tag{3.29}$$

where $[L_i] = p_i \bar{n}(r,t)$.

3.2.12 Termination inside particles

The polymer chains inside the particles can undergo mutual termination. The rate of termination inside particles of size r is given by

$$\Re'_{termination}(r) = \frac{k_{tav}\bar{n}(r,t)^2}{V_p(r)N_A} \tag{3.30}$$

where $k_{tav} = \sum_{i=1}^{2}\sum_{j=1}^{2} p_i p_j k_{tij}$. $V_p(r)$ is the volume of a particle of size r.

3.3 Solution Technique

The population balance equation, which is a hyperbolic partial differential equation, is discretized in the particle radius (r) domain using orthogonal collocation on finite elements (Finlayson, 1980; Gupta, 1995). The r-domain is divided into a number of finite elements that each have a certain number of collocation points. The PDE is satisfied identically at each of the internal collocation points (see Figure 3.1).

The solution of the PDE within each finite element is approximated as a polynomial of degree N. Any polynomial of degree N can be expressed as a linear combination of orthogonal polynomials of degrees 0 to N. Thus, the solution at any collocation point can be approximated as a linear combination of orthogonal polynomials as

$$F_i(t) \approx F(r_i, t) = \sum_{j=0}^{N} d_j P_j(r_i) \tag{3.31}$$

where $F_i(t)$ is the approximate value of the density function at the collocation point r_i at time t (solved by some numerical technique), $F(r_i, t)$ is the accurate value, P_j is an orthogonal polynomial and d_j's are time-dependent coefficients. One class of orthogonal polynomials is the Jacobi polynomial, which satisfies the orthogonality condition defined as:

$$\begin{aligned} \int_a^b W(x) P_i(x) P_j(x) dx = 0, \quad & i \neq j \\ = C_i, \quad & i = j \\ i, j = 0, 1, 2...N & \end{aligned} \tag{3.32}$$

where C_i is a non-zero constant and $W(x) = (1-x)^\alpha x^\beta$ is a weighting function. For the case where $a = 0$, $b = 1$ and $\alpha = \beta = 0$, one gets the shifted *Legendre polynomial*, which finds wide application in chemical engineering problems.

Equation (3.31) can be recast by substituting the polynomials $P_j(r_i)$, as

$$F_i(t) \approx F(r_i, t) = \sum_{j=0}^{N} b_j r_i^j \tag{3.33}$$

where b_j's are new coefficients, in terms of the original coefficients d_j's. The collocation points are chosen to be the roots of the shifted *Legendre polynomial* of degree N. This choice evenly distributes the error in the approximation across the finite element. Also, the error introduced in the evaluation of the integrals involving the distribution (N_p, A_p^s, V_p *etc.*) is much lower using the quadratures of the

orthogonal polynomials. This is of particular significance for coagulation modeling. From Equation (3.33), one could get the coefficients b_j's, which express the solution at *all* points within the finite element. The continuity of the solutions across the finite elements is obtained by enforcing the constraint $F_N^j(t) = F_0^{j+1}(t)$, where F_N^j is the value of the function at the N^{th} (last) collocation point of finite element j and F_0^{j+1} is its value at the first collocation point of the $(j+1)^{th}$ finite element. Smoothness across the finite elements is ensured by enforcing the equality of the derivatives $\frac{\partial F^j(r_N,t)}{\partial r} = \frac{\partial F^{j+1}(r_0,t)}{\partial r}$. Thus, at the intersection of the finite elements, the PDE is not satisfied, and instead the equality of the derivatives is enforced. Also, it is essential to provide a proper boundary condition for the first collocation point of the first finite element (corresponding to particles of the smallest size). Saldivar *et al.* (1998) suggest that when the growth rate is non-zero, a pseudo steady state can be assumed corresponding to this radius, and one gets $\Re_{nuc} = \Re_{growth} + \Re_{coag}$. This can be provided as the boundary condition. Thus, at the boundary point (for $\Re_{coag} = 0$),

$$F(r_{nuc}, t)\frac{dr}{dt}|_{r=r_{nuc}} = \Re_{nuc} \tag{3.34}$$

For the discretization, 40 finite elements are used, with 5 collocation points per element (including the external collocation points). The complete system of differential-algebraic equations (DAE) that result from the discretized PDE and the material balance equations are solved using the DAE-solver DDASSL. A multi-component Newton-Raphson technique is employed to solve the monomer partitioning equations. As a minor detail, the aqueous phase species – monomer, initiator radicals, oligomers – are defined in absolute terms (moles) instead of in intrinsic units (moles/liter). This takes into account the volume change of the reactor contents in the semi-batch reaction scheme.

In using DDASSL, one has to provide a consistent set of initial conditions for the system states. To determine consistent initial conditions, one must solve

the algebraic equations first (for a fixed initial condition for the differential states), to force the residuals of those equations to zero. Since the discretized PDE representing the intersection of the finite elements are replaced by the equality of the derivatives (to ensure smoothness), which are algebraic equations, this becomes a complex implicit problem. The complete set of the algebraic equations forms a non-linear system. But, the subset involving the particle-related states alone forms a tri-diagonal system, whose solution can be found using Thomas' Algorithm (Holland and Liapis, 1983; Gupta, 1995). However, the particle-related algebraic states are coupled with the other algebraic states through the boundary condition. So, an iterative solution strategy, which exploits the efficient Thomas' Algorithm within, is employed. Once the consistent initial conditions for the algebraic states are obtained, one could then find the initial values of the derivatives for the differential states from the differential equations, such that the residual is *zero* for these differential equations.

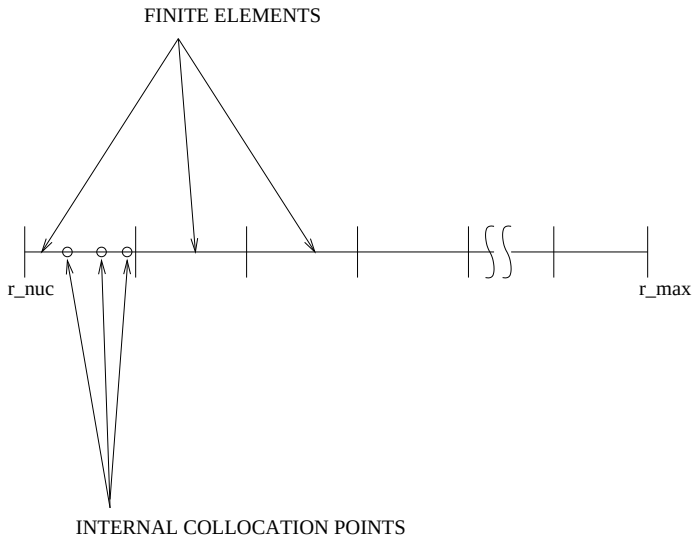

Figure 3.1: Discretization of the r-domain.

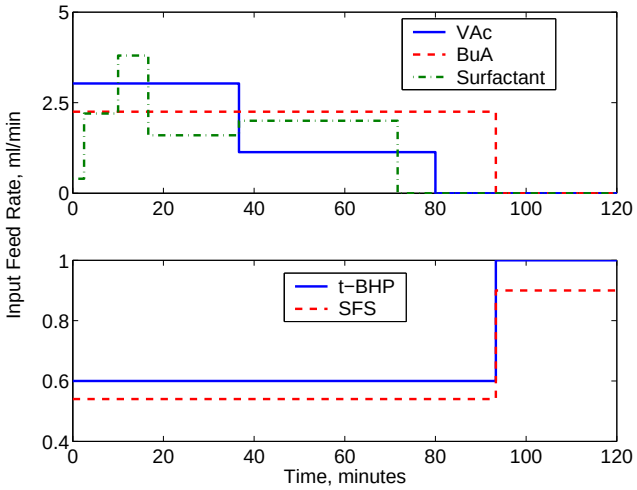

Figure 3.2: Feed profile for semi-batch emulsion polymerization.

3.4 Results and Discussion

Several of the model parameters employed for the nominal base case simulation were drawn from literature sources (Delgado et al., 1988; Perry and Green, 1984; Urretabizkaia et al., 1994; Urretabizkaia et al., 1993), and are shown in Table 3.2. Table 3.3 shows nominal values for the uncertain parameters, that would need to be refined.

Simulations are performed using the formulation defined by Equation (3.18) to describe the distribution of the average number of radicals per particle. The collision model ($n = 2$ in Equations (3.11), (3.12), (3.24) and (3.25)) is used to calculate the entry rates into micelles and particles. Coagulation is assumed to be negligible. Figure 3.2 shows the feed profile for VAc, BuA, surfactant, tBHP and SFS that was employed in the simulation. The monomer streams are pure components, the surfactant feed is a 22.7 weight% aqueous solution, the t-BHP feed is a 3.33 weight% solution and SFS feed is a 3.41 weight% solution. The initial mixture consists of 1 liter DI Water, 0.6 moles of VAc and 2×10^{-4} moles of ferrous ammonium sulphate catalyst. The polymerization is initiated in the aqueous phase, and forms the aqueous phase oligomers as seen in Figure 3.3(a). In this *ab initio* batch (no

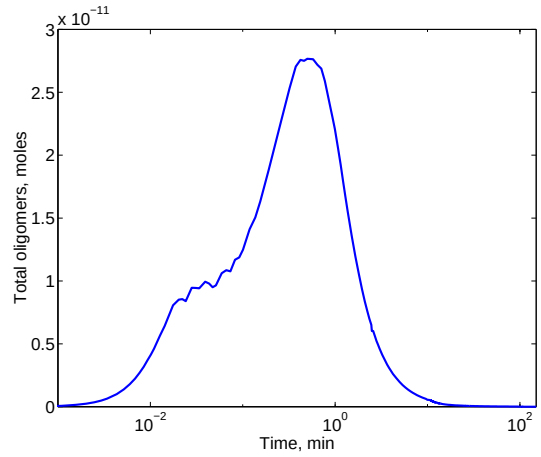

(a) aqueous phase oligomers

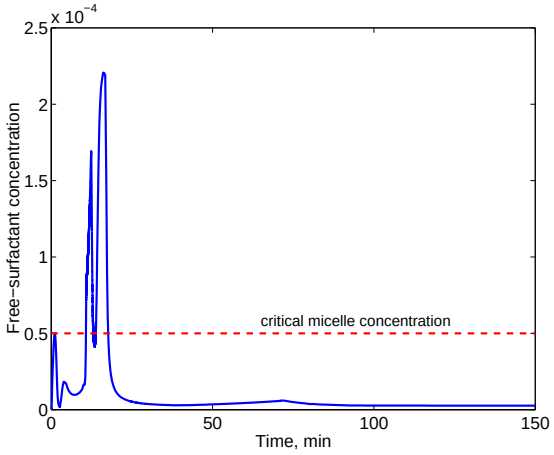

(b) concentration of surfactant in the aqueous phase, S_w

Figure 3.3: Aqueous phase oligomers and free surfactant concentration.

particles in the system at the early times) the oligomers formed propagate and attain the critical chain length causing homogenous nucleation. Figure 3.4(a) shows the rates of micellar and homogenous nucleation during this run. This figure shows that the rate of homogenous nucleation increases at first with the formation of more aqueous-phase oligomers. When a sufficient number of particles have been nucleated, the rate of homogenous nucleation decreases, as the freshly formed oligomers enter into existent particles before they reach the critical chain length. Homogenous nucleation nearly ceases at about 0.2 minutes. Figure 3.4(a) also shows that the first burst of micellar nucleation occurs at around 1 minute. This corresponds to the first point where the free surfactant concentration S_w exceeds the critical micelle concentration, cmc, as can be seen from Figure 3.3(b). After this point, the total number of particles, N_p remains constant until about 12 minutes, as can be seen in Figure 3.4(b). Subsequently, two more bursts of micellar nucleation occur as seen in Figure 3.4(a). The partial reason for this is the increase in the surfactant feed rate at this time (Figure 3.2), which results in the cmc-crossings seen in Figure 3.3(b). N_p essentially remains constant after this point (Figure 3.4(b)).

Figure 3.5(a) shows the distribution of the average number of radicals/particle, $\bar{n}(r,t)$. At any given time, a larger particle size r leads to a larger value of $\bar{n}$. The peak seen in the distribution of $\bar{n}(r,t)$ corresponds to the peak in the aqueous phase oligomers, and hence in the entry rates of the radicals into the particles. Figure 3.5(b) shows the global average $n_{ave}(t)$ (calculated using the distribution $\bar{n}(r,t)$ in Equation (3.20)). The high values are consistent with the values documented in earlier studies (Dimitratos et al., 1989; Liotta, Georgakis and El-Aasser, 1997). Corresponding to the increase in the total number of particles N_p, the concentration of oligomers drops to low values (Figure 3.3(a)), due to the higher capture (entry) rates into particles. Figure 3.6(a) shows the rate of polymerization of VAc and BuA. Also corresponding to the nucleation events is the increase in the total rate of

consumption of VAc and BuA. Figure 3.6(b) shows the pseudo-homopolymer probability in the particle and the aqueous phase, *i.e.,* the fraction of the live polymer radicals that have a VAc end-group. While this is very high at the initial time, it drops to a very low value once BuA feed enters the system, the reason being the high reactivity of BuA relative to VAc, as can be seen from Table 3.2 (r_1 and r_2).

At 80 minutes and 95 minutes respectively, the feeds of VAc and BuA end (Figure 3.2). Thereafter, the concentrations of the monomers in the particles drop to lower values. This results in a decrease in the rate of polymerization (in spite of an increase in the feed rates of the initiator components), as seen in Figure 3.6(a). Figure 3.6(c) shows the instantaneous conversion of the two monomers. Figure 3.6(c) shows that BuA is essentially completely converted to polymer after this point, while the conversion of VAc is only about 60%. This results in an increase in the pseudo-homopolymer probability (Figure 3.6(b)). Termination rates increase now, as the VAc-ended chains are more susceptible to termination (refer Table 3.2). Thus, $\bar{n}(r,t)$ is reduced (Figures 3.5(a) and 3.5(b)) and the conversion of VAc asymptotes at 60%.

Figure 3.7 shows the evolving weight-averaged PSD (probability density function (PDF)), defined as $W(d,t) = \frac{r^3 F(r,t)}{\sum r^3 F(r,t)}$. The initial modes of particles, formed by the homogenous and the primary micellar nucleation (1 minute), grow rapidly until the nucleation of the other modes of particles by the secondary micellar nucleation (starting at about 12 minutes). After that, there is a reduced growth rate. Figure 3.8 shows the size-dependent growth rate $\frac{dr}{dt}$ (Equation (3.21)) – the growth kernel – at various times in the batch. This registers the falling growth rate with the decrease in $\bar{n}(r,t)$ that accompanies the increase in the total particles N_p, as seen by the plots at 1 minute, 10 minutes and 13 minutes. After the first 60 minutes of the batch, the growth rates drop to very low values as seen by the 70 minute plot in Figure 3.8. This is due to the decrease in the concentration of the monomers inside the particles. One can observe the distribution becoming more diffuse with growth

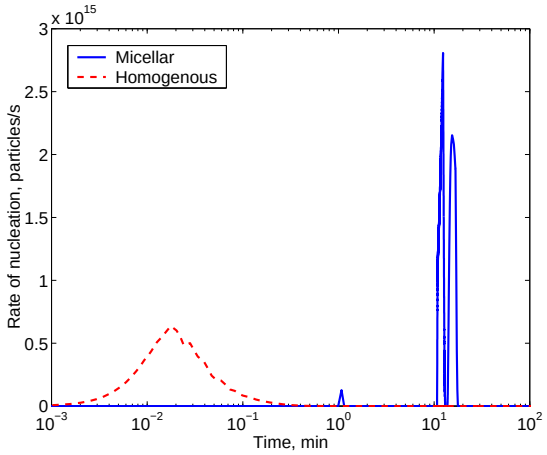

(a) rates of the homogenous and micellar nucleation events during the batch

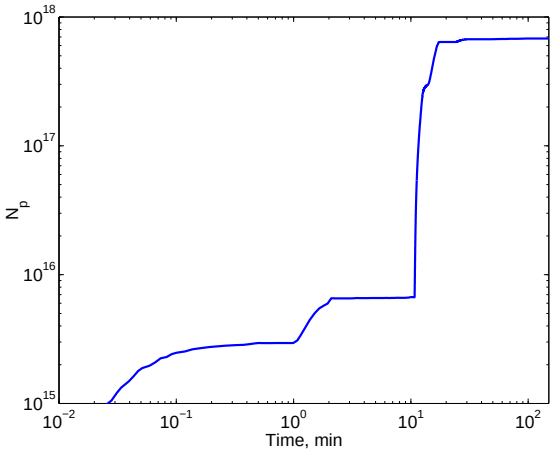

(b) total number of particles, N_p

Figure 3.4: Profile of the nucleation rates and total particles.

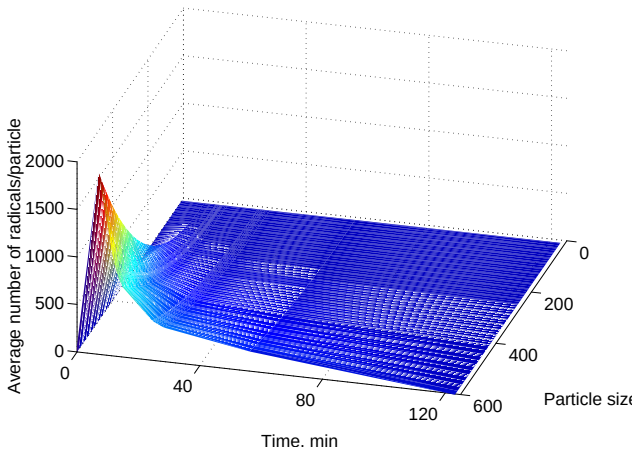

(a) distribution of the average number of radicals per particle $\bar{n}(r,t)$

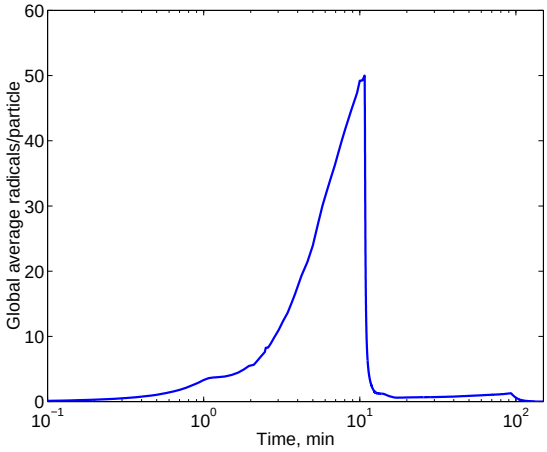

(b) global average number of radicals per particle, $n_{ave}(t)$

Figure 3.5: Average number of radicals/particle, $\bar{n}(r,t)$.

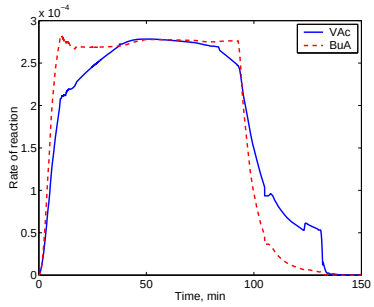

(a) rates of consumption of VAc and BuA during the batch

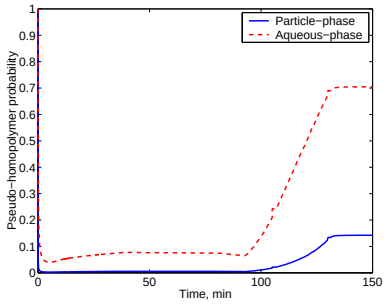

(b) the pseudo-homopolymer probability in the particle-phase, p_1, and in the aqueous-phase, p_{w1}

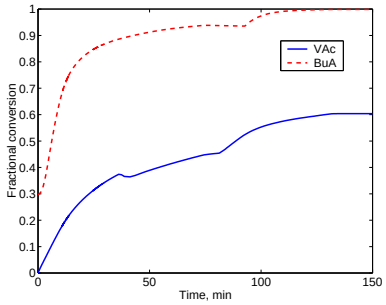

(c) instantaneous conversion of monomer i = 1-(moles unreacted monomer i)/(total moles of i fed until that time)

Figure 3.6: Profile of some miscellaneous process variables.

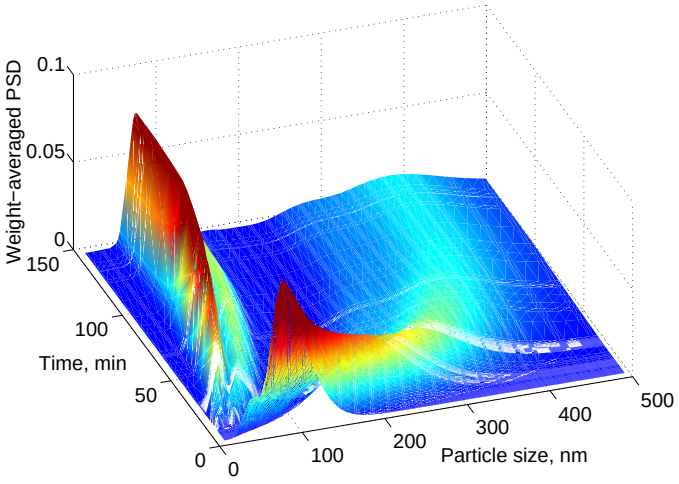

Figure 3.7: Evolution of the probability density function (PDF) $W(d,t)$, versus the unswollen particle diameter.

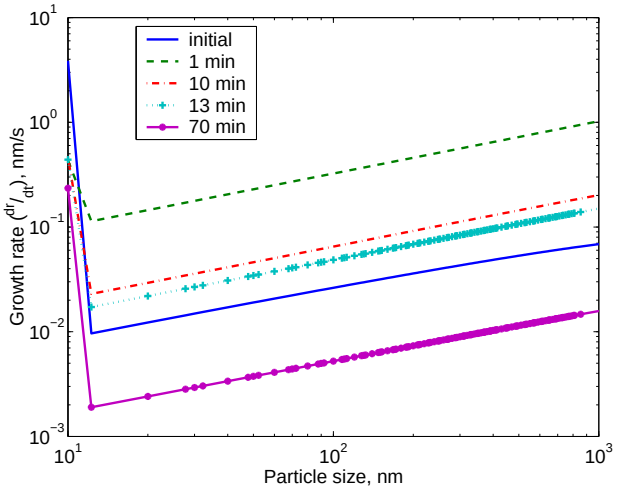

Figure 3.8: The size-dependent growth kernel at various times in the batch.

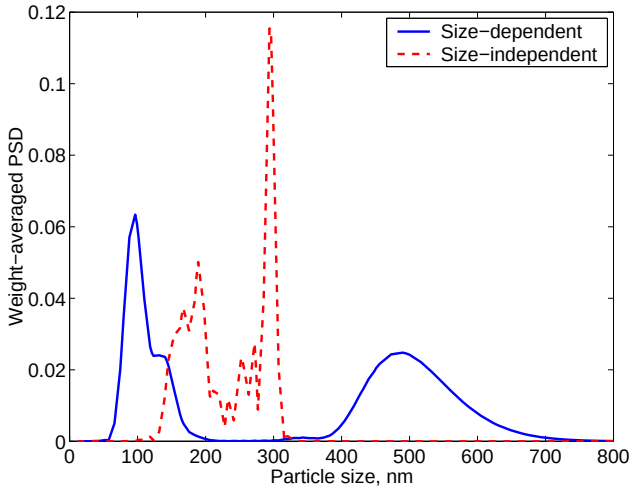

Figure 3.9: Comparison of the PSD for size-dependent $\bar{n}$ with size-independent $\bar{n}$.

in Figure 3.7. This is due to the size-dependent growth, with the larger particles growing faster than the smaller ones, as seen in Figure 3.8.

3.4.1 Effect of size-dependence of $\bar{n}$ on the simulation results

Most of the previous modeling studies have employed a single average number of growing radicals/particle to all particles, irrespective of their size, usually in the form of Smith-Ewart equations or adaptations of them. This approach can lead to very different results, as can be seen from Figure 3.9. The reason for this can be seen from the plot of the distribution of the average number of radicals/particle in Figure 3.5(a), and the resultant size-dependent growth seen in Figure 3.8. In the simulation for the size-independent case, $n_{ave}(t)$ (Equation (3.20)) is used in calculating the growth rates inside all particles. This predicts a narrow distribution, and also a sharp front in the PSD, which do not agree with the experimental observations. Also, the particles are much smaller. To match the experimentally observed PSD results, size-dependent growth is to be incorporated. While other methods have been proposed to allow size-dependent growth, including artificial dispersion of the distribution, this is a physically more meaningful approach. Based on experimental

results, one can see that a collision model (n=2 in Equations (3.24) and (3.25)) is more apt to account for the dispersion of the distribution, as opposed to the relatively lower size-dependence offered by the diffusion model (n=1).

3.5 Comparison with experimental results

Figure 3.10 compares the simulation results with those observed in an experimental facility, corresponding to the recipe shown in Figure 3.2. Figure 3.10(a) compares the PSD predicted by the model after 2 hours of batch time, with that observed experimentally at this time. As was discussed earlier, the simulation shows an initial homogenous nucleation followed closely by a primary micellar nucleation, and a delayed but prominent secondary micellar nucleation. This results in the three modes of particles seen in Figure 3.10(a) (solid line), centered at approximately 400 nm, 300 nm and 100 nm. The experimentally-observed distribution (dashed line) also shows the presence of three modes, centered at approximately 350 nm, 200 nm and 70 nm. But the modes are more diffuse and interconnected. Figure 3.10(b) compares the total particles from the simulations with that calculated from measurements. The experimental result suggests a gradual and prolonged nucleation, as opposed to the rapid nucleation simulated by the model. This rapid nucleation is a feature of the current PBE models for PSD in emulsion polymerization. An earlier and more gradual secondary micellar nucleation would also reduce the total particles N_p, since some surfactant would be utilized to stabilize the particles nucleated earlier (which would be growing too) – unlike in this case with rapid nucleation where all of it is available for nucleation. Accounting for coagulation could satisfy some of these requirements, while improvements in the nucleation models might also be necessary. An early secondary micellar nucleation event would also result in an early drop in the growth rates, resulting in the size of the larger modes matching between the experimental and simulation results. Figure 3.10(c) compares the polymer content of the emulsion as calculated using the model and gravimetric

experimental data. Again, the mismatch is due to the error in the nucleation, and its cascaded effect on particle growth.

Figure 3.11 compares the model predictions with the experimental results for a slightly different recipe from the one shown in Figure 3.2. In this recipe, the feed rate of VAc up to 16.7 minutes was reduced by about 20%, and this monomer was fed in towards the end. The experimental data on the total particles N_p in Figure 3.11(b) shows a prolonged nucleation, which is relatively rapid initially, then more gradual up to about 40 minutes, but steeply increases at that time, coinciding with the decrease in the feed rate of VAc. A probable reason for this is the depletion of monomer droplets from the system, and the release of surfactant absorbed within them back into the aqueous phase. Even though the simulation result shows a similar trend, the timings and magnitudes are in disagreement. The major discrepancy could be because the simulation predicts a larger initial homogenous nucleation, which cascades into a reduced primary micellar nucleation and hence a hastened secondary micellar nucleation. This results in the mismatch in the PSD seen in Figure 3.11(a). The reduced primary micellar nucleation also results in larger growth rates at early times, resulting in the early modes growing to a larger size than observed in the experimental data. This in turn accounts for the higher solids content predicted by the model, as seen in Figure 3.11(c).

Figure 3.12 compares the simulation and experimental results for yet another recipe, where the surfactant feed rate between 10 and 15 minutes was reduced by about 40% relative to the one shown in Figure 3.2. The amount of surfactant withheld at this time was fed at a reduced rate towards the end of the batch. The experimental data of the total particles in Figure 3.12(b) shows a near-constant N_p up to about 20 minutes, and then N_p increases to a modest order of 10^{16}. On the other hand, the simulation result shows a reduced N_p at early times, and an order of magnitude larger N_p at later times. The mismatch could be either because

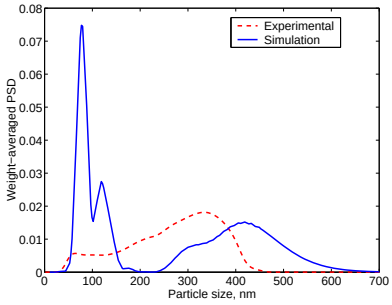

(a) comparison of the end-point PDF between the experimental and modeling results

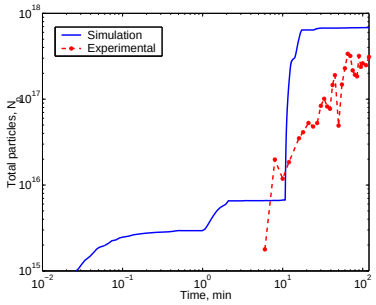

(b) comparison of the N_p profiles

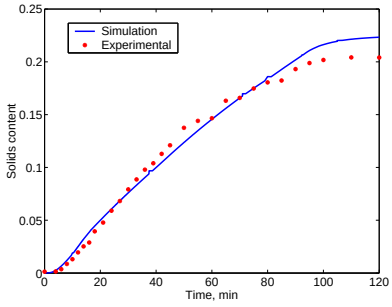

(c) comparison of the solids content, defined as (weight of polymer + surfactant)/(total weight of the latex)

Figure 3.10: Comparison of the simulation and experimental results for the recipe shown in Figure 3.2.

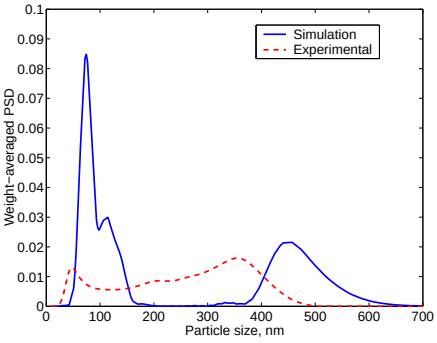

(a) comparison of the end-point PDF between the experimental and modeling results

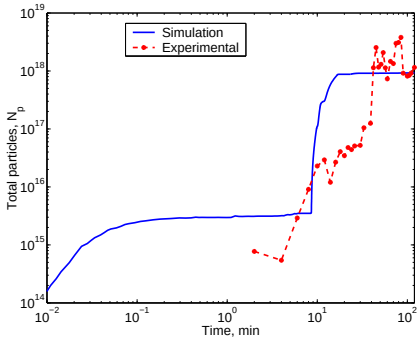

(b) comparison of the N_p profiles

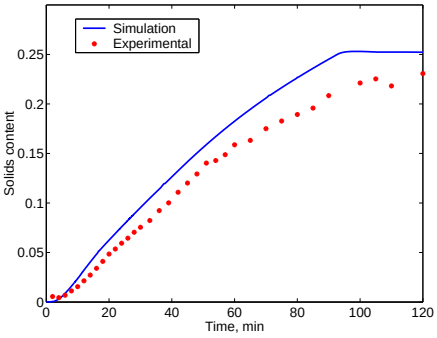

(c) comparison of the solids content

Figure 3.11: Comparison of the simulation and experimental results for a recipe where VAc feed rate is perturbed relative to that shown in Figure 3.2.

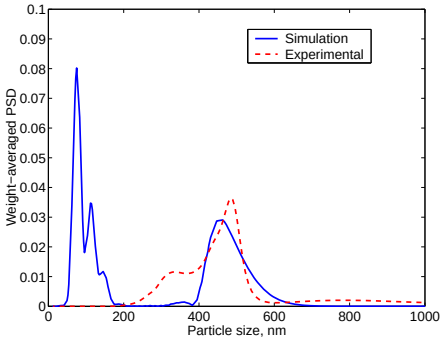

(a) comparison of the end-point PDF between the experimental and modeling results

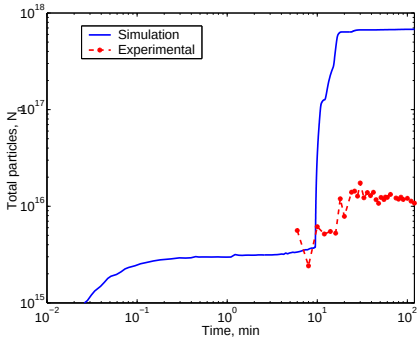

(b) comparison of the N_p profiles

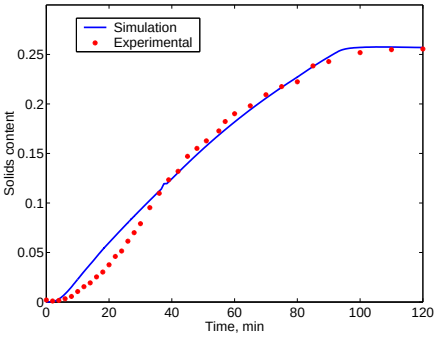

(c) comparison of the solids content

Figure 3.12: Comparison of the simulation and experimental results for a recipe where surfactant feed rate is perturbed relative to that shown in Figure 3.2.

of (i) a reduced homogenous and primary micellar nucleation or (ii) an enhanced homogenous nucleation which results in the reduced primary micellar nucleation. (The latter effect was observed in the earlier result too, and hence is the more probable one). One of the above causes the secondary micellar nucleation to happen earlier, and also to be more prominent. The above effects manifest themselves in the form of the mismatch in the PSD at the end of 2 hours, as seen in Figure 3.12(a). Figure 3.12(c) compares the solids content for this batch. The higher solids simulated at early times could be due to the larger N_p at these times, and the lower values after 40 minutes could be because of the reduced growth rates.

The above comparisons of the simulation and experimental results suggest that the uncertainty in the surfactant partitioning parameters and the initiator parameters could be the underlying cause for the discrepancies observed. A parametric sensitivity study is detailed in the following section to examine this probability.

3.6 Parametric Sensitivity

In this section, the sensitivity of the model predictions to some of the uncertain parameters will be explored. Such a study is relevant for the following reasons:

1. The previous section on the comparison of the simulation results with the experimental results highlighted possible reasons for the discrepancies between the two. A parametric sensitivity study would identify those parameters that can address these issues. It will also identify the most sensitive parameters among the unknown/uncertain parameters. In addition, it gives an idea of the search direction for those parameters that would be fit using experimental data on PSD and other process variables. Moreover, in such complex models, multiple parameters could affect the same aspects of the process. The sensitivity studies aid in discerning the nuances in the effects of the different parameters, which is essential in parameter estimation, to retain the predictive capabilities of the model.

2. These sensitivity results can be used to qualitatively validate the predictive abilities of the model, based on prior experience with the processes. From another perspective, these results elucidate the process of the evolution of PSD in emulsion polymerization – which is important to formulate an effective control strategy.

3. In a complex process, with several parallel and interacting subprocesses, the prominent and rate determining steps depend upon the set of parameters that characterize the system. Certain subprocesses, however, would be relatively insensitive under all sets of parameters. Identification of such subprocesses would enable robust model reduction for more efficient computation, which is important for on-line control.

Tables 3.4 and 3.5 summarize the results of the parametric sensitivity studies with respect to the nominal parameters. In most of these cases, the perturbation in the parameter has a direct effect at an early stage. This effect then cascades through the process in several ways, due to complex interactions, and either augments the original effect or offsets it. Also, the nucleation phenomena is affected the most, and usually, though not always, the effects on the other processes are a result of the effects on the nucleation phenomena. For purposes of brevity, only two of these results are detailed here.

Figure 3.13 shows the effects of Γ_∞ on the simulation results. Γ_∞ is the amount of surfactant adsorbed per unit surface area of particles, on monolayer formation. As Γ_∞ increases, the amount of surfactant adsorbed onto the surface of the particles in equilibrium with the amount in the aqueous phase increases. This lowers the free surfactant concentration S_w, (to satisfy the mass balance (Equation (3.23)), as seen in Figure 3.13(a). Thus, the primary burst of nucleation is delayed but is stronger with the increase in Γ_∞ from 4.5×10^{-6} to 4.6×10^{-6} mol/m^2, as seen in Figure 3.13(b). This results in the separation of the homogenous mode

and the primary micellar mode, as is evident in Figure 3.13(c). The effect on the primary mode cascades into the secondary micellar mode. Due to the larger number of particles at the larger Γ_∞ value ($4.6 \times 10^{-6}\ mol/m^2$), more surfactant is utilized for particle stabilization, resulting in a reduced secondary micellar nucleation (as is evident from Figure 3.13(b) – loglog plot). Further increase in Γ_∞ almost completely eliminates the primary micellar nucleation, resulting in a single micellar nucleation at about 12 minutes. In this case, the reduction in the secondary micellar nucleation is due to the larger growth rates and particle sizes (of the homogenously-nucleated mode). Thus, in these coagulation-free simulations, Γ_∞ influences the micellar nucleation phenomenon, and the effect cascades through the batch. Under coagulation-prone conditions, this parameter could have an effect on coagulation.

Figure 3.14 shows the effect of D_{w1} (related to the mass transfer coefficient of oligomers of type 1) on the PSD and nucleation rate. Unlike the effect of the surfactant-related parameters (Γ_∞, for instance), which had an impact on the primary micellar nucleation first, and then cascaded through the secondary micellar nucleation and the rest of the process, the effect of D_{w1} is observed even earlier, in the homogenous nucleation. As D_{w1} increases from 20 cm/s to 40 cm/s, a monotonic decrease in the homogenous nucleation rate after about 10^{-2} min is observed. This is because the rate of entry of oligomers into the particles increases with D_{w1}. Due to the reduced number of homogenously-nucleated particles at higher D_{w1}, the total surface area of the particles decreases at these early times. This in turn makes more surfactant available for the primary micellar nucleation. As explained earlier, this effect on the primary micellar nucleation then feeds back through the rest of the process. There is no direct effect of D_{w1} on growth rate (in fact, the particle populations are smaller at larger D_{w1}). This is either due to the lower pseudo-homopolymer probability of species 1 oligomers, or due to the negative feed back from the micellar nucleation events.

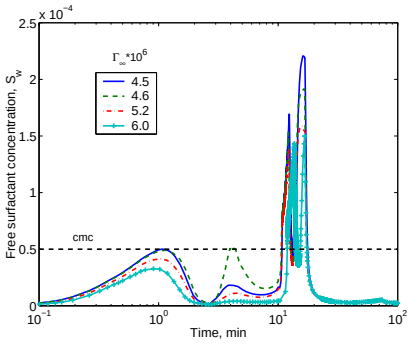

(a) effect of Γ_∞ on S_w

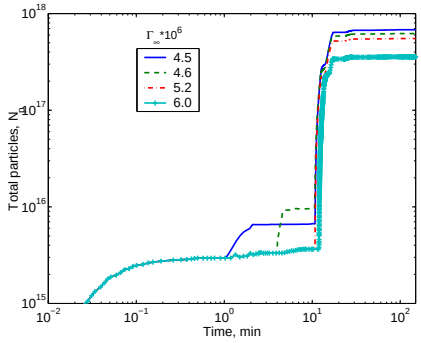

(b) effect of Γ_∞ on N_p

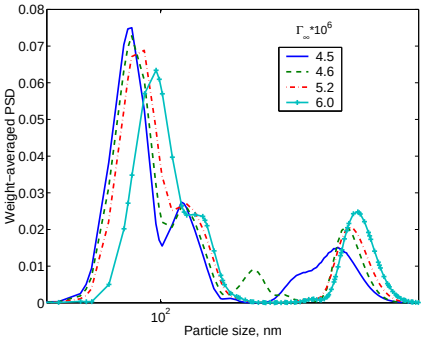

(c) weight-averaged PSD $W(d,t)$ at the end of 150 minutes

Figure 3.13: The modes formed by the initial homogenous nucleation and the primary micellar nucleation are separated with an increase in Γ_∞. Further increase in Γ_∞ eliminates the primary micellar nucleation. Overall, there is a reduced micellar nucleation with increase in Γ_∞.

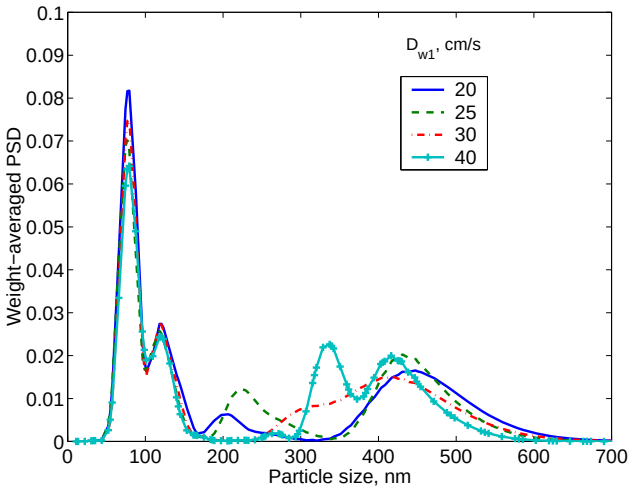

(a) weight-averaged PSD $W(d,t)$ at the end of 150 minutes

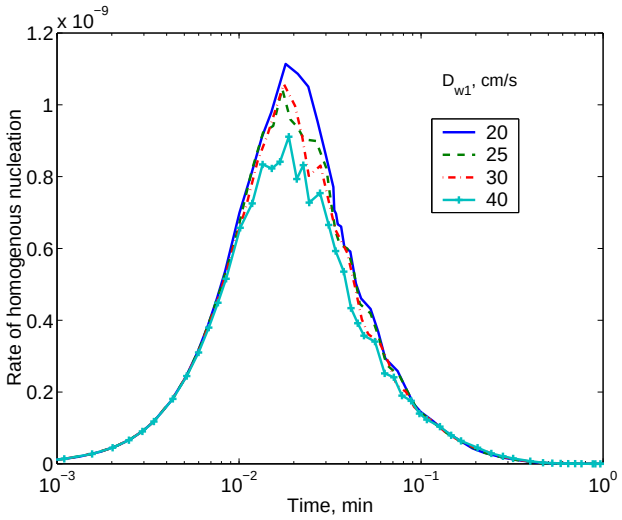

(b) effect on the rate of homogenous nucleation

Figure 3.14: An increase in D_{w1} decreases the number of particles formed by the homogenous nucleation. Effect is seen after a sufficient number of particles have been nucleated. The mode corresponding to the primary micellar nucleation shifts closer to that due to the homogenous nucleation, and also becomes more prominent, with increase in D_{w1}.

These and other sensitivity results elucidate that the uncertainty in some of the parameters could account for the errors in the magnitudes and timings of the nucleation events. Correcting these could in turn correct the errors in the growth rates, and the size of the peak. However, these results also suggest that accounting for particle coagulation is necessary. This is particularly so at later times, when the solids content increases and the surface coverage of the particles with surfactants decreases.

3.7 Coagulation Modeling

The discrepancies seen in the predicted distributions and profiles relative to the experimental measurements, and the inability to account for these completely in parametric sensitivity studies, clearly highlight the importance of incorporating the coagulation events into the model, even in the low solids content regime employed in this study. The modeling of the coagulation events is described next.

The coagulation term $\Re_{coag}(r,t)$ involves two terms, one accounting for the formation of a particle by coagulation of particles of smaller sizes, and the other accounting for the depletion of a particle by coagulation with other particles. Thus, $\Re_{coag}(r,t) = \Re_{formation}(r,t) - \Re_{depletion}(r,t)$. The formation term $\Re_{formation}(r,t)$ (in moles/m-s) is modeled as:

$$\Re_{formation}(r,t) = \frac{1}{V_w} \int_{r'=r_{nuc}}^{\frac{r}{2^{\frac{1}{3}}}} \beta(r',r'')F(r',t)F(r'',t)dr'\frac{dr''}{dr} \tag{3.35}$$

In the above equation, r' and r'' denote the sizes of the two (smaller) particles that form a particle of size r upon coagulation. These are related by a volume additivity condition as $(r')^3 + (r'')^3 = r^3$. Thus, the term $\frac{dr''}{dr}$ in Equation (3.35), which represents the differential of the size of the second particle (involved in coagulation with the first particle of fixed size r') to the differential of the size of the particle formed, is given by:

$$\frac{dr''}{dr} = \frac{r^2}{(r^3 - (r')^3)^{\frac{2}{3}}} \tag{3.36}$$

Thus, the formation term becomes:

$$\Re_{formation}(r,t) = \frac{1}{V_w}\int_{r'=r_{nuc}}^{\frac{r}{2^{\frac{1}{3}}}} \beta(r',r'')F(r',t)F(r'',t)\frac{r^2}{(r^3-(r')^3)^{\frac{2}{3}}}dr' \qquad (3.37)$$

The upper limit of integration $\frac{r}{2^{\frac{1}{3}}}$ is to avoid double counting the coagulation events, and corresponds to the case in which the two coagulating particles are of the same size. The depletion term is given by:

$$\Re_{depletion}(r,t) = \frac{1}{V_w}\int_{r_{nuc}}^{r_{max}} \beta(r,r')F(r,t)F(r',t)dr' \qquad (3.38)$$

where r_{max} is the size of the largest particle that can participate in coagulation.

The calculation of the intrinsic coagulation rate (coagulation kernel) β involves considerations of the forces and potentials between the particles. In the current study with non-ionic surfactants, the stabilizing mechanism is assumed to be steric hindrance, which is caused by the bulkiness of the surfactant chains that prevents the particles onto which the chains are adsorbed from approaching each other. As stated previously, there are few studies addressing the modeling of the steric potential, particularly in the context of population balances in emulsion polymerization. It is essential to develop a model that can predict the experimental results well, while simultaneously being of a low computational complexity. Thus, in this study, simple expressions for the steric potential (analogous to those commonly employed for electrostatic and van der Waals' potentials) are used. The steric repulsive potential between two flat objects due to the surfactant chains adsorbed onto their surfaces, is given by (Israelachvili, 1998) (page 295):

$$\psi_R^f(D) = \frac{100L}{\pi}\Gamma^{\frac{3}{2}}kTe^{-\frac{\pi D}{L}} \qquad (3.39)$$

where D is the separation distance between the objects. The above equation is valid for separation distances up to twice the extensional length (L) of the surfactant chain into the aqueous phase, which is given by $L = \Gamma^{\frac{1}{2}}R_F^{\frac{5}{3}}$. Γ is the surface coverage of the

particles with surfactants (based on the partitioning calculation of the surfactants among the various phases) modeled as:

$$\Gamma = \frac{\Gamma_\infty K_{ad} S_w N_A}{1 + K_{ad} S_w} \tag{3.40}$$

In the above equation, K_{ad} is the adsorption equilibrium constant for the surfactants and Γ_∞ is the equilibrium surface coverage (Langmuir constants), N_A being the Avogadro number. R_F is the Flory radius, which is related to the radius of gyration of the polymeric surfactant chain (R_g) as $R_F = \alpha R_g$. Here, α accounts for the interaction of the surfactant with the solvent (water). The radius of gyration can be calculated as $R_g = \frac{l\sqrt{n}}{\sqrt{6}} = \frac{l\sqrt{\frac{M}{M_0}}}{\sqrt{6}}$, where l is the effective segment length (of the polymeric surfactant chain), n is the number of segments in the chain, M is the molecular weight of the surfactant chain, and M_0 is the molecular weight of a monomeric unit in the chain.

The Derjuguin approximation (Israelachvili, 1998) can be employed to extend Equation (3.39) to obtain the repulsive potential between spherical particles. Thus, the repulsive force between two spherical particles of size r and r', separated by a distance D is given by:

$$F_R(D) = \frac{2\pi r r'}{r + r'} \frac{100L}{\pi} \Gamma^{\frac{3}{2}} kT e^{-\frac{\pi D}{L}} \tag{3.41}$$

This equation is again valid for $(r + r') < D < 2L$. Using the relation between force and potential, $F_R(D) = -\frac{\partial \psi_R(D)}{\partial D}$, one can obtain the steric potential as:

$$\psi_R(D) = -\int F_R(D) d(D) = \frac{2rr'}{r+r'} \frac{100L^2}{\pi} \Gamma^{\frac{3}{2}} kT e^{-\frac{\pi D}{L}} + c \tag{3.42}$$

where c is a constant of integration. An adjustable constant is introduced into the above equation to account for the various mechanistic and parametric uncertainties in the model, thereby casting the repulsive potential as:

$$\psi_R(D) = c_2 \frac{2rr'}{r + r'} \frac{100L^2}{\pi} \Gamma^{\frac{3}{2}} kT e^{-\frac{\pi D}{L}} + c' \tag{3.43}$$

where c_2 is the adjustable constant, and $c' = c_2 c$.

The van der Waals' attractive potential is relatively well known, and is modeled as (for all $D > (r + r')$):

$$\psi_A(D) = \frac{A}{6}\left(\frac{2rr'}{D^2 - (r+r')^2} + \frac{2rr'}{D^2 - (r-r')^2} + ln\left(\frac{D^2 - (r+r')^2}{D^2 - (r-r')^2}\right)\right) \quad (3.44)$$

In this equation, A is the Hamakar constant, which accounts for the effects of the various intrinsic (internal) interactions between the particles that result in the net attractive potential.

The net interaction potential, $\psi(D) = \psi_R(D) - \psi_A(D)$, can be utilized to calculate the intrinsic coagulation rate using established procedures (Melis et al., 2000), as follows: the Fuch's stability ratio $W(r, r')$, which has a reciprocal relationship to the fraction of collision events that result in a successful coagulation event (activation barrier), is calculated as:

$$W(r, r') = (r + r') \int_{D=(r+r')}^{\infty} \frac{exp(\frac{\psi(D)}{kT})}{D^2} d(D) \quad (3.45)$$

(k is the Boltzmann constant and T is the temperature of the emulsion). The stability ratio is related to the intrinsic coagulation rate using the first order Smoluchowski equation as follows:

$$\beta(r, r') = c_1 \frac{4\pi D_0 (r + r')}{W} \quad (3.46)$$

In Equation (3.46), c_1 is another adjustable constant which subsumes the constant c' in Equation (3.43), besides providing a way to account for the shear effects. This is based on the hypothesis that the shear effects enhance the coagulation rate over that under shear-free conditions (diffusion versus convection analogy) (Evans and Wennerstrom, 1999). The diffusion co-efficient D_0 is given by:

$$D_0 = \frac{kT}{6\pi\mu}\left(\frac{1}{r} + \frac{1}{r'}\right) \quad (3.47)$$

Here, μ is the viscosity of the emulsion latex, related to the solids content as $\mu = \frac{\mu_0}{(1-\frac{sc}{sc_{ref}})^2}$, μ_0 being the viscosity of water at the reaction temperature, sc, the latex solids content and sc_{ref}, a reference solids content.

3.8 Coagulation-inclusive Model Results

Table 3.6 lists the modified model parameters, the other parameters being the same as in Tables 3.2 and 3.3. The straightforward solution methodology based on orthogonal collocation on finite elements results in a stiff system of equations, with condition numbers of the order of 10^4 in the regime of nucleation. This in turn results in large computation times. Incorporating the coagulation effects further increases the computational load, due to the intensive nature of the coagulation calculations. To circumvent this problem, an efficient computational technique, based on an order reduction effected by the decomposition of the fast and the slow kinetics, is employed (Chapter 4). Also, to reduce the computational load, the intrinsic coagulation rate $\beta(r, r')$ is updated only once every 10 min of batch time.

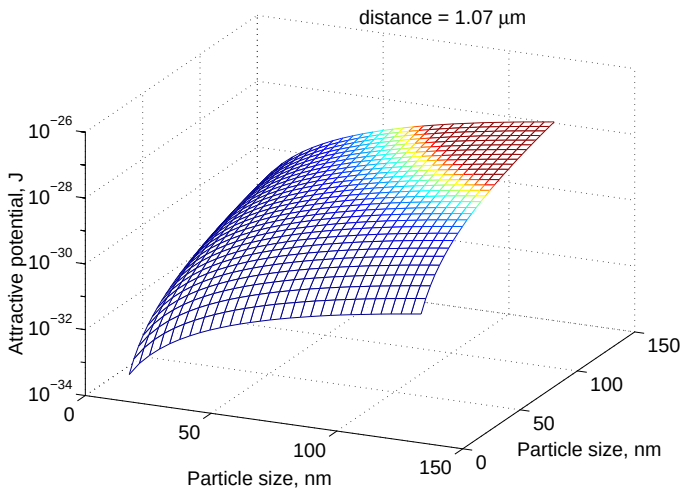

Figure 3.15: van der Waals' attractive potential between particles separated by a representative distance of $D = 1.07\mu m$.

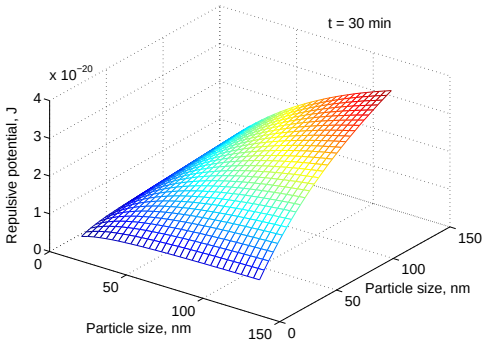

(a) $t = 30\ min,\ S_w = 0.9 \times 10^{-4}\ moles/liter$

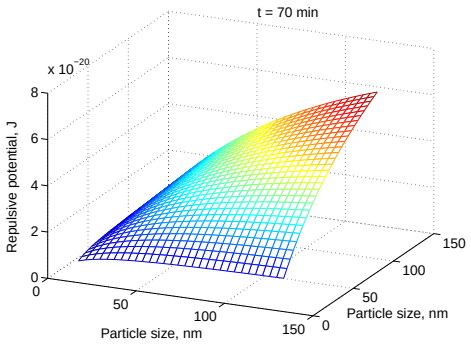

(b) $t = 70\ min,\ S_w = 3.8 \times 10^{-4}\ moles/liter$

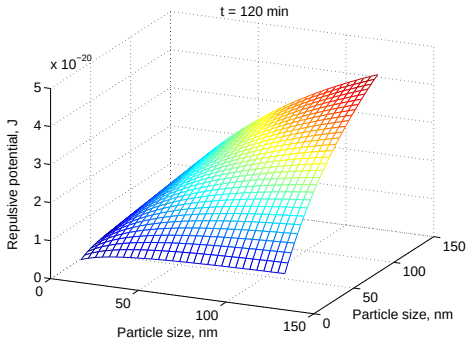

(c) $t = 120\ min,\ S_w = 1.2 \times 10^{-4}\ moles/liter$

Figure 3.16: Steric repulsive potential between particles separated by a distance of $D = 1.07\mu m$ at different time instants, indicating the dependence on the free surfactant concentration, S_w.

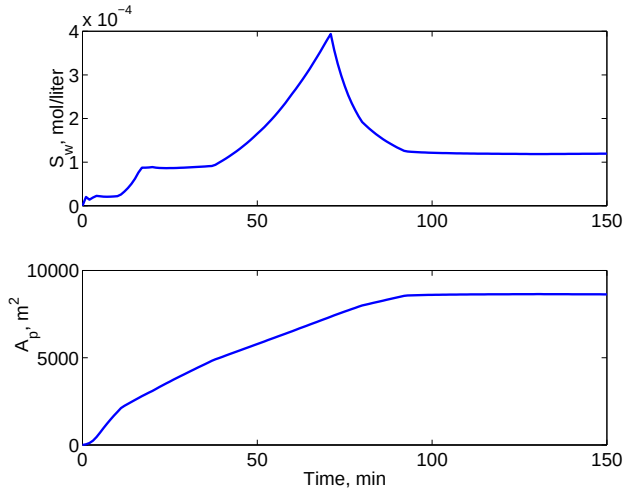

Figure 3.17: Free surfactant concentration, S_w, and the total swollen particle surface area, A_p, corresponding to the base case recipe.

3.8.1 Analysis of Base Case Recipe

A simulation result corresponding to the recipe shown in Figure 3.2 is presented next, with particular emphasis to the analysis of the coagulation kernel and its sensitivity to the process inputs. A comparison of the improvement obtained relative to the previous coagulation-free model predictions, and validation against experimental data are presented in the next subsection. Figure 3.15 shows a plot of the van der Waals' attractive potential between particles of various sizes, separated by a representative distance of $D = 1.07\mu m$. Figure 3.16 show similar plots of the repulsive potential between particles of various sizes, separated by the same distance of $1.07\mu m$. Figures 3.16(a), 3.16(b) and 3.16(c) correspond respectively to 30 min, 70 min and 120 min of the recipe shown in Figure 3.2. As an attempt to draw a correlation between the coagulation kernel and the free surfactant concentration, Figure 3.17 shows the profile of the free surfactant concentration S_w over the course of the batch (top plot) and the total swollen particle area (bottom plot). The plot shows that S_w varies profoundly during the batch. It increases from 10 min up to approximately 17 min, caused partly by the increase in the surfactant feed rate at

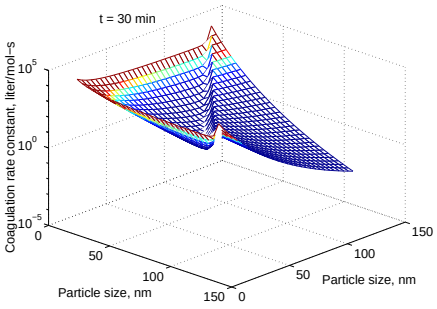

(a) $t = 30\ min$, $S_w = 0.9 \times 10^{-4}$ $moles/liter$

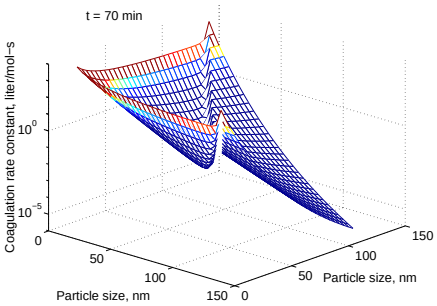

(b) $t = 70\ min$, $S_w = 3.8 \times 10^{-4}$ $moles/liter$

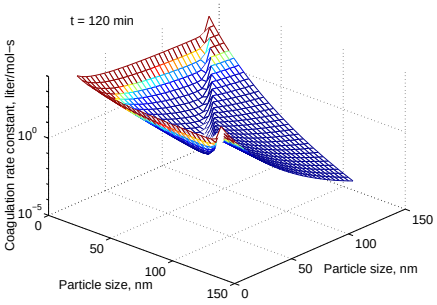

(c) $t = 120\ min$, $S_w = 1.2 \times 10^{-4}$ $moles/liter$

Figure 3.18: The size-dependent intrinsic coagulation rate β – Equation (3.46), reflecting the sensitivity of the repulsive potential to the free surfactant concentration, S_w. The rapid decrease in the coagulation rate constant at larger sizes can be exploited to reduce the computational load.

this time (Figure 3.2), but also due to the depletion of the monomer droplets and the associated release of *absorbed* surfactants (figure not shown). Subsequently, it remains almost constant up to approximately 37.5 min, as the reduced feed rate of the surfactant solution at this time is just sufficient to compensate for the increase in the total surface area of the particles due to growth (Figure 3.17 – bottom plot). After 37.5 min, S_w begins to increase again due to the increased feed rate, up to about 70 min. Thereafter, S_w drops until approximately 95 min (due to adsorption onto the growing particles). Beyond 95 min, S_w remains almost constant as there is no further increase in the particle surface area. The repulsive potential (Figure 3.16) shows a considerable sensitivity to the free surfactant concentration, S_w, as expected (through the dependence on Γ). The high value of S_w at 70 min results in a higher repulsive potential at this time, compared to that at the other times. Figure 3.18 shows the intrinsic coagulation rates (coagulation kernel) corresponding to these same time instances, which reflect the sensitivity shown by the repulsive potential to the free surfactant concentration. The intrinsic coagulation rate is lower at 70 min relative to that at 30 min. Also, it is higher at 120 min by about four-fold compared to that at 70 min (not perceptible in the plot), as an effect of the variation in S_w. These results elucidate the potential to manipulate the coagulation rate by employing the surfactant feed.

Each of the plots in Figure 3.18 illustrate a rapid decrease in the coagulation rate constant with increase in the particle size(s). This observation was exploited to further reduce the computational load. A cut-off size was fixed, above which the particles were assumed to be colloidally-stable, thereby eliminating the need to compute the coagulation terms for these larger size particles. This approach is consistent with earlier approaches. Richards *et al.* (1989) defined two particle populations, one accounting for the unstable smaller size particles, and the other for the stable larger size ones. A similar approach was adopted by Araujo *et al.* (2001) in

a full population balance framework (resulting in two population balance equations). The present approach eliminates the need for two partial differential equations. However, a sensitivity study was performed to identify the suitable cut-off size.

The simulation results are analyzed further to study the evolution of the distribution. This analysis is also useful in the next subsection, in comparing the simulation results with the experimental data. Figures 3.19(a) and 3.19(b) show the rate of micellar nucleation and the profile of total particles over the course of the batch, respectively. The homogenous nucleation is restricted to very early times (before 1 min), contributing to the early particles seen in Figure 3.19(b). On the contrary, micellar nucleation begins at about 1 min, and is prevalent through the entire course of the batch. The profile of the total particles records decreases in the particles count due to the coagulation events, which are seen to be the least evident at times of high free surfactant concentration (Figure 3.17). The high value of the intrinsic coagulation rate close to the end-point (Figure 3.18(c)), coupled with the higher particle concentration at these times, cause higher rates of coagulation towards the end of the batch thereby leading to a large drop in the number of particles. Figure 3.20 shows the global average number of radicals/particle, $n_{ave}(t)$, calculated from the distribution, $\bar{n}(r,t)$. It is seen that for most part of the batch, $n_{ave}(t)$ is above unity justifying the use of a general model for a VAc-BuA copolymer system. Figure 3.21 shows the profile of the instantaneous overall conversion, which reaches about 78% at the end of 150 min with a modest solids content of about 22%. Figure 3.22 shows the evolution of the PSD along the course of the batch. The end-point PSD shows a large mode centered at approximately 400 nm, a diffuse mode at around 250 nm, and another mode at approximately 100 nm (separate plot shown later).

In summary, the model captures all relevant aspects of the evolution of the

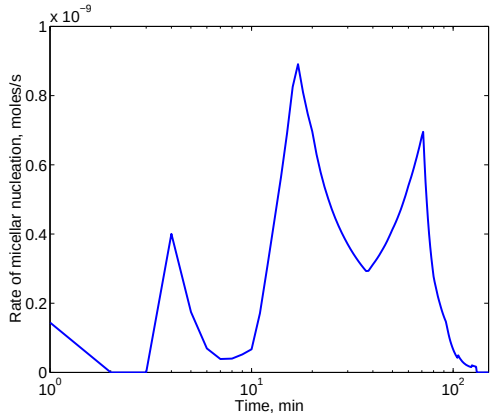

(a) micellar nucleation rate

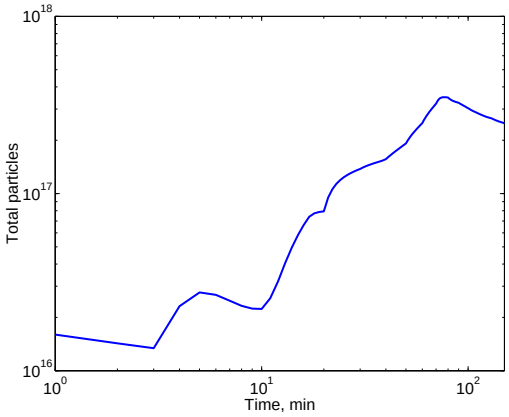

(b) profile of total particles

Figure 3.19: Profiles of the nucleation rate and total particles for the base case recipe.

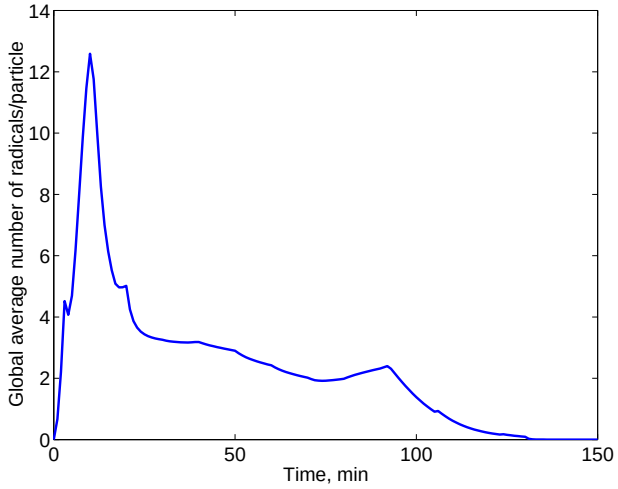

Figure 3.20: Global average number of radicals/particle, calculated from the complete distribution $\bar{n}(r,t)$, corresponding to the base case recipe.

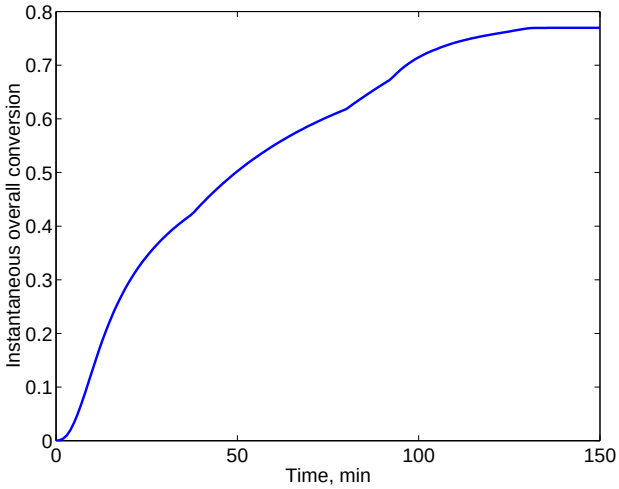

Figure 3.21: Instantaneous overall conversion of the monomers along the batch corresponding to the base case recipe.

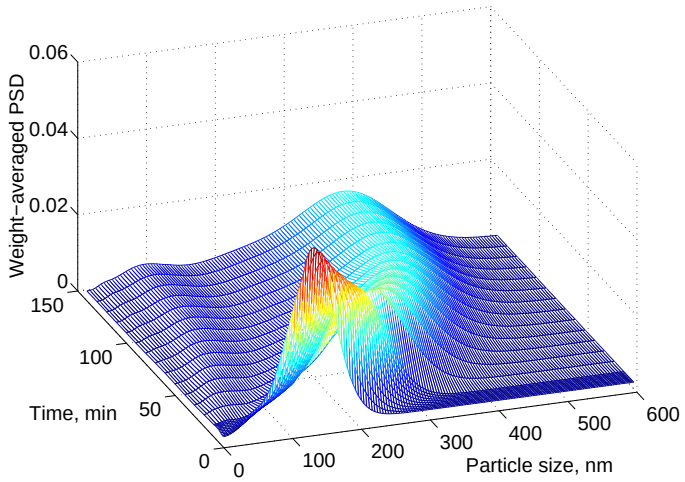

Figure 3.22: Evolution of the PSD along the course of the batch corresponding to the base case recipe.

PSD, including the complications in the nucleation events associated with the non-ionic surfactants. It can be employed to simulate all industrially-pertinent recipes, such as *ab initio* and seeded polymerizations.

3.8.2 Validation of the Simulation Results with Experimental Data

The comparison of the simulation results with the experimental data for various recipes is presented next. In the first comparison case, simulation results both with and without the coagulation events are presented to illustrate the improvement obtained in accounting for the coagulation phenomenon. Figure 3.23 compares the simulated end-point PSD and the profiles of the total particles and solids content (corresponding to the cases with and without coagulation), with the experimental data. The recipe for the experiment is the one shown in Figure 3.2 (base case), which was discussed in the previous subsection. The experimentally-observed distribution in Figure 3.23(a) (dashed line) shows diffuse and interconnected modes, one centered at approximately 320 nm, another at approximately 210 nm, and a third at approximately 70 nm. In the coagulation-free case (dash-dot line), the model simulates two diffuse and interconnected modes at the larger size end, similar to

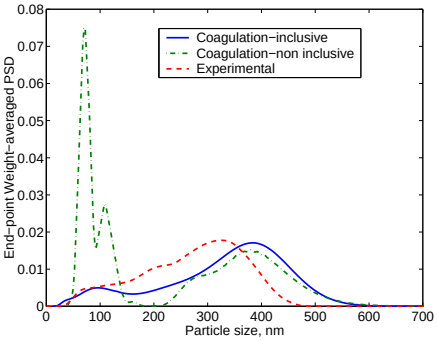

(a) comparison of the end-point PSD between the experimental and simulation results

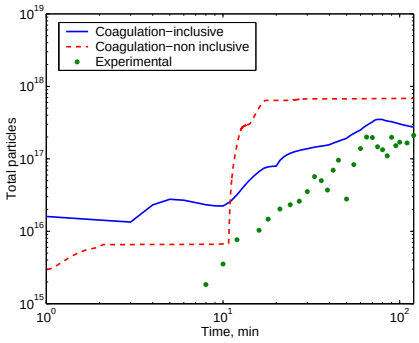

(b) comparison of the profiles of total particles

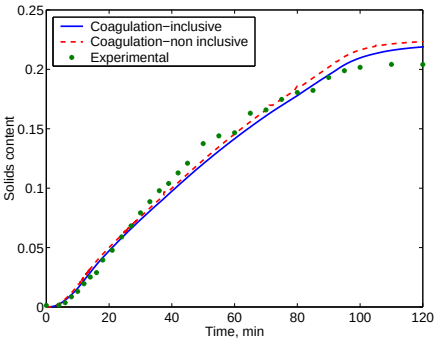

(c) comparison of the profiles of solids content

Figure 3.23: Comparison of the simulation results with the experimental data for the vinyl acetate-butyl acrylate co-polymerization recipe shown in Figure 3.2 (base case).

the experimental observation. However, it predicts a delayed but larger secondary micellar nucleation event (Figure 3.23(b) – dashed line), resulting in the separate and large peak centered at approximately 100 nm (Figure 3.23(a)). Parametric sensitivity studies presented in section 3.6 indicates that this discrepancy is not entirely due to the uncertainty in the values of the parameters. On the other hand, the coagulation-inclusive simulation result captures these interconnected nucleation events well, and also preserves the relative magnitudes of the various peaks, as seen in Figures 3.23(a) and 3.23(b). However, in the simulation results, the early modes are still larger than in the experimental data. Such discrepancies seen in the profiles and the distribution can be attributed to the parametric uncertainty. Thus, there are clear improvements obtained upon incorporating coagulation events into the model, the complete model showing a qualitative and a partly quantitative validity.

A detailed parametric sensitivity study was performed with the coagulation-inclusive model. Based on this study, some of the parameters were adjusted (c_1, c_2, Γ_∞, K_{ad}, cmc, k_{r1} and k_{t11}) to best match the simulated PSD with the experimentally-observed PSD (Table 3.6). The matching of the experimental and simulated profiles (total particles, solids content) was not considered in this parameter identification exercise. However, there are several sources of uncertainty in the experimental results, caused by discrepancies in the feed rates delivered by the pumps, delays in step changes in the feed rates, temperature fluctuations *etc.*, which need to be accounted for in a more rigorous parameter identification exercise. The parameter values determined here are employed for all subsequent simulations without further adjustment. Also, the complete coagulation-inclusive results alone are presented henceforth, to make the plots more legible.

Figure 3.24 shows the simulation results pertaining to the recipe shown in Figure 2.25, and Figure 3.25 compares the predictions of the end-point PSD and the profile of solids content with the corresponding experimental data. In this case,

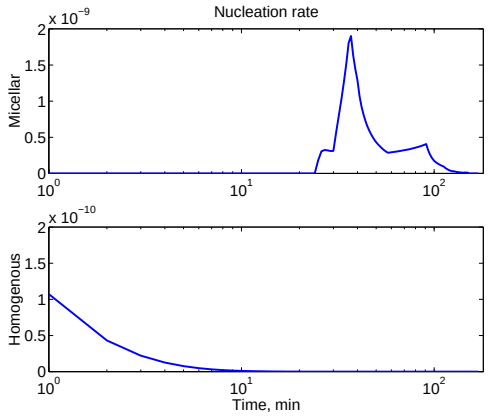

(a) micellar and homogenous nucleation rates in units of moles/s along the course of the batch

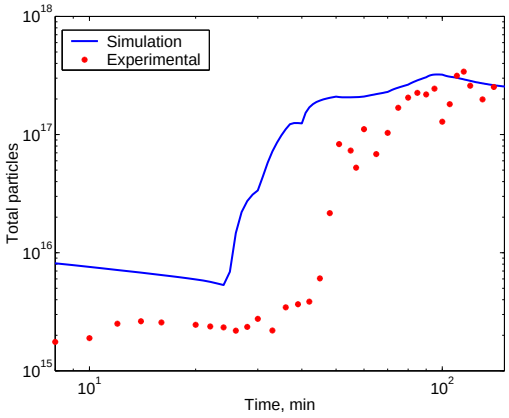

(b) comparison of the profile of total particles along the course of the batch

Figure 3.24: Nucleation rates and total particles profile for a recipe in which the feed of the monomers and the surfactant solution shown in Figure 3.2 is delayed by 20 min (the initial mixture contains VAc monomer, but no surfactant).

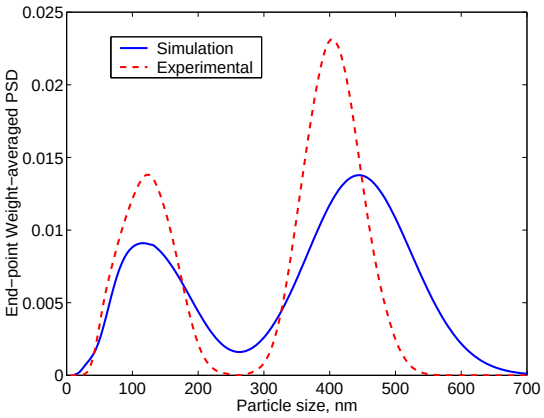

(a) comparison of the end-point PSD between the experimental and modeling results

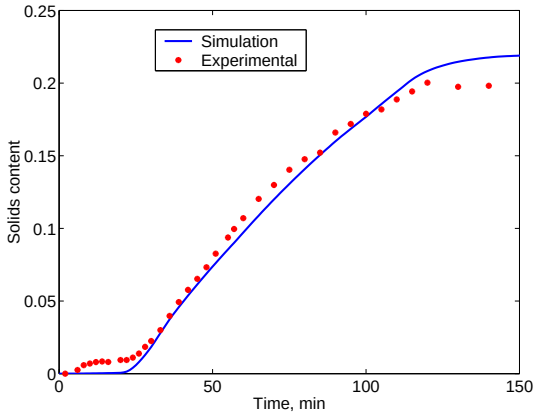

(b) comparison of the profile of solids content

Figure 3.25: Comparison of the simulation and experimental results for a recipe with delayed feed of surfactant and monomer (corresponding to the case in Figure 3.24).

while the initial mixture was the same as in the base case, the feed of VAc, BuA and surfactant solution were delayed by 20 min. During the first 20 minutes of the batch, no external surfactant or BuA monomer are present in the reactor. When the initiator components tBHP and SFS (which are not delayed) enter the reactor, the VAc monomer in the initial batch (52 g) is initiated, and particles are formed by the homogenous mechanism (Figure 3.24(a) – lower plot). Homogenous nucleation rate remains appreciable until about 10 min, because of the higher solubility of the VAc monomer in the aqueous phase. Thereafter, there is a decline in the number of particles (Figure 3.24(b)) due to coagulation. At about 20 min, the feed of surfactant and the two monomers is started. Micellar nucleation begins shortly after this, and is prevalent for most part of the batch (Figure 3.24(a)). The resultant PSD at the end of the batch is a prominent bimodal distribution, shown in Figure 3.25(a) (solid line). The comparison of the experimental data on the end-point distribution (Figure 3.25(a)) and the profiles of total particles (Figure 3.24(b)) and solids content (Figure 3.25(b)), with the corresponding simulation results, shows a reasonable match. (Note that the plot in Figure 3.25(a) is of the relative distribution, which causes the simulated peaks to be lower due to the presence of particles bridging the two modes).

Figures 3.26-3.29 compare the simulations and experiments for four different recipes, which were obtained by perturbations in the feed rates of BuA, VAc, surfactant solution and initiator solution, respectively, with respect to the recipe shown in Figure 3.2. In each case, the simulation results show very similar qualitative trends with the experimental results, in terms of the nucleation, growth and coagulation events. These are evident by a comparison of the number of modes and their relative magnitudes between the simulations and the experimental data. The simulation results corresponding to the base case (particularly Figure 3.19(a)) are used as a reference to interpret these results.

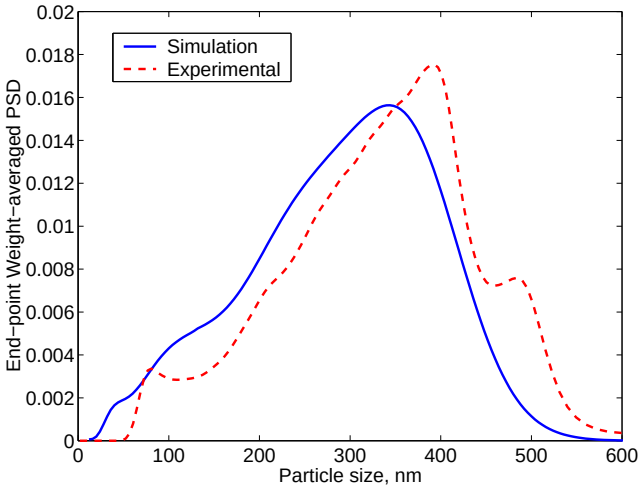

Figure 3.26: Comparison of the simulation and experimental end-point PSD for a recipe obtained by a 22% reduction in the BuA feed rate relative to Figure 3.2, up to 94 min.

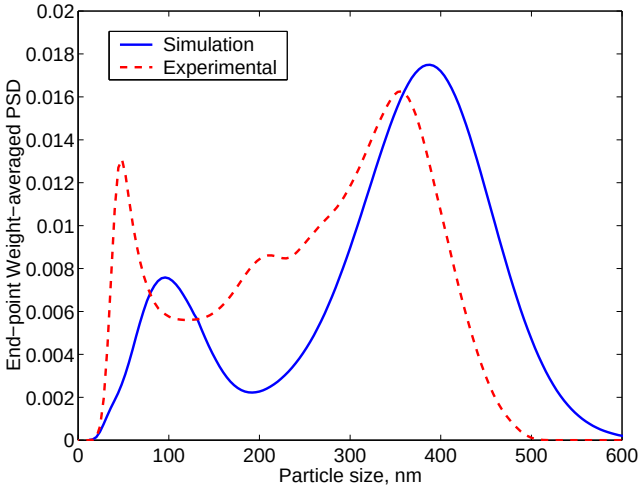

Figure 3.27: Comparison of the simulation and experimental end-point PSD for a recipe obtained by a 28% reduction in the VAc feed shown in Figure 3.2 up to 16.7 min.

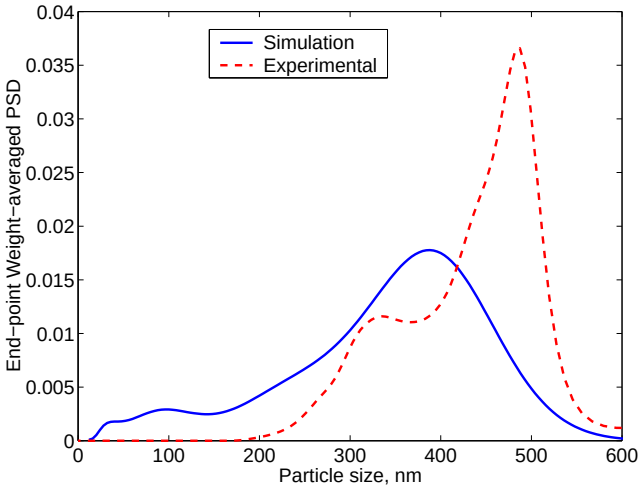

Figure 3.28: Comparison of the simulation and experimental end-point PSD for a recipe in which the step increase in the surfactant feed at 10 min, shown in Figure 3.2, is delayed to 15 min.

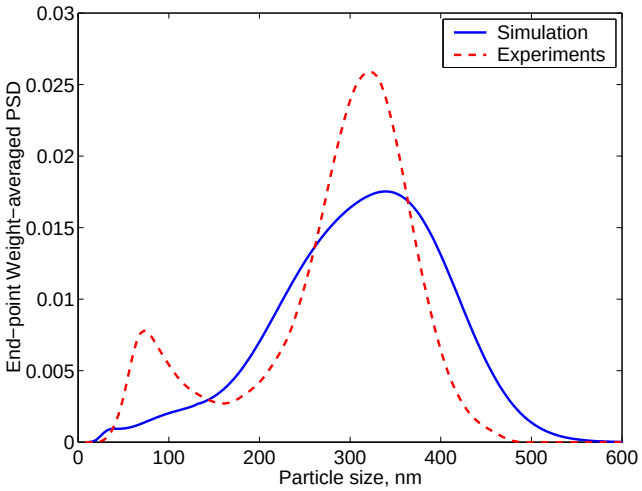

Figure 3.29: Comparison of the simulation and experimental end-point PSD for a recipe in which the concentration of initiator components is doubled compared to the recipe shown in Figure 3.2.

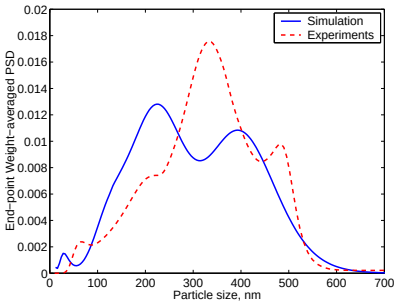

(a) comparison of the end-point particle density function between the experimental and modeling results

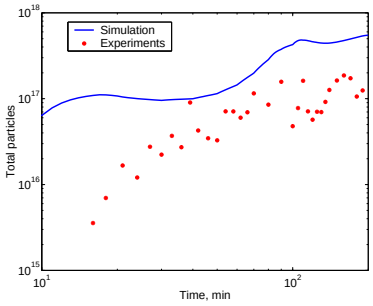

(b) comparison of the total particles

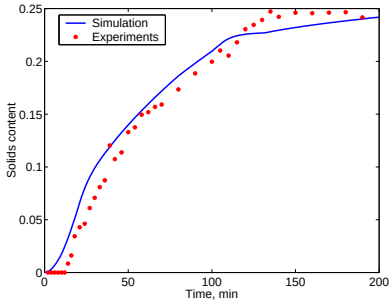

(c) comparison of the solids content

Figure 3.30: Comparison of the simulation and experimental results for a different family of recipe, aimed at achieving a higher solids content, and involving a longer batch time.

Figure 3.26 corresponds to a recipe in which the BuA feed rate was reduced by 22% relative to the original recipe (base case) up to 94 *min*, and there after the feed rate was raised to the level in Figure 3.2. The total quantity of BuA in the recipe was maintained the same as in the earlier recipe. The VAc-BuA co-polymerization system is characterized by a high reactivity ratio, with BuA being the more reactive monomer. Due to this reason, the reduced BuA feed results in much reduced growth rates (relative to the base case), and hence, a high free surfactant concentration and micellar nucleation rate between 3-6 *min* (see Figure 3.19(a)). This in turn cascades into a reduced micellar nucleation rate at the later times. After 94 *min*, there is a substantial increase in the reaction rates, that results in the de-swelling of the particles (due to the monomer consumption) and the release of the surfactants (*adsorbed* onto their surface) back into the aqueous phase. This in turn causes enhanced nucleation rates towards the end of the batch. Hence the broad PSD seen in Figure 3.26. Also, both the simulation and the experimental PSD show the same trend.

For the result presented in Figure 3.27, the VAc feed rate up to 16.7 *min* was reduced by 28% compared to Figure 3.2. There was a prolonged feed of VAc due to this, to maintain the same amount of VAc in the two recipes. In the perturbed case, there is a larger value of the average number of radicals/particle at early times, and hence, larger growth rates. This results in reduced nucleation rates between 3-6 *min*. The monomer droplets disappear from the system earlier in this case (before 12 *min*), resulting in the release of surfactants *absorbed* into them back into the aqueous phase. This causes a more prominent nucleation at these times. Both the simulation and the experimental results show the same trend, though the simulation predicts an even smaller nucleation at the intermediate times (3-6 *min*) – attributable to uncertainty in the surfactant partitioning parameters.

In the case of Figure 3.28, the step increase in the surfactant feed rate at

10 *min* in Figure 3.2 was delayed to 15 *min*. The monomer droplets disappear in both cases at about 12 *min*, releasing the *absorbed* surfactants into the aqueous phase, and thereby resulting in increased rates of micellar nucleation (again, see Figure 3.19(a)). However, in the current case, there is a relatively reduced micellar nucleation at this time, but a more substantial nucleation event at later times. Although the experimental result shows a larger growth rate, and/or an earlier completion of the nucleation events compared to the simulation results, the overall trend is very similar (with the simulated PSD being a stretched version of the experimental one).

Figure 3.29 presents results in which case the concentration of the initiator components were doubled relative to that employed in the base case recipe. In the current case, there is a larger homogenous nucleation initially, which results in lower values of $\bar{n}(r,t)$, and hence lower growth rates. This causes the total surface area to be lower, thereby raising the value of S_w and the nucleation rates in the 3-6 *min* time range. Soon after, the value of $\bar{n}(r,t)$ increases, causing the surface area A_p to increase above that in the base case (higher concentration of the initiator components), and in turn causing reduced rates of nucleation. This results in the PSD seen in the figure. The larger mode comprises the particles nucleated up to about 6 *min* (initial homogenous and the intermediate micellar nucleation events). The tail corresponds to the particles nucleated at later times of the batch. The experimental results show a more prominent secondary peak. This could be either due to an even earlier (and hence reduced) primary micellar nucleation event before 3 minutes in the experimental case, or due to the later nucleation events occurring at larger rates than predicted.

Figure 3.30 considers a different family of recipe, for a batch spanning 200 *min*. In this case, the solids content achieved is slightly higher than the other cases, under which condition one can expect more coagulation events. The experimental

results show three peaks, at approximately 70 nm, 320 nm and 500 nm, and a shoulder at about 200 nm. The simulated distribution also shows these modes, although the corresponding peak sizes are staggered. Also, there is an overall preservation of the relative magnitudes of the various peaks.

3.9 Summary

A population balance model is developed for the PSD in emulsion polymerization, accounting for the nucleation, growth and coagulation phenomena. In addition to consolidating the various theories on each of these phenomenon into a single study, the model presented here introduces several modifications to the population balance model for PSD in emulsion polymerization. A significant modification as regards the nucleation event is the incorporation of the partitioning of the surfactants into the bulk of the dispersed phases, which accounts for the alterations in the nucleation pattern under non-ionic surfactants. In modeling the growth phenomenon, a first principles-based formulation is proposed to model the average number of radicals/particle. The proposed formulation preserves the size-dependence of the growth kernel, captures the broadening of the distributions with growth (both effects seen experimentally), and also obviates the need for incorporating artificial dispersion terms in the population balance equation. The improvements obtained with this modification clearly indicate the disadvantages with lumped parameter modeling, and motivate the use of a distributed approach where possible. The calculation of the size-dependent intrinsic coagulation rate and the coagulation terms for emulsion recipes employing non-ionic surfactants is demonstrated. Steric stabilization under the influence of *adsorbed* surfactants in modeled as the primary stabilizing mechanism. However, empirical allowances are introduced into the calculations to account for other mechanisms that influence coagulation, including the shear imparted on the particles due to the mixing in the reactor. In formulating the population balance equation, the particle size is used as the internal coordinate. This is mainly due to

two reasons, namely that the measurement available is as a size distribution (and not volume distribution, for example); and that the range of particle size is narrower than the range of particle volume, which makes the choice of size beneficial with respect to numerical solution (number of finite elements, *etc.*). This choice of size as the internal coordinate introduces minor, though critical, changes to the coagulation kernel, which are clearly developed in this paper.

The model can be used to simulate all types of emulsion recipes that are of interest to practitioners. The simulation results were compared with experimental data. In general, the model demonstrates a good ability to predict the experimental observations. Also, there is a substantial improvement over the coagulation-free simulation results. The discrepancies between the complete coagulation-inclusive simulation results and the experimental observations can be attributed not only to parametric uncertainty, but also experimental uncertainty (disturbances, delays in pump startups, errors in the feed rates, *etc.*). The cascaded effects of the parametric uncertainties on the evolution of the distribution were also discussed. The parameters were adjusted manually to provide an overall fit of the PSD in one case, and the same set of parameters were used in the simulation of all the cases. It might be beneficial to perform a rigorous parameter identification, utilizing all the experimental cases, and simultaneously accounting for experimental uncertainties. For the purposes of on-line control of PSD, a combined parameter-state estimator can be employed, to account for the uncertainties in the model simultaneously, while inferring the relevant feedback informations necessary for control.

Table 3.1: Emulsion Polymerization Kinetic Scheme

Aqueous phase	
Initiator decomposition	$I_w + Y_1^r \overset{k_{d_1}}{\rightarrow} R_w + Y_1^o + side\ products$
	$Y_1^o + r_I Y_2 \overset{k_{d_2}}{\rightarrow} Y_1^r + side\ products$
Initiation	$R_w + M_{iw} \overset{k_{r_i}}{\rightarrow} P_{iw}^1, \quad i = 1,2$
Propagation	$P_{iw}^l + M_{jw} \overset{k_{pij}^w}{\rightarrow} P_{jw}^{l+1}, \quad l = 0,1...j_{cr}-1, \quad i,j = 1,2$
Chain transfer to monomer	$P_{iw}^l + M_{jw} \overset{k_{trij}^w}{\rightarrow} P_{jw}^0 + Dead\ chains$
Termination	$P_{iw}^l + P_{jw}^m \overset{k_{tij}^w}{\rightarrow} Dead\ polymer$
Nucleation	$P_{iw}^l + Micelle \overset{e_{i,micelle}^l}{\rightarrow} L_i, \quad l = 0,1...j_{cr}-1, \quad i = 1,2$
	$P_{iw}^{j_{cr}-1} + M_{jw} \overset{k_{pij}^w}{\rightarrow} L_i, \quad i,j = 1,2$
Particle phase	
Entry	$P_{iw}^l \overset{e_i^l(r)}{\rightarrow} L_i, \quad i = 1,2, \quad l = 0,1,...j_{cr}-1$
Propagation	$L_i + M_{jp} \overset{k_{pij}}{\rightarrow} L_j$
	$L_i^0 + M_{jp} \overset{k_{pij}}{\rightarrow} L_j, \quad i,j = 1,2$
Termination	$L_i + L_j \overset{k_{tij}}{\rightarrow} Dead\ chains, \quad i,j = 1,2$
Chain transfer to monomer	$L_i + M_j \overset{k_{tr_ij}}{\rightarrow} Dead\ chains + L_j^0, \quad i,j = 1,2$
Desorption	$L_i^0 \overset{k_{dM_i}(r)}{\rightarrow} P_{iw}^0, \quad i = 1,2$
	L_i: Live polymer chain of type i inside particles
	L_i^0: Live monomeric radical of type i inside particles
	P_{iw}^l: Aqueous phase oligomers of type i and chain length l
	P_{iw}^0: Aqueous phase monomeric radicals of type i

Table 3.2: Kinetic and Physical Constants

$k_{p11} = k^w_{p11}$	3.29×10^3 liter/mol-s
$k_{p12} = k^w_{p12}$	8.9×10^4 liter/mol-s
$k_{p21} = k^w_{p21}$	3.9×10^1 liter/mol-s
$k_{p22} = k^w_{p22}$	2.47×10^2 liter/mol-s
$r_1 = \frac{k_{p11}}{k_{p12}}$	0.037
$r_2 = \frac{k_{p22}}{k_{p21}}$	6.33
$k_{tr11} = k^w_{tr11}$	9.3×10^{-3} liter/mol-s
$k_{t11} = k^w_{t11}$	3.49×10^7 liter/mol-s
$k_{t22} = k^w_{t22}$	1.6×10^3 liter/mol-s
$k_{t12} = k_{t21}$	$\sqrt{k_{t11} k_{t22}}$
ρ_{M_1}	934 g/liter
ρ_{M_2}	894 g/liter
K_{p1}	32
K_{p2}	460
K_{d1}	46
K_{d2}	2140
$[M_1]^{sat}_p$	7.5 mol/liter
$[M_2]^{sat}_p$	1.5 mol/liter
MW_1	86.09
MW_2	128.17
N_A	6.023×10^{23}
MW_{surf}	616

Table 3.3: Nominal values for uncertain parameters

Γ_∞	$4.5 \times 10^{-6}\ mol/m^2$
K_{ad}	$1 \times 10^{6}\ liter/mol$
cmc	$5 \times 10^{-5}\ mol/liter$
K_s	0
K_s^d	15.5
α_{ms}	$3.69 \times 10^{-19}\ m^2/molecule$
$r_{nuc} = r_{micelle}$	5 nm
ρ_P	1120 g/liter
j_{cr}	5
D_{w1} $(n = 2)$	$30\ cm/s$
D_{w2} $(n = 2)$	$55\ cm/s$
$\bar{D}_{w1}$	$1.0 \times 10^{-6}\ cm^2/s$
$\bar{D}_{w2}$	$1.5 \times 10^{-5}\ dm^2/s$
$k_{tr21} = k_{tr12} = k_{tr22}$	9.3×10^{-3} liter/mol-s
k_{r1}	0.2 liter/mol-s
k_{r2}	0.2 liter/mol-s
k_{d1}	400 liter/mol-s
k_{d2}	400 liter/mol-s
r_I	1

Table 3.4: Summary of Parametric Sensitivity Studies

	Root cause of response to perturbation	End effects
cmc	Affects timing and magnitude of the primary micellar nucleation	Lower values of the cmc lead to earlier and stronger primary micellar nucleation. This in turn results in a reduced secondary micellar nucleation
K_{ad}	Affects magnitude of the primary micellar nucleation	Larger quantity of surfactant adsorbed onto the particles at larger K_{ad}, resulting in reduced primary micellar nucleation, which cascades through the rest of the process. The nonlinearity in the process is evident.
Γ_∞	Affects timing and magnitude of the primary micellar nucleation	Monotonic effect, unlike in the case of K_{ad}. Larger values of Γ_∞ lead to more delayed and reduced primary micellar nucleation. The effect cascades to secondary micellar nucleation events (Figure 3.13).
D_{w1}	Affects the rate of homogenous nucleation	An increase in D_{w1} decreases the number of particles formed by homogenous nucleation. This causes the primary micellar nucleation to occur sooner and be more prominent (Figure 6.37).
D_{w2}	Affects the rate of homogenous nucleation	Similar effect to the case of D_{w1}. No direct effect on growth, but only the cascaded effect caused by the effect on the nucleation phenomena.
k_{tr22}	Affects the rate of desorption of monomeric radicals	Non-intuitive results seen in the effect of k_{tr22}. As k_{tr22} increases, excessive chain transfer inside the particles and subsequent desorption of the monomeric radicals results in reduced $\bar{n}(r,t)$ and growth rates. But micellar nucleation is still reduced at high k_{tr22}, contrary to expectation.
k_{tr21}	Affects the rate of desorption of monomeric radicals	Similar effect to the case of k_{tr22}. An increase in the solids content and reaction rates with increase in k_{tr21}.

Table 3.5: Summary of Parametric Sensitivity Studies

	Root cause of response to perturbation	End effects
j_{cr}	Affects the rate of homogenous nucleation	Larger values of j_{cr} lead to more delayed and reduced initial homogenous nucleation. This results in a larger primary micellar nucleation.
k_{r1}	Affects the rates of generation of oligomers and homogenous nucleation	Lower values of k_{r1} lead to lower rates of homogenous nucleation, which cause enhanced primary micellar nucleation and cascade to the secondary micellar nucleation. Also, k_{r1} has a direct effect on growth. Lower values of k_{r1} lead to lower values of $\bar{n}(r,t)$ and reduced growth rates.
k_{d1}	Affects the rates of generation of oligomers and homogenous nucleation	Nonlinear effect – as k_{d1} decreases, the rate of homogenous nucleation decreases at first, and then reverses direction.
r_I	Affects concentration of aqueous phase oligomer	As r_I decreases, the concentration of the aqueous phase oligomers increases. This leads to increased initial homogenous nucleation, but also higher $\bar{n}(r,t)$, resulting in higher growth rates and a reduced primary micellar nucleation. Nonlinearity evident too.
$r_{micelle}$ $/r_{nuc}$	Affects homogenous nucleation through a different route	At larger values of r_{nuc}, homogenous nucleation rate is reduced (after substantial homogenous nucleation has occurred) due to the larger entry rates of radicals before reaching the critical chain length. This effect cascades through the micellar nucleation and the rest of the process.
ρ_p	Affects the particle growth rate (Equation (3.21))	Obviously, larger values of ρ_p lead to lower growth rates, resulting in a lower surface area of particles. This increases the free surfactant concentration, and advances and strengthens the primary micellar nucleation.

Table 3.6: Constants employed in the coagulation-inclusive model

A	5.5×10^{-21} J
$k_{t11} = k_{t11}^{w}$	1.05×10^{7} liter/mol-s
Γ_{∞}	7.5×10^{-6} mol/m^2
K_{ad}	4×10^{4} $liter/mol$
cmc	2×10^{-5} $mol/liter$
k_{r1}	0.1 liter/mol-s
sc_{ref}	0.6
c_1	1×10^{-5}
c_2	1×10^{-10}
l	1 nm
M	616 g/mol
M_0	68.4 g/mol
$r_{cut-off}$	66 nm

Table 3.7: Nomenclature

r	particle radius
$F(r,t)$	particle density function
$\bar{n}(r,t)$	average number of active radicals in particles of size r at time t
$n_{ave}(t)$	global average number of radicals per particle
K_{ad} and Γ_∞	Langmuir adsorption constants
A_p^s	total swollen surface area of particles
S_w	free surfactant concentration
cmc	critical micelle concentration
$r_{micelle}, r_{nuc}$	radius of a micelle/nucleation size
j_{cr}	critical chain length
N_A	Avogadro Number
$F_R(D)$	repulsive force between particles separated by distance D
$\psi_R^f(D)$	repulsive potential between flat objects separated by distance D
$\psi_R(D)$	repulsive potential between spherical particles separated by distance D
R_g	radius of gyration
R_F	Flory radius
α	interaction parameter between polymer (surfactant) and solvent (water)
l	effective length of a segment of surfactant chain
L	extension length of adsorbed surfactant into the aqueous phase
A	Hamakar constant
$\beta(r,r')$	intrinsic coagulation rate between particles of size r and r'
$W(r,r')$	Fuch's stability ratio for particles of size r and r'
D_0	effective diffusion co-efficient
μ	viscosity of latex
μ_0	viscosity of water
sc	solids content of latex
sc_{ref}	reference solids content
k	Boltzmann constant
T	Reactor temperature
$r_{cut-off}$	size above which the particles are colloidally-stable
k_{ri}	Rate constant for reaction between initiator and monomer i
k_{tij}	Rate constant for termination of polymer of type i with another polymer of type j
r_s	Swollen particle radius
r_I	Initiator stoichiometric ratio
I_w	Oxidant in aqueous phase
Y_1^r	Reduced form of Iron (catalyst)
Y_1^o	Oxidized form of Iron (catalyst)
Y_2	Reducer
R_w	Initiator radicals
M_i	Moles of monomer i in the reactor
MW_j	Molecular weight of monomer j
j_{cr}	critical chain length

Table 3.8: Nomenclature (Cont'd)

$[M_i]_w$	Concentration of monomer i in the aqueous phase
$[M_i]_p$	Concentration of monomer i in the particles
$[M_i]_w^{sat}$	Saturation concentration of monomer i in the aqueous phase
$[M_i]_p^{sat}$	Saturation concentration of monomer i in the particles
P_{iw}^l	Oligomer of type i and chain length l in the aqueous phase
P_{iw}^0	Monomeric radicals in the aqueous phase
k_{d1}	Rate constant for oxidation step of initiation
k_{d2}	Rate constant for reduction step of initiation
k_{pij}	Rate constant for propagation of polymer of type i with monomer j
k_{trij}	Rate constant for chain-transfer to monomer j from polymer of type i
k_{tij}	Rate constant for termination of polymer of type i with polymer of type j
k_{pij}^w	Rate constant for propagation in the aqueous phase
k_{trij}^w	Rate constant for chain-transfer to monomer in the aqueous phase
k_{tij}^w	Rate constant for termination in the aqueous phase
L_i	Live polymer chains of type i, $(i = 1, 2)$ inside particles
V_{aq}	Volume of the aqueous phase
v_i	Molar feed rate of component i
$F(r,t)$	particle density function
$\bar{n}(r,t)$	Average number of active radicals in particle of size r at time t
$n_{ave}(t)$	Global average number of radicals per particle
p_i	probability that a radical is of type i in the particles
p_{wi}	probability that a radical is of type i in the aqueous phase
ρ_p	density of polymer
ρ_{M_i}	density of monomer i
K_{pi}	Partition coefficient for monomer i between particles and water
K_{di}	Partition coefficient for monomer i between droplets and water
S_T	Total moles of surfactant in reactor
K_s	Partition coefficient for surfactant between particles and water
K_s^d	Partition coefficient for surfactant between droplets and water
$\alpha_{m,s}$	Area occupied by one surfactant molecule
$e_i^l(r)$	entry rate constant of aqueous phase oligomers into particles
$e_{i,micelle}^l$	entry rate constant into micelles for oligomers of chain length l and type i
$D_{w,i}$	Diffusion coefficient for monomer i in the aqueous phase
$D_{w,i}$	Parameter in entry rate coefficient
N_A	Avogadro Number
$k_{dMj}(r)$	Rate constant for desorption of monomeric radical from particles
$F_i^j(t)$	Approximate solution for $F(r,t)$ at the i^{th} collocation point of the j^{th} finite element at time t
$V_{i,j}$	Volume of monomer i in phase j (j=d-droplets;p-particles;w-aqueous)
V_w^T	Total volume of the aqueous phase
V_p^s	Swollen particle volume
V_p	Unswollen particle volume
V^d	Volume of droplets

Chapter 4

COMPUTATIONALLY-EFFICIENT SOLUTION OF POPULATION BALANCE MODELS

4.1 Solution Techniques for Population Balance Models

Various solution techniques have been considered to solve population balance equations. See (Ramkrishna, 1985) for a detailed review on this topic. The most popular techniques are based on approximating the infinite-dimensional partial differential equation system as a finite-dimensional ordinary differential equation system. The solution techniques can be classified broadly into the method of moments and discretization methods. The simplest among these methods is the method of moments, wherein the moments of the distribution are computed. The k^{th} moment is defined as $\mu_k = \int_{\eta_{min}}^{\eta_{max}} \eta^k \zeta(\eta, t) d\eta$. This definition can be applied to the overall population balance equation (Equation 1.1) to derive one ordinary differential equation representing each moment (say, μ_0, μ_1, μ_2, μ_3, *etc.*) (Chiu and Christofides, 1999). While the solution of the resultant system of ODEs is simple, the application of the technique requires the number of moments considered to be limited. Thus, it is restricted to distributions that are relatively smooth and ideally unimodal. In applying the method of moments, usually the equation representing a given moment depends upon higher moments. In specifying a cut-off moment, one needs to define a closure condition to form a closed set of equations. The definition of a proper closure condition is important in applying the method of moments.

The most popular techniques for the solution of PDEs in general, and population balance models in particular, are the discretization techniques. In this case, the PBE is sought to be identically satisfied at a certain number of points only (at

certain values of η within the domain spanning η_{min} and η_{max}). The simplest among the discretization techniques is the Finite Difference (FD) methods. In this technique, the derivatives (usually with respect to the internal coordinate η alone, but sometimes with respect to both t and η), are approximated by finite differences of a certain order (typically 1 – Taylor's expansion, or 2). This approximation results in either a system of ODEs or algebraic equations. While this method can be employed to solve for more complex and multi-modal distributions, it results in spurious oscillations and in numerical dispersions in the distributions, due to the truncation error introduced in approximating the derivatives. In employing FD techniques, a large enough size domain is to be covered, to prevent errors from backtracking (Crowley et al., 1999). Some studies have employed moments at larger size to solve this closure problem (Melis et al., 2000). While most researchers employ a standard ODE solver beyond this step (for the discretization of the time domain), some studies have considered customized strategies. In a recent study on crystallization systems, Ma *et al.* (2002) have proposed modifications to the FD approximations of the derivatives to avoid spurious oscillations and numerical dispersion.

The second type of discretization methods is the method of weighted residuals (MWR). In this case, the solution within the domain of interest $[\eta_{min}, \eta_{max}]$, or in sub-domains within the overall domain, is expressed in terms of basis functions and weighting functions. The weighted sum of the residuals of the PBE, in terms of these chosen solution forms (at certain chosen points), are driven to zero. This technique is further classified into two types based on the choice of the weighting functions, namely, collocation techniques and Galerkin's method. Collocation techniques employ orthogonal polynomials as local basis functions and the Dirac delta function as the weighting function. Thus, the residual of the population balance equation at the chosen points of discretization are driven to zero, *i.e.,* the population balance equation is identically satisfied at the chosen points. To avoid the use of a single basis

function to cover the whole domain $[\eta_{min}, \eta_{max}]$ (and hence the need for a high degree polynomial as the basis function), the whole domain is divided into sub-domains called Finite Elements (FEs), and a local basis function is chosen to represent the solution within each FE. In approximating the derivatives with respect to η, unlike in the FD techniques wherein only one or both neighboring points (to the point at which the derivative is calculated) are utilized, all discretization points within each FE are utilized. Thus the numerical dispersion and oscillation problems common in the FD techniques are subdued in collocation techniques. The most common basis functions are orthogonal polynomials, which result in the Orthogonal Collocation on Finite Elements (OCFE) method (for example, (Saldivar, 1996; Crowley et al., 2000)). Other class of basis functions, such as orthonormal wavelets (Liu and Cameron, 2001), have also been employed in the collocation technique. Unlike the collocation methods, the Galerkin's method sets the weighting function identical to the basis function (Godin et al., 1999; Chiu and Christofides, 1999; Mahoney, 2001). Mahoney & Ramkrishna (2002) apply the Galerkin's method for the solution of distributions characterized by discontinuities, exploiting physical understanding of the source of the discontinuity. Moving finite element techniques (Rawlings and Ray, 1988a) have been proposed to reduce the number of FEs, remove the source of potential errors due to closure problems, and also to capture sharp moving fronts where they exist. In this case, the upper limit of the domain η_{max} moves with time, linked to the growth phenomenon in the population balance model.

A special sub-class of population balance problems to which the discretization techniques have been employed are pure aggregation/breakage problems. Kumar and Ramkrishna (1996b) provide an excellent review of the literature on this class. These systems are characterized by integro-differential equations (Hounslow et al., 1988; Kumar and Ramkrishna, 1996b). In calculating the integrals, the particles are assumed to be concentrated at a single point (called the pivotal point) within each

element. During a coagulation or breakage event, the particles that result may not fall at any pivot size, and will need to be assigned to two or more adjacent elements. The preservation of the mass and the number of particles during this assignment is critical. Kumar and Ramkrishna propose a new method which conserves both number and mass, or any two property of interest. In a sequel publication (Kumar and Ramkrishna, 1996a), they propose a method of adapting the pivot size within each finite element.

One other solution class, which falls under probabilistic methods, is the Monte Carlo method (see, for example (Hollander et al., 2001)). This technique uses the Markov conditional probability of a particular state proceeding to any other state in determining the solution. Besides predicting the ensemble average properties, it also predicts the fluctuations, as pointed out by Ramkrishna (1985).

4.1.1 Model Reduction Strategies and Approximate Solutions

Despite increasingly faster computers, the solution of the population balance-based models for on-line applications such as process control is still problematic. This is particularly challenging for certain stiff systems, and for systems involving complex kernels of nucleation, growth, coagulation and breakage. These aspects motivate a model reduction strategy to enable efficient computation. The method of moments in itself, with appropriate closure conditions, is an order reduction technique. Another well-known approach is the decomposition of the fast and slow kinetics. Many engineering systems are characterized by widely varying eigenvalues, and thereby, some of the system states reach their equilibrium or steady state values faster than the others (stiff systems). This difference in time scales of stiff systems lead to special consideration in their numerical solution. One traditional way to tackle these systems is to use the pseudo-steady state assumption for the fast states (Maas and Pope, 1992). Several formal model reduction strategies have been developed, which essentially are based on this concept of fast versus slow modes and

the pseudo-steady state assumption. One such strategy to model reduction is to use the inertial manifold. This enables the expression of the slow modes in terms of the fast modes, and hence results in an order reduction. The calculation of the inertial manifolds constitutes solving partial differential equations themselves, and hence, methods are proposed to calculate Approximate Inertial Manifolds (AIM). Maas and Pope (1992) and Rhodes and Morari (1997) develop a method for calculating the inertial manifold for combustion systems. Chiu and Christofides (1999) and Adrover *et al.* (2002) employ the AIM for order reduction of the infinite-dimensional PDE systems.

In certain systems, the application of these general model reduction techniques is of a limited value, for instance due to the size and complexity of the problem, necessitating system-specific computational algorithms for efficient solutions. In the combustion literature, a computation technique based on decomposing the fast and the slow kinetics is employed typically, along the lines of Maas and Pope (1992). In this case, the fast kinetics are integrated first, and the solution of this integration is provided as the initial condition to re-integrate the slow kinetics over the same time interval. The second integration is cast an an inertial manifold, which is tabulated off-line. As a further extension, to balance the memory requirements and the efficiency of look-up on the one hand with the on-line computational load on the other, an adaptive tabulation technique is presented by Pope (1997), in which the table is built as the simulation progresses. Thus, only the accessed region for the particular simulation is actually tabulated, instead of the whole reachable region. Besides reducing the memory requirements, it also reduces the retrieval time for the data from the table. While most of the integration involved in the second step is performed (and stored) at the start of the simulation, the table evolves, and the retrieval operation dominates over the integration and storage operations.

In the present study, a simple and straightforward algorithm is presented

for the efficient solution of a population balance model, describing the evolution of the particle size distribution (PSD) in emulsion co-polymerization. The method is essentially based on the understanding that the PSD is determined by the interplay of nucleation, growth and coagulation. Although the method is based on a finite element discretization of the domain of the PSD, the method is not based on a discretization of the PBE itself. Instead, the accounting of the particles in the various FEs is done by resorting to the underlying phenomena. The nucleation, growth and coagulation processes that occur in each of the FE are considered individually to update the particle count. To provide a different mathematical perspective, the algorithm takes a step back in the derivation of the PBE (Equation (1.1)) to formulate the particle balance. The nucleation, growth and coagulation processes are determined by the underlying thermodymanic and kinetic events, governed by relatively simpler equations with relaxed stiffness characteristics. Thereby, the associated stiffness in the full solution is removed by the effective segregation of the nucleation, growth and coagulation processes, and also no approximations are necessary for the derivatives (and hence no truncation-related errors). Although the code is presented specifically for PSD modeling in emulsion polymerization, the approach is sufficiently general to allow treatment of a broad class of PBEs (since it involves only the calculation of the rates of nucleation, growth, coagulation/aggregation and breakage, as relevant). The technique developed is efficacious for on-line feedback applications, while not losing any process information. The proposed algorithm has the same two-tier strategy as the algorithm of Pope (1997) (and most other model reduction strategies), the model reduction being achieved based purely on process considerations however.

4.2 Algorithm Development

The model for PSD in emulsion polymerization involves two population balance equations (chapter 3), one for the particle density, and another for the average

number of radicals/particle – the latter in discretized form. In addition, it involves the material balance equations for the monomers, surfactants, initiators and aqueous phase oligomers, and the partition calculations for the monomers and surfactants. In the solution of the above model, a discretization technique based on Orthogonal Collocation on Finite Elements (OCFE) was employed (as described in Chapter 3). The nucleation processes have typical time constants of the order of 0.02 s (lowest), while the growth and the coagulation processes have time constants of the order of $50 - 100$ s. However, the nucleation events occur only for a portion of the overall batch, whenever the concentration of the surfactants in the aqueous phase exceeds the critical micelle concentration values of the surfactants. While this enables larger step sizes in non-nucleating regimes, it makes the system very stiff, with condition numbers of the order of 10^4. Thereby, the solution of these equations necessitate employing stiff integrators, with adaptive step sizes, which need to be checked and adapted at each step in the integration. The net effect is very large computation times, typically about 38 *minutes* on a SunBlade 1000 processor (dual processor of 800 MHz each, and 1 GB memory), for the simulation of a batch spanning 150 *minutes* – for coagulation-free conditions (See Table 4.1, last row). While this renders the model of reduced utility for on-line purposes, the coagulation-inclusive complete model (which is very computation-intensive) is of a reduced utility even for off-line purposes. This clearly motivates the development of a more efficient algorithm, to enable on-line model-based control of PSD.

As emphasized previously, the evolution of the particle size distribution in emulsion polymerization is determined by three major phenomena – nucleation of new particles, the growth of the particles by polymerization, and the coagulation of the particles with each other. Control of these individual mechanisms leads to a better control of the full PSD than that obtained by directly dealing with the PSD,

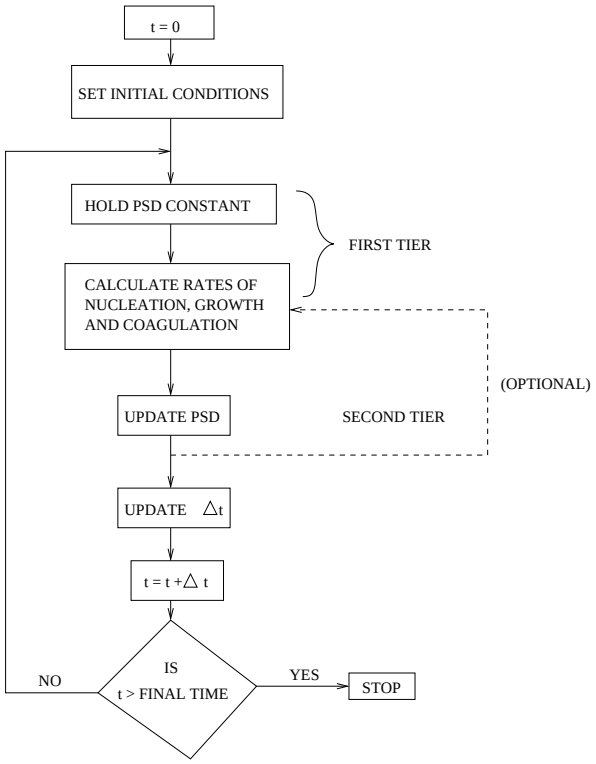

Figure 4.1: The schematic of the proposed hierarchical two-tier algorithm. The first tier involves the calculation of the rates of the individual sub-processes (nucleation, growth, coagulation, breakage) holding the PSD constant. The PSD is then updated in the second tier. Iteration over these two tiers is optional.

as will be demonstrated in Chapter 6. In this chapter, it is shown that this decomposition of the full process, implemented in a two-tier hierarchical solution strategy, results in very efficient numerical solutions. Although the strategy is presented in a specific framework in this section, a later section describes extensions of the approach to broad classes of population balance systems. Figure 4.1 shows a schematic representation of the proposed algorithm. The first tier involves the calculation of the rates of nucleation, growth and coagulation by solving a system of equations comprising ODEs and algebraic equations. The PSD is then updated in the next tier. The calculation then proceeds to the next time step. The new algorithm discretizes the domain of the PSDs into Finite Elements (FE) or 'bins'. Sufficient number of FEs are provided to cover the entire span of the PSD, to prevent backward propagation of errors. Within each FE, a representative size (mid-point) is chosen (see Figure 4.2(a)), based on which the size-dependent properties are calculated, and are assumed to hold within the whole element. Also, the particles are assumed to be uniformly distributed within each FE (constant particle density). This is different from the pivotal point assumption used in solving growth-free PBE models – wherein the particles are assumed to be concentrated at a single point within each element – and is more analogous to the second approach to mean value theorem indicated in Kumar and Ramkrishna (1996b) (M-II approach in their nomenclature). Further, the FE width chosen in this work is considerably lower than normal, to capture the distribution with greater fidelity.

The individual rates of nucleation, growth and coagulation are dependent on the concentration of the monomers, surfactants, the aqueous phase oligomers, the particle phase radicals and the particles themselves. The concentrations of the monomers, surfactants, the aqueous phase oligomers and the particle phase radicals are in turn calculated from material balances and partitioning calculations. Thus, the first or the inner tier involves the calculation of the rates of nucleation,

growth and coagulation while holding the PSD fixed. This involves the solution of ODEs and algebraic equations. In the present study, an iterative solution strategy coupled with Newton-Raphson methods is employed for the algebraic equations, and a predictor-corrector technique for solving the differential equations. A time step Δt is defined. This is divided into four sub-intervals, each of width $\frac{\Delta t}{4}$ (See Figure 4.2(b)). The solution is performed over each of these sub-intervals. Based on these solutions, the rates of nucleation, growth and coagulation are computed at each of these sub-intervals (using the equations presented in Chapter 3). At the end of this time interval, Δt, the PSD information is updated as follows: the total moles of particles within a FE j, F_j, is defined as $F_j = \int_{rb_{j-1}}^{rb_j} F(r,t)dr$, for $j = 2, 3...N$, and $F_1 = \int_{r_{nuc}}^{rb_1} F(r,t)dr$ (See Figure 4.2(a)). Applying this definition to the PBE (Equation (3.15)), one gets:

$$\int_{rb_{j-1}}^{rb_j} \frac{\partial}{\partial t}F(r,t)dr + \int_{rb_{j-1}}^{rb_j} \frac{\partial}{\partial r}(F(r,t)\frac{dr}{dt})dr = \int_{rb_{j-1}}^{rb_j} \delta(r - r_{nuc})\Re_{nuc}(t)dr + \int_{rb_{j-1}}^{rb_j} \Re_{coag}(r,t)dr \tag{4.1}$$

Changing the order of differentiation and integration, and employing Leibnitz rule results in:

$$\frac{d}{dt}F_j + (F_j\frac{dr}{dt})|_{rb_j} - (F_{j-1}\frac{dr}{dt})|_{rb_{j-1}} = \delta_{j=1}\Re_{nuc}(t) + \int_{r_{j-1}}^{r_j} \Re_{coag}(r,t)dr \tag{4.2}$$

The case wherein the coagulation events are absent (or negligible) is presented first, and the results are compared with the results obtained with the OCFE-based DDASSL solution. In the following sub-section, the complete coagulation-inclusive case is presented.

4.2.1 Coagulation-free emulsion polymerization

In the present study, the nucleation event is restricted to the first element (extension of the algorithm for the case in which nucleation is prevalent over a longer range of particle size is straightforward). Thus for elements 2, 3, ... N, the RHS of

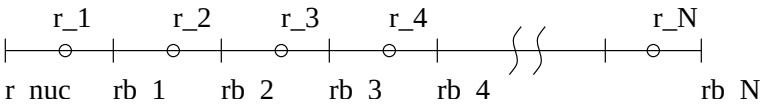

(a) finite element discretization of the domain of particle size; r_{nuc} is the size of the nucleus, rb_i is the upper boundary of finite element i, and r_i is the representative size for finite element i

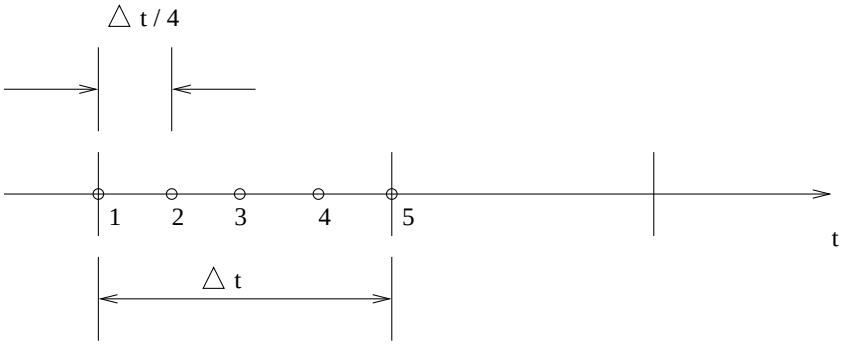

(b) the discretization along the time axis. Points 1-5 correspond to the sub-steps of integration (inner tier) of width $\Delta t/4$, within the overall main time step Δt (outer tier)

Figure 4.2: Discretization along the size and time domains.

the PBE (Equation (4.2)) becomes zero for the coagulation-free case, and the PBE reduces to:

$$\frac{d}{dt}F_i + (F_i\frac{dr}{dt})|_{rb_i} - (F_{i-1}\frac{dr}{dt})|_{rb_{i-1}} = 0 \tag{4.3}$$

The expression for the growth rate (Equation (3.21)) has an explicit dependence on the dependent variable, r. Upon rearrangement, it becomes:

$$\frac{dr^3}{dt} = \frac{3}{4\pi\rho_p}\sum_{i=1}^{2}\sum_{j=1}^{2} k_{pij}p_i\frac{\bar{n}(r,t)}{N_A}[M_j]_p MW_j = \Re_{Growth}(r,t) \tag{4.4}$$

where the RHS has no explicit dependence on the dependent variable (r^3), nor on the PSD itself. The value of $\Re_{Growth}(r,t)$ is calculated for each FE, at each of the sub-interval points $t+\frac{\Delta t}{4}$, $t+\frac{\Delta t}{2}$, $t+\frac{3\Delta t}{4}$ and $t+\Delta t$. In order to exploit the explicit form of the ODE representing growth (Equation (4.4)) (particularly with respect to the PSD), the accounting of the growth event in updating the PSD is done as follows. The fraction of particles in the various FE, that would grow into the adjoining FE at the next time step is calculated: a cut-off particle size ri_j in Finite Element j is defined such that all particles above that size in this FE will move onto the next FE at the next time step. The width of the FEs are such that the particles in a given FE do not grow beyond their immediately neighboring FE. The value of $\Re_{Growth}(r,t)$ is available at five time instances within this time step Δt (see Figure 4.2(b)). The cut-off size is calculated using these values of $\Re_{Growth}(r,t)$ at the sub-interval points, with a single application of a sixth order implicit Simpson method as follows:

$$ri_j^3 = rb_j^3 - (\Delta t/4)(14\Re_{Growth_{j,1}} + 64\Re_{Growth_{j,2}} + 24\Re_{Growth_{j,3}} + 64\Re_{Growth_{j,4}} + 14\Re_{Growth_{j,5}})(\tfrac{1}{45}) \tag{4.5}$$

where $\Re_{Growth_{j,i}}$ is the value of the $\Re_{Growth}(r,t)$ of Equation (4.4) at the i^{th} sub-step within this main step. Then, the particle count for bins 2, 3, ... N is updated as

$$F_{new,j} = F_j - F_j\frac{(rb_j - ri_j)}{\Delta R_j} + F_{j-1}\frac{(rb_{j-1} - ri_{j-1})}{\Delta R_{j-1}} \tag{4.6}$$

where ΔR_j is the width of finite element j. For the first FE, in which the nucleation of new particles occurs, the particle count is updated as

$$F_{new,1} = F_1 - F_1\frac{(rb_1 - ri_1)}{\Delta R_1} + (\Delta t/4)(14\Re_{nuc,1} + 64\Re_{nuc,2} + 24\Re_{nuc,3} + 64\Re_{nuc,4} + 14\Re_{nuc,5})(\tfrac{1}{45}) \tag{4.7}$$

where $\Re_{nuc,i}$ is the nucleation rate at the i^{th} time sub-step. The last term arises from a sixth order implicit Simpson method. The choice of four sub-steps within each main step is arbitrary. One could choose other configurations (*e.g.,* less conservative), and employ appropriate implicit integration formulae.

A constant step size of $\Delta t = 0.1\ s$, and a constant width for all the finite elements, $\Delta R = 2\ nm$, are employed. Figure 4.3 compares the end-point PSD, the profile of total particles, and the profile of solids content pertaining to the current algorithm, with the DDASSL solutions. The current algorithm follows the timings and the magnitudes of the nucleation events predicted by the earlier algorithm closely (as evident from the comparison of the profile of total particles), and also captures the growth rates as seen in the solids content plot. However, the current algorithm captures the intermediate nucleation event (between 3 and 4 minutes), and thereby produces an interconnected PSD at the end of the batch, resulting in a better match of the experimentally-observed distribution. Figure 4.3(a) shows a plot of the weight-averaged distribution at the end of the batch. The OCFE/DDASSL solution predicts much sharper segregation of peaks, which is contrary to the experimental results. On the other hand, the current algorithm predicts a more smoothened distribution due to an inter-related accounting of the nucleation and growth events. The peaks in the current result are lower than the corresponding peaks in the OCFE/DDASSL result due to the presence of particles in the range 150-250 nm. Overall, the current results are closer to the experimentally-observed distribution. The CPU time for a constant step size of 0.1 s, with 500 FEs, and a width of $2nm$ per element is 4.5

minutes on a SunBlade 1000 dual processor with 800 MHz each, and 1 GB memory, for the simulation of a batch spanning 150 *minutes* (see Table 4.1, first row).

4.2.2 Coagulation-inclusive emulsion polymerization

In this case, the full form of Equation (4.2) is employed to update the PSD. The nucleation and the growth effects are incorporated as explained previously. This section details the accounting of the coagulation effects. Coagulation modeling using discretization techniques has elicited wide interest in pure aggregation/breakage problems, as was mentioned previously. In this case, the conservation of mass and number are critical, due to particular assumptions made in the discretization. As shown in Chapter 3, $\Re_{coag}$ is defined as $\Re_{coag}(r,t) = H(r_{upper} - r)\Re_{formation}(r,t) - \Re_{depletion}(r,t)H(r_{cut-off} - r)$. Here, $H(.)$ is the Heaviside function (which is unity when the argument is non-negative, and zero otherwise), $r_{cut-off}$ is the cut-off size below which the particles are prone to coagulation, and r_{upper} is the maximum size of particles that could result by the coagulation of smaller particles, related to $r_{cut-off}$ as $r_{upper} = 2^{\frac{1}{3}} r_{cut-off}$. Considering these separately, $\Re_{formation}(r,t)$ accounts for the formation of particles of size r at time t. Thus, the rate of formation of particles in bin j at time t is given by (from Equation (3.37)):

$$\Re_{formation_j}(t) = \frac{1}{2V_w} \int_{rb_{j-1}}^{rb_j} \int_{r'=r_{nuc}}^{(r^3 - r_{nuc}^3)^{\frac{1}{3}}} \beta(r', (r^3 - r'^3)^{\frac{1}{3}}) F(r',t) F((r^3 - r'^3)^{\frac{1}{3}}, t) \frac{r^2}{(r^3 - (r')^3)^{\frac{2}{3}}} dr' dr \tag{4.8}$$

Introducing a change of coordinate $r'' = (r^3 - r'^3)^{\frac{1}{3}}$, to simplify the integrand and thereby facilitate analytical solutions, will render the domain of integration nonlinear. In order to render the domain of integration bounded by linear boundaries, the radius-based FEs are converted to volume-based FEs (only for the calculation of the coagulation rates). Note that a linear grid choice on a radius-basis would result in a geometric grid when converted to a volume basis. The rate of formation of particles

of volume between V and $V + dV$, due to coagulation of smaller size particles, is given by

$$\frac{1}{V_w}\beta(V', V'')F_V(V', t)F_V(V'', t)dV'dV'' \tag{4.9}$$

where V' and V'' are related by the linear relationship $V' + V'' = V$. Thus, the total rate of formation of particles in bin 'j' becomes:

$$\frac{1}{2V_w}\int_{V=V_{j-1}}^{V_j}\left[\int_{V'=V_{nuc}}^{V-V_{nuc}}\beta(V', (V-V'))F_V(V', t)F_V((V-V'), t)dV'\right]dV \tag{4.10}$$

where $F_V(V, t)dV = F(r, t)dr$, and $dV = 4\pi r^2 dr$, giving $F_V(V, t) = \frac{F(r,t)}{4\pi r^2}$. In discrete form, the particle density in bin 'j' on a volume basis is given by, $F_{V,j} = \frac{F_j}{\Delta R_j 4\pi r_j^2}$, due to the assumption of uniform particle density within each FE. Figure 4.4(a) shows the domain of integration (shaded region) for the double integral in Equation (4.10). Introducing a change of variables $V'' = V - V'$, the total rate becomes:

$$\begin{aligned}&\tfrac{1}{2V_w}\textstyle\int_{V'=V_{nuc}}^{V_{j-1}-V_{nuc}}\left[\int_{V''=V_{j-1}-V'}^{V_j-V'}\beta(V', (V-V'))F_V(V', t)F_V((V-V'), t)dV''\right]dV' + \\ &\tfrac{1}{2V_w}\textstyle\int_{V'=V_{j-1}-V_{nuc}}^{V_j-V_{nuc}}\left[\int_{V''=V_{nuc}}^{V_j-V'}\beta(V', (V-V'))F_V(V', t)F_V((V-V'), t)dV''\right]dV'\end{aligned} \tag{4.11}$$

The corresponding domain of integration is shown in Figure 4.4(b). Using this description, the coagulation events are exact. Thus, there is a consistency in terms of the number of particles, and a preservation of the mass during the coagulation event.

In modeling the coagulation event, the calculation of the intrinsic coagulation rate (coagulation kernel) β is performed on-line, as the simulation progresses. These calculations, as well as the calculations of the coagulation rates themselves, involve intensive computations. However, the form of the coagulation rate expression (as it occurs in population balance systems in general) is amenable to performing some of the calculations off-line analytically (once, at the start of the simulation), leading to

a substantial reduction in the computational load. This approach is similar to the one followed by Mahoney & Ramkrishna (2002), although in their case numerical approximations to the domain of integration were employed, unlike the analytical solutions employed in this work. The analytical solutions are derived as follows (note that they can be easily adapted for general systems):

The space between V_{nuc} and $(V_{j-1} - V_{nuc})$ along the V' axis in Figure 4.4(b) can span several finite elements, depending on FE 'j' in which the particle formation is under consideration. Within each of these FEs, the value of $F_V(V', t)$ is a constant. Considering one such FE 'i' shown in this Figure (by vertical dashed lines), the rate of formation of particles in bin 'j' by coagulation of particles in bin 'i' with other particles is given by:

$$\begin{aligned} &\frac{1}{2V_w} \int_{V'=V_{i-1}}^{V_i} \left[\int_{V''=V_{j-1}-V'}^{V_j - V'} \beta(V', (V - V')) F_V(V', t) F_V((V - V'), t) dV'' \right] dV' \\ &\quad = \frac{F_V(V', t)}{2V_w} \int_{V'=V_{i-1}}^{V_i} \left[\int_{V''=V_{j-1}-V'}^{V_j - V'} \beta(V', (V - V')) F_V(V - V', t) dV'' \right] dV' \end{aligned} \tag{4.12}$$

The domain of integration is shown in Figure 4.5. This domain in turn spans several FEs along the V'' axis, *i.e.,* the points j_1, j_2, j_3 and j_4 could (all or some) lie in different FEs. Identification of the FEs in which j_1, j_2, j_3 and j_4 lie will enable a simplification of the double integrals, and will allow each integral to be cast in terms of multiplications and additions. Figure 4.5 shows a split of the domain of integration in terms of the various finite elements in the V'' axis (horizontal dash-dot lines). Consider the most general case in which each of these points j_1, j_2, j_3 and j_4 lie in different FEs, with other FEs between each of them. For the FE j_1, the coagulation term becomes,

$$\frac{\beta_{i,j_1} F_{V,i} F_{V,j_1}}{2V_w} \int_{V'=V_{j-1}-V_{j_1}}^{V_i} \left[\int_{V''=V_{j-1}-V'}^{V_{j_1}} dV'' \right] dV' \tag{4.13}$$

which is the rate of formation of particles in bin 'j' due to the coagulation of particles in bin 'i' with the particles in bin 'j_1'. This simplifies to

$$\frac{\beta_{i,j_1} F_{V,i} F_{V,j_1}}{2V_w}[(V_{j_1} - V_{j-1})(V_i - V_{j-1} + V_{j_1}) + \frac{1}{2}(V_i^2 - (V_{j-1} - V_{j_1})^2)] \qquad (4.14)$$

The term within the square brackets represents the portion of the particles in this domain that could contribute to particles in bin 'j' by coagulation.

Similarly, for any bin between 'j_1+1' and 'j_2−1', say 'j_5', the rate of formation of particles in bin 'j' due to coagulation of particles in bin 'i' with particles in bin 'j_5' is given by:

$$\frac{\beta_{i,j_5} F_{V,i} F_{V,j_5}}{2V_w}\left[\int_{V'=V_{j-1}-V_{j_5}}^{V_{j-1}-V_{j_5-1}}\left(\int_{V''=V_{j-1}-V'}^{V_{j_5}} dV''\right)dV' + \int_{V'=V_{j-1}-V_{j_5-1}}^{V_i}\left(\int_{V''=V_{j_5-1}}^{V_{j_5}} dV''\right)dV'\right] \qquad (4.15)$$

This simplifies to

$$\frac{\beta_{i,j_5} F_{V,i} F_{V,j_5}}{2V_w}[(V_{j_5} - V_{j_5-1})(V_{j_5} - V_{j-1}) + \frac{1}{2}(V_{j-1} - V_{j_5-1})^2 - \frac{1}{2}(V_{j-1} - V_{j_5})^2 + (V_{j_5} - V_{j_5-1})(V_i - V_{j-1} + V_{j_5-1})] \qquad (4.16)$$

The rate of formation of particles in bin 'j' due to coagulation of particles in bin 'i' with particles in bin 'j_2' is given by:

$$\frac{\beta_{i,j_2} F_{V,i} F_{V,j_5}}{2V_w}\left[\int_{V'=V_{i-1}}^{V_{j-1}-V_{j_2-1}}\left(\int_{V''=V_{j-1}-V'}^{V_{j_2}} dV''\right)dV' + \int_{V'=V_{j-1}-V_{j_2-1}}^{V_i}\left(\int_{V''=V_{j_2-1}}^{V_{j_2}} dV''\right)dV'\right] \qquad (4.17)$$

This simplifies to

$$\frac{\beta_{i,j_2} F_{V,i} F_{V,j_2}}{2V_w}[(V_{j_2} - V_{j-1})(V_{j-1} - V_{j_2-1} - V_{i-1}) + \frac{1}{2}(V_{j-1} - V_{j_2-1})^2 - \frac{1}{2}(V_{i-1})^2 + (V_{j_2} - V_{j_2-1})(V_i - V_{j-1} + V_{j_2-1})] \qquad (4.18)$$

The rate of formation of particles in bin 'j' due to coagulation of particles in bin 'i' with particles in bin 'j_3' is given by:

$$\frac{\beta_{i,j_3} F_{V,i} F_{V,j_3}}{2V_w} \left[\int_{V'=V_{i-1}}^{V_j - V_{j_3}} \left(\int_{V''=V_{j_3-1}}^{V_{j_3}} dV'' \right) dV' + \int_{V'=V_j - V_{j_3}}^{V_i} \left(\int_{V''=V_{j_3-1}}^{V_j - V'} dV'' \right) dV' \right] \tag{4.19}$$

This simplifies to

$$\frac{\beta_{i,j_3} F_{V,i} F_{V,j_3}}{2V_w} [(V_{j_3} - V_{j_3-1})(V_j - V_{j_3} - V_{i-1}) + (V_j - V_{j_3-1})(V_i - V_j + V_{j_3}) - \tfrac{1}{2}(V_i)^2 + \tfrac{1}{2}(V_j - V_{j_3})^2] \tag{4.20}$$

For any bin between '$j_2 + 1$' and '$j_3 - 1$', say 'j_5', the rate of formation of particles in bin 'j' due to coagulation of particles in bin 'i' with particles in bin 'j_5' is given by:

$$\frac{\beta_{i,j_5} F_{V,i} F_{V,j_5}}{2V_w} \left[\int_{V'=V_{i-1}}^{V_i} \left(\int_{V''=V_{j_5-1}}^{V_{j_5}} dV'' \right) dV' \right] \tag{4.21}$$

This simplifies to

$$\frac{\beta_{i,j_5} F_{V,i} F_{V,j_5}}{2V_w} [(V_{j_5} - V_{j_5-1})(V_i - V_{i-1})] \tag{4.22}$$

These are the bins that entirely contribute to particles in bin 'j' upon coagulation (this interpretation can be understood from Figure 4.5, envisaging bins (horizontal lines) between j_2 and j_3). For the present choice of FE widths, this case does not arise, *i.e.,* j_2 and j_3 were either in the same bin or in immediately neighboring bins. For any bin between '$j_3 + 1$' and '$j_4 - 1$', say 'j_5', the rate of formation of particles in bin 'j' due to coagulation of particles in bin 'i' with particles in bin 'j_5' is given by:

$$\frac{\beta_{i,j_5} F_{V,i} F_{V,j_5}}{2V_w} \left[\int_{V'=V_{i-1}}^{V_j - V_{j_5}} \left(\int_{V''=V_{j_5-1}}^{V_{j_5}} dV'' \right) dV' + \int_{V'=V_j - V_{j_5}}^{V_j - V_{j_5-1}} \left(\int_{V''=V_{j_5-1}}^{V_j - V'} dV'' \right) dV' \right] \tag{4.23}$$

This simplifies to

$$\frac{\beta_{i,j_5}F_{V,i}F_{V,j_5}}{2V_w}[(V_{j_5}-V_{j_5-1})(V_j-V_{j_5}-V_{i-1})+(V_j-V_{j_5-1})(V_{j_5}-V_{j_5-1})-\tfrac{1}{2}(V_j-V_{j_5-1})^2 \\ +\tfrac{1}{2}(V_j-V_{j_5})^2] \tag{4.24}$$

The rate of formation of particles in bin 'j' due to coagulation of particles in bin 'i' with particles in bin 'j_4' is given by:

$$\frac{\beta_{i,j_4}F_{V,i}F_{V,j_4}}{2V_w}\left[\int_{V'=V_{i-1}}^{V_j-V_{j_4-1}}\left(\int_{V''=V_{j_4-1}}^{V_j-V'}dV''\right)dV'\right] \tag{4.25}$$

This simplifies to

$$\frac{\beta_{i,j_4}F_{V,i}F_{V,j_4}}{2V_w}\left[(V_j-V_{j_4-1})(V_j-V_{j_4-1}-V_{i-1})-\frac{1}{2}(V_j-V_{j_4-1})^2+\frac{1}{2}(V_{i-1})^2\right] \tag{4.26}$$

A slight modification is necessary when $i=j-1$, in which case, V_i should be replaced by (V_i-V_{nuc}). A more substantial change is needed for the case where $i=j$, as is evident in Figure 4.4(b), since the domain of integration is now a triangular region (instead of the rhombus that characterized the domains of the earlier double integrals). (Note that this case accounts for the formation of particles in bin 'j' by coagulation of particles in bin 'j' with smaller particles. However, the loss of the particles is accounted for in the depletion term, resulting in a net cancellation). The rate of formation of particles in bin 1 due to coagulation is given by $\Re_{formation,1}(t)=\frac{1}{2V_{aq}}\beta_{1,1}F_{V,1}^2(V_1-2V_{nuc})^2$.

The terms within the square brackets in each of these integral evaluations depend only on the grid details. Hence *they can be computed once, at the start of the simulation*, and employed throughout. In this form, the integrals have been reduced to algebraic equations. Thus, at each time step, once the intrinsic coagulation rate β is calculated, the calculation of the coagulation rate $\Re_{coag}$ involves straightforward multiplications and additions. Due to this semi-analytic solution for the

coagulation terms, there is still an exact preservation of number and mass, subject to the assumption of uniform particle density within each FE. This is an alternate approach to the one employed in earlier studies (Kumar and Ramkrishna, 1996b), which also account for the conservation of properties based on the assumption that all the particles are concentrated at a single point within each finite element. In the latter approach, particles are assigned to different bins, some smaller and some larger than that which would actually result from the coagulation event. Such re-assignments are not required in the present approach, which coupled with the small FE widths, gives good performance.

Unlike the terms involved in the calculation of the formation of particles by coagulation, the terms involved in the calculation of the depletion of particles by coagulation are much more benign. The rate of depletion of particles in bin 'j' by coagulation with other particles is:

$$\Re_{depletion,i} = \frac{F_{V,i}}{V_{aq}} \Sigma_{j=1}^{j_{cut-off}} \beta_{i,j} F_{V,j} \tag{4.27}$$

The coagulation-induced formation and depletion terms for each FE are computed at each sub-interval point within the main time interval (as was done for the nucleation and growth rates). The PSD information is then updated in this coagulation-inclusive case as follows:

$$\begin{aligned} F_{new,1} = F_1 - F_1 \tfrac{(rb_1 - ri_1)}{\Delta R_1} + (\Delta t/4)(14\Re_{nuc,1} + 64\Re_{nuc,2} + 24\Re_{nuc,3} + 64\Re_{nuc,4} + \\ 14\Re_{nuc,5})(\tfrac{1}{45}) + (\Delta t/4)(14\Re_{formation_{1,1}} + 64\Re_{formation_{1,2}} + 24\Re_{formation_{1,3}} + \\ 64\Re_{formation_{1,4}} + 14\Re_{formation_{1,5}})(\tfrac{1}{45}) - (\Delta t/4)(14\Re_{depletion_{1,1}} + \\ 64\Re_{depletion_{1,2}} + 24\Re_{depletion_{1,3}} + 64\Re_{depletion_{1,4}} + 14\Re_{depletion_{1,5}})(\tfrac{1}{45}) \end{aligned} \tag{4.28}$$

and for $j = 2, 3...N$

$$F_{new,j} = F_j - F_j\frac{(rb_j - ri_j)}{\Delta R_j} + F_{j-1}\frac{(rb_{j-1} - ri_{j-1})}{\Delta R_{j-1}} + H(j_{upper} - j)(\Delta t/4)(14\Re_{formation_{j,1}} + 64\Re_{formation_{j,2}} + 24\Re_{formation_{j,3}} + 64\Re_{formation_{j,4}} + 14\Re_{formation_{j,5}})(\tfrac{1}{45}) - H(j_{cut-off} - j)(\Delta t/4)(14\Re_{depletion_{j,1}} + 64\Re_{depletion_{j,2}} + 24\Re_{depletion_{j,3}} + 64\Re_{depletion_{j,4}} + 14\Re_{depletion_{j,5}})(\tfrac{1}{45}) \tag{4.29}$$

where $\Re_{formation_{j,i}}$ and $\Re_{depletion_{j,i}}$ are the total rates of formation and depletion, respectively, of particles in bin 'j' at the i^{th} time sub-step, and $H(.)$ is the Heaviside function, while j_{upper} and $j_{cut-off}$ are the bins corresponding to r_{upper} and $r_{cut-off}$, respectively.

Also, the intrinsic coagulation rate $\beta_{i,j}$ can be updated only periodically, instead of being updated at every time sub-step. In this case, the terms $\Re_{formation_{j,i}}$ and $\Re_{depletion_{j,i}}$ can be computed only at one of the sub-time steps, and the coagulation update reduces to a simple explicit Euler step. Considering the implicit nature of all preceding integration steps, this is not a serious concern for stability, as will also be demonstrated in the next section. Figure 4.6 compares the PSD resulting from a complete coagulation-inclusive simulation of a batch spanning 150 *minutes*, with that from a coagulation-free simulation. The simulation time on a SunBlade 1000 Unix dual processor with 800 MHz each, and 1 GB memory, using 200 finite elements of 2 *nm* width each, is 16 *minutes* and 5 *s*, employing a constant step size of 0.1 *s*, for a batch spanning 150 *minutes* (second row in Table 4.1).

4.3 Stability and Accuracy Considerations and Adaptive Step Size

The first tier of the algorithm, in which the rates of nucleation, growth and coagulation are computed, involves solving ODEs and algebraic equations. While this solution can be obtained with an arbitrary method, the current study employs

an in-built algorithm. The differential equations were solved using Adams-Moulton-Bashforth predictor-corrector techniques, employing an explicit predictor and an implicit corrector. By virtue of the implicit technique, the stability of the algorithm is ensured. The algebraic equations were then solved employing Newton-Raphson methods. In the second tier of the algorithm, the integration equations employed to update the PSD (Equation (4.2)) are implicit sixth order methods (due to the 4 sub-step strategy that was followed here). The particular form of growth was exploited to enable a single application of the implicit method. The stability of the second step is also guaranteed due to its implicit nature in a coagulation-free simulation. However, as mentioned previously, the coagulation-inclusive case involves an explicit update of the PSD information (equivalent to a first order Euler step), particularly when the intrinsic coagulation rate β is not updated within a time step. One might consider employing a predictor-corrector framework for the coagulation update. In the present case, the solutions show good stability even with a single step PSD update in the second tier. This is seen in Figure 4.7, wherein the coagulation-inclusive result is compared for the case in which a predictor-corrector method was employed to update the PSD (for the second tier), with that for the case in which the PSD is updated in a single step (as shown in Equations (4.28) and (4.29)). This figure suggests that a single step PSD update is adequate (iteration is not essential).

In the above cases, the accuracy of the solution is ensured by maintaining conservative time steps. In a predictor-corrector technique, the estimate of the error in the integration can be obtained from the predicted and corrected solutions. The predictor technique is fourth order, with an error approximately $O(h^4)$ and the corrector is fifth order with an error approximately $O(h^5)$. Thus, the predicted value is given by $x^p = x_{exact} + O(h^4)$, while the corrected value is given by $x = x_{exact} + O(h^5)$. The error between the predicted and the corrected values, $e = abs(x - x^p)$ is approximately $O(h^5)$. In simulations without an adaptive step size calculation, a

step size of 1×10^{-5} s is employed for the first step. The step size is then doubled at each subsequent step, until the attainment of a value close to 0.1 s. Thereafter, the step size is maintained constant at this last value. This conservative step size maintains the error estimates within acceptable bounds.

However, one could implement an adaptive step size calculation technique, to produce solutions that meet a specified tolerance, while at the same time employing the maximum allowable step size values. If the error at any step, for each term in the vector e, is less than the corresponding tolerance values, then the step size can be potentially raised for the next time step. Otherwise, the step size must be lowered for the next time step to obtain an acceptable accuracy in the solution. Thus, if $e(j) > tol(j)$ for any component j in vector e, then $h_{new} = {}^{min}_{i} \left(h_{old} (\frac{tol(i)}{e(i)})^{(\frac{1}{5})} \right)$, where i refers to each component in vector e. Else, $h_{new} = min \left({}^{min}_{i} \left(h_{old} (\frac{tol(i)}{e(i)})^{(\frac{1}{4})} \right), 2 * h_{old} \right)$. In each case, only the smallest suggested step size is adopted. The exponent is increased in the case of an increasing step ($e(j) < tol(j)$ for all j) as a safety margin (from 0.20 to 0.25) (Press et al., 1992). Another safety margin is provided by restricting the step size to not exceed twice the earlier step size. In both cases, the integration results of the current time step are accepted (Press et al., 1992). If a predictor-corrector technique is employed in the PSD update step (second tier) to accommodate the explicit involvement of the PSD information in the coagulation term, then another step-size adaptation could be built around this term, to work in tandem with the first one.

Figure 4.8 compares the simulation results pertaining to the adaptive step size with that pertaining to a constant step size. The tolerance values set for the variables are adjusted to yield a good match. The solution time for the adaptive step size case is about 37 s in a 800 MHz dual processor with 1 GB memory, for a simulation spanning 150 *minutes*, as shown by the entry in the third row of Table 4.1. The solution time when a predictor-corrector technique is employed for the

PSD updating stage (second tier) increases to 39 s in this same processor (fourth row of Table 4.1). The FE widths chosen in each of these cases are very conservative values (at least five times smaller than typical values (Crowley et al., 1999)). An added feature of the current solution technique is its robustness to a range of recipes. The stiffness characteristics of the OCFE-discretized original system caused the integrator employed to be unsuccessful under conditions of excessive nucleation. In particular, the code could not handle high initial surfactant concentrations, nor simulate 'pre-nucleation' conditions (during which time the seed particles are generated, typically lasting about 10 *minutes*, which are quite common in industrial practice). The current solution technique can simulate most industrially-relevant recipes, and hence has a wider utility.

4.4 Summary and Extensions to General Population Balance Systems

This paper presents a new algorithm for solving population balance models. The algorithm is based on a discretization of the domain of particle size into finite elements or 'bins'. The algorithm follows a two step strategy – one to calculate the individual rates of nucleation, growth and coagulation, and the other to update the PSD based on these individual rates. In the current implementation, each time interval is divided into four sub-intervals. The rates of nucleation, growth and coagulation are calculated at the four sub-interval points within the main interval, by holding the PSD information constant. The particle count within each finite element is then updated by a single semi-implicit step. In the case of a constant step size, the overall time step chosen (for the outer step) is very conservative (0.1 s). Also, an adaptive step size strategy is presented, which gives solution times of 39 s in a 800 MHz dual Sun Blade 1000 processor with 1 GB memory (and less than a minute in a single 333 MHz processor), for the simulation of a batch spanning 150 *minutes*.

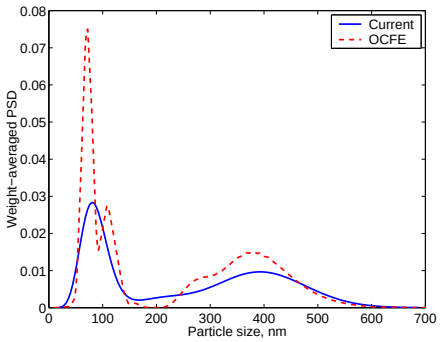

(a) comparison of the end-point PSD produced by the current solution with that produced by the OCFE/DDASSL solution

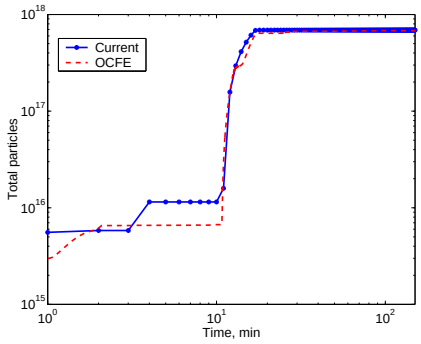

(b) comparison of the profiles of total particles between the two solutions

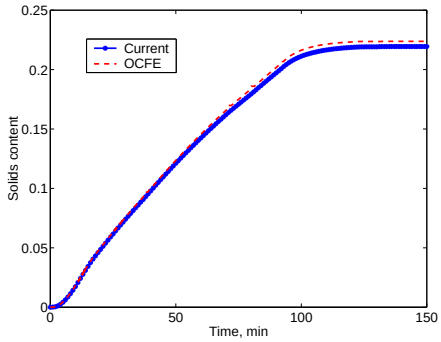

(c) comparison of the profiles of solids content between the two solutions

Figure 4.3: Comparison of the simulation results from the current algorithm (500 Finite Elements of 2 nm width each) with those from the solution of a OCFE-based discretization of the PBE, and employing DDASSL integrator to solve the resultant DAE system (40 Finite Elements having 3 internal collocation points per element).

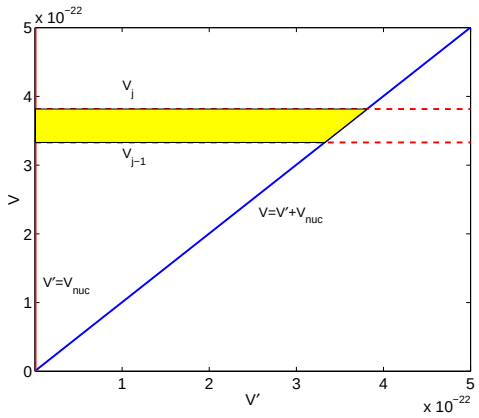

(a) the domain of integration (shaded region) for the formation of particles in bin 'j' due to coagulation between two smaller particles

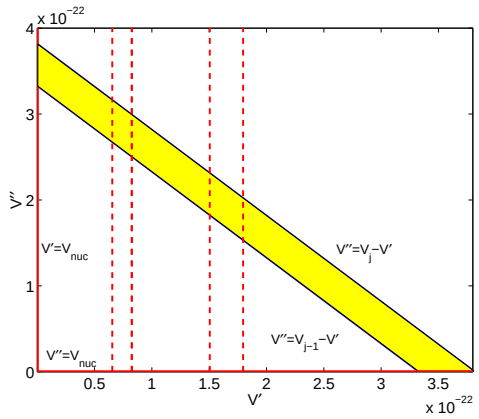

(b) the new domain of integration upon a change of variable ($V'' = V - V'$) in the original integral

Figure 4.4: The domain of integration for the double integrals.

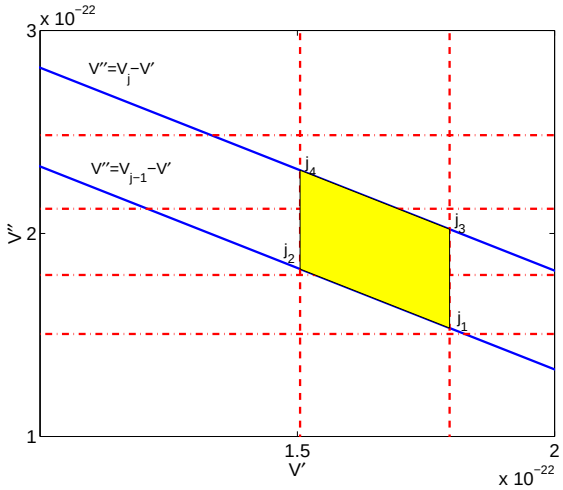

Figure 4.5: The domain of integration for the formation of particles in bin 'j' due to coagulation of particles in a particular bin 'i' (shown between vertical dashed lines in Figure 4.4(b)), with other particles.

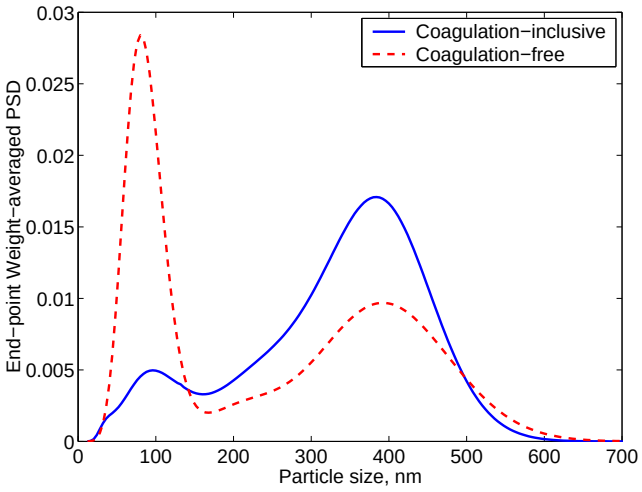

Figure 4.6: The end-point PSD simulated by the current algorithm, for the complete case including nucleation, growth and coagulation (250 Finite Elements of 2 nm width each), compared with the case without coagulation (500 Finite Elements of 2 nm width each).

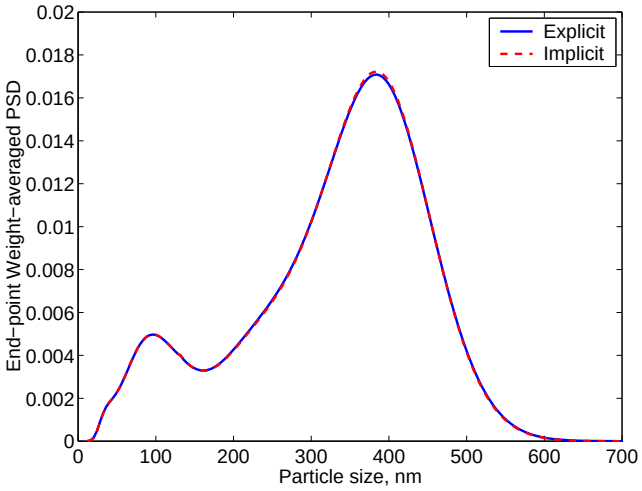

Figure 4.7: The comparison of the end-point PSD corresponding to a predictor-corrector strategy to update the PSD, with the case of an explicit step to update the PSD (250 Finite Elements of 2 nm width each, in both the cases).

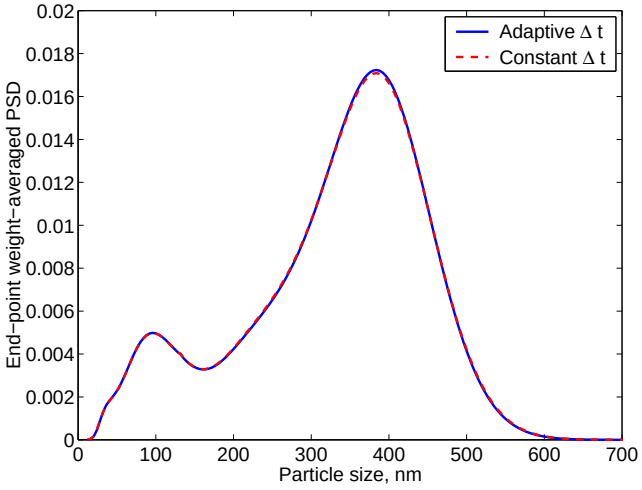

Figure 4.8: The comparison of the end-point PSD corresponding to the case of a constant step size (0.1 s) with that corresponding to an adaptive step size (250 Finite Elements of 2 nm width each).

In the more traditional approach of discretizing the PBE (which implicitly accounts for the nucleation, growth and coagulation processes), the discretization results in a system of stiff differential algebraic equations (with condition numbers exceeding 10^4 in the emulsion polymerization application that was presented here). This stiffness problem is due to the huge disparity in the time constants of the nucleation, growth and coagulation events. The current technique circumvents the stiffness problem due to the decomposed strategy that is employed.

In coagulation modeling, the method gives very good solution times. It also compares favorably with the other methods presented for pure-aggregation/breakage systems in that it accounts for internal consistency in terms of the number of particles and the mass of the particles. However, this is subject to the assumption of a uniform particle density within each bin, just as the previous results are subject to specific assumptions in the discretization. But the widths of the finite elements employed in this study (2 nm uniformly) are at least five times smaller than those typically employed, and deemed acceptable, thereby justifying the assumption of a uniform particle density within each FE.

This new hierarchical solution technique compares very favorably in terms of computation times (even including the intensive coagulation calculations) compared to a technique based on the discretization of a full PBE, as can be seen from Table 4.1. While the *coagulation-free* solution using the OCFE-technique and the DDASSL integrator takes about 38 *minutes* typically, the current algorithm gives solution times of about 37 s for the *coagulation-inclusive* simulation with adaptive step sizes. This brings the problem of on-line PSD control within the feasibility realm, at least from a computational stand point. In addition to this advantage, the current code is very robust to a variety of operating conditions that one might encounter in industrial practise, including very high nucleation rates.

Although the application presented here focused on emulsion polymerization,

the algorithm is generic enough to be easily extended to other population-balance systems. The major and obvious difference is in the calculation of the rates of nucleation, growth, coagulation and breakage, as relevant, in the first tier of the algorithm. Certain assumptions made in the algorithm and restrictions imposed by the system itself in this particular application to PSD modeling in emulsion polymerization are highlighted below, and their relaxation/extension for other PBE systems is discussed.

1. In the present study, custom-built algorithms were employed in solving the relevant equations to obtain the individual rates of nucleation, growth and coagulation. A fourth order predictor-corrector technique was employed, thereby necessitating four sub-intervals within each main interval. However, these solutions may be performed using any suitable method with the appropriate set of equations.

2. Nucleation was assumed to be restricted to the first FE, but relaxing this assumption is straightforward.

3. With respect to coagulation, the only difference is in the method of calculating the intrinsic coagulation rate β. The rest of the algorithm, including the semi-analytical off-line computations, carry over to general systems.

4. Growth phenomenon is the only mechanism that might require system-specific considerations, especially to exploit the explicitness as was done in this study. However, if a predictor-corrector technique is employed in the PSD update step, as was demonstrated here, this concern is obviated. In that case, even if an explicit form cannot be obtained for the growth term, the PSD can be updated using the original growth term in Equation (4.2).

5. Breakage is uncommon in emulsion polymerization, and hence the modeling of the breakage phenomenon was not presented here. However, it can be

cast into the same framework as the coagulation phenomenon, and the analytical solutions derived quite easily compared to the coagulation case, to facilitate computation. Consider a typical breakage process, the cell division process (Daoutidis and Henson, 2001). The accounting of the loss of cells due to breakage is straightforward. The rate of formation of cells due to the division of larger cells is modeled as

$$\Re_{formation}^{breakage}(V,t) = \int_{V=V_{j-1}}^{V_j} \left[\int_{V'=V}^{V_{max}} \Gamma(V') p(V,V') F(V',t) dV' \right] dV \qquad (4.30)$$

where $\Gamma(V')$ is the rate constant for the division of a cell of volume V', and $p(V,V')$ is the probability that the division of a cell of volume V' results in a cell of volume V. This probability would satisfy the condition $\int_{V=0}^{V'} p(V,V')dV = 1$, with $p(V,V') = 0$ for $V > V'$. Casting this solution in a discretized framework using analytical solutions is quite simple. No change of variables is necessary in this case. One needs to identify the finite elements along the V' axis, from V_{j-1} to V_{max}, and the analytical solutions can be derived in a straightforward manner (subject to the assumption of a uniform particle density within each FE).

Table 4.1: Comparison of the solution times for the simulation of a batch spanning 150 *minutes* in a Sun Blade 1000 Unix processor, equipped with two 800 MHz processors and 1 GB memory.

Case	Time	Details
Coagulation-free	4 *minutes* 28 *s*	500 finite elements of 2 *nm* width each Constant step size of 0.1 *s*
Coagulation-inclusive	16 *minutes* 5 *s*	250 finite elements of 2 *nm* width each Constant step size of 0.1 *s*
Coagulation-inclusive	37 *s*	250 finite elements of 2 *nm* width each Adaptive step size
Coagulation-inclusive	39 *s*	250 finite elements of 2 *nm* width each Adaptive step size Predictor-corrector technique for PSD update (second tier)
OCFE-based discretization and DDASSL-based solution (Coagulation-free)	37 *minutes* 54 *s*	40 finite elements, 3 internal collocation points per element (330 state-DAE system)

Chapter 5

SENSITIVITY STUDIES AND REACHABILITY ANALYSIS

5.1 Introduction

Distributed parameter systems (DPS) are characterized by partial differential equations (infinite-dimensional systems), for which there are limited theoretical controllability results. In addition, these systems are characterized by discontinuities that necessitate special consideration. These systems are approximated as lumped multivariable systems, usually with a very high ratio of the number of correlated outputs (controlled variables) to the number of inputs (manipulated variables). To motivate the controllability issue from a physical standpoint, there are certain constraints on the type of distributions that can be produced in the emulsion. Even in producing a monodisperse population, there is an upper limit on the particle size, to enable producing a dispersion of solids in the aqueous phase with an appreciable solids content in the latex. In other words, as the particle size of the monodisperse population increases, the achievable solids content is reduced. Further, the relative rates of nucleation and growth limits the attainable polydispersity of monodisperse populations. Allowing for a distribution of particle sizes in the population expands the attainable domain of solids content. However, the attainable distributions are dictated by the rates of particle nucleation and growth, and on the particle stability. These sub-processes strongly interact with each other. Although there are process inputs to control some of these aspects independently, there is a high degree of coupling with certain inputs. Considering all these issues and the constraints on the

inputs, the actual reachable distributions are limited. The analysis becomes more involved in the case of multi-modal distributions.

Formal controllability studies on particulate systems, aimed at determining the controllable distributions, are rather limited. To avoid unattainable set-points, some studies in the past on the control of distributions have utilized a partial control-like strategy, in which a few of the outputs are controlled while the rest are allowed to evolve in an open-loop manner (Gatzke and Doyle III, 2001; Daoutidis and Henson, 2001). Other studies used target PSDs that are known to be attainable *a priori* (Crowley et al., 2000). The present study is restricted to an analysis of the reachability of the distributions. Reachability refers to the ability to steer an output from an initial state to a final state in a finite time using the available inputs, while controllability also includes the ability to maintain the output at this final state beyond the end-point.

Recently, there have been studies which address the development of the reachable regions through the solution of optimization problems (Kauchali et al., 2002; Wang and Doyle III, 2002). The latter study deals with determining the reachable regions of PSD in styrene emulsion polymerization. In this study, Wang and Doyle III have identified the reachable domains in terms of the "ε-reachability", which is the domain of distributions that are reached with an error less than ε in the defined objective function. However, there are also other approaches that rely on simple simulations in arriving at the reachable regions (Liotta, Georgakis, Sudol and El-Aasser, 1997), and in analyzing the processes (Russel et al., 2002).

In the current study, a combination of experiments and simulations using population balance models are employed to analyze the evolution of PSD in the semi-batch emulsion co-polymerization of vinyl acetate (VAc) and butyl acrylate (BuA), using non-ionic surfactants. The experimental studies are mainly used to

identify a suitable control configuration and the manipulated variables. The analysis addresses the hierarchy of the individual sub-processes of nucleation, growth and coagulation, where possible. The simulation studies extend the analysis to identify the reachable unimodal and bimodal distributions. In the next section, the experimental sensitivity studies are presented, and their implications for the control of PSD are highlighted. The following section presents the simulation-based reachability studies. Here, the first part examines the nominal reachability under various configurations — using a single manipulated variable; using different combinations of multiple manipulated variables; the effect of particle coagulation; and the effect of the parameterization of the inputs. The second part presents the effect of uncertainties and disturbances on the reachable region. These include the effect of a mid-course stochastic/deterministic disturbance, and uncertainties in the initial conditions. This analysis provides information on the effectiveness of in-batch feedback control in the process, which assume importance considering the irreversibility characteristics of the process.

5.2 Experimental Sensitivity Studies

The experimental facility is utilized to study the sensitivities in the process of evolution of PSD. The objective of the study was to identify the best manipulated variables, and an effective control strategy. This is done through a series of experiments described below. The experiment described in Figure 3.2 is used as the base case recipe. This base case recipe is subjected to various perturbations, and their effects on the process are studied. These studies are used to infer the design- and control-relevant issues of the process. The experiments and the inferences from them are described below.

5.2.1 Effects of Surfactant

The experiment described in this section was designed to determine the effect of changing the surfactant feed profile on the PSD and the conversion of the monomers. The surfactant feed rate was perturbed as shown in Figure 5.1. Figure 5.2(b) compares the profiles of total particles in the current and the base case experiments. The total number of particles nucleated in this experiment is much lower ($\sim 10^{16}$), and also nucleation is not prolonged, unlike in the earlier experiment. This is mainly due to the decrease in the surfactant feed rate between 10 and 15 minutes (compared to the base case experiment). This decrease in the number of particle in the latex results in larger growth rates, thereby causing the particles to grow to a larger size (Figures 5.2(a)). This figure also shows some large size particles (larger than 600 nm), suggesting a coagulation event that could have occurred during the reduced surfactant feed rate. Figure 5.2(c) compares the profiles of solids content, which shows that the end-point solids content increases to slightly over 25% at a final overall conversion of approximately 95% (almost 20% higher than in the base case). This aspect clearly demonstrates the complex and non-intuitive behavior of the system. Increasing the surfactant feed rate to effect secondary nucleation and a bimodal end-point distribution could cascade into lower growth rates and particle sizes, and a lower conversion too. This necessitates using other inputs in the process, such as the feed rates of initiators and monomers, to correct this situation. Another aspect of the process that is evident from this experiment is the competitive particle growth phenomenon. This is seen in Figure 5.3, which shows the evolution of the bimodal distribution (number-averaged plot) along the course of the batch. It shows a more interconnected and diffuse distribution at the intermediate time range which becomes separated into a more clear bimodal distribution towards the end of the batch. This is due to the strongly size-dependent growth, with the larger particles growing faster than the smaller ones. The size-dependent growth and the

lack of inputs to manipulate this phenomenon demonstrate the importance of the timings and durations of the various nucleation events. In producing a multi-modal distribution, the polydispersity of each mode and the separation between the modes is mainly influenced by the duration and the timings of the nucleation events.

5.2.2 Effects of Monomer – Vinyl Acetate

The next experiment was designed to investigate the influence of the feed rate of one of the monomers on the evolution of the PSD and other pertinent outputs. Vinyl acetate feed rate was perturbed as shown in Figure 5.4. Figures 5.5(b) and 5.5(c) compare the profiles of total particles and solids content between the two experiments. In spite of the reduced feed rate of the VAc monomer at the start of the reaction, there is no appreciable difference between the two cases at early times (through 30 minutes) of the batches. A plausible explanation is that the system still remains saturated with the monomers. But unlike in the base case, there is a steep increase in the number of particles at approximately 37.5 minutes, coinciding with the drop in the VAc feed rate at this time (Figure 5.4). One plausible explanation is that all the monomer droplets disappear rapidly from the system coinciding with the decrease in the feed of VAc at 37.5 minutes. This results in releasing all the absorbed surfactants back into the aqueous phase and causing rapid nucleation. The end-point distribution (Figure 5.5(a)) shows appreciable mass of very small particles, due to the larger number of particles nucleated at the later times and also due to the prolonged monomer addition in this experiment. The solids content in this experiment increases by about 3%. These results clearly show that the monomer feed affects the PSD by influencing not only the rate of growth, but also the rate of nucleation. While a monomer-starved condition might decouple the effect of monomer feed on the nucleation process, it would result in reduced growth rates.

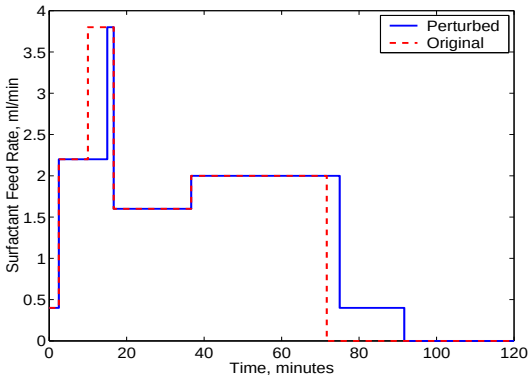

Figure 5.1: Comparison of surfactant feed between the present experiment and the base case experiment.

5.2.3 Effects of Monomer – Butyl Acrylate

Figure 5.7 depicts results corresponding to a perturbation in the feed rate of BuA monomer (shown in Figure 5.6). There is a much reduced nucleation rate in this case, as is seen from the profile of the total particles (Figure 5.7(b)), and the nucleation process continues through the course of the batch. The end-point PSD (Figure 5.7(a)) shows a signature of coagulation in the form of the large particles (larger than 600 nm). The results suggest a complex dependence of the surfactant partitioning on the monomer composition. One explanation is the surfactant solubility in the monomer droplets is larger at higher VAc composition in the droplets. Due to lack of detailed knowledge on these phenomena, it is preferable to omit BuA as a manipulated variable for the control of PSD.

5.2.4 Effects of Initiator

Figure 5.8 shows sensitivity results from an experiment in which the concentration of the redox initiator pair (tBHP and SFS) were doubled relative to the base case. Figure 5.8(b) compares the profiles of total particles, which shows that in this case there is a larger nucleation event at the initial times (up to 15-20 minutes).

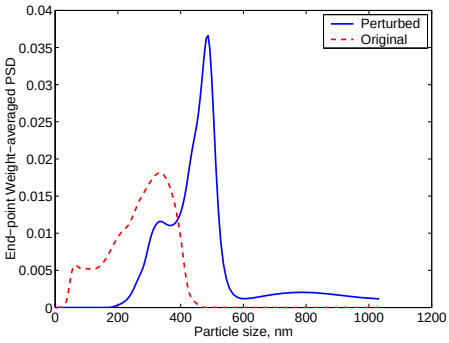

(a) comparison of the end-point PSD

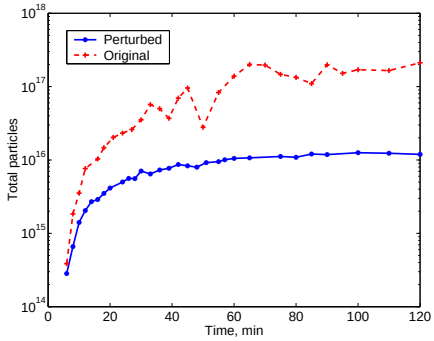

(b) comparison of the profile of total particles

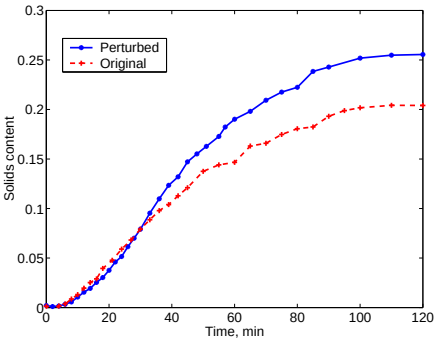

(c) comparison of the profile of solids content

Figure 5.2: Effect of a perturbation in the surfactant feed rate relative to the base case experiment.

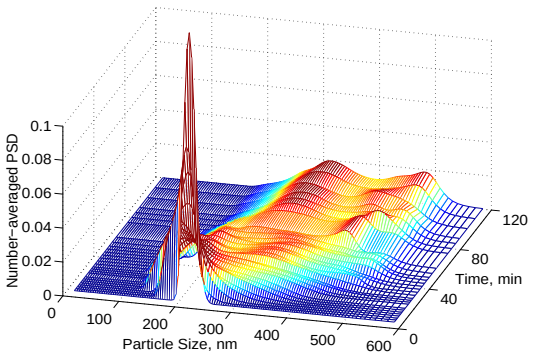

Figure 5.3: Evolution of the PSD with the surfactant-perturbed recipe.

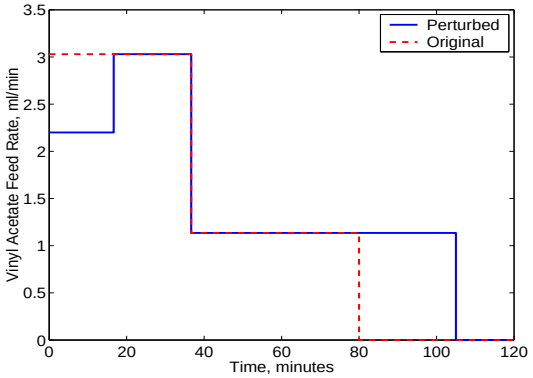

Figure 5.4: Comparison of vinyl acetate feed between the present experiment and the base case experiment.

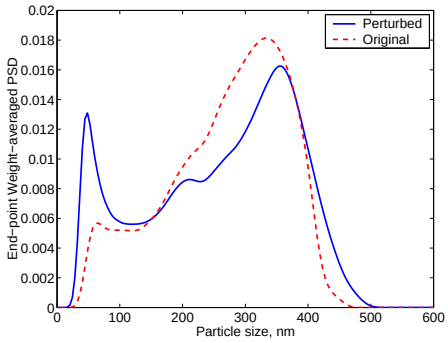

(a) comparison of the end-point PSD

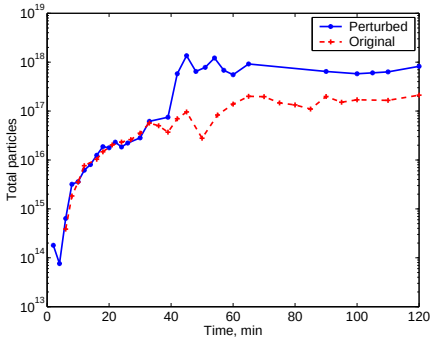

(b) comparison of the profile of total particles

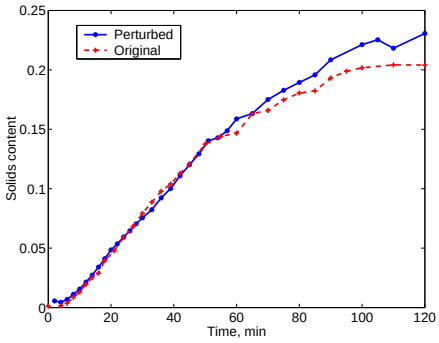

(c) comparison of the profile of solids content

Figure 5.5: Effect of a perturbation in the VAc feed rate relative to the base case experiment.

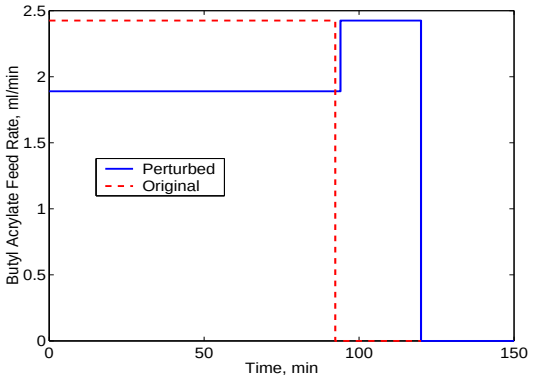

Figure 5.6: Comparison of butyl acrylate feed between the present experiment and the base case experiment.

Thereafter, the total number of particles remains relatively constant until approximately 40 minutes, at which time there is a second nucleation event. Thus, the end-point distribution is a more prominent bimodal distribution (as seen in Figure 5.8(a)). This could be attributed to a larger nucleation event at the early times (by either of micellar or homogenous mechanisms or both), which depletes the micelles and thereby prevents further nucleation events until approximately 40 minutes when more micelles are formed. Either the increase in the surfactant feed or the drop in the VAc feed (and the associated depletion of the droplets) could have contributed to the new batch of micelles. Thus, there are two clearly distinct nucleation events, contrary to the prolonged micellar nucleation event that characterizes the base case experiment. This clearly demonstrates the strong ability to influence the nucleation events through initiator feed rates or composition. Thus, the rate limiting step in this case was clearly the formation of micelles. There is no appreciable effect on growth, as seen by the comparable particle sizes.

5.2.5 Implications of the sensitivity results for the control of PSD

The effects of the manipulative variables on the PSD and solids content were studied experimentally. Each of the feeds of the surfactant, monomers and initiators

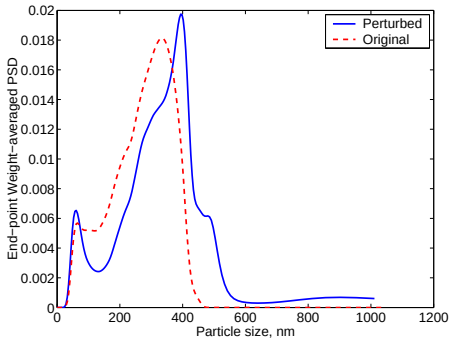

(a) comparison of the end-point PSD

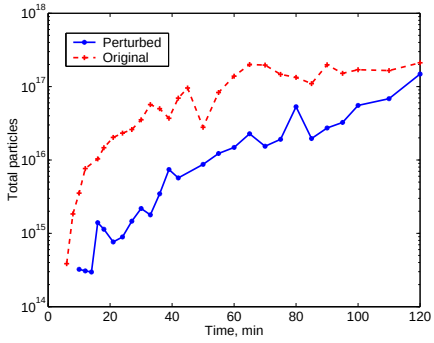

(b) comparison of the profile of total particles

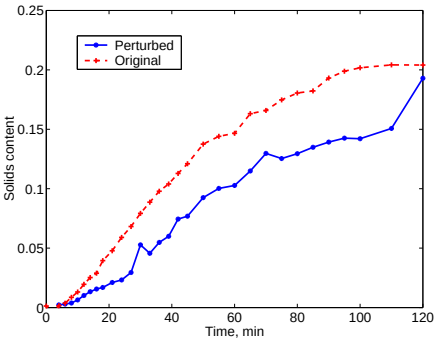

(c) comparison of the profile of solids content

Figure 5.7: Effect of a perturbation in the BuA feed rate relative to the base case experiment.

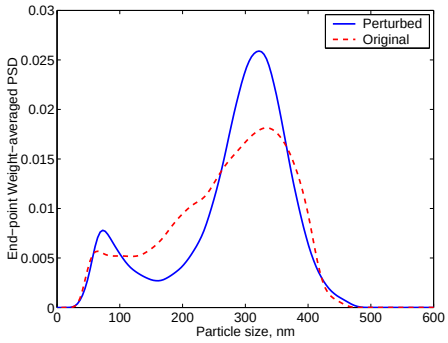

(a) comparison of the end-point PSD

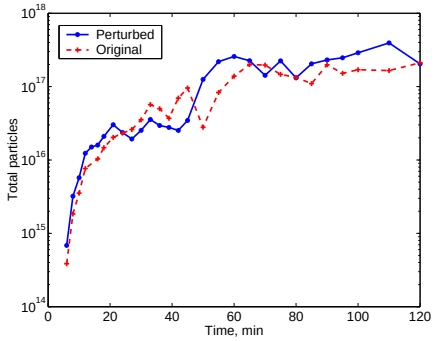

(b) comparison of the profile of total particles

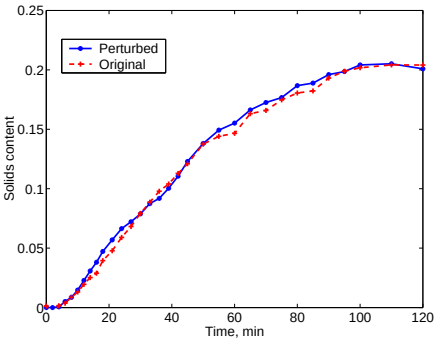

(c) comparison of the profile of solids content

Figure 5.8: Effect of a perturbation in the initiator concentration relative to the base case experiment.

have profound influences on the evolution of the distribution. However, the observed influences are complex and non-intuitive. It is natural to expect the surfactants to affect the nucleation phenomenon and particle stability, and the initiators and monomers to affect mainly the growth phenomenon. Thus, it is logical to utilize the feed rates of surfactant and initiator as manipulated variables for the control of PSD, as was done with ionic surfactants by other researchers (Crowley et al., 2000; Flores-Cerrillo and MacGregor, 2002). However, in the current case, it is seen that all the reagents – surfactant, monomer and initiator – influence the nucleation phenomena, albeit in different ways. Monomer affects the growth phenomenon, while the effect of the initiator on growth is seen to be minimal. Surfactants, whose major role is particle stabilization (emulsification), do affect the coagulation phenomenon. In addition to these direct effects, the variables also have secondary effects, which come into play because of the interaction among nucleation, growth and coagulation. For instance, the surfactants can affect the growth process indirectly, by affecting the number of radicals/particle and the monomer concentration inside the particles (by varying the particle number). Also, the behavior observed is quite complex, and cannot be adequately represented in terms of any simple dynamics (for example, first order, time delays, inverse responses *etc.*), even for continuous processes. Thus, a detailed model-based optimization and control strategy is appropriate for this process.

Another aspect that is revealed in the current study is the strong size-dependence seen in the growth phenomenon, which results in a relative broadening of the distribution with growth. Note that this is in contrast to the observations made by Liotta *et al.* (Liotta, Georgakis, Sudol and El-Aasser, 1997), who observed a relative narrowing of seeded bidisperse populations with growth. Modeling studies also support the observation on the broadening of the distribution (Chapter 3). This

is a clear example of the unsuitability of lumped parameters in certain cases, lending strong support to pursue the distributed parameter route. The lack of inputs to manipulate the size-dependent growth necessitates tight control on the timings, durations and magnitudes of the nucleation events in producing the desired distributions – mean sizes and standard deviations of the modes. Once the nucleation event has occurred, there is very little latitude to alter the competitive growth.

A third aspect that is evident from these experiments is the irreversibility that is characteristic of these processes. Each of the nucleation, growth and coagulation processes exhibit a certain irreversible character. For example, in producing a unimodal distribution, if the actual nucleation rate deviated from the desired rate, the effect of this error on the particle sizes can be corrected by suitably modifying the growth rate (by recruiting multiple process inputs). But the effect of this error on the breadth of the distribution cannot be rectified. (The import of this irreversibility on the breadth of the distributions depends on the end applications). Similarly, in producing multi-modal distributions, if the nucleation rate for the first nucleation event is erroneous in implementation, this can be corrected (in a relative sense, and bearing with the skewness of the distributions) by correcting not only the growth, but also all the subsequent nucleation rates. On the other hand, if the primary nucleation event is implemented as planned, but the secondary nucleation event is erroneously implemented, it might leave an incorrectable effect on the distribution. Similarly, a larger growth rate might result in larger sizes, which again cannot be corrected (no shrinkage possible with respect to the polymer mass in the particles). A strong coagulation event would also leave an indelible mark on the distribution (see Chapter 6 for examples of these). The interactive nature between nucleation, growth and coagulation again advices caution in the control of distributions.

From the preceding analysis, it is evident that one must employ multiple inputs for the control of distributions, with the surfactant and VAc monomer being

the most suitable inputs. Initiator feed could also be recruited, but mainly to control the nucleation phenomenon. Also, the irreversibility considerations and the interactions suggest an hierarchical strategy, in which the sub-processes (nucleation, growth and coagulation) are controlled individually, thereby producing the target distribution. A monomer-starved (droplet-free) condition might be preferable to render the nucleation event a prerogative of the surfactant feed alone (and the initiator feed, if utilized). However, too low concentrations would result in sub-optimal growth rates. Although coagulation could potentially be used to shape the distributions, the best strategy is to minimize coagulation events to the extent possible.

5.3 Simulation-based Reachability Analysis

In the previous section, experimental sensitivity results were presented, which were obtained by perturbing either the timing of a step change in input or the magnitude of a step change. However, only one such perturbation was performed with respect to each variable. A more exhaustive sensitivity study would examine the effect of all possible perturbations on the distribution. This becomes almost impossible experimentally (although the results presented above are some of the most relevant perturbations). However, more comprehensive sensitivity studies can be performed using the detailed population-balance model.

5.3.1 Effect of Surfactants – Coagulation-free Case

In the first case presented here, the coagulation events are assumed to be absent and sensitivity to surfactant feed is examined. A typical semi-batch recipe is considered, which is divided into 11 intervals of a fixed duration of 11 minutes each. The feed rates of the reagents are held constant within each interval. The feed of the monomers and the initiators are fixed. The surfactant feed rate in the

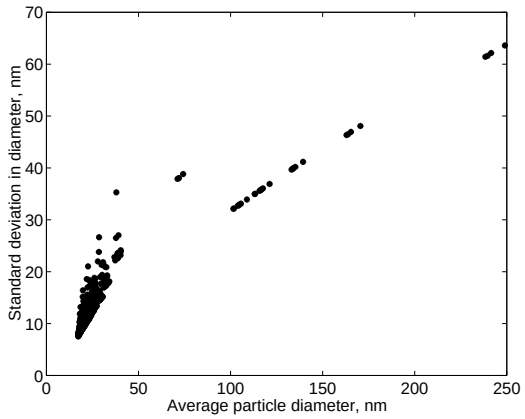

(a) standard deviation versus mean

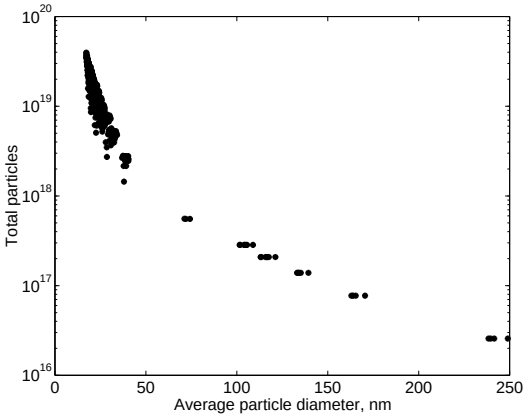

(b) total particles versus mean

Figure 5.9: The unimodal distributions produced with surfactant alone as the manipulated variable, under coagulation-free conditions.

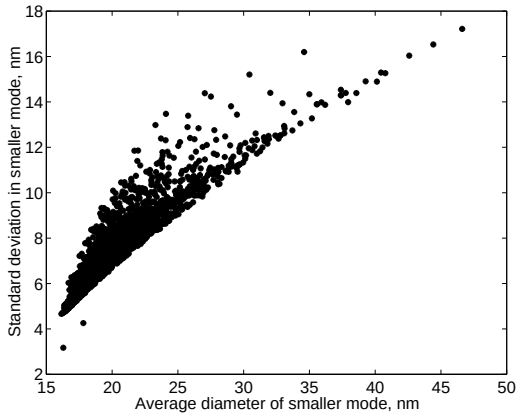

(a) standard deviation versus mean

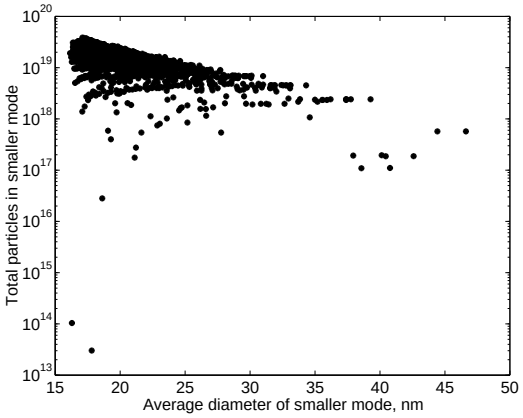

(b) total particles versus mean

Figure 5.10: Characterization of the smaller (secondary) mode, in the bimodal distributions produced with surfactant alone as the manipulated variable, under coagulation-free conditions.

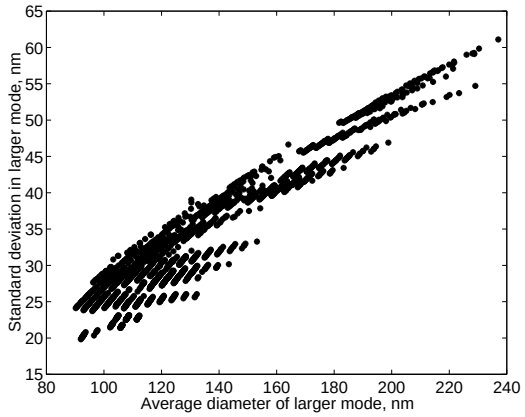

(a) standard deviation versus mean

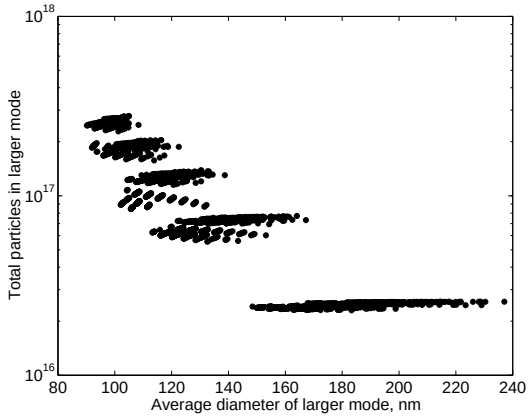

(b) total particles versus mean

Figure 5.11: Characterization of the larger (primary) mode, in the bimodal distributions produced with surfactant alone as the manipulated variable, under coagulation-free conditions.

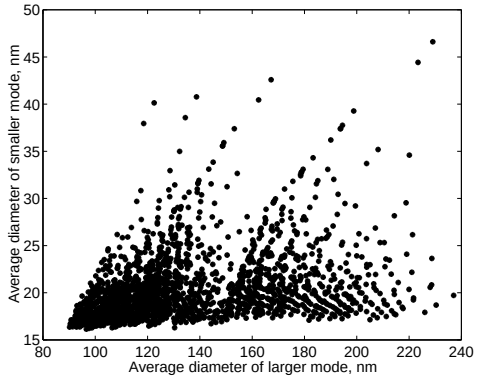

Figure 5.12: Relation between the mean size of the two modes in the bimodal distributions produced with surfactant alone as the manipulated variable, under coagulation-free conditions.

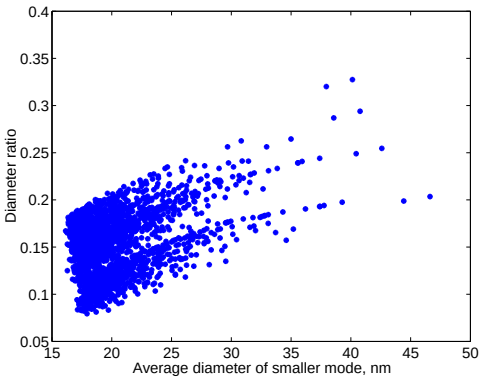

Figure 5.13: Ratio of the mean diameter of the two modes in the bimodal distributions produced with surfactant alone as the manipulated variable, under coagulation-free conditions.

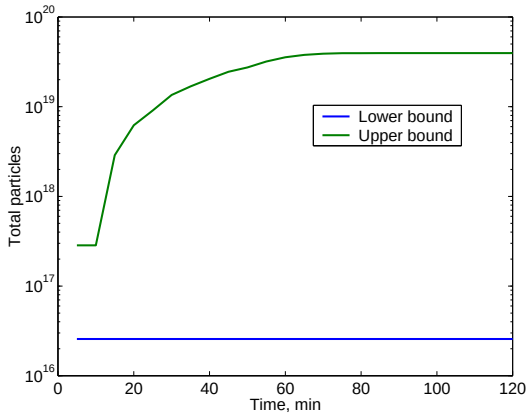

(a) profiles of total particles

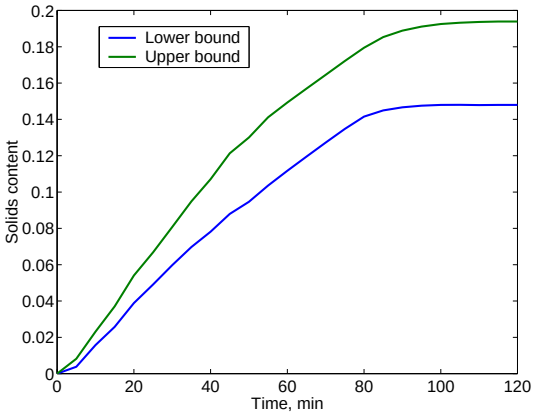

(b) profiles of solids content

Figure 5.14: Limits on the attainable profiles of total particles and solids content when surfactant alone is used as the manipulated variable, under coagulation-free conditions.

first five intervals are varied, and the sensitivities with respect to each of these variables are analyzed. The surfactant feed rate in the first interval is constrained to lie between 0.83 ml/min and 4.16 ml/min of 22.7% by weight aqueous solution. While the lower limit is fixed to enable considerable micellar nucleation at early times (there is no surfactant in the intial mixture), the upper limit is constrained to allow a later secondary nucleation. A feed rate above the upper limit would result in the nucleation of a very large number of particles initially, which upon growth would render it impossible to cause the surfactant concentration in the aqueous phase to exceed the critical micelle concentration (which is a pre-requisite for causing a micellar nucleation event) subject to the upper constraints on the pumps. Homogenous nucleation is found to be negligible after very early times of the batch, once the particles are formed (see Chapter 3). The feed rates in the remaining four intervals is constrained only by the limits of the pumps. Five different feed rate values are considered within each interval, and simulations are performed for all combinations of feed rate values in the five intervals. The end-point distributions produced in each of these cases are analyzed. The distributions are approximated as Gaussian distributions (combinations of Gaussians for multi-modal distributions), for the purposes of characterization. Thus, each mode is characterized by a mean size, standard deviation in size, and the total particles in the mode. An analysis of the ratio of the mean diameters of the bimodal distributions (among all the distributions produced) shows a monotonic yet nonlinear dependence on the feed rate of the surfactant in each of these intervals. This suggests that the distributions produced envelope all the attainable distributions (subject to the discretization of the input profiles, the constraints imposed, and the modeling errors). This is also seen in the study of Wang and Doyle III (2002), in which a plot of the objective function defining the deviation of the attained distribution from the target distribution, when plotted against the mean and standard deviation of the target distribution (unimodal), is

seen to be convex and monotonic with a single minimum. Thus, one can draw an envelope of the reachable domains around these points, which characterize the exactly reachable distributions. One can also infer the ε-reachability domains from these (see Wang and Doyle III (2002)). Figure 5.9 shows the unimodal distributions that are exactly reachable, from among all the distributions produced in these simulations, characterized in terms of the mean, standard deviation and total particles. These plots show a long tail, corresponding to lower number of particles, which result in larger growth rates and larger particle sizes. Also, in these cases, the distributions are much broader (larger standard deviation), suggesting a prolonged but low nucleation rate. As the total particles increases (above 10^{18}), there is a much reduced growth rate, resulting in smaller particle sizes. As the total particles increases further, there is a decrease in the standard deviation and a decrease in the particle size, resulting in a cone-shaped reachable region. It can be inferred from these plots that one cannot produce a narrow unimodal distribution with an average particle size larger than 100 nm. Alternatively, in producing a broad unimodal distribution of size above 100 nm, the total particles are reduced, which might have implications on the molecular weight distribution, although not necessarily on the solids content.

Figures 5.10-5.13 show results pertaining to the bimodal distributions that are produced in these simulations. Figures 5.10 and 5.11 characterize the distributions in terms of the means and the standard deviations of the two modes. As seen in Figure 5.11(a), as the size of the larger mode (corresponding to the primary nucleation) increases, the reachable standard deviations are reduced. However, the reachability of the size of the smaller mode (corresponding to the secondary nucleation) increases (Figure 5.12) – subject to the assumption of convexity. As seen in Figure 5.10(a), as the size of the smaller mode increases, the choices available for the standard deviation of the smaller mode are reduced. Also, as the number of particles nucleated

in the secondary mode increases, the size of the particles decreases (Figure 5.10(b)). Figure 5.13 shows a plot of the diameter ratio of bimodal distributions against the average size of the smaller mode, which identifies an almost rectangular reachable region. One aspect that is revealed in these results is that the number of particles in the smaller (secondary) mode is generally larger than that in the larger (primary) mode. This could be an effect of the partitioning of the non-ionic surfactants into the dispersed phases. Larger initial surfactant feed rates lead to larger primary nucleation events. There is a loss of surfactants into the monomers (at the initial times), proportional to the early surfactant feed rates. Thus, there is also a larger amount of surfactant lost into the monomer droplets at larger initial surfactant feed rates. Hence, the secondary nucleation event, which is aided by the surfactants released from the depleting droplets, is also enhanced.

Figure 5.14 shows the lower and upper limits on the profiles of total particles and solids content corresponding to all the simulations. (Note that these limiting profiles (or the various points on the profiles) *might not* necessarily belong to a single simulation, but rather to different simulations). It shows that the profile of solids content that can potentially be followed is relatively narrow, and the attainable end-point solids content lies in the range of 14.8% to 19.2%. These plots show that the rates diminish towards the end of the batch, suggesting that these reachable distributions are retained beyond the end-point of the distribution. The reachable distributions are useful in setting proper targets for the optimization problem involved in designing a recipe to achieve a target end-point distribution. Similarly, these profiles of the total particles and solids content aid in setting proper targets for the optimization problem involved in designing a recipe that tracks a particular PSD trajectory in leading to a target end-point PSD. Such a problem is presented in Chapter 6, in which the optimization problem is formulated in a multi-objective

framework. The distribution trajectory is re-cast as equivalent trajectories of nucleation and growth rates, which in turn are converted into equivalent trajectories of total particles and solids content.

5.3.2 Effect of Surfactants and Vinyl Acetate – Coagulation-free Case

The sensitivity of the results to the feed rate of VAc in the first five intervals of the batch is studied next. As before, the coagulation events are neglected. In this case, the feed rates of both the surfactant and VAc monomer were perturbed within constraints, and the simulations are performed for all combinations of feed rate values for the two reagents. Even though the distributions showed sensitivity to the feed rates of VAc, the distributions generally lie within the same overall reachable region. (The plot of the diameter ratio of the bimodal distributions alone is shown in Figure 5.15). This suggests a potential for mid-course correction, in which an error introduced by the uncertainty in the feed rate of surfactant can be corrected by manipulating the monomer feed rate and vice versa. However, it considerably enlarges the attainable limits for the solids content (Figure 5.14(b) compared with Figure 5.16(b)), more so on the lower limit. This result is in perfect agreement with the findings from the experimental studies presented previously, on the interaction between nucleation and growth, and the effects of surfactant and VAc on the process. To re-visit the scenario that was presented among the experimental results, a lower nucleation rate (caused by a lower than intended feed rate of the surfactant) would necessitate a decrease in the growth rate by reducing the monomer feed (to offset the interaction between nucleation and growth). Thus, one could manipulate the monomer feed to prevent the particles from growing to a larger size than in the target, which would be the case if no correction is made in the monomer feed. But this would result in a lower solids content.

Unlike the earlier case in which the number of particles in the smaller mode was almost always larger than the number of particles in the larger mode, in this case

there are more distributions in which that relation is violated (Figure not shown). Thus, in conditions with a low monomer feed at the early intervals, the initial surfactant loss into the monomers is lower. In this situation, a higher surfactant feed at the early times results in a larger number of particles in the primary mode, but the number of particles in the secondary mode are not necessarily higher.

5.3.3 Effect of Surfactants and Vinyl Acetate – Coagulation-inclusive Case

In the above cases, the coagulation events were assumed to be negligible, and a coagulation-free model was utilized for the simulations. But coagulation events are always present, even in the low solids regime. So, in the next case, a coagulation-inclusive model is used to study the sensitivity with respect to both VAc and surfactants. Figure 5.17 characterizes the unimodal distributions that resulted from these simulations in terms of the means and standard deviations. In this case, the distributions are completely altered. Coagulation has scattered the attainable distributions compared to the more concentrated distributions seen in the coagulation-free case, and also has considerably reduced the maximum number of particles. However, the relation of the size and spread of the distributions to the total particles is still retained. Figure 5.18 characterizes the bimodal distributions that are produced in the simulations. Here again, the scattering of the distributions along the size and the standard deviation axes is evident, and the particles cover a larger size domain in both the modes. Also, the plot of the diameter ratio of the bimodal distributions (Figure 5.19) has transformed from its rectangular form to a form that is more pointed towards the lower size end. Figure 5.20 shows the limits on the profiles of the total particles and solids content, which indicate a substantial downward shift in the upper limit on the profile of total particles, and an overall upward shift on both the limits of the profile of solids content. The range of reachable end-point solids content lies between 19% and 24%.

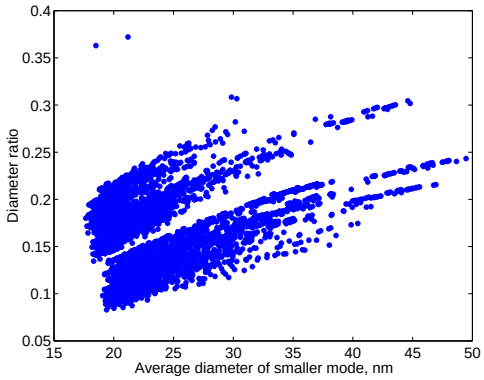

Figure 5.15: Ratio of the mean diameter of the two modes in the bimodal distributions produced with surfactant and VAc monomer as the manipulated variables, under coagulation-free conditions.

5.3.4 Effect of Surfactants and Butyl Acrylate – Coagulation-inclusive Case

In the simulation studies presented thus far, the feed rates of the surfactant and the primary monomer VAc were considered as manipulated variables. This was mainly motivated by the experimental studies, which show some complexity in the perturbations of BuA feed. However, BuA is a more reactive monomer than VAc. So, in the next case, the feeds of surfactant and BuA monomer are considered as the manipulated variables (under coagulation-inclusive conditions). In this case, the reachable regions of the bimodal distributions are not considerably altered (see Figure 5.21). Nor are the limits on the profiles of total particles changed much (Figure 5.22(a) compared with Figure 5.20(a)). But the limits on the profiles of solids content is substantially altered, with the reachable region of the end-point solids content lying between 17.5% and 29% – a considerably wider region compared to the case with surfactant and VAc as the manipulated/design variables (Figure 5.22(b) compared with Figure 5.20(b)). This is the effect of the considerably larger reactivity of BuA compared to VAc, resulting in a larger sensitivity in the growth rates, although the nucleation rates remain largely unaffected. However, since the

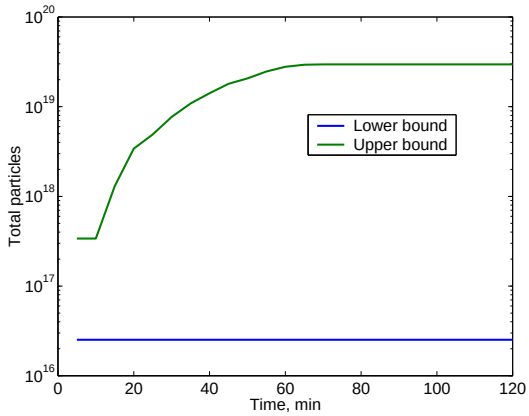

(a) profiles of total particles

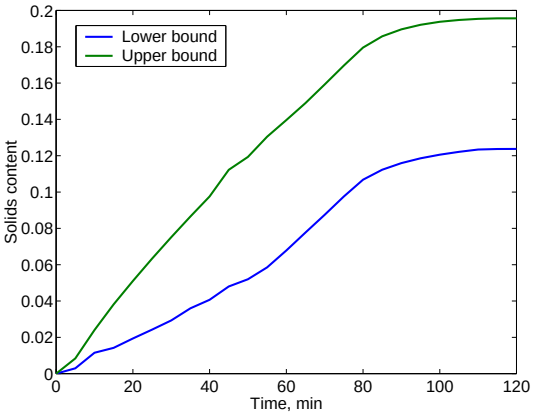

(b) profiles of solids content

Figure 5.16: Limits on the profiles of total particles and solids content, when surfactant and VAc monomer are used as the manipulated variables, under coagulation-free conditions.

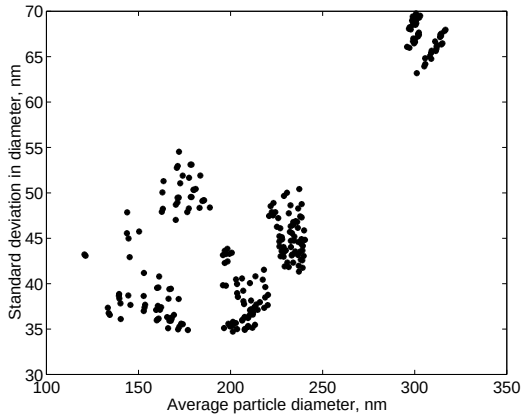

(a) standard deviation versus mean

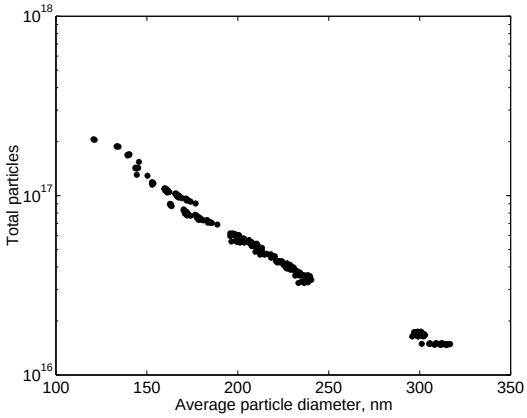

(b) total particles versus mean

Figure 5.17: The unimodal distributions produced with surfactant and VAc monomer as the manipulated variables, under coagulation-inclusive conditions.

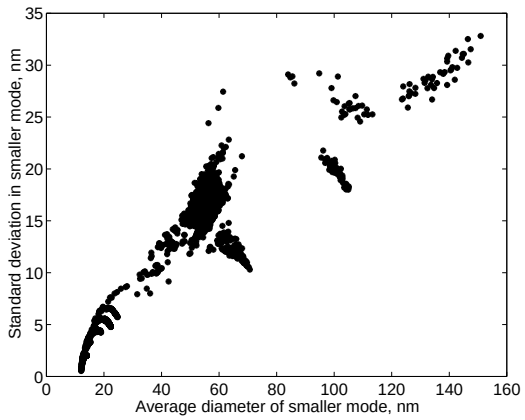

(a) standard deviation versus mean of the smaller (secondary) mode.

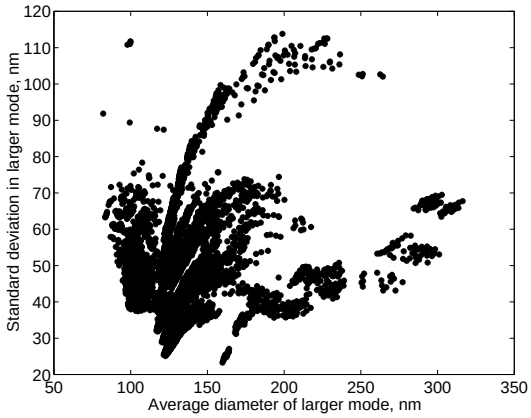

(b) standard deviation versus mean of the larger (primary) mode.

Figure 5.18: The bimodal distributions produced with surfactant and VAc monomer as the manipulated variables, under coagulation-inclusive conditions.

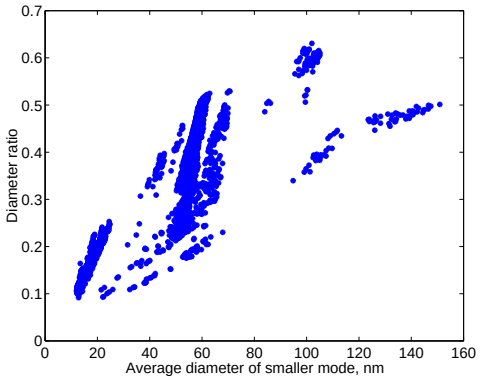

Figure 5.19: Ratio of the mean diameter of the two modes in the bimodal distributions produced with surfactant and VAc monomer as the manipulated variables, under coagulation-inclusive conditions.

complexity of the dependence of the surfactant partitioning on the composition of the monomer droplets are not incorporated into the model, care should be exercised in utilizing these results.

5.3.5 Effect of Parameterization of Inputs

The results presented thus far employed a constant time interval (11 minutes), with the feed rates held constant within each interval (zero order hold). The next result examines the sensitivity to such a parameterization of the inputs. VAc and surfactant feed are used as manipulated variables, under coagulation-inclusive conditions. The first three intervals are allowed different time durations. Simulations are performed for all combinations of feed rate values (of surfactants and VAc) and the time durations of the first three intervals. It is seen that a larger interval at early times results in very large primary nucleation rates, particularly at larger surfactant feed rates in these intervals. This deprives the system of its ability to cause a secondary nucleation event (for which it needs to breech the cmc-barrier). This clearly highlights the importance of having small enough intervals in the process in producing multi-modal distributions, particularly for open-loop optimization.

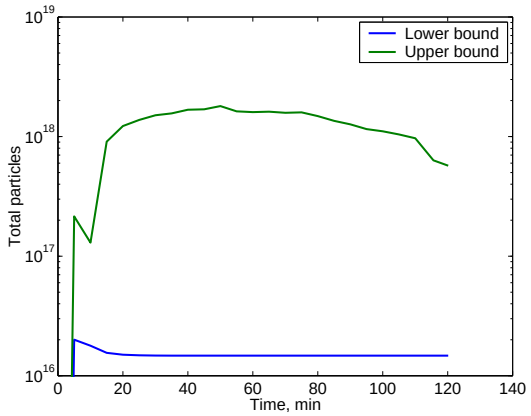

(a) profiles of total particles

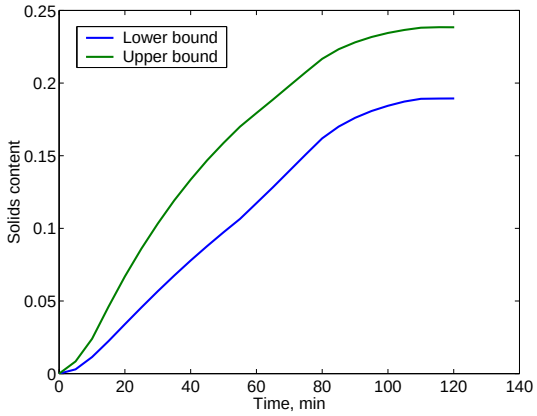

(b) profiles of solids content

Figure 5.20: Limits on the profiles of total particles and solids content, when surfactant and VAc monomer are used as the manipulated variables, under coagulation-inclusive conditions.

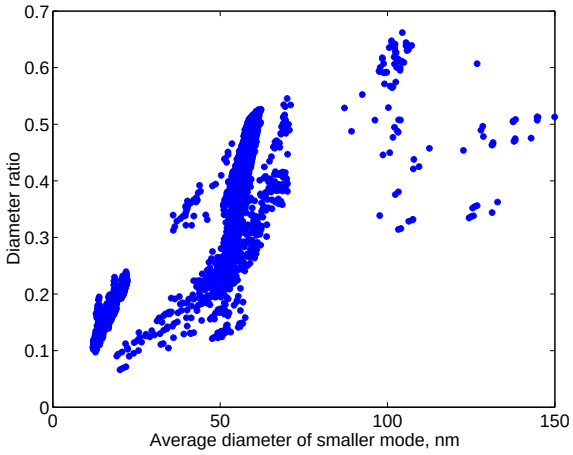

Figure 5.21: Ratio of the mean diameter of the two modes in the bimodal distributions produced with surfactant and BuA monomer as the manipulated variables, under coagulation-inclusive conditions.

Thus, one can also pose the problem of allowing the duration of the intervals as optimization variables (Biegler, 2000). The attainable solids content range (7.5% to 21%) is much wider, and also considerably different from the earlier case with VAc and surfactant feeds as manipulated variables (Figure 5.23(b) compared with Figure 5.20(b)).

5.4 Effect of Uncertainties and Disturbances on the Reachable Regions

The nominal reachability analysis of the distributions were presented in the previous section. This section presents results on the analysis of the effect of disturbances and uncertainties on these reachable distributions.

5.4.1 Effect of Early In-batch Disturbances

Figures 5.24-5.26 show results that examine the effect of an early disturbance in the process, that is rectified mid-course, on the reachable PSDs. Figure 5.24 shows the perturbed distribution relative to the nominal one, at 22 minutes in the batch. This corresponds to a time when a nucleation event is underway (as seen by the large peak of particles in the smallest end). This perturbation can arise

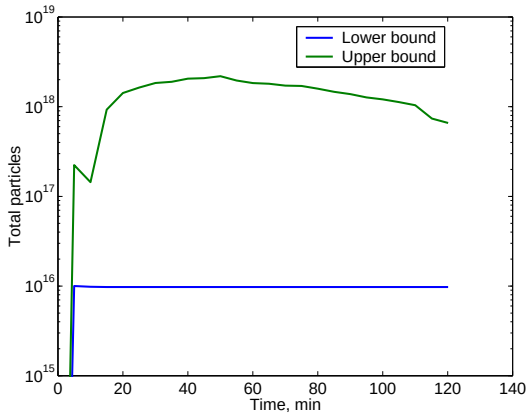

(a) profiles of total particles

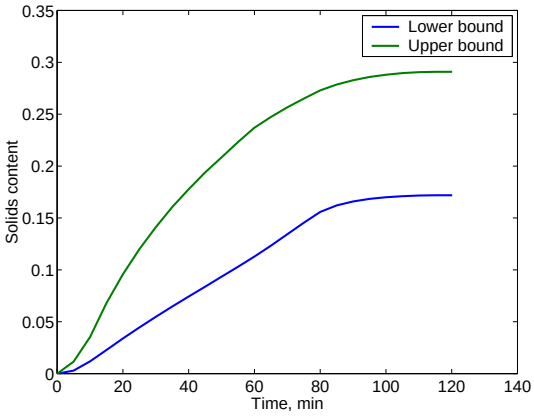

(b) profiles of solids content

Figure 5.22: Limits on the profiles of total particles and solids content, when surfactant and BuA monomer are used as the manipulated variables, under coagulation-inclusive conditions.

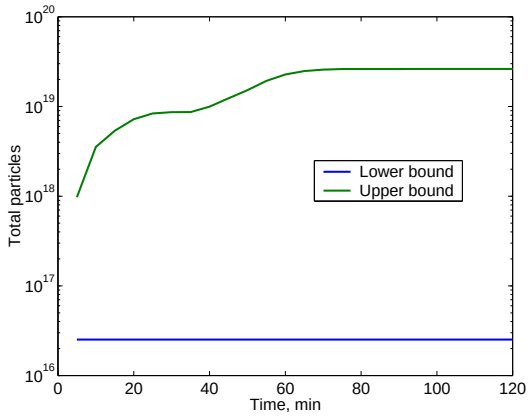

(a) profiles of total particles

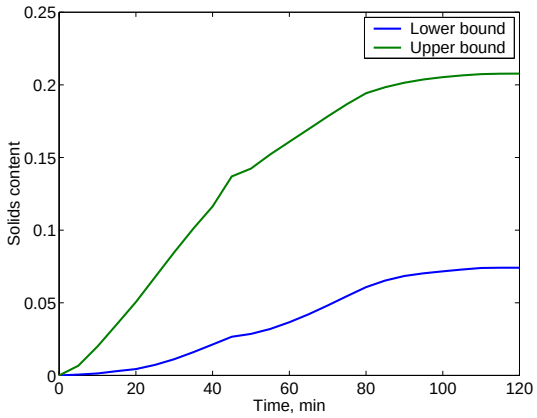

(b) profiles of solids content

Figure 5.23: Limits on the profiles of total particles and solids content, when surfactant and VAc monomer are used as the manipulated variables, under coagulation-inclusive conditions, when the duration of each interval is allowed to vary.

for several reasons, including model and parameter uncertainties, implementation errors, and shear-induced coagulation (stochastic effect). Figure 5.25(a) shows the end-point distributions that are reached in nominal case. If there are no further stochastic effects, or if the source of the uncertainty that caused the deviation in the distribution at 22 minutes has been corrected, then the resultant distributions at the end of the batch are shown in Figure 5.25(b), which shows a very profound difference when compared to Figure 5.25(a) even for such a small variation. Figure 5.26 characterizes the attainable bimodal distributions in terms of the means, standard deviations and the diameter ratio. The nominal reachable region is much more concentrated than the reachable region corresponding to the perturbed distribution. Given the convexity with respect to the inputs, one could conclude that *at least* part of the nominal region lies within the perturbed region. This region of intersection is amenable to feedback correction, while a target in the complementary region (to the perturbed region) cannot be attained after this mid-course disturbance. In the latter case, if the source of this uncertainty is a deterministic disturbance, then the best recourse is to employ a batch-to-batch control strategy (Clarke-Pringle and MacGregor, 1998). On the other hand, if it is caused by stochastic effects, then the law of averages applies, and one must design against expected variations.

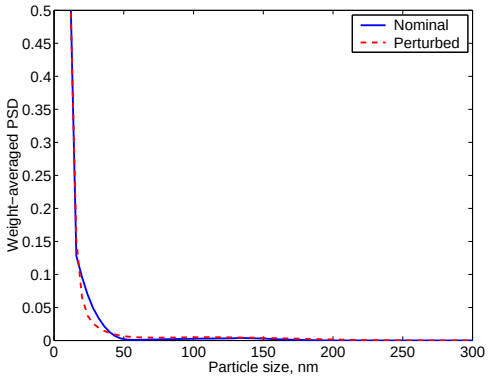

Figure 5.24: The perturbed distribution at 22 minutes into the batch, relative to the nominal distribution, due to an early disturbance in the batch.

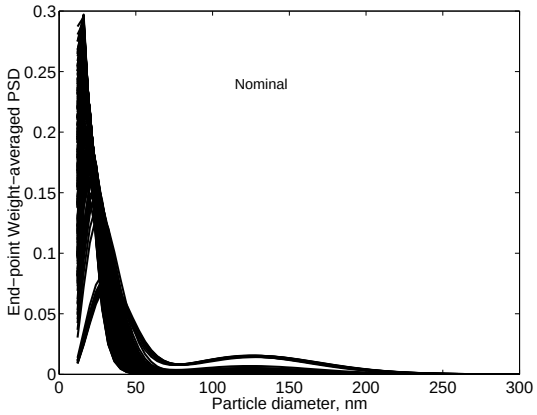

(a) end-point distributions corresponding to the nominal case

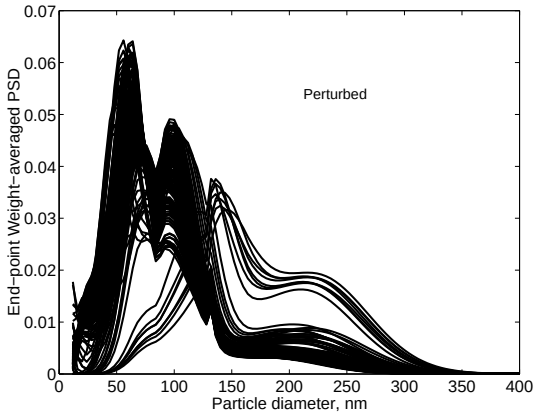

(b) end-point distributions corresponding to the perturbed case

Figure 5.25: Comparison of the end-point distributions that result in the nominal case, with those that result after the source of an early disturbance has been removed mid-course (at 22 minutes into the batch spanning 121 minutes).

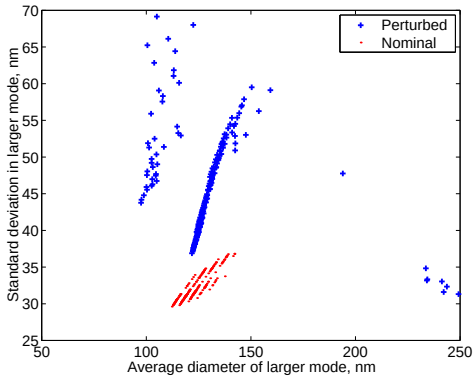

(a) comparison of the larger modes of the resultant bimodal distributions

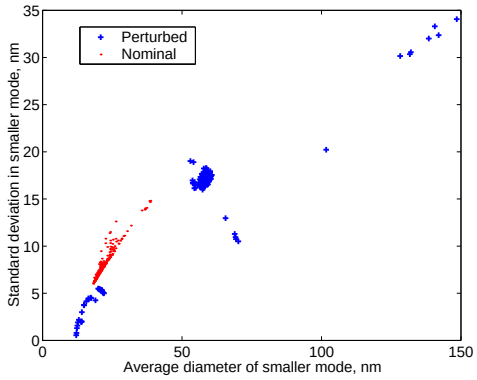

(b) comparison of the smaller modes of the resultant bimodal distributions

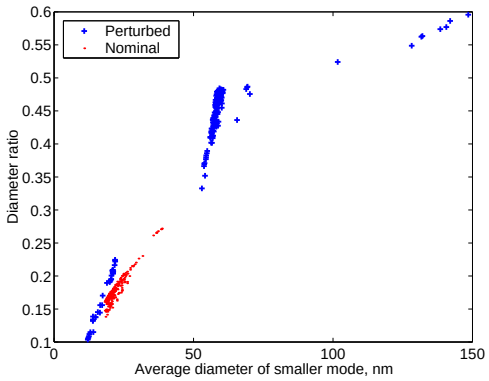

(c) comparison of the diameter ratio of the resultant bimodal distributions

Figure 5.26: Characterization of the distributions that result from the nominal case, and from the case in which the source of an early disturbance has been removed mid-course (at 22 minutes into the batch spanning 121 minutes).

5.4.2 Effect of Initial Condition Disturbance

Batch-to-batch latex carry-over is a prevalent issue in industrial practice, and its effect on the reachable distributions should be ascertained. Figures 5.27-5.29 show results that examine the effect of an uncertainty in the initial conditions on the reachable distributions. Figure 5.27 shows the initial distribution (obtained from one of the experiments), with an initial solids content of less than 0.5%. Both VAc and surfactant feeds were considered as manipulated variables, and the coagulation effects were considered. The simulations did not produce any unimodal distributions in this case, unlike in the nominal case. Although most of the nominal reachable region is covered in this perturbed case, there are other possible distributions that can be reached in the face of this uncertainty in the initial condition (particularly with respect to the secondary (smaller) mode, as seen in Figure 5.28(b)). The reason for the region of large sizes in Figure 5.28(a) is that at low surfactant feed rates at the early intervals, the initial particles prevent any primary nucleation event by taking up most of the surfactants, and also grow rapidly with the high concentration of the monomers, until the nucleation of the secondary mode. The nucleation of the secondary mode occurs earlier in these cases, accounting for the larger particles (larger than 150 nm) in the secondary mode (Figure 5.28(b)). At higher feed rates of surfactants in the initial intervals, the new particles nucleated dominate the particles in the initial batch, thereby preventing them from being evident in the end-point distribution. The implication of these results is that running a batch in open loop with pre-optimized inputs *might* result in considerable difference in the resultant distribution compared to the target. Thus one needs to employ in-batch feedback control, which can correct these errors and drive the distribution towards the target. However, even though feedback can be used to bring the distribution back to the target (as seen by the nominal region lying entirely within the perturbed region in Figure 5.28), the large particles are still present. The lower limit in the

profile of total particles is reduced (Figure 5.29(a) compared with Figure 5.20(a)), corresponding to the case of no initial nucleation in the current batch. Also, the entire lower limit on the profile of solids content is reduced relative to the nominal case (Figure 5.29(b) compared with Figure 5.20(b)). However, the upper limit essentially follows the nominal case except at the early times (where both limits are above the nominal case due to the initial particles). This again is a result that indicates that multiple manipulated variables can bring the distributions back to the target (in a relative sense), although one might have to sacrifice performance on the solids content tracking.

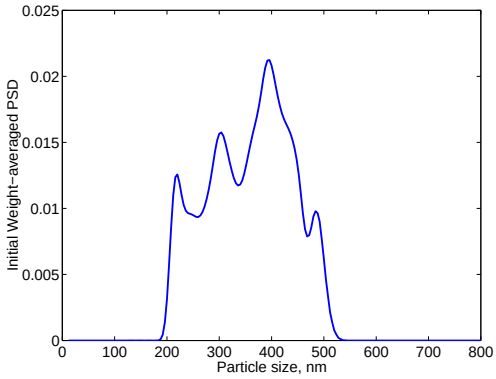

Figure 5.27: The initial distribution (due to unintended carry-over from the earlier batch).

5.4.3 Effect of Large Initial Disturbance/Seed

Figures 5.30-5.33 present results that examine the effect of a larger mass of initial particles but with a much reduced particle sizes and a narrower distribution. This initial distribution is shown in Figure 5.30. This case can be considered as a larger initial disturbance with over 1% solids content, or as seeded emulsion polymerization. In this case, unimodal distributions do result, which predominently pertain to a combination of the initial seed along with the particles nucleated at the early time intervals. Figure 5.31 compares the reachable unimodal distributions with the

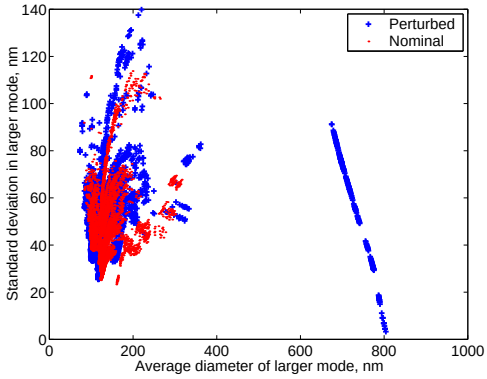

(a) comparison of the larger modes of the resultant bimodal distributions

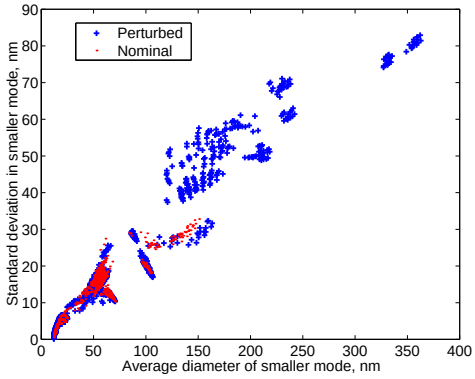

(b) comparison of the smaller modes of the resultant bimodal distributions

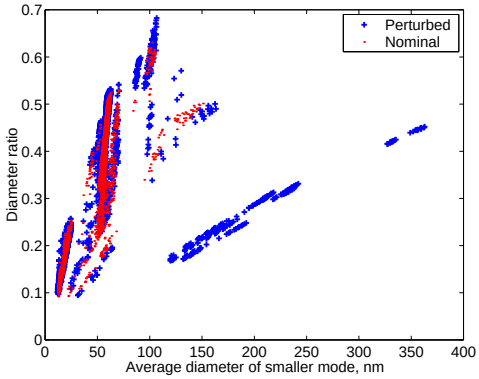

(c) comparison of the diameter ratio of the resultant bimodal distributions

Figure 5.28: Effect of the initial distribution (of small mass) on the reachable distributions.

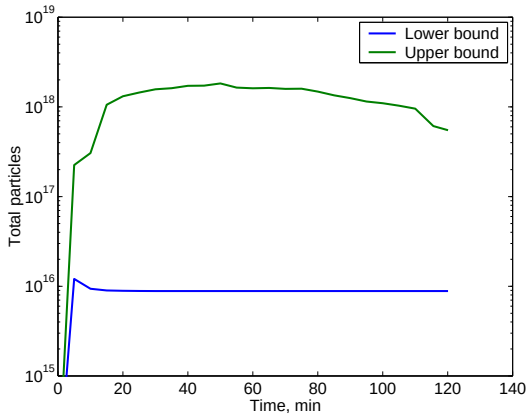

(a) profiles of total particles

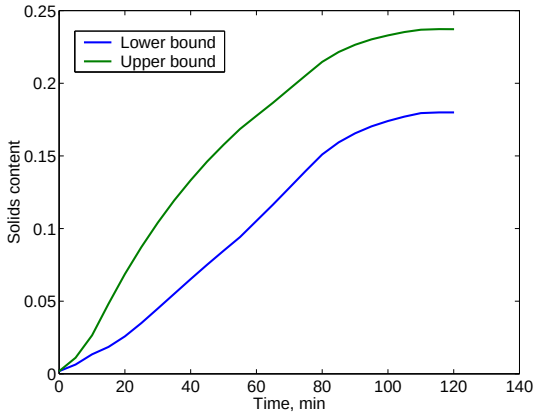

(b) profiles of solids content

Figure 5.29: The limits of the attainable profiles of total particles and solids content in the face of the uncertainty in the initial distribution.

nominal (*ab initio*) case presented earlier — with surfactant and VAc as manipulated variables under coagulation-inclusive conditions. The large size particles seen at low number of total particles (less than 4×10^{16}) in the nominal case, which correspond to recipe with low surfactant feed rates throughout, are not present in the current case (Figure 5.31(b)). But the seed particles add to the nucleated particles, thereby causing a reduced growth rates and reduced particle sizes. Figure 5.32 compares the reachable bimodal distributions, which indicates an inverse effect from what was seen in the previous case with a lower mass of initial particles. In the current case, the perturbed distributions cover a smaller domain than the nominal case. Thus, in-batch feedback has a limited utility in this case. For example, very large sizes of the larger mode is again not possible (Figure 5.32(a)) (as was observed in the case of the unimodal distributions). The distributions with very large sizes in the larger mode (larger than 250 nm - Figure 5.32(a)) seen in the nominal case correspond to low surfactant feed rates in the early intervals and larger feed rates at the later intervals. The particles with the larger size range in the smaller mode (above 80 nm in Figure 5.32(b)) are also not possible due to the cascaded effect of the seed and growth on the nucleation event. The lower limit on the profile of total particles is substantially increased (Figure 5.33(a) compared with Figure 5.20(a)) – the drop around 15 minutes corresponding to a coagulation event. But both the lower and upper limits of the profiles of solids content are shifted upward compared to the nominal case (Figure 5.33(b) compared with Figure 5.20(b)).

5.5 Summary

The sensitivities in the process of the evolution of PSD in semi-batch emulsion co-polymerization using non-ionic surfactants were studied via experiments and simulations. The experimental studies indicate the following:

- The need for multiple process inputs for the control of PSD.

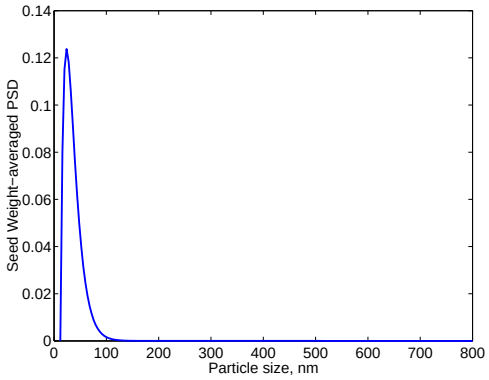

Figure 5.30: The initial PSD, corresponding to a larger mass of initial seed.

- Surfactant and at least one monomer (in this case the primary monomer VAc) as the manipulated variables, particularly when employing non-ionic surfactants.

- The suitability of a hierarchical control strategy, in which the individual rates of nucleation, growth and coagulation are controlled to produce the desired complete distribution.

- The need for employing the detailed first-principle model for the open-loop and closed-loop control of PSD.

- Irreversibility in several aspects of the process – while some of these such as the skewness of the distributions may not be critical depending upon the end-use applications, others such as the effect of a larger growth rate or a stronger coagulation rate might leave an intolerable deviation in the distribution.

- Inherent limitations within the process that restrict the type of distributions that can be produced, for example the size-dependent growth phenomenon and the lack of inputs to manipulate it.

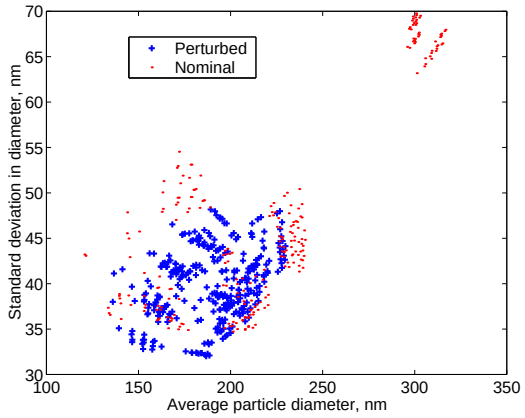

(a) standard deviation versus mean

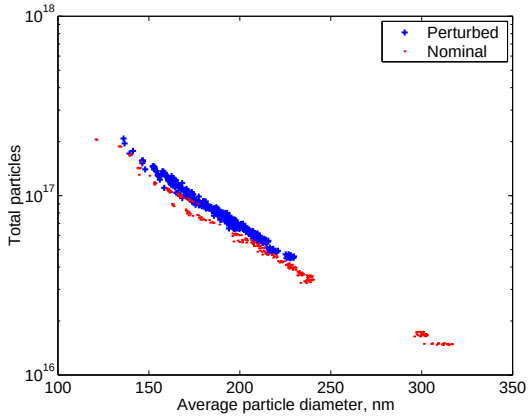

(b) total particles versus mean

Figure 5.31: Comparison of the unimodal distributions that are produced in the current seeded case with those produced in the nominal (*ab initio*) case.

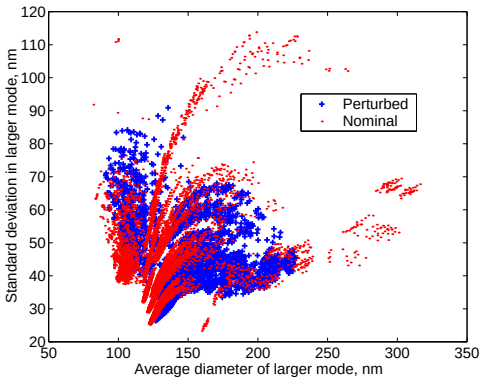

(a) comparison of the larger modes of the resultant bimodal distributions

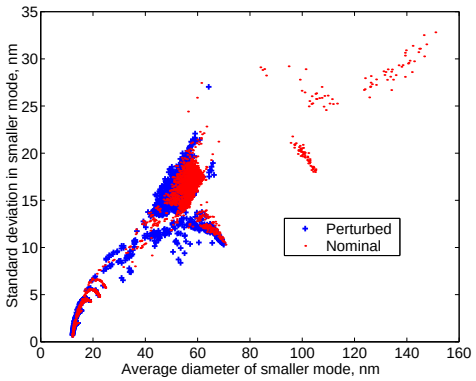

(b) comparison of the smaller modes of the resultant bimodal distributions

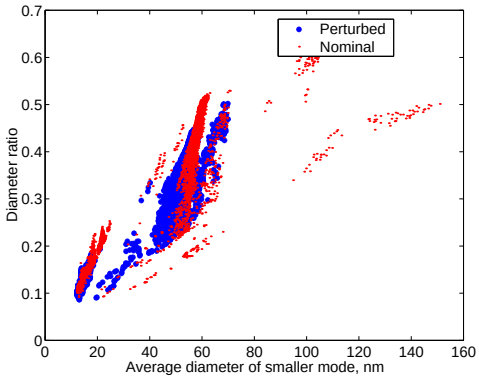

(c) comparison of the diameter ratio of the resultant bimodal distributions

Figure 5.32: Comparison of the bimodal distributions that are produced in the current seeded case with those produced in the nominal (*ab initio*) case.

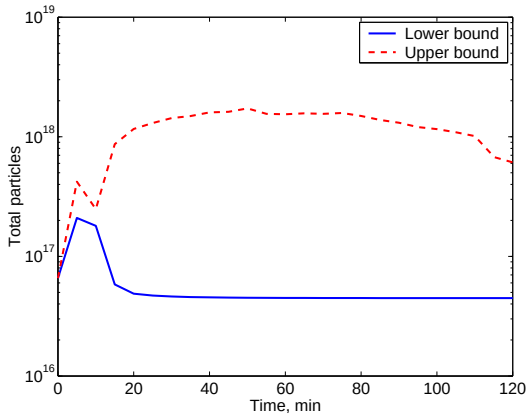

(a) profiles of total particles

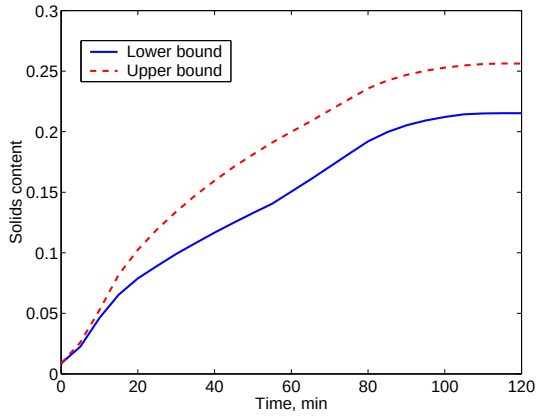

(b) profiles of solids content

Figure 5.33: Limits on the reachable profiles of total particles and solids content, given the initial seed of particles.

- The limitations in the process that in some cases translate into lower solids content (and hence have a bearing on the economy of the process), in employing feedback to correct the correctable errors in the distribution.

The simulation studies were used to gain further insights into the potentials and limitations in the process, and to determine the type of distributions that can actually be produced considering system and external limitations. A controllability analysis based on a linearized model is unsuitable due to the discontinuity in the process, and its highly nonlinear character. A rigorous mathematical analysis of the reachability and controllability is also beyond the reach of this process, due to the underlying complexity. Thus, a simple simulation-based analysis was performed. The study gave insight into the restrictions on the types of distributions that can be produced, and also revealed the effect on these restrictions under different control configurations. Also, the study identified the types of exactly reachable distributions (currently restricted to a low solids regime). Key aspects of the distributions (such as the mean diameter ratio of bimodal distributions) were found to have a convex and monotonic (though nonlinear) dependence on the inputs. Reachability domains can be inferred from these reachable points based on this observation. A particular discretization of the inputs along the batch, and a fixed reaction time were considered in this study. Relaxation of these restrictions were examined. These gave further insight into the optimization and control of PSD.

Further, the effect of uncertainties and disturbances on the reachable distributions were analyzed. The results reveal two different scenarios:

- One in which an open-loop operation is deleterious, and in-batch feedback control is essential and feasible.

- Another in which in-batch feedback control might not be effective in correcting the errors.

Some of these analyses were based on a mid-course disturbance detection and correction. Others were based on the assumption that the initial condition disturbances are detected very early in the batch. In the latter case, the early detectibility adds another layer of constraints to the feedback capabilities, which will be addressed in the next chapter. These situations advocate a combination of in-batch and batch-to-batch feedback control strategy for the control of PSD in semi-batch emulsion polymerization.

Chapter 6

OPEN-LOOP AND FEEDBACK CONTROL STUDIES

6.1 Introduction

In this chapter, model-based optimization and control studies for the full PSD are presented. Genetic Algorithm (GA), a global optimization technique based on direct optimization, is employed. The sensitivity results from Chapter 5 are exploited in formulating these problems. First, optimization studies based on a straightforward formulation of the problem is presented. The implementation of the optimal feed policies in the experimental facility is discussed. Next, a novel hierarchical strategy is proposed to overcome some of the limitations with direct control of PSD. Experimental implementation of these optimal recipes are also presented. This is followed by an evaluation of the effectiveness of in-batch feedback to correct the discrepancies introduced by the unavoidable disturbances and uncertainties. This involves the evaluation of several state/parameter estimation strategies, and a determination of the requirements for successful state estimation. These strategies are employed in off-line feedback calculations, to investigate their effectiveness. This effectiveness analysis is motivated by the delayed and sparse measurements, the irreversibilities in the process, and clear indications in the sensitivity results of Chapter 5.4, and also in other studies (Wang and Doyle III, 2002) of possible cases in which in-batch on-line feedback would not be able to rectify a discrepancy in the distribution. The importance of state estimation in these feedback calculations is evinced.

6.2 Optimization of the Feed Profiles using a Genetic Algorithm

A Genetic Algorithm (GA) is utilized to perform the optimization. The GA is a conceptually-simple and easy-to-program global optimization technique (Goldberg, 1989). It is a facilitated random search technique, which exploits the supposed understanding of the genetic evolution phenomena to find an optimal solution of a given problem. In most cases, GA can determine (arbitrarily closely) the global optimum of non-convex optimization problems. One starts with a generation containing N_{pop} randomly-generated members. The "fitness" of the N_{pop} members of the generation is determined based on the desired objective. The population is reproduced into the next generation in proportion to the fitness of its members, emulating the concept of the survival of the fittest. The members of the new population are allowed to cross-over and mutate subject to certain probabilities. The cross-over and mutation operations drive the members downhill towards the optimal solution, and also introduce a globality into the solution. The processes of selection, cross-over, and mutation are repeated over several generations to arrive at one or more optimal solutions.

In addition to its straightforward formulation, the GA does not require the calculation of gradients and Hessian matrices, which are required for formal optimization schemes. Also, it provides a global solution with the right choice of parameters (defined subsequently), while globality in the gradient-based schemes is tied to the convexity of the feasible region. Crowley *et al.* (2000) found that the solution obtained by gradient-based techniques depends on the initial guess, suggesting that these PSD optimization problems could be non-convex. However, unlike gradient-based techniques, the GA provides only a sub-optimal solution (or requires several generations to provide the accurate solution) and hence might be complemented with a local optimization technique. The GA has found application

in several interesting chemical engineering problems including polymerization applications (Bhaskar et al., 2000), hydrogen reforming reactors (Rajesh et al., 2001) and in on-line applications for the maximization of cell mass in bioreactors (Na et al., 2001).

In formulating the optimization problem, the duration of the batch is divided into 11 equal intervals, each spanning 11 minutes (PSD measurement frequency). The feed rate of each reagent is held constant in each interval. The value of the feed rate in each interval is the decision variable to be determined by the optimizer. The algorithm is initialized with the first generation containing N_{pop} randomly-generated members. Each member of the population is characterized by a set of chromosomes, one each for each decision variable. The chromosomes are represented as binary digits of length l_{chrome}. These binary digits are generated using a random-number generator for the first generation. The chromosomal information is translated into feed rates employing the following linear interpolation:

$$\frac{u_i - u_{min}}{u_{max} - u_{min}} = \frac{\sum_{k=1}^{l_{chrome}} u_{bk} 2^{k-1}}{\sum_{k=1}^{l_{chrome}} 2^{k-1}} \tag{6.1}$$

where u_i is the reagent feed rate in interval i, u_{min} and u_{max} account for the range of values for the input and u_{bk} is the binary value of the string at position k. Each member of the population (with a particular set of values for the decision variables) are simulated using the process model, and the objective function value for each member is determined. The objective (θ) is defined to meet the target PSD in some sense – number-averaged, weight-averaged; 2-norm; min-max *etc.* While the constraints on the inputs are explicitly met in the formulation (Equation (6.1)), the constraints on the outputs are added as penalties to the objective function θ (soft constraints). The penalty for any constraint $c_{min} < c < c_{max}$ is defined as (Rajesh et al., 2001):

$$penalty = (c - c_{max}) + |c - c_{max}| - (c - c_{min}) + |c - c_{min}| \tag{6.2}$$

Whenever a constraint is violated, the penalty takes a non-zero value. Thus, the combined objective function θ_i^{comb} for the i^{th} member is defined as the weighted sum of θ^i and the penalty terms. Once the values of θ_i^{comb} for all $i = 1, ...N_{pop}$ are determined, the fitness of each member of the population is calculated as:

$$fit_i = \theta_{ref} - \theta_i^{comb}, \tag{6.3}$$

where $\theta_{ref} = (\overset{max}{i} \quad \theta_i^{comb}) \times \omega$. Here, ω is a factor greater than unity, introduced to provide a non-zero fitness to the member with the highest objective function value. Each member is reproduced with probability $\frac{fit_i}{\sum_{j=1}^{N_{pop}} fit_j}$ into the next generation, based on a random integer number between 0 and 100. A series of numbers $m_i, i = 1, ...N_{pop}$ are defined as $m_1 = Round[\frac{fit_1}{\sum_{j=1}^{N_{pop}} fit_j} * 100]$ and $m_i = m_{i-1} + Round[\frac{fit_i}{\sum_{j=1}^{N_{pop}} fit_j} * 100], i = 2, ...N_{pop}$. N_{pop} random numbers are generated. If the j^{th} random number lies between m_{i-1} and m_i, then the i^{th} member of the previous generation becomes the j^{th} member of the current generation. Thus, the members are reproduced into the next generation in proportion to their fitness.

The new members are crossed with each other in pairs ('i' and '$i+1$', $i = 1, 3, 5...$), subject to a probability p_{cross}. During the cross-over operation of two members, a certain location of the chromosome is determined at random and each of the chromosomes (binary numbers) of the two members are swapped after this location. Similarly, the members of the population are subjected to a mutation operation based on a small probability, p_{mut}. In this operation, a random location of the chromosome between 1 and l_{chrome} is flipped from 1 to 0 or vice versa. The resultant new generation is simulated again, and the objective function values and fitnesses of its members are determined. The cross-over and mutation operations introduce both uphill and downhill variations into the generation. While the uphill moves ensure globality, the downhill moves drive the solutions towards the optima. However, if the uphill change results in a member with very low fitness, that member gets rejected during the selection process. These operations are carried out for a

certain number of generations, N_{gen}. The optimal solutions obtained at the end of these generations are pointers to the global optimum, and can potentially be refined using local optimization methods.

The parameter values employed in this study are: $N_{gen} = 8$, $N_{pop} = 17$, $l_{chrome} = 24$, $\omega = 1.2$, $p_{cross} = 0.7$, and $p_{mut} = 0.001$.

6.3 Results and Discussion

The target PSD is generated by simulating a target recipe, which is designed taking into consideration certain industrially-relevant factors, while also simultaneously ensuring a challenging distribution as the target for the optimizer to attain. The ratio of the surfactant to the total monomer used in the recipe are commensurate to those used in industrial practice, thereby validating the target PSD. In industrial practice, a typical batch spans between 2-7 hours. This study is restricted to a 2 hour batch and a low solids content to minimize the artifacts of coagulation. This regime of low solids is existent in all experimental batches and thus supports the theoretical framework. The target PSD is a bimodal distribution, which has almost comparable mass in both the modes, but the number of particles in the smaller size mode is over an order of magnitude higher than in the larger size mode. Thus, the choice of objective function is critical.

6.3.1 Case 1 – Optimization of the Surfactant Feed

In the first set of the results described here, the surfactant feed rate is used as the sole decision variable, and the feed rates of the monomers and the initiator components are fixed a priori. Furthermore, the feed of surfactant is completed mid-course. This is done to prevent the distribution from wandering from the target distribution after the target end time, as discussed by Crowley *et al.* (2000). Although surfactant might be needed for particle stabilization beyond this point, it would be made available by depleting droplets as well as by the particles, as they

shrink with the consumption of the monomers. Thus, in this case, there were 5 decision variables, the feed rates of the surfactant solution in the first 5 intervals. In the GA, one need not provide an initial guess, but only provide a range of values for the decision variables (u_{min} and u_{max} in Equation (6.1)). It proceeds from these to a solution which is potentially globally-optimal, as mentioned previously. Even though the values of u_{min} and u_{max} could be set as the pump limits, the number of generations required for convergence can be substantially reduced by providing a narrower range. In providing the range of input values for the various variables, the feed rate of the surfactant solution in the first interval is restricted to lie between relatively low values of 3×10^{-4} to 5×10^{-4} moles/s. In the second interval, the feed rate is restricted to take values between 1.5×10^{-3} and 2.3×10^{-3} moles/s, while for the next three intervals, the feed rate is restricted between 0.8×10^{-3} and 1.7×10^{-3} moles/s. The rational behind this choice is as follows: in producing a multi-modal distribution, there is an upper bound on the primary nucleation event, to enable effecting a secondary nucleation event at the required time during the batch. This is to preclude the event of not being possible to exceed the cmc-barrier essential to cause secondary micellar nucleation, due to the constraints in the surfactant feed. Once the nucleation events are complete, the surfactant feed could be maintained at a level just sufficient to provide adequate surface coverage. Towards the end of the batch, as the monomer swelling the particles are being depleted, no surfactant feed may be needed. The objective function was set as the 2-norm of the error in matching the absolute PSD at the end of the batch to the absolute target PSD, *i.e.,*

$$\theta^i = \int_{r_{nuc}}^{r_{max}} (F(r, t_f) - F_{ref}(r))^2 dr, \tag{6.4}$$

where θ^i is the objective function value for the i^{th} member of the population, $F(r, t_f)dr$ is the particle density at the end time for the i^{th} member, and $F_{ref}(r)$ denotes the target PSD. It is desired to achieve an appreciable solids content in the latex, and also an appreciable conversion of the monomers. Since the feed rate and

the total amount of the monomers are fixed, a single constraint on the solids content would ensure both the requirements. The solids content was required to lie between 15% and 25%. In addition, there was a constraint on the total amount of surfactant fed to the batch, in order to maintain the proportion of the surfactant to the total monomer within a prescribed range. Figure 6.1(a) shows the value of the objective function for each member of the population for each of the eight generations, and Figure 6.1(b) shows the minimum objective function value in each generation. From Figure 6.1(b), it is seen that the solution converges to the near-optimal value within 3-4 generations. Interestingly, the slightly better solution obtained in Generation # 5 is lost in the selection process, and the optimizer settles at a relatively sub-optimal solution. One could retrieve the lost solution and provide it as the initial guess of a local optimization scheme. Figure 6.2 shows the end-point PSD corresponding to the successful members in Generations 1 and 8. Even though the initial random input generates a wide range of PSDs, the last generation shows the solutions converge near the target (dashed line).

Figure 6.3 shows the sub-optimal input profile and the resultant PSD. The dashed lines in these plots show the target PSD and the original recipe that was used to generate the target PSD. Providing this PSD as the target for the optimizer has the advantages that the distribution is known to be reachable and that the optimal solution is also known a priori. There is an acceptable match between the target and the sub-optimal result, even though the objective function was based on absolute PSD tracking. Also, none of the constraints were violated. Figure 6.4 compares the total number of particles as it evolves during the batch for the case of the original input and the solution. The tight correspondence in these plots also highlights the possibility of multiple solutions. In generating these solutions, the upper limit set for the feed rate of the surfactant in the first interval (5×10^{-4}) is lower than the value used in generating the target (5.16×10^{-4}) – which occurence is quite

possible in actual practice, where the target recipe is unknown. Due to this reason, the predicted input for the second and third intervals is lower than in the original input, to maintain the relative proportion of the two modes. Fortunately, there is no appreciable effect on the growth rates, and the particle sizes match between the target and the solution, causing the solids content to be within acceptable levels. It should be noted that the surfactant feed rate over the rest of the batch has no effect on particle nucleation. This explains the observed difference between the sub-optimal and original feed rates corresponding to the other two intervals. If the surface coverage of the particles or some other surfactant-related variable is to be matched, then the optimizer could potentially match the feed rates of surfactant in these later intervals with the target feed rate values.

6.3.2 Case 2 – Optimization of the Surfactant and Monomer Feed

In the second case study, the feed rates of both the surfactant solution and VAc monomer are used as degrees of freedom, with the feed rate of BuA fixed. The feed rate of VAc in the first interval was left at the same value as in the original recipe, while its value in the last three intervals was set to zero, so as to bring the polymerization to completion at the end of the batch and prevent the PSD from moving away from the target after this time. The feed rate in the remaining 7 intervals were to be determined by the optimizer, along with the values of the feed rate of surfactant in the first 5 intervals (12 decision variables). The range set for the possible values of VAc feed rate in the early intervals was below the value used in the original recipe. Again the objective was to match the absolute distribution as in Equation (6.4). In addition to the 2 constraints on the solids content and the total amount of surfactant, a third constraint on the total amount of VAc was also incorporated into the formulation this time.

Figure 6.5 compares the sub-optimal feed rates of surfactant and VAc generated by the optimizer with the original recipe. In this case, none of the 3 constraints

were violated. The above optimal recipe was implemented in the experimental facility. Figures 6.6(a) and 6.6(b) show the evolution of the experimental and simulated PSD for this recipe. At the outset, the trends look similar between the two plots. But the experimental plot shows some very large particles (between 200 and 500 nm) at initial times. This touches upon the issue of batch-to-batch carryover that was discussed in Chapter 5, and is prevalent in industrial practice. Even though the reactor systems used to prepare the emulsions are washed after every batch, a thorough caustic cooking is performed only periodically. So, the pipelines and the vessels themselves have some residual latex from earlier batches. Emulating this industrial practice, the laboratory reactor was thoroughly cleaned before conducting the experiment; however the tubing was only rinsed with DI water. This results in the carry-over of small amounts of large particles from previous batches to the current batch. These particles in the initial batch consume some early surfactant, resulting in a delayed, but stronger and more persistent micellar nucleation at about 6 minutes, and hence a very late secondary micellar nucleation after 95 minutes. On the other hand, the simulation result in Figure 6.6(b) shows a rapid initial micellar nucleation resulting in a narrow peak, which later becomes diffuse with growth. Also, the secondary micellar nucleation occurs much earlier – at about 25 minutes – due to the accumulation of the surfactant fed during the second interval.

Figures 6.7(a) and 6.7(b) compare the end-point PSD corresponding to the sub-optimal recipe, as observed experimentally and as predicted by the simulation. The target PSD is also shown. The objective of matching the absolute PSD is not perfect, as seen by the large mismatch in the weight-averaged PSD. The reason for this can be seen in Figure 6.8, which plots the total number of particles between the original recipe and the sub-optimal recipe (simulation-based). The number of particles nucleated initially is much lower in the sub-optimal case, resulting in a larger growth rate initially (a high concentration of the monomers inside the

particles and larger number of radicals/particle), and in turn resulting in the larger mode being larger than in the target. This result highlights an opportunity for mid-course correction. If this discrepancy in the larger mode is predicted earlier, then the nucleation of the second mode has to be reduced to preserve the relative magnitude of the peaks (to control the relative distribution), but the timing of the secondary nucleation has to be advanced to match the sizes, and hence preserve the shape of the distribution. Monomer feed rate would also have to be recruited to obtain acceptable conversion levels. (Recruiting the feed rate of DI water might result in rendering the absolute PSD controllable too). So, a mid-course correction strategy at a fixed time with surfactant as the only input (Flores-Cerrillo and MacGregor, 2002) might not be the best strategy in all cases, although it definitely is a straightforward approach. The larger mode in the experimental result falls in the same range as the target because of the disturbance from earlier batches, which resulted in a stronger (and delayed) primary micellar nucleation, and hence reduced growth rates and smaller size particles.

Figure 6.9 shows the solids content profile for this case. While the simulation predicts a solids content close to 20% at the end of the batch for this recipe, the experimentally obtained solids content is 16%. The constraint set on the solids content was between 15% and 25%. Figure 6.10 shows the rate of reaction of the two monomers (simulation-based). For most parts of the batch, the ratio of the reaction rate of VAc to BuA is a constant, suggesting that the composition of the copolymer is a near constant in the batch. Also, the rate of reaction goes to zero towards the end of the batch, ensuring that the distribution does not deviate from the one corresponding to 121 minutes.

The input profiles and the end-point PSD corresponding to all the members of each generation in this off-line study are archived. This enables one to re-analyze the data and determine the best among them to match a different objective than the

one specified to the optimizer. For example, one can pick out the member among these members that gives the best match to the weight-averaged PSD. However, this best recipe need not be an optimal one. Figure 6.11 shows the recipe which gives the best match to the weight-averaged PSD (gives the least error in a min-max formulation between the two modes). While this batch met the constraints on the solids content and the total amount of surfactant fed, it violated the constraint on the total amount of VAc. It utilized about 6.75% less VAc than the allowable limit (which implies a higher conversion level as the solids content is within limits). Figures 6.12(a) and 6.12(b) compare the number-averaged and weight-averaged PSD for this recipe (experimental and simulation) with the target PSD. The match between the simulation and the target is good in both the plots, although the experimental results show differences, attributed mainly to the mis-match between the nominal model and the process. A close scrutiny of the experimental results showing the evolution of PSD (Figure 6.13) shows that there is an initial rapid nucleation as seen by the narrow distribution (narrower than in the previous experimental plot), which broadens with growth. Early in the process (at approximately 16 minutes), a shoulder appears in the distribution, which is a signature of coagulation (not accounted for in the nominal model). The secondary nucleation occurs much earlier in this case, at around 40 minutes, and is also stronger relative to the previous experimental result. Figure 6.14 shows a good match of the total number of particles as it evolves in the batch – and hence the nucleation rates– between the "best" recipe and the original recipe. Figure 6.15 compares the solids content for this case. The end-point solids content is within the constraints in both the cases, although it is lower in the experimental case by about 2% relative to the simulation case. The experimental results show a slight drop in the growth rate (slope of the solids content plot) at about 16 minutes, corresponding to the appearance of the shoulder in the distribution. This could be due to the sudden decrease in the average number

of radicals per particle, and possibly the concentration of the monomers, accompanying the coagulation event. The reaction rates diminish at the end of the batch, ensuring the stability of the distribution beyond this point.

From the perspective of on-line control, the splitting of the larger mode, even if detected early in the batch, cannot be rectified externally. This necessitates an explicit accounting of coagulation – both, that induced by inter-particle forces and that induced by shear forces – in the model used by the optimizer. Alternatively, precautions need to be taken to minimize coagulation. One could set a constraint on the fractional surface coverage of the particles by surfactants. However, under excessive shear in the reactor due to mixing, sufficient surface coverage does not guarantee colloidal stability.

Figure 6.16 presents the sub-optimal results generated by GA to match the weight-averaged PSD, *i.e.* $\theta^i = \int_{r_{nuc}}^{r_{max}} (W(r,t_f) - W_{ref}(r))^2 dr$, where the weight-averaged distribution is defined as $W(r,t) = \frac{r^3 F(r,t)}{\int_{r_{nuc}}^{r_{max}} r^3 F(r,t) dr}$ (a new optimization run). An additional constraint on the surface coverage for the post-nucleation regime was set as $1.5 < K_{ad} S_w < 9$, where K_{ad} is the adsorption equilibrium constant for surfactants onto the particle surface, and S_w is the free surfactant concentration in the aqueous phase. This translates into a fractional surface coverage between 0.6 and 0.9. As seen in the comparison of the target and the sub-optimal PSD (Figure 6.16(b)), the match of the larger mode is relatively better than the match of the smaller mode. None of the four constraints were violated by this recipe. To better the sub-optimal result, a min-max formulation was considered, with explicit accounting of the errors in matching the two modes. It was sought to optimize the maximum of the two errors. Figure 6.17 compares the sub-optimal results generated using GA in a min-max formulation, on a weight-average and 2-norm basis. Thus, θ^i is defined as:

$$\theta^i = max \left(\int_{r_{nuc}}^{r_1} (W(r,t_f) - W_{ref}(r))^2 dr, \quad \int_{r_1}^{r_{max}} (W(r,t_f) - W_{ref}(r))^2 dr \right), \quad (6.5)$$

where r_1 was chosen as 75 nm. In this case again, there was a 17% violation of the constraint on total VAc (on the lower side - hence a higher conversion level). Even though the match between the target and the sub-optimal distributions is reasonable, refinement might be possible using a gradient-based technique.

6.4 Multi-Objective Formulation

In this work, bimodal targets with clearly separated modes are of interest, characterized by complex relations in terms of the number of particles in the two modes and the mass of the particles in the two modes. These distributions are not captured adequately by any straightforward objective function, as was seen in the previous results. The choice of a proper objective function to capture all aspects of the distribution is a difficult task, and usually varies from target to target. A strategy is presented next to redress this issue, which employs the hierarchical strategy proposed in Chapter 5. The sensitivity studies presented in Chapter 5 suggest the benefit of regulating the nucleation, growth and coagulation processes separately, and hence controlling the PSD in a hierarchical framework. An advantage in this framework is that it is applicable to all types of target distributions. Another advantage is that it facilitates the tracking of a target PSD trajectory along the course of the batch – say, to guide the distribution to the target along a path that avoids problematic regimes, or to monitor the evolution of the distribution and decide upon the appropriate feedback measure. Figure 6.18 depicts the proposed hierarchical strategy. As observed in the previous section, coagulation is one of the most important sources of irreversibility, and it is more difficult to manipulate coagulation to shape the distribution in emulsion polymerization. Thus, it is advisable to minimize coagulation to the extent possible. In following the trajectory of nucleation and growth, the idea of the control of instantaneous properties can be utilized (Kozub and MacGregor, 1992a; Saldivar and Ray, 1997; Urretabizkaia et al., 1992). Exploiting this

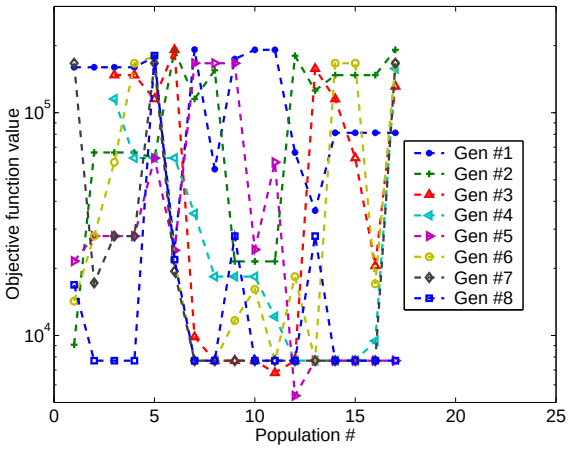

(a) objective function value for the members of each generation

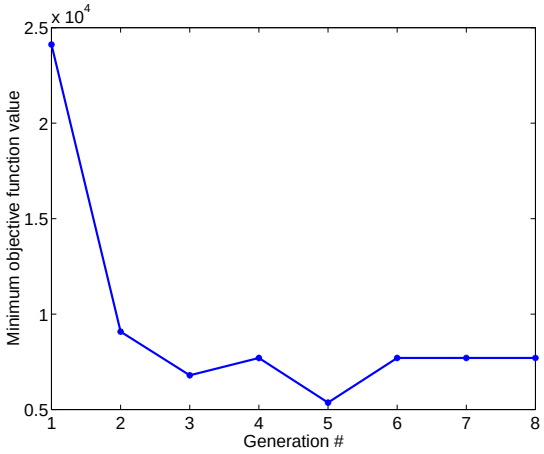

(b) objective function value of the best member of each generation

Figure 6.1: Objective function values of the members as they evolve through the generations to an optimal population.

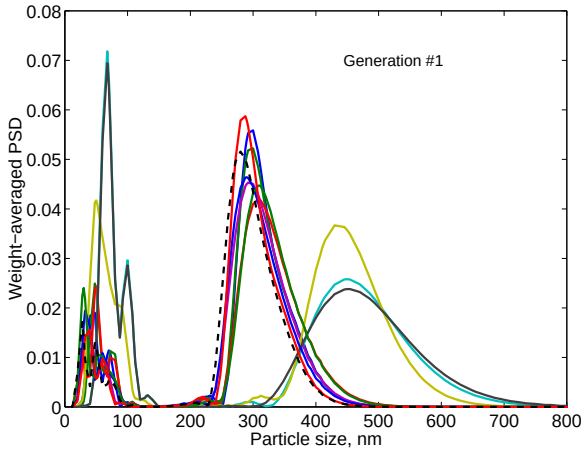

(a) first generation

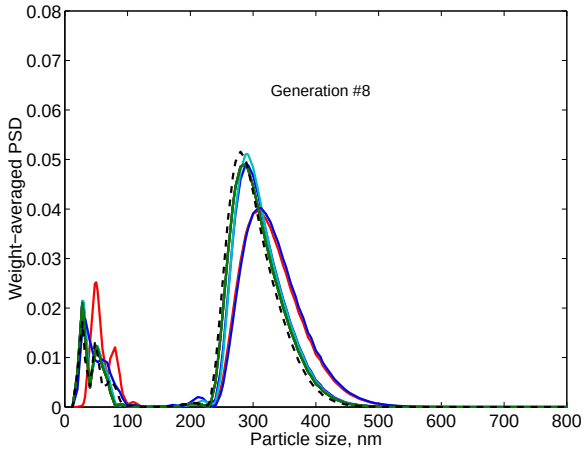

(b) last generation

Figure 6.2: The end-point PSD corresponding to members of particular generations. (The target PSD is shown as a dashed line).

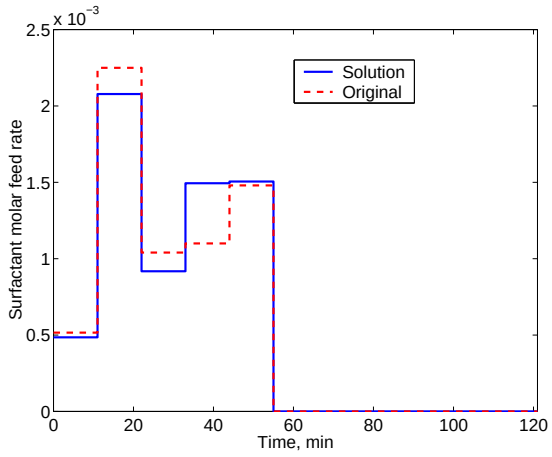

(a) feed profile for the surfactant solution

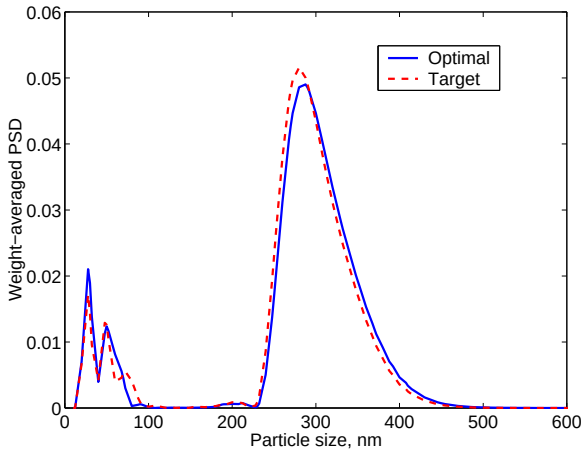

(b) end-point PSD

Figure 6.3: Comparison of the recipe generated by the optimizer and the resultant PSD with the target.

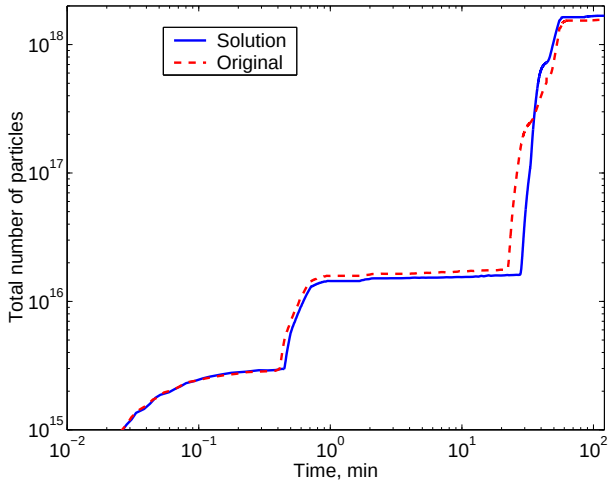

Figure 6.4: Evolution of the total number of particles during the batch.

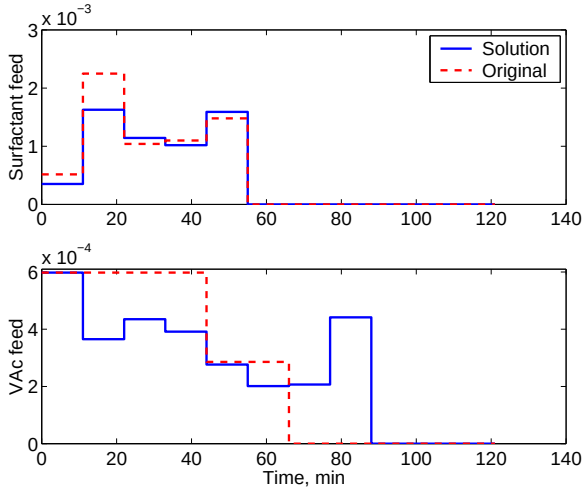

Figure 6.5: Comparison of the optimal recipe for both surfactant solution and vinyl acetate monomer with the recipe originally used to generate the target.

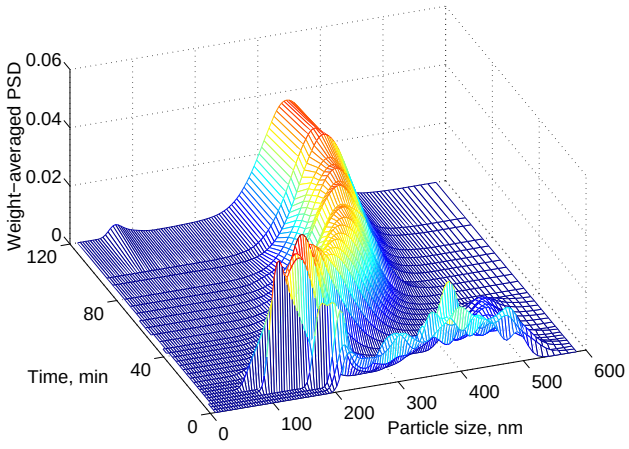

(a) experiment-based

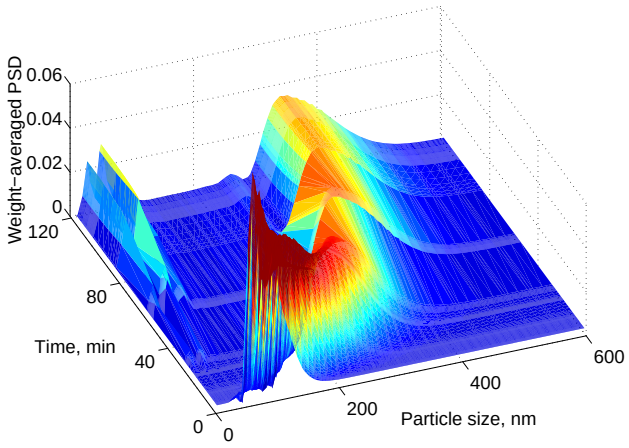

(b) simulation-based

Figure 6.6: Evolution of PSD during the course of the batch for the sub-optimal recipe.

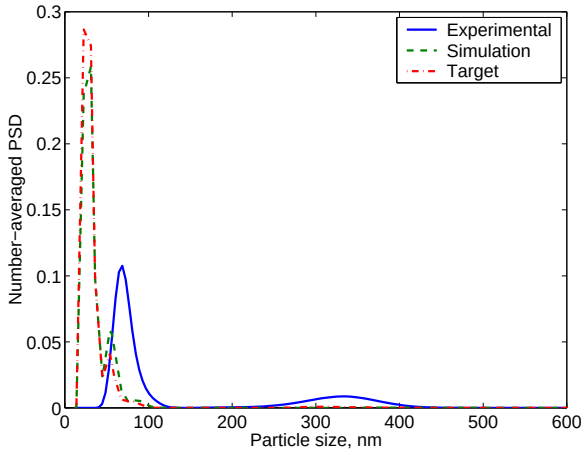

(a) number-average basis

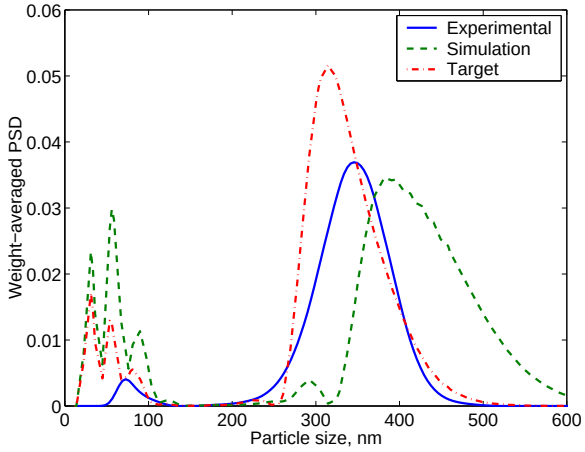

(b) weight-average basis

Figure 6.7: Comparison of the end-point PSD pertaining to the sub-optimal recipe with the target distribution.

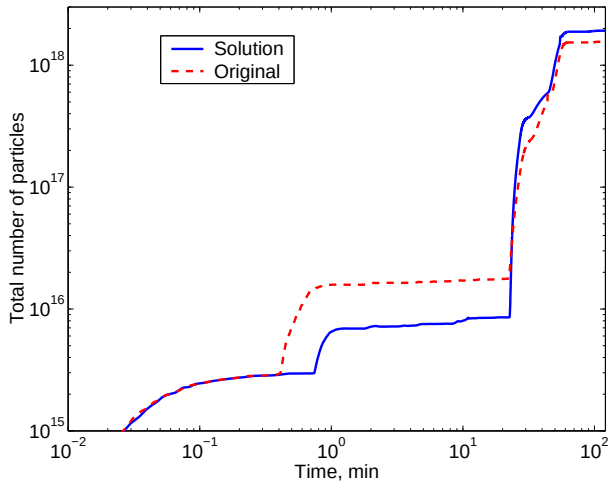

Figure 6.8: Comparison of the total particles corresponding to the sub-optimal recipe with that corresponding to the original recipe, during the course of the batch.

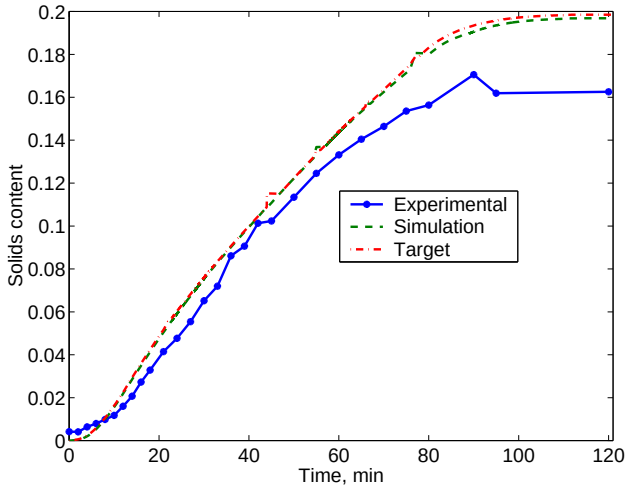

Figure 6.9: Comparison of the solids content profile of the original recipe with that obtained from the sub-optimal recipe – both from simulation and experiment.

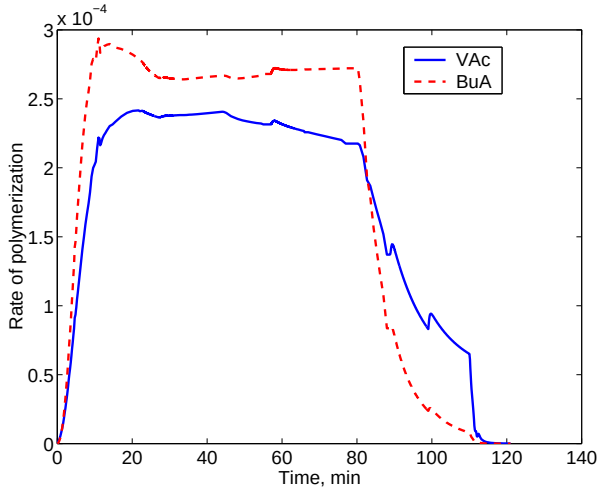

Figure 6.10: Rate of consumption of the two monomers along the profile of the batch.

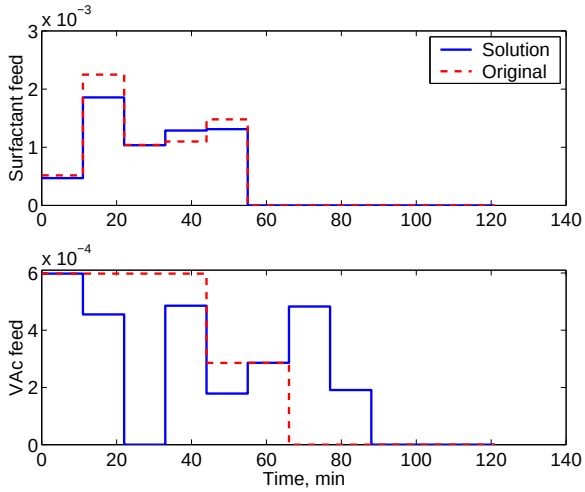

Figure 6.11: Comparison of the best recipe for matching the weight-averaged PSD (for both surfactant solution and vinyl acetate monomer) with the recipe originally used to generate the target.

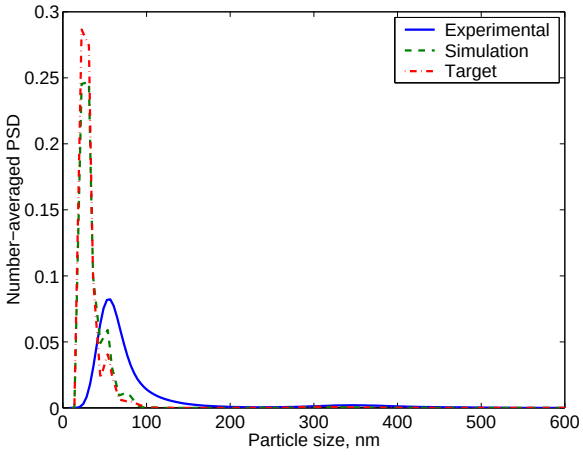

(a) number-average basis

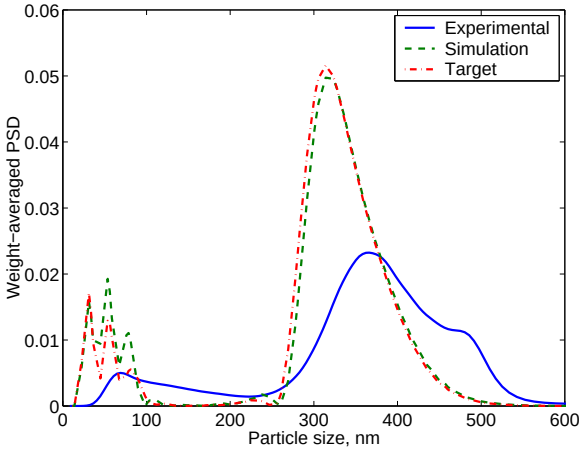

(b) weight-average basis

Figure 6.12: Comparison of the end-point PSD corresponding to the best recipe with the target distribution.

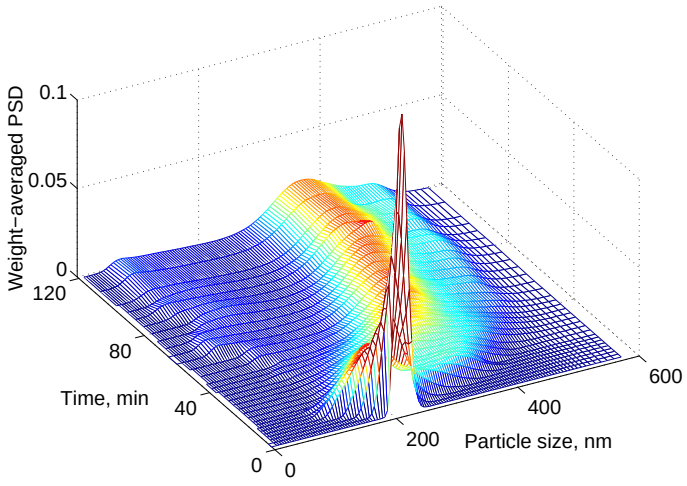

Figure 6.13: Evolution of PSD during the course of the batch, observed in the experimental implementation of the best recipe.

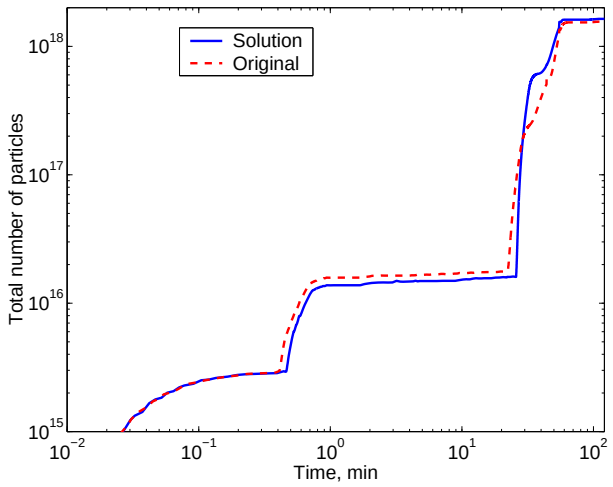

Figure 6.14: Comparison of the total particles corresponding to the best recipe with that corresponding to the original recipe, during the course of the batch.

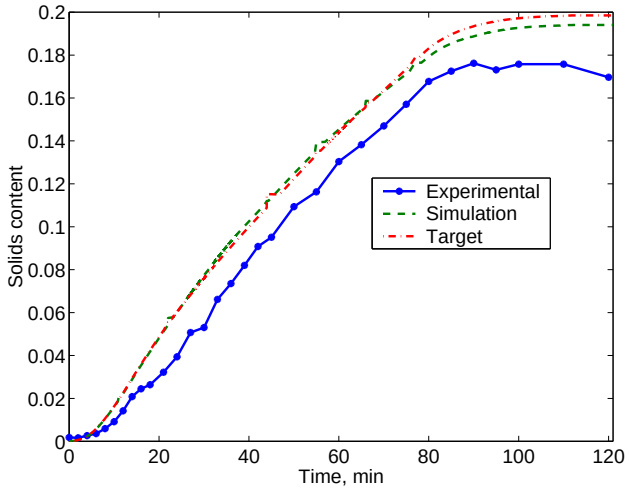

Figure 6.15: Comparison of the solids content of the original recipe along the course of the batch with that obtained from the best recipe – both from simulation and experiment.

idea, the trajectory of the nucleation rate can be controlled by regulating the profile of total particles, while the trajectory of the growth rate can be controlled by regulating the profile of solids content.

Thus, the problem of following a target PSD trajectory is transformed first into an equivalent problem of tracking the profiles of nucleation and growth rates, with coagulation minimized. This in turn is transformed into another equivalent problem of tracking the profiles of total particles and solids content, with coagulation minimized. The transformed problem is a multi-objective optimization problem, in which the first objective (denoted θ_1) is the tracking error of the total particles, and the second objective (θ_2) is the tracking error of the solids content. These are defined as follows:

$$\theta_1 = \sum_i w_i^1 (N_{p,i} - N_{p,i}^{ref})^2 \tag{6.6}$$

$$\theta_2 = \sum_i w_i^2 (sc_i - sc_i^{ref})^2 \tag{6.7}$$

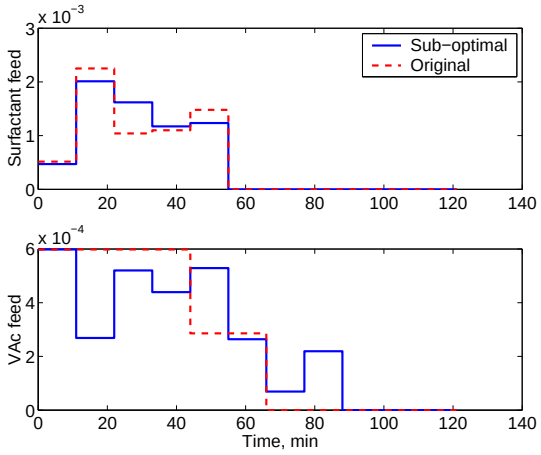

(a) sub-optimal input profile

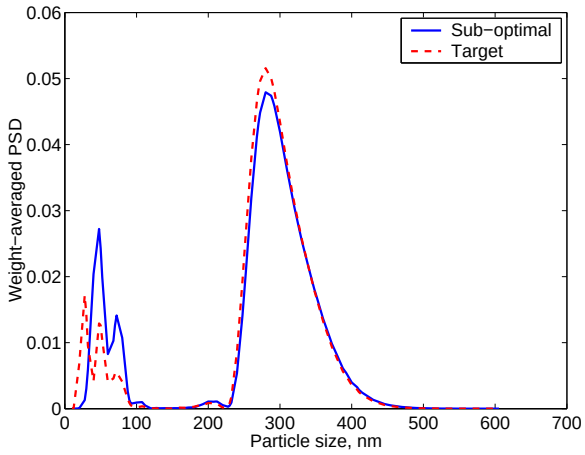

(b) end-point PSD, plotted against the unswollen particle diameter

Figure 6.16: Comparison of the recipe generated by the optimizer and the resultant PSD with the target, to match the entire weight-averaged PSD.

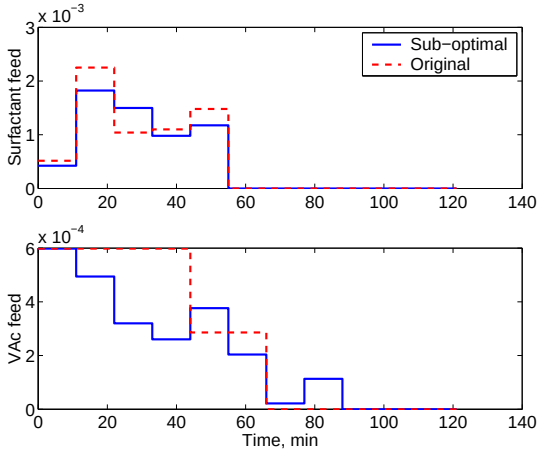

(a) sub-optimal input profile

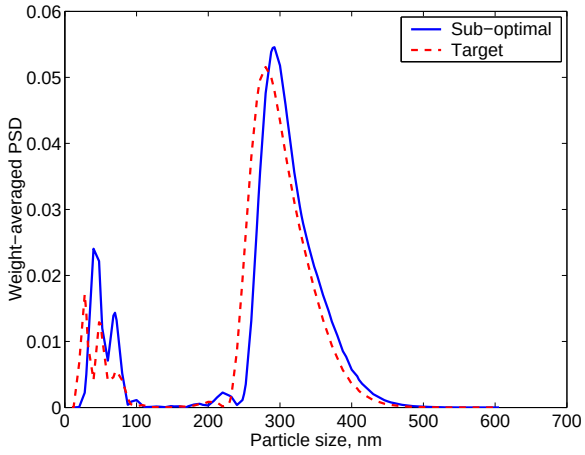

(b) end-point PSD, plotted against the unswollen particle diameter

Figure 6.17: Comparison of the recipe generated by the optimizer and the resultant PSD with the target, for a minmax formulation of the objective function on a weight-average basis.

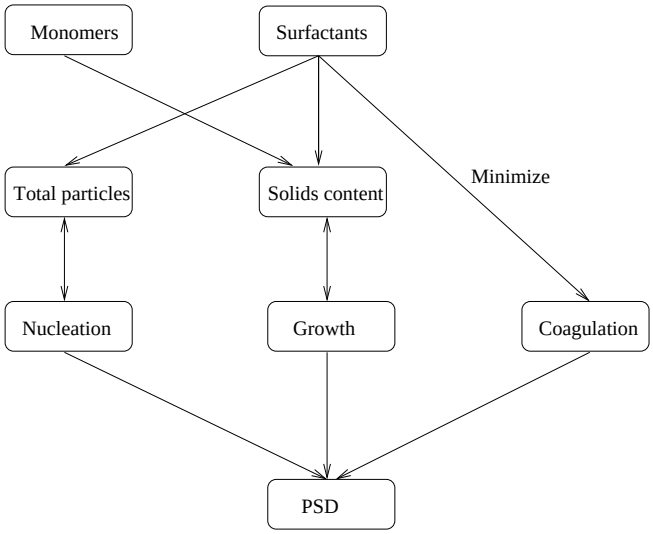

Figure 6.18: Schematic of the proposed hierarchical strategy for the control of PSD, by regulating the nucleation, growth and coagulation events individually, in a multi-objective framework. The target PSD trajectory is transformed into trajectories of the individual rates of the nucleation and growth events (with minimization of the coagulation events). Further, the idea of the control of instantaneous properties is exploited to re-cast the trajectories of nucleation and growth rates as equivalent profiles of total particles and solids content.

where $N_{p,i}$ (sc_i) is the value of total particles (solids content) at time instant 'i', and $N_{p,i}^{ref}$ and sc_i^{ref} are the corresponding target values at this time instant. w_i^1 and w_i^2 are appropriate weights. A third objective can also be considered for the end-point distribution error ($\theta_3(t_f)$), defined as follows:

$$\theta_3(t_f) = \int_{r_{nuc}}^{r_{max}} (W(r,t_f) - W_{ref}(r))^2 dr \tag{6.8}$$

Here, $W(r,t_f)$ is the weight-averaged PSD at the end time t_f and $W_{ref}(r)$ is the target weight-averaged PSD, r_{nuc} and r_{max} being the minimum and maximum particle sizes in the population. θ_1 and θ_2 can be collapsed into a single weighted objective and the problem can be solved using the regular single-objective GA. However, these objectives conflict with each other, with improvement in one objective leading to a potential worsening of the other (due to the interaction between nucleation, growth and coagulation). Also, in order to alleviate the problems with the choice of a proper weight, a multi-objective formulation is employed.

Multi-objective optimization is very common in engineering applications. For example, in the model predictive control (MPC) algorithm, one wants to attain a desired objective in the output while simultaneously minimizing the usage of the inputs. A typical pair of objectives in optimizing the performance of chemical reactors is to maximize the conversion and minimize the by-products. More generally, one is often faced with the tradeoff between an engineering objective versus an economic objective (Luyben and Floudas, 1994). It is common practice to combine these multiple objectives through suitable weights – by emphasizing one objective and relegating to a lower position the other. Although this is acceptable in most cases, there are a number of situations in which the objectives are in competition. This is particularly true in several polymerization applications, prompting the use of multi-objective strategies for these applications (Tsoukas et al., 1982; Choi and Butala, 1991; Mitra et al., 1998; Bhaskar et al., 2000). A common strategy used for multi-objective optimization is the ϵ-constraint method, wherein only one of the

objective is chosen for the optimization, and all the other objectives are appended as inequality constraints in the optimization problem (Tsoukas et al., 1982; Choi and Butala, 1991; Luyben and Floudas, 1994). This problem is amenable to gradient-based optimization techniques. Thus, a series of optimization problems are solved to find a pareto-optimal set of solutions. Among these pareto solutions, improvement in one objective leads to a worsening of one or more of the other objectives, thereby rendering each of them equally acceptable or tradeoff solutions. A different technique that directly obtains the pareto curve, and has found wide applications, is the Non-dominated Sorting Genetic Algorithm (NSGA) (Mitra et al., 1998; Bhaskar et al., 2000; Silva and Biscaia Jr., 2001). This is based on an extension of the genetic algorithm to multi-objective problems.

NSGA is employed to solve the multi-objective problem in this study. The algorithm is similar to the one presented in the previous single-objective case, except in the method of calculation of the fitness of the members. As mentioned previously, a multi-objective optimization problem produces solutions which are not necessarily optimal with respect to any of the objectives considered separately, but are the best tradeoff solutions. In multi-objective optimization, a solution is considered better than another only if it is better with respect to all the objectives. In this case, the better solution is assigned a superior rank and a higher fitness for selection. On the other hand, if one solution is better than another with respect to one objective, while the second is better with respect to a different objective, then the two solutions are considered non-dominated or equivalent, and are called pareto solutions. Pareto solutions are assigned equal rank and fitness in the algorithm. Thus, if $\theta_{1,i} < \theta_{1,j}$ and $\theta_{2,i} < \theta_{2,j}$, where i and j represent two members of the population, then, member i is superior to member j, and is assigned a better rank. If $\theta_{1,i} < \theta_{1,j}$ but $\theta_{2,i} > \theta_{2,j}$, then i and j are non-dominated or non-inferior or pareto solutions.

The discretization of the inputs is done as described in the previous section.

The members of the first generation are determined at random. The objective function values of the members are evaluated by solving the population balance model. The members are sorted into pareto sets using the non-domination concept and are assigned ranks. All members having the same rank are assigned equal fitness, defined as follows (Silva and Biscaia Jr., 2001):

$$fit_i = \frac{N_r - k + 1}{SS} \tag{6.9}$$

where

$$SS = \frac{1}{P_n} \sum_{k=1}^{N_r} (N_r - k + 1) P_{sk} \tag{6.10}$$

In the above equations, P_n is the size of the population, N_r is the total number of ranks in the generation (or the highest rank), P_{sk} is the size of rank k (the number of members assigned that rank), and fit_i is the fitness of any member i (which depends on its rank k).

The members are reproduced into the next generation in proportion to their fitness values, emulating the concept of the survival of the fittest. The pareto-set filter is introduced, and all members assigned the first rank are stored in this filter. Some of the members of the new generation are selected at random and exposed to cross-over and/or mutation operations, subject to certain probabilities p_{cross} and p_{mut}, respectively. The members of the new generation are evaluated. If a new member is better than its parent in at least one attribute (*i.e.,* with respect to at least one objective), the new member is accepted into the current generation. If not, the parent member is sent into the current generation. This concept is called the Niche operator, introduced in the NSGA technique (*e.g.,* (Silva and Biscaia Jr., 2001)) to avoid a genetic drift. The members of the current generation are sorted and ranked. The members assigned rank 1 in the current generation are appended to those already present in the pareto-set filter. The members in the filter are sorted and ranked, and only the first ranked members are retained. The current

generation is again subjected to selection, and the entire operation is repeated for a certain number of generations. At the end of any generation, the pareto-set filter has the current pareto-optimal solutions. These solutions form a classical pareto tradeoff curve.

6.4.1 Two-objective Formulation – Coagulation-free Case

In this section, a two-objective optimization problem is considered (total particles, θ_1 and solids content, θ_2). The coagulation-free model is utilized, with solution based on the orthogonal collocation on finite elements technique. The feed rate of the surfactant solution in the first five intervals and the VAc monomer in the first seven intervals are the decision variables. The feed rates of these reagents in the other intervals are set equal to zero. The NSGA parameters employed are $N_{pop} = 25$, $l_{chrome} = 24$, $p_{cross} = 0.7$ and $p_{mut} = 0.001$. Figure 6.19 shows the sorting of some of the members pertaining to the first generation. The solution #1 is better than the rest with respect to both the objectives, and is assigned rank 1. The solutions marked #2 are paretos (non-dominated) to each other. Hence, these are both assigned rank 2, and so on. Solution #1 is stored in the pareto-set filter after the first generation. The operations of selection, cross-over and mutation, and the updating of the pareto-set filter are repeated generation after generation. The inset in Figure 6.19 shows the pareto-set filter at the end of five generations. It has four solutions, each of which have bettered solution #1 from the first generation. Table 6.1 lists the values of the target variables corresponding to these four pareto-optimal solutions. It can be seen that pareto #1 is the *best* with respect to the tracking of the profile of total particles (θ_1), while pareto #4 is the *best* with respect to the tracking of the profile of the solids content (θ_2). This table also provides the value of $\theta_3(t_f)$ (end-point PSD tracking error) corresponding to each of these pareto solutions.

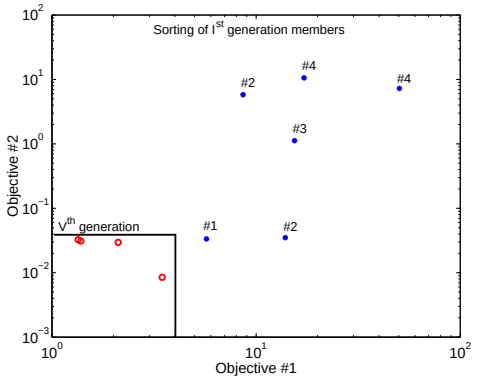

Figure 6.19: Evolution of the pareto-optimal solutions from generation I to generation V. The inset shows the pareto-set filter corresponding to the fifth generation.

One can see from this table, and also from Figure 6.20, that pareto #4 gives the best match to the end-point PSD. The decrease in the value of θ_2 from pareto #1 to pareto #3 is more than countered by the increase in value of θ_1, resulting in the degradation of the match in the end-point PSD $\theta_3(t_f)$. However, the drop in θ_2 between paretos #3 and #4 results in a substantially better match of the end-point PSD in spite of the increase in θ_1. The non-uniform trend in the value of θ_3 suggests regions in the pareto-curve where a different objective is dominant, indicative of a multi-objective problem. Figure 6.21 shows a comparison of the feed profiles of the surfactant solution and VAc monomer corresponding to the four non-dominated solutions with the actual feed profiles that were originally used to generate the target distribution.

Table 6.1: Objective function values corresponding to the four pareto-optimal solutions.

Pareto #	θ_1	θ_2	$\theta_3(t_f)$
1	1.3428	0.0325	5.63×10^{-4}
2	1.3852	0.0311	6.97×10^{-4}
3	2.1088	0.0296	1.5×10^{-3}
4	3.4663	0.0085	1.45×10^{-4}

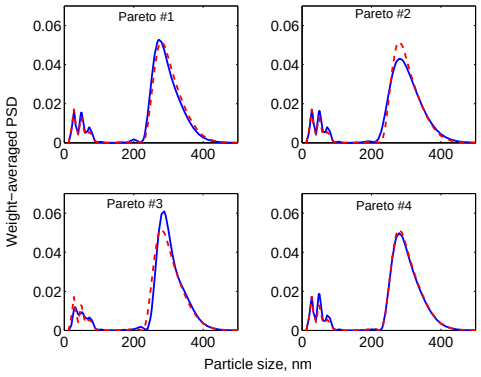

Figure 6.20: Performance of the pareto-optimal solutions obtained at the end of five generations, with respect to the end-point PSD target.

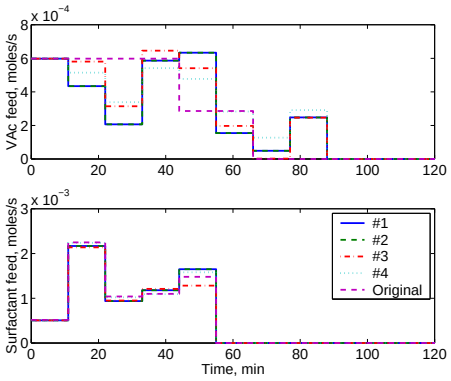

Figure 6.21: Comparison of the optimal feed profiles characterizing the four pareto solutions, with the target (original) recipe.

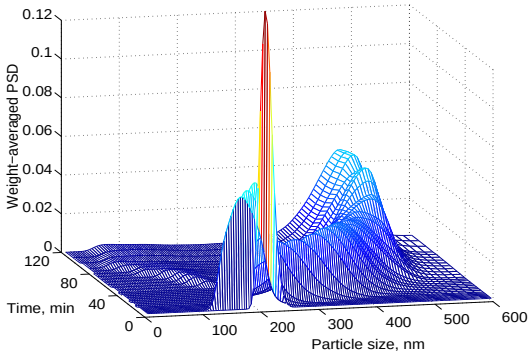

Figure 6.22: Evolution of the (weight-averaged) PSD in the experimental implementation of pareto # 4. Input profiles were those depicted in Figure 6.21.

Among the four pareto-optimal solutions obtained from the NSGA, in the absence of the information on the third objective θ_3, the user could select any of the four solutions for implementation in the process. In light of the values of $\theta_3(t_f)$ for the four solutions, the user would likely choose pareto #4 for implementation. The pareto solution #4 was implemented in an experimental reactor system. Figure 6.22 shows the evolution of the PSD over the course of the batch corresponding to this recipe. Figure 6.23 shows a comparison of the estimates of the profiles of total particles and solids content from the experimental data, with the target profiles. It also depicts the end-point PSD obtained experimentally and the target end-point PSD. The experimental data for the total particles (Figure 6.23(a)) shows that the primary nucleation event is quite delayed (a longer induction period), and also shows the presence of a coagulation event, that result in lower number of particles at early times. This in turn results in larger values of the average number of radicals/particle and monomer concentrations inside the particles, resulting in larger growth rates. Hence the difference in the size of the larger mode, relative to the target (Figure 6.23(c)).

6.4.2 Three-objective Formulation – Coagulation-free Case

In the previous results, the profiles of nucleation and growth rates that characterize the desired PSD trajectory were re-cast as equivalent profiles of total particles and solids content (exploiting the idea of the control of instantaneous properties). Viewing this approach from a different perspective, total particles and solids content are related to the moments of the distribution. Consequently, tracking the profiles of total particles and solids content might not guarantee the attainment of a desired multi-modal distribution with complex shapes. In light of this, the third objective on the end-point weight-averaged PSD ($\theta_3(t_f)$) is explicitly included into the formulation. The non-uniformity in the value of $\theta_3(t_f)$ in the pareto solutions (Table 6.1) with respect to θ_1 and θ_2 also supports this formulation. Figures 6.24 and 6.25

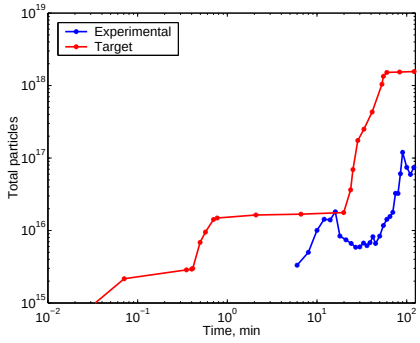

(a) comparison of the profile of total particles

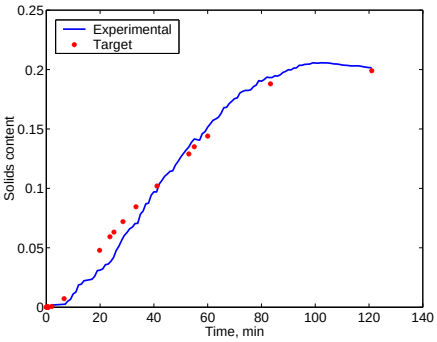

(b) comparison of the profile of solids content

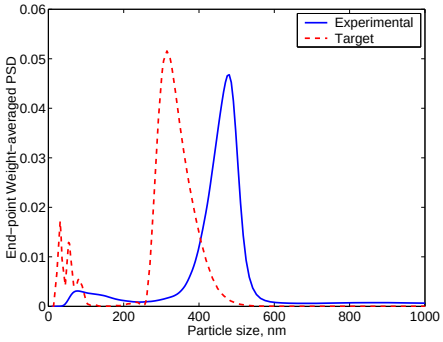

(c) comparison of the end-point PSD

Figure 6.23: Comparison of the experimental results observed on implementing pareto # 4 (from Table 6.1 – Two-objective formulation) with the target.

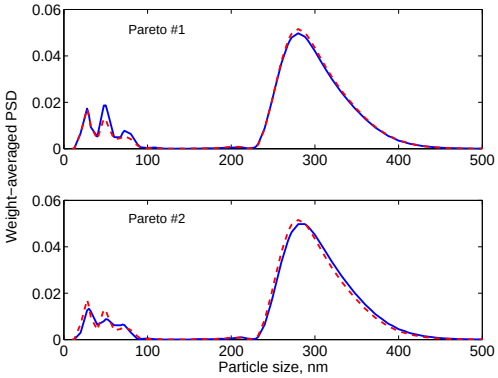

Figure 6.24: Performance of the pareto-optimal solutions obtained at the end of five generations in the three-objective problem, with respect to the end-point PSD target.

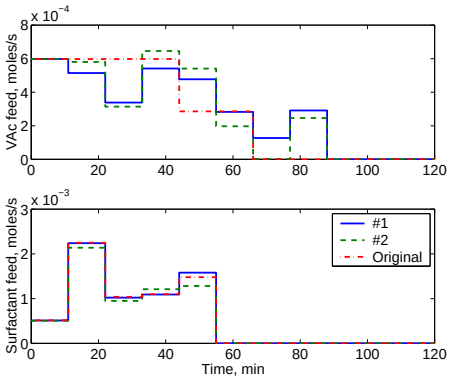

Figure 6.25: Comparison of the optimal feed profiles characterizing the two pareto solutions with the target recipe (that was originally used to generate the target distribution) – three-objective formulation.

show the results pertaining to the three-objective optimization problem. In this case, the algorithm generates two non-dominated solutions (after five generations), one of which is the same as that obtained in the earlier two-objective formulation (pareto #4). Table 6.2 lists the objective function values corresponding to these two solutions. For implementation purpose, one could select the solution which gives the maximum surface coverage to the particles with surfactants – based on the hypothesis that larger surface coverage leads to lower coagulation events. Alternatively, the user could employ other process information (not built into the mathematical framework) in deciding which solution to implement.

Table 6.2: Objective function values corresponding to the two pareto-optimal solutions – three-objective formulation.

Pareto #	θ_1	θ_2	θ_3
1	3.4663	0.0085	1.45×10^{-4}
2	2.3652	0.0279	2.94×10^{-4}

6.4.3 Convergence Tests

It is well-known that in most cases, a Genetic Algorithm produces a solution in the vicinity of the global optimum, but not the exact optimum. This solution can be improved using a local optimization technique. Alternatively, one has to employ a very large number of generations to obtain a solution close to the optimum. In the case of a multi-objective optimization, the solution(s) obtained (either a pareto-optimal set of non-dominated solutions or a unique solution) are not necessarily optimal in a formal sense, but are the *best* tradeoff solutions. The actual optimal point with respect to the different objectives (considered separately) is called a *utopia* point, to reflect its ideality. This is the implicit tradeoff in optimizing multiple objectives separately. However, in the current case, *the solutions obtained are very close to the targets*, leaving little room for further refinement. Also, previous studies based on optimizing a single target shows that the solutions converge (to within an

accuracy dictated by the choice of objective function) in about *three* generations (of a total of *eight* generations) – Figure 6.1(b). Thus, in this NSGA application, the search was restricted to 5 generations. However, two measures were undertaken to confirm that the solutions had converged to the 'optimal' ones. The first was to run the algorithm for a larger number of generations, specifically 10. Another was to parameterize the input space, and perform a systematic search (contrasted with the facilitated random search that GA signifies) – by solving a combinatorial problem. In these cases, different solutions were obtained, but these were paretos to the ones found already. Table 6.3 lists all the solutions from the different strategies. In summary, five generations were found to be adequate to develop the optimal pareto curve.

Table 6.3: Objective function values corresponding to the pareto-optimal solutions obtained from different strategies

Pareto #	θ_1	θ_2	$\theta_3(t_f)$	Technique
1a	3.4663	0.0085	1.45×10^{-4}	5 Generations
2a	2.3652	0.0279	2.94×10^{-4}	NSGA
1b	2.0651	0.02758	4.28×10^{-4}	
2b	2.05693	0.02738	5.48×10^{-4}	10 Generations
3b	2.0096	0.02789	3.37×10^{-4}	NSGA
4b	1.11708	0.03884	3.11×10^{-3}	
1c	9.9468	0.0238	1.22×10^{-4}	Systematic
2c	2.3881	0.0140	4.73×10^{-4}	search

6.4.4 Three-objective Formulation – Coagulation-inclusive Case

In the previous studies, a coagulation-free model was utilized in performing the optimization. Coagulation events were minimized by setting constraints on the surface coverage of the particles with surfactants. Such an approach was required because of the computational burden associated with the complete coagulation-inclusive model. This strategy was revised due to the excessive coagulation events in the experimental implementation of the optimal recipe (see Figures 6.12(b) and

6.23(a)). Thus, the complete coagulation-inclusive model, based on the efficient solution technique presented in Chapter 4, was employed in the next case. The algorithm produces two pareto-optimal solutions (shown in Table 6.4), which track the target profiles of total particles and solids content closely, and also attain the target end-point PSD. One of these solutions is shown in Figure 6.26. The input profiles that are determined by the algorithm match the target input profiles rather closely. Experimental implementation of this recipe is shown in Figure 6.27. Clearly, there is no evidence of a strong coagulation event in the experimental distribution (Figure 6.27(c)). However, there is a discrepancy between the target distribution and the experimental distribution. This is attributed to model and parametric uncertainties, and input disturbances.

Table 6.4: Objective function values corresponding to the two pareto-optimal solutions – three-objective formulation, using a coagulation-inclusive model.

Pareto #	θ_1	θ_2	θ_3
1	7.4774	0.0057	1.122×10^{-6}
2	7.5131	0.0056	1.069×10^{-6}

6.5 Feedback Analysis

The process of evolution of PSD in emulsion polymerization is quite complex, comprising the phenomena of nucleation, growth and coagulation. The mechanisms that characterize each of these sub-processes in turn are complex and not completely well characterized. As newer processes are developed to address environmental impacts or to produce better products, they add to the complications and to the unknown mechanisms in the model. For example, the use of ionic surfactants results in undesired properties in the final products relative to their water-resistance characteristics. Thus, the ionic surfactants are being replaced with non-ionic ones. But the latter result in considerable alterations in the nucleation and coagulation phenomena (and indirectly on the growth phenomenon) due to their tendency to

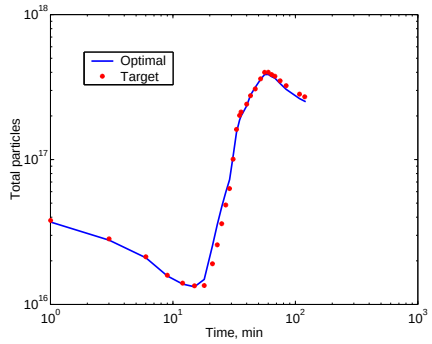

(a) profile of total particles

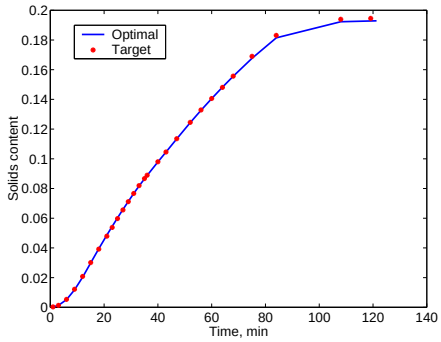

(b) profile of solids content

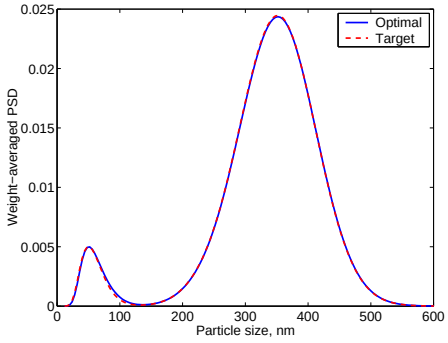

(c) end-point PSD

Figure 6.26: Comparison of NSGA-generated 'optimal' solution with the target, utilizing a coagulation-inclusive model to perform the optimization.

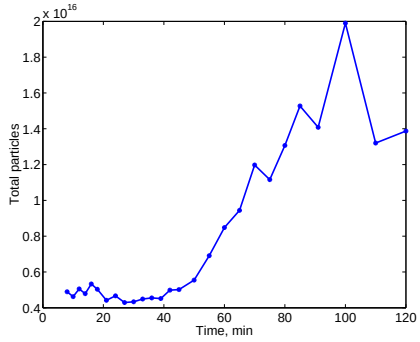

(a) profile of total particles

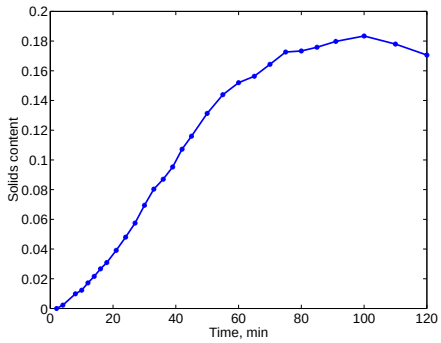

(b) profile of solids content

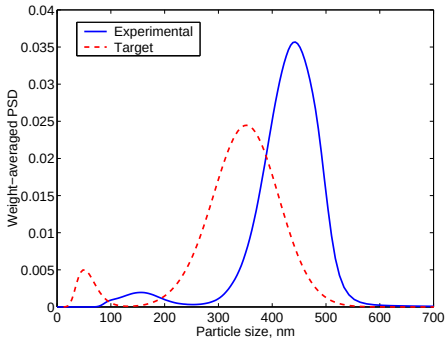

(c) end-point PSD

Figure 6.27: Experimental implementation of the open-loop optimized recipe corresponding to the solution shown in Figure 6.26, and comparison of the obtained end-point PSD with the target.

partition into the dispersed phases. Since these aspects and mechanisms are still subjects of active research, the model developed at this point has associated uncertainties. There are also a number of parameters in the model that are uncertain.

Although the experimental implementation of the open-loop optimized recipe produced encouraging results, there is a clear need for improvement through feedback. However, there are also indications that in-batch feedback may not be effective to account for disturbances in semi-batch emulsion polymerization(Chapter 5;Wang & Doyle III (2002)). For example, in the experimental implementation presented previously (Figure 6.23), the primary nucleation event is delayed considerably, and also there is a coagulation event. The resultant decrease in the number of particles caused the primary mode to grow to a much larger size than desired. This is due to the interactive effect of the nucleation phenomenon (decrease in the number of particles) on growth. To correct this error (in a relative sense – and hence preserve the shape of the distributions), one might need an earlier secondary nucleation event (of a reduced magnitude) and also a drop in the growth rate. These highlight an opportunity for improvement with feedback, subject to measurement limitations. Feedback information on the total particles (or the free surfactant concentration relative to the critical micelle concentration) could enable rectification of these errors. However, it depends on whether these states are observable without the PSD measurements, as the very first PSD measurement is not available until at least 12 minutes into the batch. In general, the PSD measurements are both sparse and delayed, which could potentially make them of a reduced utility to correct the rapid and irreversible processes. Also, there are cases in which, a strong coagulation event could occur, leaving an irreparable impact on the distribution (Figure 6.12(b)). This is mainly a concern due to the randomness associated with shear-induced coagulation.

The previously described attributes challenge the application of control for

this process. Generally, there are two feedback corrective measures that have been proposed – in-batch feedback (Flores-Cerrillo and MacGregor, 2002), and batch-to-batch feedback (Crowley et al., 2001). The in-batch feedback approach presented by Flores-Cerrillo and MacGregor (2002) is based on a single point re-computation. This requires a determination of the most effective time to perform the re-optimization. As described in the earlier scenario (reduced nucleation at early times), the cascaded effects of the errors motivate earlier corrective action. On the other hand, corrective action taken too early may lead to erroneous action influenced by faulty measurements. Hence, it is of interest to identify the most opportune time to perform the first corrective action. Also, a single re-computation may not be effective, and one might need a full nonlinear model predictive control (MPC) formulation in a receding horizon framework to correct the errors. There are several efficient solution techniques that have been developed (Mahoney and Ramkrishna, 2002), which can render a full nonlinear MPC feasible. But it is important to determine whether physical limitations can be overcome with on-line feedback subject to the process constraints. If these strategies prove ineffective, it is better to employ the batch-to-batch feedback strategy presented by Crowley *et al.* (2001), with the possibility of improvement in subsequent batches.

The present study evaluates these tradeoffs with a two-fold objective. One is the evaluation of different state estimation strategies to determine the configuration that leads to a reasonable convergence of the estimates in the available time. The second objective is to employ these estimation techniques to address the important question of effectiveness of feedback. This study is carried out off-line using real experimental data.

6.5.1 Biased State Estimation Strategy

As mentioned earlier, successful feedback measures rely on the availability of successful and robust estimation techniques – which take the measurements from

the process and reconcile them with the model to estimate the actual process states. The on-line measurements available to monitor the process of the evolution of PSD in the system considered here are (Chapter 2):

1. the relative PSD measurements, available typically every 11-12 minutes from a capillary hydro-dynamic fractionator
2. latex density measurements from a densitometer
3. feed rate measurements (from flow meters and load cells).

In typical MPC applications using linear models on continuous processes, a classical approach to correcting for disturbances and model mismatch is to bias the outputs against the measurements, and hold the bias constant for the rest of the prediction horizon (Garcia and Morari, 1982; Garcia and Morshedi, 1986). A similar idea can be used in this semi-batch process, in a receding horizon framework.

This approach is an extension of the strategy presented in Chapter 2. In that case, estimation was accomplished using sensor measurements combined with process calculations using simple steady state models. It was seen that latex density and feed rate values could be used to infer the conversion of the monomers and the solids content. Combining this information with the relative PSD measurements from the CHDF, the absolute PSD can be obtained, and all the particle-related states including the total particles can be calculated. A major implication of this study is the ability to observe all important process states. Dynamic state estimation is possible if the above estimation technique is combined with a dynamic model. The dynamic model based on the hierarchical strategy presented in Chapter 4 has the generic structure

$$\begin{aligned} \dot{x} &= f(x, p, y, z, u) \\ y &= g(x, p) \\ z &= h(y) \end{aligned} \tag{6.11}$$

Here the vectors y and z represent the inertial manifold or the pseudo-steady state variables. A sequential solution technique is employed. The vectors, x represent the states of the system, p the parameters, and u the inputs. The model reduction itself is obtained purely from process considerations, and the underlying mechanisms. The vector z comprises the PSD at discrete points and other outputs such as the total particles and solids content. The vector y comprises the faster modes such as the average number of radicals/particle corresponding to the discrete points of the PSD, and the partitioning equations. They also comprise the individual rates of nucleation, growth and coagulation. The states x comprises the slower modes, mainly the material balance equations. At each time instant measurements (including the PSD) are available, the process calculations are performed, and the variables in z are forced to calculated values z_{calc} (akin to an initial condition update). The solution is continued in a receding horizon implementation.

6.5.1.1 Multi-objective Re-optimization Based on Biased Estimation

The experimental results from the open-loop optimized recipe using the coagulation-inclusive model (Figure 6.27) are utilized for this study. Note that more frequent PSD data – than the typical 11 minutes – are utilized at the early times, based on off-line sampling. The very first successful measurement in this experiment corresponds to the sample taken at 8 minutes, which would be available at approximately 19-20 minutes (due to delay in measurements). Earlier measurements are not possible owing to the low particle concentrations (below 0.5%) that cannot be detected by the instrument. The model prediction is biased against the measured/calculated value at 8 minutes ($z = z_{calc}$), and the new end-point PSD, and the new trajectories of total particles and solids content are estimated. Based on this estimate, the receding horizon multi-objective problem is re-optimized (based on target variables θ_1, θ_2 and θ_3), to find the inputs that would drive the solution back to the target trajectory. The inputs from the third interval forward (22

minutes) are re-optimized. Figure 6.28(c) shows a biased estimate of the end-point distribution based on the 8-minute sample, which shows much larger size particles in the larger (primary) mode relative to the target, and a much larger ratio of the number of particles in the smaller mode to that in the larger mode, relative to the target. This is mainly due to a reduced nucleation rate at early times as seen by the estimates of total particles in Figure 6.28(a), which causes larger growth rates at these early times. It also causes an earlier and larger secondary nucleation event. The re-optimized input profiles (surfactant feed and VAc feed) after 22 minutes (third interval forward) bring the trajectory back to the target profile of total particles, as seen in Figure 6.28(a). The optimizer reduces the surfactant feed in the third interval (Figure 6.29(a)) to the lower limit that was set in the algorithm, to reduce the nucleation rate, and to bring the profile of total particles back to the target. Thus, the peak corresponding to the secondary nucleation is reduced (Figure 6.28(c)). However, it is still broader than the target, as the secondary nucleation is initiated at about 15 minutes (Figure 6.28(a)). Similarly, it is not possible to reduce the size of the larger mode in the end-point distribution, since a decrease in the VAc feed rate in most of the intervals (required to reduce the growth rates) would result in lower solids content values and, hence, would violate the target trajectory of solids content. Due to these conflicts, the optimizer balances on this particular solution.

6.5.1.2 Single-objective Re-optimization Based on Biased Estimation

In the previous case, the inputs were re-optimized to bring the trajectory back to the original profiles of total particles and solids content. However, owing to the error that has occurred, the end-point distribution targeting suggests that one should not follow the original trajectory of total particles and solids content, which represent a particular nucleation and growth rate trajectory. Instead, these

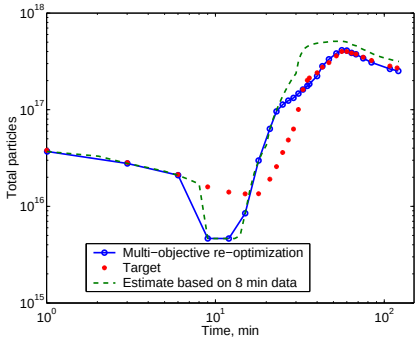

(a) re-optimized profile of total particles

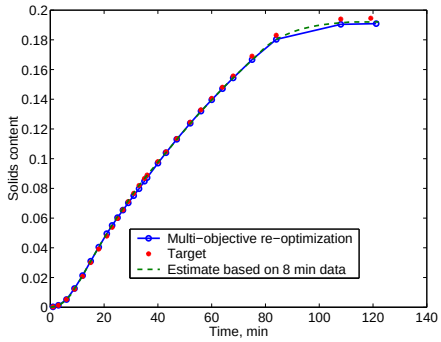

(b) re-optimized profile of solids content

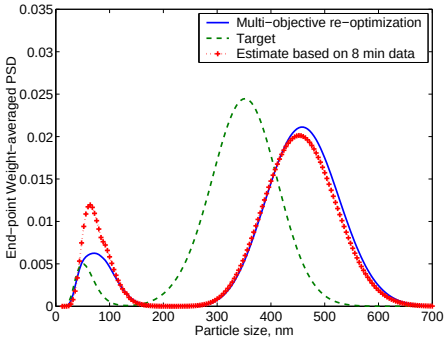

(c) re-optimized end-point PSD

Figure 6.28: Multi-objective re-optimization of the inputs, using measurements available at 8 minutes into the batch - based on a biased estimation strategy.

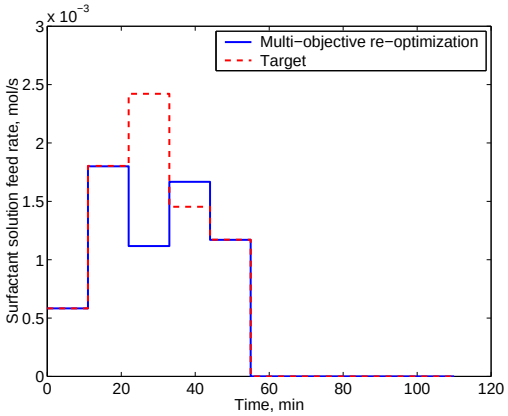

(a) re-optimized profile of surfactant feed rate

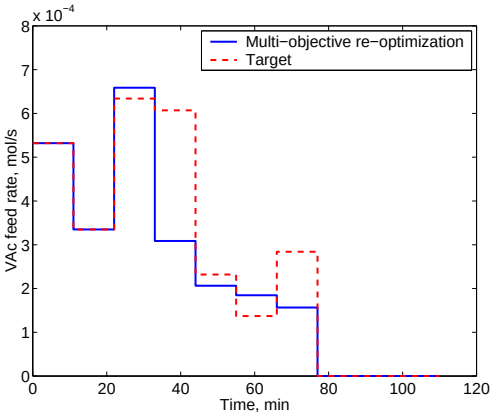

(b) re-optimized profile of VAc feed rate

Figure 6.29: Mutli-objective re-optimized inputs corresponding to the results in Figure 6.28. The dashed lines in the plot ('Target') represent the open-loop optimized recipe.

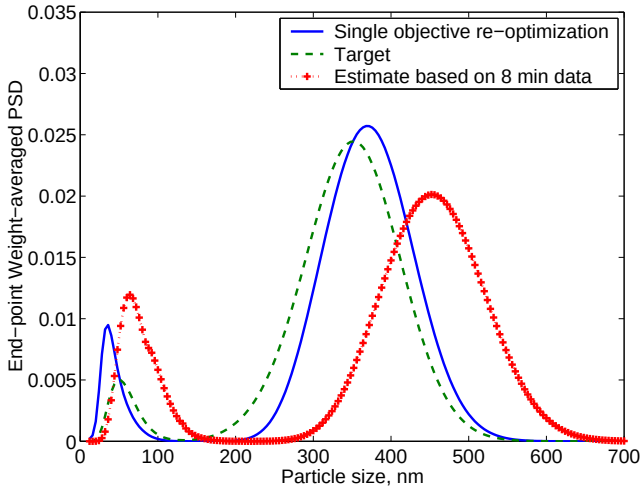

Figure 6.30: End-point PSD obtained by a single-objective re-optimization, using measurements available at 8 minutes into the batch - based on a biased estimation strategy.

trajectories need to be re-computed. For example, the decrease in the particles nucleated in the primary mode would necessitate a decrease in the particles nucleated in the subsequent nucleation event to preserve the relative magnitudes of the distributions. In addition, it might necessitate an earlier secondary nucleation event to preserve the distance between the modes. Thus, in the next case, a single objective optimization problem is solved, based on the end-point distribution alone (on a weight-averaged basis – as defined in $\theta_3(t_f)$). In this case, there is no target for the profiles of total particles and solids content. The single-objective algorithm is utilized for this purpose. The surfactant feed in intervals 3-5, and the feed of both the monomers (VAc & BuA) in intervals 3-7 are re-computed. Note that it is essential to include the feed rate of BuA as a decision variable. Figures 6.30 and 6.31 present the results corresponding to this single objective optimization problem. It is seen in Figure 6.30 that the size of the particles are reduced considerably, and the larger mode is brought closer to the corresponding mode in the target. Also, the secondary nucleation event is reduced, and the secondary mode is brought closer to that in

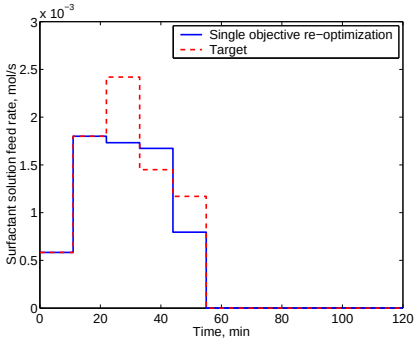

(a) re-optimized profile of surfactant feed rate

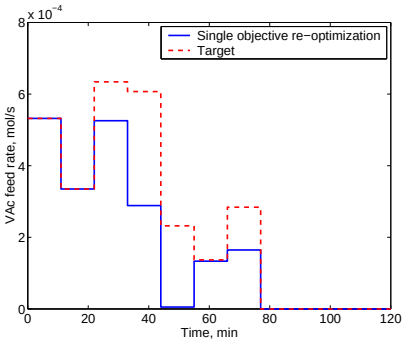

(b) re-optimized profile of vinyl acetate feed rate

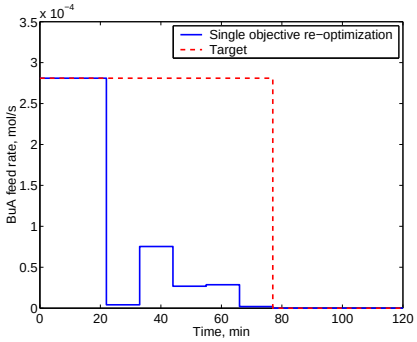

(c) re-optimized profile of butyl acrylate feed rate

Figure 6.31: Single-objective re-optimized inputs corresponding to the results in Figure 6.30.

the target. But the two modes are farther apart from each other in the solution than in the target. This shows that, to correct for the reduced primary nucleation event, the secondary nucleation event must have started before 15 minutes, or the growth rate must be reduced at very early times (recall that the first PSD data is not available until 20 minutes). The current solution has a significantly reduced solids ($\sim$ 10%) at the end of the batch, confirming the observation made in the multi-objective re-optimization case above. Further receding horizon optimization as the batch proceeds (a full nonlinear MPC) could potentially improve upon these results, as more data becomes available and more information about the experiment can be inferred.

In the above cases, a simple biased-estimate (analogous to a constant disturbance) was used. This predicts a secondary nucleation event that starts by approximately 15 minutes, and also is stronger than in the nominal case (as seen in Figure 6.28(a) – dashed line). However, a closer look at Figure 6.27(a) reveals that the secondary nucleation event does not happen until about 40 minutes in the actual case. This clearly highlights a shortcoming of basing the feedback calculation on too few measurements. This also shows the ineffectiveness of the biased estimate *in most cases*, particularly without a parameter update. To elaborate upon the latter aspect first, the model predicts a larger primary nucleation event compared to the actual experimental occurrence. This is probably due to the errors in the surfactant-partitioning parameters and the critical micelle concentration (cmc) value (discounting the effect of inhibitors such as residual dissolved oxygen in the initial mixture – which might occur in spite of the purging of the reaction mixture with nitrogen gas). For example, either the cmc value used in the model is lower than the actual value, or the partitioning parameters are such that they predict a larger free surfactant concentration in the aqueous phase. One or both of these uncertainties result in predicting a larger concentration of the micelles, and a larger

micellar nucleation rate. Now, when the distribution is updated at 8 minutes based on the measured value, the total particles and the total surface area are reduced (to the values calculated from the measurements). This results in an even larger free surfactant concentration than in the nominal case, and hence, the prediction of an earlier and larger nucleation event. This clearly shows the need for a parameter update in addition to output biasing. There are situations in which a pure biasing of the outputs alone (without parameter updating) is effective in driving the simulations to the experimental results, however, one needs to employ enough data points. This is seen in Figure 6.32(b), in which, at early times, the biasing results in a prediction of an even larger nucleation rate and number of particles. The very first data point corresponding to 6 minutes shows 3.8×10^{14} particles – not seen in the plot in Figure 6.32(b) – that is considerably lower than the predicted value. Biasing against this value results in raising the predicted value to $\sim 10^{17}$ at this time compared to $\sim 1.5 \times 10^{16}$ in the open-loop case. After about 30 minutes, the predicted profile closely follows the observed data (and the estimated end-point PSD and the experimental PSD match closely – Figure 6.32(a)). However, since the biasing method is not consistent in all cases, a more formal estimation strategy is considered next.

6.5.2 Luenberger Observer

For the next case, a Luenberger observer is proposed, in which the complete system becomes:

$$\begin{aligned} \dot{x} &= f(x, p, y, z, u) \\ y &= g(x, p) \\ z &= h(y) \\ w &= q(z) \end{aligned} \tag{6.12}$$

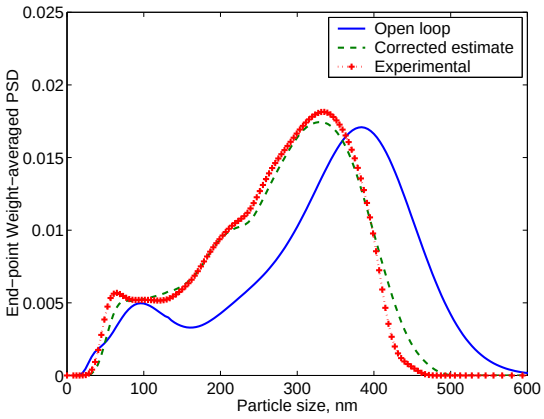

(a) end-point distribution

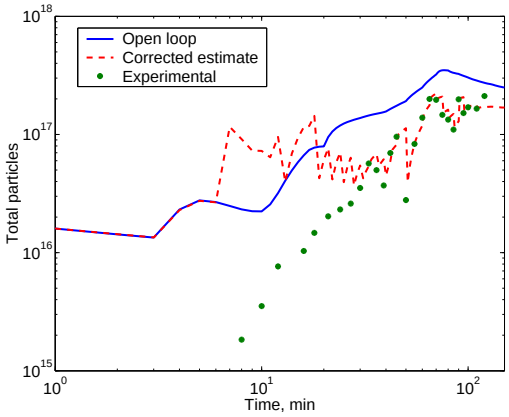

(b) profile of total particles

Figure 6.32: Biased estimation strategy without parameter updating, showing the convergence of the results beyond 30 minutes.

where w is the actual output (measurements), which represents the relative (weight-averaged) PSD – discretized at different points in the size domain, and lumped variables such as total particles and solids content. The auxiliary variables z (250×1) account for the absolute PSD at more refined intervals than the outputs w, based on the finite element discretization chosen (see Chapter 4). The vector z give the actual absolute distribution, while the outputs w represent the actual measurements. Three of the states x (M_1 & M_2 – the two monomers, and R_w – the aqueous phase initiator-derived radicals) are chosen for update in the estimator framework, and the rest are allowed to evolve in open-loop. The disturbances and noise are not incorporated at present. An estimator of the form

$$\begin{aligned} \dot{\hat{x}} &= f(\hat{x}, p, \hat{y}, \hat{z}, u) + L_i(w_k - q(\hat{z})) \\ \hat{y} &= g(\hat{x}, p) \\ \hat{z} &= h(\hat{y}) \end{aligned} \tag{6.13}$$

is defined (the character $\hat{}$ denotes estimates of the corresponding variable), where L_i (over a time interval i) is a Luenberger gain, designed such that the eigenvalues of $(A - L_iCD)$ lie in the LHP. Here A is the Jacobian of $f(x)$ at $\tilde{x}$, C is the Jacobian of $h(g(x,p))$ at $\tilde{x}$, and D is the Jacobian of $q(z)$ at $z = h(g(\tilde{x},p))$, $\tilde{x}$ being a representative point in the time interval i. w_k is the measured output value at time instant k (held constant until another measurement is available). The states are corrected using combinations of the error in the weight-averaged PSD at different discrete points of the distribution. Accordingly, the three non-zero rows of the matrices L_i (corresponding to the states M_1, M_2 and R_w) have non-zero elements at different points to catch the value of the PSD at different discrete points. Although the tuning of L_i is done using the Luenberger concept, the estimator has a Kalman-like structure. The gain matrices L_i are calculated at the start in this off-line study,

such that the convergence criterion is satisfied along the entire batch, by dividing the entire batch into intervals spanning 10 minutes each. A state-estimation scheme without a parameter update is again found to be inadequate. Instead, a discrete (static) parameter update was performed for the cmc, Γ_∞ (one of the surfactant-partitioning parameter), k_{p11} (propagation rate constant for polymer of type 1 – with a VAc end group, with monomer 1 – VAc). The structure of the continuous-discrete observer is given by:

$$\begin{aligned}
\dot{\hat{x}} &= f(\hat{x}, \hat{p}, \hat{y}, \hat{z}, u) + L_i(w_k - q(\hat{z})) \\
\hat{y} &= g(\hat{x}, \hat{p}) \\
\hat{z} &= h(\hat{y}) \\
\dot{\hat{p}} &= 0 \\
\hat{p}^-_{k+1} &= \hat{p}^+_k \\
\hat{p}^+_{k+1} &= \hat{p}^-_{k+1} + L^p(w_{k+1} - q(\hat{z}))
\end{aligned} \tag{6.14}$$

Here, L^p is the fixed gain used to update the parameters. The supercript $^-$ denotes the value of the parameter before updating – an infinitesimal time instant before the measurement, and the supercript $^+$ denotes the value after updating using the current measurement. Essentially, the parameters are updated at each time instant a measurement is available, and are held constant until the next measurement. The error in the lumped outputs, total particles and solids content (which represent moments of the full distribution), are used to update the parameters, *i.e.,* only those corresponding rows of w are utilized.

Figure 6.33 compares the estimated profiles of total particles and solids content, and the end-point PSD, with the experimental observations. The estimation scheme captures the delay in the secondary nucleation event and also reduces the

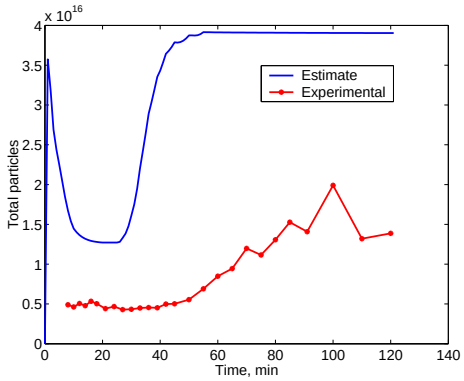

(a) profile of total particles

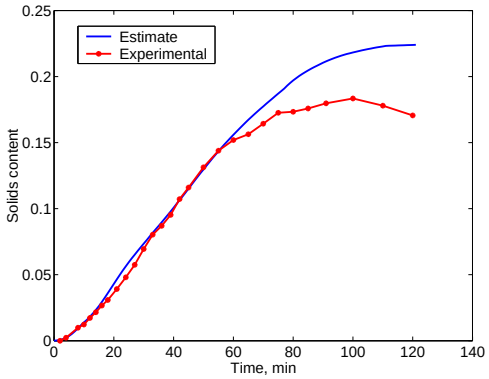

(b) profile of solids content

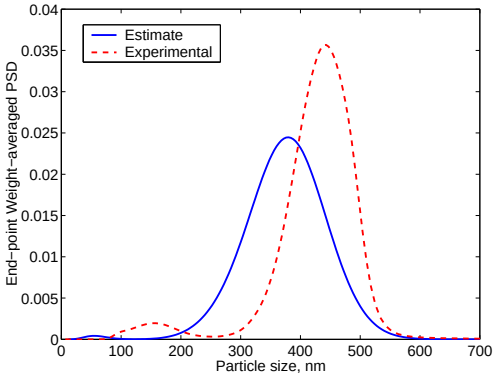

(c) end-point distribution

Figure 6.33: Comparison of the estimates based on a Luenberger estimator with parameter updating, with the experimental data.

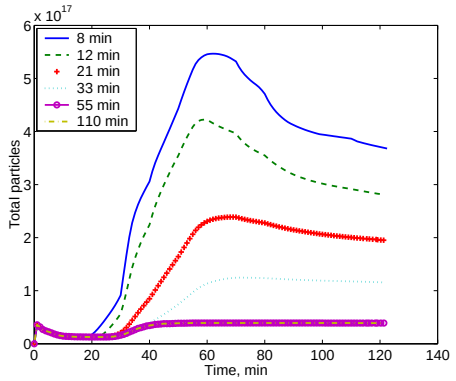

(a) profile of total particles

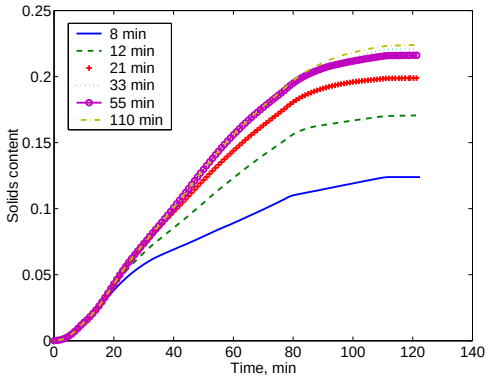

(b) profile of solids content

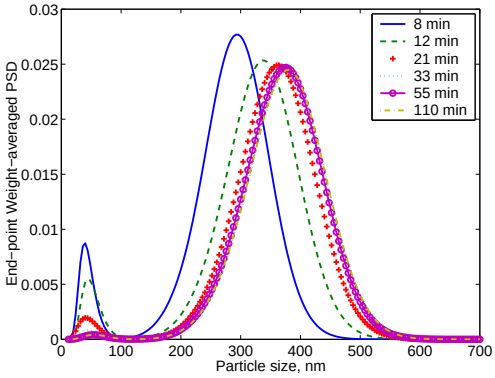

(c) end-point distribution

Figure 6.34: The convergence of the estimates based on Luenberger estimator, with availability of additional data.

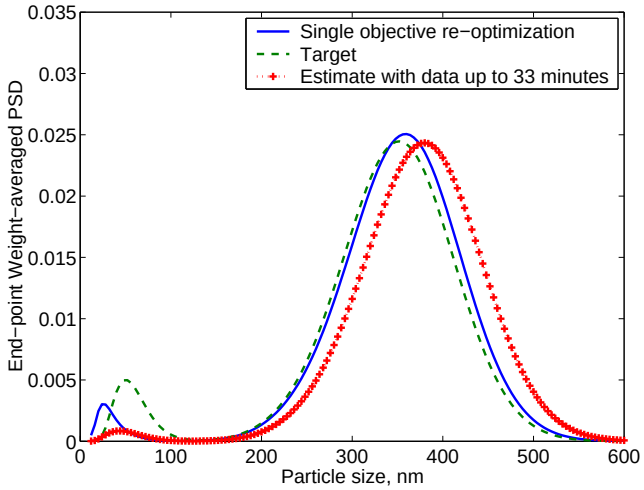

Figure 6.35: Single-objective re-optimization of the inputs, based on a Luenberger estimator with parameter updating, utilizing data up to 33 minutes into the batch.

number of particles nucleated during the secondary nucleation event. The parameter updating also corrects the overall growth rate, and pushes the particles closer to the experimental end-point PSD, by correcting k_{p11}. However, this results in an increased error in the solids content. The discrepancy seen in the end-point PSD is mainly due to the irreversible effects during the first sample time in the batch. This suggests the need for not only a parameter update as one progresses with the batch (receding horizon), but *a need to update the initial conditions* (and simulate the entire batch after each data is available). Since the model simulates a larger number of particles at early times, there is a reduced growth rate which accounts for the discrepancy in the size of the larger mode. Although the size can be corrected by adjusting the parameters, the spread of the distribution is dictated by the early nucleation rate and cannot be corrected in a receding horizon formulation (there is no input to manipulate the competitive growth). Also, the relative magnitude of the two modes cannot be corrected as the number of particles nucleated in the primary mode cannot be taken away in a receding horizon formulation.

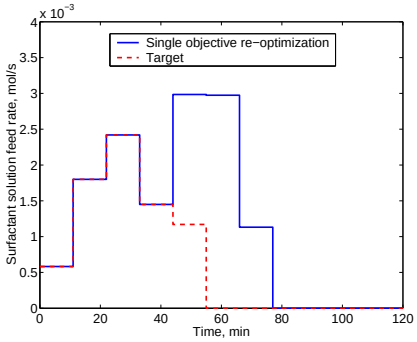

(a) profile of surfactant feed rate

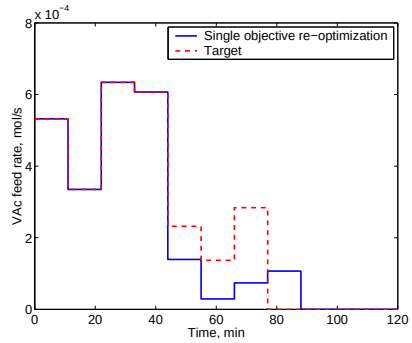

(b) profile of vinyl acetate feed rate

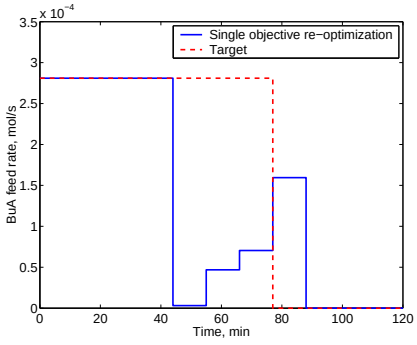

(c) profile of butyl acrylate feed rate

Figure 6.36: Inputs corresponding to the results presented in Figure 6.35, re-optimized from 44 minutes into the batch.

Figure 6.34 shows the change in the estimates as more samples are utilized. As one would expect, these results indicate a better convergence as more data are utilized. The estimates utilizing the samples up to 55 minutes converge completely with the one corresponding to using all the samples (and no better estimates are available beyond this time point). Even at an earlier time, say 21 or 33 minutes, the estimation is quite close to convergence. These earlier estimates capture the delaying of the nucleation, and also partially capture the reduced secondary nucleation event. Although it may not be advisable to base the re-computation of the inputs on the sample at 8 minutes alone, or even on samples at 8 minutes and 12 minutes, one can choose a time between 21-33 minutes to perform the *first* re-computation. This could prevent any irreversible effects on the distribution.

6.5.2.1 Single-objective Re-optimization Based on Luenberger Observer

Figures 6.35 and 6.36 show the results corresponding to a re-computation of the inputs using the data sampled up to 33 minutes (available at approximately 44 minutes). This is based on a single objective re-optimization, namely, minimization of the deviation in the end-point weight-averaged PSD ($\theta_3(t_f)$). The surfactant feed in intervals 5-7, and the feed of both monomers in intervals 5-8 are re-computed. The inputs in this case drive the solution closer to the target, relative to the estimate (Figure 6.35). The error in the smaller mode is partly due to limitations with the objective function choice that was discussed earlier – with no single objective function having the capability to describe all aspects of the distribution. In this case, the surfactant feed in the fifth interval hits the upper constraint, and that in the sixth interval is close to the upper constraint, to cause a larger nucleation event (Figure 6.36(a)). The monomer feeds in these immediate intervals are reduced significantly to affect the growth rates and the particle sizes (Figures 6.36(b) and 6.36(c)). Thereafter, nucleation is reduced, and the optimizer tries to raise the growth rate to accommodate the smaller mode within the target.

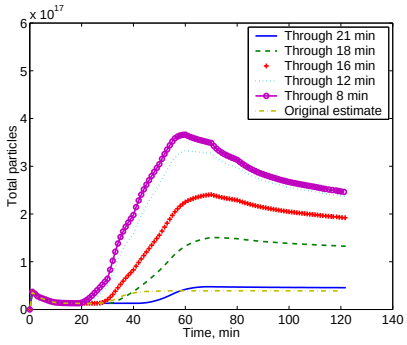

(a) profile of total particles

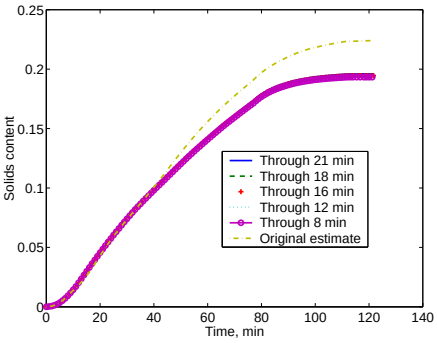

(b) profile of solids content

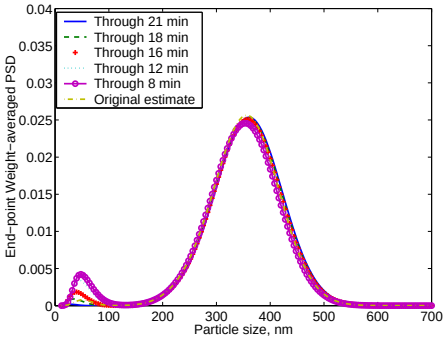

(c) end-point distribution

Figure 6.37: Estimates based on discrete parameter updating using the early measurements of solids content, compared with the estimates based on the Luenberger continuous-discrete state/parameter estimator. The parameter updating is stopped after the time shown in the legend of the various cases.

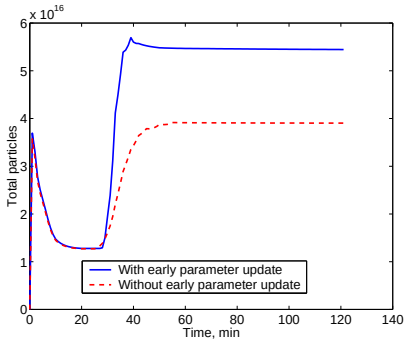

(a) profile of total particles

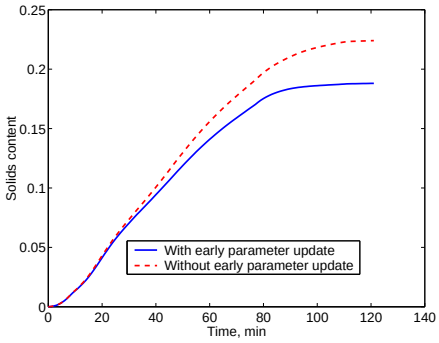

(b) profile of solids content

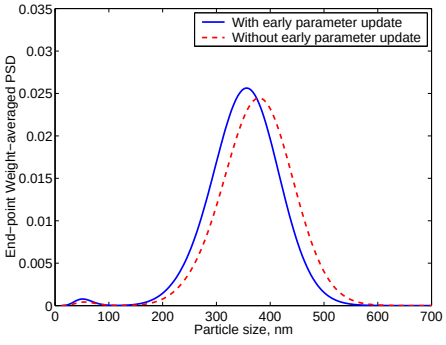

(c) end-point distribution

Figure 6.38: Estimates based on utilizing both the early solids content data for parameter updating, and later measurements (PSD, total particles and solids content) for state/parameter updating (labeled as 'sc and PSD data'). These are compared with the case when the early solids content data are not employed for parameter updating.

6.5.3 Observability Issues Based on Solids Content Measurements

The potential benefit of feedback control that was described previously, is predicated on observability of key states at early batch times. An evaluation of that observability is performed as follows. The parameters (alone) are updated based on the solids content measurements until the time when the first PSD measurement is available. Thereafter the batch is run in open-loop. The corresponding observer is given below:

$$\begin{aligned}
\dot{\hat{x}} &= f(\hat{x}, \hat{p}, \hat{y}, \hat{z}, u) \\
\hat{y} &= g(\hat{x}, \hat{p}) \\
\hat{z} &= h(\hat{y}) \\
\dot{\hat{p}} &= 0 \\
\hat{p}^{-}_{k+1} &= \hat{p}^{+}_{k} \\
\hat{p}^{+}_{k+1} &= \hat{p}^{-}_{k+1} + L^{p}(w_{k+1} - q(\hat{z}))
\end{aligned} \tag{6.15}$$

Figure 6.37 shows the estimated profiles of total particles and solids content, and the estimated end-point PSD, when solids content samples up to various cut-off times are utilized to update the parameters. The estimates corresponding to the earlier state-parameter estimator (utilizing all measurements) are also shown in these figures (labeled as 'Original estimate'). It is seen that using all solids content measurements through 21 minutes (which is approximately the time when the first PSD measurement is available) gives very close estimates to the ones obtained from the earlier estimation strategy. Figure 6.38 examines the case wherein the early parameter updating (based on the solids content measurements) is combined with the later state/parameter correction in the continuous-discrete formulation that was presented earlier. These show improvements, particularly in the profile of solids content. But the major impact is the ability to observe the process trends at very

early times of the batch. These results show the potential to extract information on the total particles and the nucleation rates even at times before the availability of PSD data. This could substantially improve feedback control, with the early prevention of irreversible effects.

6.6 Summary

Optimal recipes to attain a target PSD in the semi-batch emulsion polymerization of vinyl acetate and butyl acrylate were developed using a Genetic Algorithm. The optimal recipes were implemented in the experimental reactor setup. The experimental implementation reveals two important aspects:

1. The unidirectionality that characterizes several aspects of the process of evolution of PSD, particularly coagulation, and hence the need for a model with very good predictive capabilities to be employed in open-loop recipe generation.

2. Feedback can be utilized to correct multi-modal distributions, especially when the objective is to only preserve the shape of the distribution (relative distribution). Utilizing the feed rate of water as an additional handle enhances the reachability of the absolute distributions as well. Due to the complexity of the process, a model predictive controller based on a nonlinear process model would be effective for feedback purposes. This is due, in large part, to the requirement of coordinating several mechanisms for the successful control of PSD. For example, to correct an error in the nucleation of the first mode, the timing and magnitude of the nucleation of the second mode needs to be carefully determined. It is also due to the multivariable nature of the process, with strong interactions.

The first aspect can be addressed in part by batch-to-batch improvements of the recipe, by correcting for the model uncertainties using the repeated batch history.

However, the shear-induced coagulation could complicate such a scheme in its role as a random process disturbance.

An extension of the study is the proposal of a novel strategy for recipe design that attains a target PSD at the end of a batch. The proposed method is hierarchical, in which the desired PSD is produced by manipulating the individual rates of nucleation, growth and coagulation over the course of the batch. The idea of the control of instantaneous properties is invoked in implementing the technique. The problem of the attainment of a desired PSD is decomposed into one of tracking profiles of nucleation and growth rates, with coagulation minimized. This in turn is re-cast as an equivalent problem of tracking profiles of total particles and solids content, with coagulation minimized. While the tracking of the two profiles constitute two specific objectives, a third objective on the full distribution itself is also added to the formulation. The Non-dominated Sorting Genetic Algorithm (NSGA) is used as the optimization technique to solve the resultant multi-objective problem, and to produce the pareto-optimal solutions. The new strategy is effective in identifying solutions that match the target very closely, compared to the previous single-objective formulation which was faced with the inability of defining a suitable objective function in terms of the full distribution. Experimental implementation produces results that are close to the target. The explicit incorporation of the coagulation events in the model avoids any conspicuous coagulation events in the results. The results however show differences attributed to the inevitable implementational and model uncertainties, thereby motivating the use of feedback control.

An analysis of several state estimation and feedback strategies is performed. The underlying on-line state estimation is very complex, consisting of multi-rate characteristics and delayed measurements. In the current study, the estimation was performed off-line. It was found that a combined state/parameter estimation strategy is essential. The estimation was performed using a Luenberger observer

with a continuous state update and a discrete parameter update. Further, it was observed that a pure receding horizon estimation would not be very effective, and an update of the initial conditions also is essential as each data point becomes available (at least for the early portion of the batch). However, there are also cases in which a simple biased estimator (even without parameter update) is effective in converging to the experimental data. It is also important to account for noise and disturbances. The last aspect was not pursued in the current study. Another observation that has a profound implication for feedback control is the ability to influence the states on the basis of the solids content values (from the more frequent densitometer and load cell measurements). The early solids content measurements can be utilized to get estimates of total particles and free surfactant concentration values. This would enable earlier feedback correction. The general aim of feedback control of PSD (as addressed in this paper) was to regulate the timing, duration and magnitude of the secondary nucleation event and the overall growth rates to thereby match the target PSD on a relative basis. These early estimates will substantially aid in regulating both the secondary nucleation event and growth. But they can also potentially aid in regulating the primary nucleation event (and hence attain the target PSD on an absolute basis). However, this is only true for negative errors in the number of particles. Also, the shape of the primary mode may not be correctable, as nucleation and growth are inter-related (and not sequential) processes.

The state estimation studies show the need to delay the re-computation until approximately 4-6 data points are available. The re-optimized results are encouraging in their ability to drive the solutions closer to the target. The implementation of a full nonlinear MPC beyond this point would be a desirable strategy. At a minimum, re-computation at several instances would be needed (as opposed to a single re-computation). A statistical fault detection tool (Flores-Cerrillo and MacGregor, 2002) might be a possibility to compensate for measurement noise. A

batch-to-batch re-computation (Clarke-Pringle and MacGregor, 1998; Crowley et al., 2001; Lee et al., 2002) could complement in-batch feedback for the control of PSD in semi-batch emulsion polymerization. An off-line parameter/state estimator similar to the one considered in this study can be employed, utilizing all data points available from previous batches. These parameter estimates can be utilized to re-optimize the inputs for the subsequent batches, using the straightforward methods presented here.

Table 6.5: Nomenclature

r	Particle radius
r_{nuc}	Smallest particle radius
r_{max}	Largest particle radius
$\Re_{nuc}$	Rate of nucleation
$\Re_{coag}$	Rate of coagulation
$\Re'_{entry}(r)$	Rate of entry of oligomers into a particle of size r
$\Re'_{desorption}(r)$	Rate of desorption of monomeric radicals from within a particle of size r
$\Re'_{termination}(r)$	Rate of termination within a particle of size r
N_{pop}	Number of members in a population
N_{gen}	Number of generations
u_i	Feed rate in interval i
u_{min}	Minimum feed rate in interval i
u_{max}	Maximum feed rate in interval i
u_{bk}	Binary value at the k^{th} position of a chromosome
c	Constrained variable
c_{min}	Lower bound on the constrained variable
c_{max}	Upper bound on the constrained variable
θ_i	Objective value of member i of the population
θ_i^{comb}	Augmented objective value of member i of the population
fit_i	Fitness of member i of the population
θ_{ref}	Reference objective value for fitness calculation
p_{cross}	Cross-over probability
p_{mut}	Mutation probability
l_{chrome}	Length of chromosomes
ω	Parameter (> 1) in fitness calculation
$F(r,t)$	Particle density function
$W(r,t)$	Weight-averaged particle density (probability density function)
$\bar{n}(r,t)$	Average number of active radicals in particle of size r at time t
$n_{ave}(t)$	Global average number of radicals per particle
$F_{ref}(r)$	Target PSD
t_f	Batch time

Chapter 7

CONCLUSIONS AND FUTURE WORK

The dissertation presents a study aimed at the control of distributions and profiles, mainly in the nanoscale and sub-micron scale. This is motivated by a potentially substantial improvement in process performance and product quality obtainable in pursuing the control of entire distributions. The major contributions of the project are summarized below, along with recommendations for future studies. The particular system investigated is the emulsion co-polymerization of vinyl acetate and butyl acrylate, employing non-ionic surfactants as emulsifier and a redox pair t-butyl hydrogen peroxide and sodium formaldehyde sulphoxylate as initiator (with ferrous ammonium sulphate as the coordination agent). The objective is the control of PSD in semi-batch operation. The dissertation treats the specific application of PSD in emulsion polymerization completely, although a certain generality for population balance systems is attempted. The instrumentation considerations and the mathematical modeling would be very specific for different systems. However, these are very crucial steps towards control of distributions, justifying the investment of time and resources in these studies. On the other hand, *the analysis, computational method, optimization and control ideas presented here are valid for all such systems*, and can be easily adapted to different applications.

7.1 Instrumentation and Monitoring

The instrumentation employed in this study include flow meters and load cells for feed rate measurements (inputs), resistance temperature detector for temperature measurement (input), densitometer for latex density measurement (output) and

most importantly, a capillary hydro-dynamic fractionator (CHDF) for PSD measurement (outputs). The CHDF enables monitoring the sub-micron phase of interest, at sufficiently rapid frequency for on-line control. This equipment in particular, but all the equipment in general, show very good reproducibility characteristics. This, coupled with the overall reproducibility of the process itself, justifies feedback control measures (in-batch and batch-to-batch).

A *mechanistic calibration procedure*, using a simple steady state model, was presented. This enables extracting all *relevant process information from fewer instruments*. Automated plant operation and historization of data were performed employing the Honeywell DCS system, Plantscape, to facilitate future on-line control studies. The study was restricted to lower solids content (below 25%) for most cases. The few experiments aimed at higher solids were faced with excessive coagulation problems and clogging of the sampling loop.

7.2 Modeling and Computational Algorithm

A detailed population balance model was developed for the evolution of PSD in semi-batch emulsion polymerization. In addition to consolidating the various theories on each of the underlying phenomena into a single study, the model presented here proposes several novel aspects for the population balance modeling of PSD in emulsion polymerization. A significant modification as regards the nucleation event is the incorporation of the partitioning of the surfactants into the bulk of the dispersed phases. This modification accounts for the more complex nucleation phenomenon observed in such systems. In modeling the growth phenomena, a first principles-based formulation is proposed to model the average number of radicals/particle – casting this distributed variable in a population balance framework. The improvements obtained clearly show the disadvantage with lumped parameter modeling, and motivate the use of a distributed approach where possible. This also hints at the additional factors that contribute to improvement of product quality

while pursuing the distributed approach, besides the ability to engineer application-specific distributions. The new formulation preserves the size-dependence of the growth kernel, captures the broadening of the distributions with growth (both effects seen experimentally), and also obviates the need for incorporating artificial dispersion terms in the population balance equation. Another primary contribution of this study is on the modeling of the coagulation kernel under steric stabilization with non-ionic surfactants. The literature on the population balance modeling of the coagulation phenomenon in emulsion polymerization deal with ionic surfactants wherein the stabilizing mechanism is electrostatic repulsion. In this study, a method is proposed for the calculation of the size-dependent intrinsic coagulation rate for emulsion recipes employing non-ionic surfactants. Steric stabilization under the influence of adsorbed surfactants is modeled as the primary stabilizing mechanism. However, empirical allowances are made to account for other mechanisms that influence coagulation, such as the shear effects.

The model can be used to simulate all types of emulsion recipes that could be of interest to practitioners. The coagulation-inclusive complete model shows a very good qualitative validity and an acceptable quantitative validity when compared to the experimental observations. The parametric sensitivity studies provide insight as to the sections of the process affected by the various parameters. This information can be utilized in parameter fitting, to preserve the extrapolative abilities of the model. However, the strong sensitivity of the results to the model parameters sets stringent requirements on the accuracy of the model parameters, from the perspective of optimization and control. Hence, a better strategy would be to identify the model parameters (particularly the most sensitive ones as revealed in this study) independently, through separate instrumentation. Such studies are underway in several research groups, and can be exploited in this multi-disciplinary research. For the purposes of on-line control of PSD, a combined parameter-state

estimator can be employed to account for the uncertainties in the model simultaneously, while inferring the relevant feedback informations necessary for control. Such state/parameter estimation studies were performed, which shows the ability to bridge the gap between theory and experiments.

A new computational technique was developed, which in essence is a order-reduction technique based on process considerations. This technique circumvents the stiffness problem inherent in the complete system, by decomposing the faster and the slower modes. Also, a semi-analytical solution strategy is adopted for the coagulation events to facilitate efficient computation. The solution times for the simulation of typical batches is such that it enables the application of on-line feedback control on the process, in a receding horizon framework. *The algorithm presented is sufficiently general to be applicable to other population balance systems.*

7.3 Process Sensitivity and Reachability Studies

Experimental studies on the sensitivity of the evolution of PSD and other relevant process variables to available inputs were studied. These identify suitable manipulated variables, reveal the uni-directionality (irreversibility) in the process – which could cause concerns for on-line control – and a possible hierarchical cascaded control strategy for PSD – by regulating the individual processes of nucleation, growth and coagulation at a lower level. In particular, they highlight the necessity of employing multiple inputs (surfactant feed and monomer feed). *Most of these aspects clearly hold for all systems characterized by nucleation, growth and coagulation/breakage (population balance systems).* However, in adapting these ideas to different systems, one needs to identify suitable manipulated variables for the specific system.

Reachability studies were performed to identify the type of distributions that can be produced under *ab initio* and seeded conditions. These were formulated such that the 'reachable' distributions are also 'controllable' (*i.e.,* retain their state

beyond the end-point). A simple simulation-based methodology is adopted here to perform the reachability analysis on the complex system, as the complexity of the system precludes the application of more formal mathematical analysis tools. The study also provides an inkling about the effect of uncertainties and disturbances, and the potential (in)ability to employ feedback correction in certain cases. However, the reachable distributions identified are reachable in an *absolute* sense, based on using a model that has been validated against experimental data. Relaxing this stringent constraint to identify distributions that are reachable within an allowable tolerance limit might be necessary and useful, and might widen the reachable regions. The reachable regions also depend upon the parameterization employed for the inputs, as revealed in the study. Thus, *more complex distributions can potentially be produced contingent upon the ability to employ complex input profiles.*

7.4 Open-loop and Feedback Studies

In performing optimization studies on the system, the traditional gradient-based optimization strategies have a limited applicability. This is partly because of the computational burden of obtaining the (numerical) gradients and Hessians. Thus, a direct optimization technique – a genetic algorithm (GA) – is employed here. Evolutionary techniques such as GA, and other direct optimization techniques such as simulated annealing, are very viable alternatives to traditional optimization techniques for complex distributed parameter problems. Formulating the optimization problem in a straightforward manner in terms of the full PSD produces satisfactory results, subject to process and target limitations. However, exploiting process knowledge gained from the sensitivity studies, and employing a hierarchical strategy to formulate the optimization problem, through the use of instantaneous property control concepts, removes the limitations in the straightforward formulation and produces much better results. This latter approach calls for a multi-objective strategy, which is again obtained from an extension of the GA – the non-dominated

sorting genetic algorithm. *The hierarchical strategy proposed here could potentially be exploited for all other systems in this class.*

Preliminary state estimation and feedback control studies were performed. This is relevant because of the irreversibility in the system, which implies that on-line feedback control might be ineffectiveness. The primary goal is to evaluate the benefits of on-line control. State estimation shows the potential to eliminate the uncertainties in the model. Requirements from a suitable state estimation strategy were identified. These include the need for parameter-augmentation of the states, and the re-estimation of the initial conditions. Observability based on early measurements indicate the ability for early corrective action, which has a profound bearing on on-line feedback control. Multiple receding horizon re-computation might be needed for in-batch feedback control of PSD. A batch-to-batch strategy along the same lines presented here is a valuable complement or alternative to in-batch correction. These aspects need to be studied in detail, and implemented on-line.

7.5 Future Work

Recommendations for future research in this subject focus on two different aspects – the extension of the study on PSD control in emulsion polymerization; and applications of the proposals made in the present study to general population balance systems.

7.5.1 Extensions to Emulsion Polymerization

1. Traditional approach to efficient process operation is based on open-loop and closed-loop optimization of the process performance. Open-loop considerations deal with the optimal design of the process. Closed-loop considerations focus on the effect of model uncertainties and process disturbances. The present study revealed the unidirectionality in the process, which adds a new dimension to efficient process operation, by limiting the capabilities of on-line feedback. This suggests a need for incorporating *robust considerations into*

the open-loop optimization of the process. One method of accounting for the uncertainties in optimal process design is based on worst-case analysis and H_∞ considerations (Ma et al., 1999; Skogestad and Postlethwaite, 1996). Robustness can be incorporated into the GA formulation by choosing the objective function to be the maximum error subject to a range of uncertain parameters Θ. For example, in the single objective optimization problem based on the absolute distribution matching, the objective function can be defined as

$$\theta^i =_{\Theta}^{max} \int_{r_{nuc}}^{r_{max}} (F(r,t_f) - F_{ref}(r))^2 dr \tag{7.1}$$

Here, the vector Θ accounts for the uncertainties including the model parameters and the implementational uncertainties (feed rates, pump delays, *etc.*). The parametric sensitivity results presented in this study can be utilized to perform this optimization. Alternatively, since the study if performed off-line, separate simulations can be carried out for every possible scenario to determine the worst-case situation.

In the study presented here, the inputs were parameterized as zero-order holds in intervals of a fixed duration. The incorporation of *the duration of the various feed intervals as decision variables* (Biegler, 2000) might be beneficial, as revealed in the sensitivity studies of Chapter 5.

The identification of target distributions that lead to desired properties in the latex is itself a challenging task. The uncertainties in this identification might also be factored into the formulation, by the *optimization of the recipe to produce a class of distributions* rather than a specific target distribution.

2. The exploration of the applicability of the concepts proposed, and particularly the model developed, to higher solids content emulsion polymerization is another area of interest, for solids content exceeding 25%. The model presented here is general in terms of the process of the nucleation, growth and

coagulation phenomena. However, the model proposed for the coagulation phenomenon is a compromise between complexity and computational requirements. Incorporation of a more detailed calculation of the coagulation kernel might be necessary in the high solids regime, in which the coagulation events assume further importance. Studies such as those presented by Kiparissides *et al.* (1993) and Fritz *et al.* (2002) can be used as a basis for this model extension. Another critical issue to be addressed is the effect of mixing. This was sought to be incorporated in an empirical manner in the current model. However, the mixing effects are very complex and might need profound modifications as more theory on these become available. In particular, *the elucidation of the relation between the mixing patterns and the energetics in the coagulation kernel is a crucial step* in solving this critical problem.

3. A detailed sensitivity analysis of the process was performed, as an attempt to correlate the available inputs with the outputs of interest. The applicability of these findings to different situations, particularly to the *emerging modifications of the process such as enzyme-catalyzed emulsion polymerization* would serve useful purpose in adapting these processes to the industrial scale.

4. Parameter identification studies, to provide better match between simulations and experiments, is a very crucial step. The important parameters are those corresponding to surfactant partitioning and the nucleation phenomena. One way to tackle the uncertainties in these parameters is to incorporate an on-line parameter update. This approach bestows a generality on the model to different surfactant and polymerization systems, based on a nominal knowledge of the parameters involved. Such an approach was briefly demonstrated in this study. Another way to tackle the parametric uncertainty is to identify the model parameters separately, employing specific instrumentation. Such

studies are underway in several research laboratories, such as in the group of Prof. Larry Duda at Penn State University.

5. A suitable on-line feedback control strategy was proposed for this process, which is a compromise between early correction and good estimation. In particular, a full nonlinear receding horizon control, but delayed until 4-5 PSD measurements are available, is a suitable strategy. However, to address the issue of irreversibility with respect to each of nucleation, growth and coagulation, a batch-to-batch improvement will prove to be a valuable complement, if not alternative, to in-batch control (Clarke-Pringle and MacGregor, 1998). Lastly, the demonstration of on-line control of PSD on the lab-scale facility is a valuable step from an industrial perspective. A major issue to tackle in this regard is the interfacing of the codes developed with the DCS system, to perform the computations on-line.

7.5.2 Applications to General Population Balance Systems

Several novel tools and algorithms were proposed in this study for PSD control in emulsion polymerization. These include the computational algorithm, the hierarchical control strategy, and the application of direct optimization techniques. Even though these developements focus on the specific problem of PSD in emulsion polymerization, the concepts are applicable to the general class of population balance systems. This was illustrated in the case of the efficient solution technique in Chapter 4, with indications to potential modifications required for different systems. Demonstration of this generality of the concepts in systems such as crystallization, granulation, cell population and precipitation, and the proposal of modification as warranted by the specific applications, are of interest. For example, the development of such efficient models for cell populations would enable the study of abnormal situations such as cancerous conditions, which in turn leads to proposition of control

measures. Addressing the issues of cell division/birth and cell growth individually would facilitate analysis and treatment.

BIBLIOGRAPHY

Adrover, A., Continillo, G., Crescitelli, S., Giona, M. and Russo, L. (2002). Construction of approximate inertial manifold by decimation of collocation equations of distributed parameter systems, *Comp. Chem. Eng.* **26**: 113–123.

Araujo, P. H. H., de la Cal, J. C., Asua, J. M. and Pinto, J. C. (2001). Modeling Particle Size Distribution (PSD) in Emulsion Copolymerization Reactions in a Continuous Loop Reactor, *Macromol. Theory Simul.* **10**: 769–779.

Astorga, C. M., Othman, N., Othman, S., Hammouri, H. and McKenna, T. F. (2002). Nonlinear continuous-discrete observers: application to emulsion polymerization reactors, *Cont. Eng. Prac.* **10**: 3–13.

Asua, J. M. (ed.) (1996). *Polymeric Dispersions: Principles and Applications*, Vol. 335 of *Applied Sciences*, Kluwer Academic Publishers.

Bandyopadhyaya, R., Kumar, R., Gandhi, K. S. and Ramkrishna, D. (1997). Modeling of Precipitation in Reverse Micellar Systems, *Langmuir* **13**: 3610–3620.

Behnken, D. W., Horowitz, J. and Katz, S. (1963). Particle Growth Processes, *Ind. Eng. Chem. Funda.* **2**(3): 212–216.

Bhaskar, V., Gupta, S. K. and Ray, A. K. (2000). Multiobjective Optimization of an Industrial Wiped-film PET Reactor, *AIChE J.* **46**(5): 1046–1058.

Biegler, L. T. (2000). Efficient Solution of Dynamic Optimization and NMPC Problems, *in* F. Allgower and A. Zheng (eds), *Progress in Systems and Control Theory: Nonlinear Model Predictive Control*, Vol. 26, Birkhauser, pp. 219–243.

Braatz, R. D. and Hasebe, S. (2001). Particle Size and Shape Control in Crystallization Processes, *in* J. B. Rawlings, B. A. Ogunnaike and J. W. Eaton (eds), *AIChE Symposium Series: Chemical Process Control-VI*, Vol. 98 of *326*, pp. 307–327.

Chen, S. and Wu, K. (1988). Emulsion polymerization: Theory of particle size distribution in copolymerization systems, *Journal of Polymer Science, Part A: Polymer Chemistry Ed.* **26**: 1487–1506.

Chern, C.-S., Lin, S.-Y., Chen, L.-J. and Wu, S.-C. (1997). Emulsion polymerization of styrene stabilized by mixed anionic and nonionic surfactants, *Polymer* **38**(8): 1977–1984.

Chiu, T. and Christofides, P. D. (1999). Nonlinear Control of Particulate Processes, *AIChE J.* **45**(6): 1279–1297.

Choi, K. Y. and Butala, D. N. (1991). An experimental study of multiobjective dynamic optimization of a semibatch copolymerization process, *Polym. Eng. Sci.* **31**: 353.

Christofides, P. D. (2002). Control of Nonlinear Distributed Parameter Systems: An Overview and New Research Directions, *AIChE J.* pp. 341–346.

Clarke-Pringle, T. and MacGregor, J. (1998). Optimization of Molecular-Weight Distribution Using Batch-to-Batch Adjustments, *Ind. Eng. Chem. Res.* **37**: 3660–3669.

Coen, E. M., Gilbert, R. G., Morrison, B. R., Leube, H. and Peach, S. (1998). Modeling particle size distributions and secondary particle formation in emulsion polymerisation, *Polymer* **39**(26): 7099–7112.

Congalidis, J. and Richards, J. (1998). Process Control of Polymerization Reactors: An Industrial Perspective, *Polymer Reaction Engineering* **6**(2): 71–111.

Crowley, T. J., Harrison, C. A. and Doyle III, F. J. (2001). Batch-to-batch Optimization of PSD in Emulsion Polymerization using a Hybrid Model, *Proc. American Control Conf.*, Arlington, VA, pp. 981–986.

Crowley, T., Meadows, E. and Doyle III, F. (1999). Numerical issues in solving population balance equations for particle size distribution control in emulsion polymerization, *Proceedings of the 1999 American Control Conference.*

Crowley, T., Meadows, E., Kostoulas, E. and Doyle III, F. (2000). Control of Particle Size Distribution described by a Population Balance Model of Semibatch Emulsion Polymerization, *J. Proc. Cont.* **10**: 419–432.

Daoutidis, P. and Henson, M. A. (2001). Dynamics and Control of Cell Populations in Continuous Biorroeact, *in* J. B. Rawlings, B. A. Ogunnaike and J. W. Eaton (eds), *AIChE Symposium Series: Chemical Process Control-VI*, Vol. 98 of *326*, pp. 274–289.

de la Rosa, L. V. (1996). *Emulsion Polymerization of Styrene using an Automated Reaction Calorimeter*, PhD thesis, Emulsion Polymerization Institute, Lehigh University.

DeGraff, A. W. and Poehlein, G. W. (1971). Emulsion polymerization of styrene in a single continuous stirred -tank reactor, *Journal of Polymer Science, Part A-2* **9**: 1955–1976.

Delgado, J., El-Aasser, M. S., Silebi, C. A., Vanderhoff, J. W. and Guillot, J. (1988). Miniemulsion copolymerization of vinyl acetate and butyl acrylate. ii. mathematical model for the monomer transport, *Journal of Polymer Science: Part B: Polymer Physics* **26**: 1495–1517.

Dimitratos, J., Georgakis, C., El-Aasser, M. and Klein, A. (1991). An Experimental Study of Adaptive Kalman Filtering in Emulsion Copolymerization, *Chem. Eng. Sci.* **46**(12): 3203–3218.

Dimitratos, J., Georgakis, C., El-Aasser, M. S. and Klein, A. (1989). Dynamic Modeling and State Estimation for an Emulsion Copolymerization Reactor, *Computers Chem. Engng.* **13**(1/2): 21–33.

Dos Ramos, J. G. and Silebi, C. A. (1993). Submicron particle size and polymerization excess surfactant analysis by capillary hydrodynamic fractionation (CHDF)., *Polymer International* **30**(4): 445–450.

Doyle III, F. J., Soroush, M. and Cordeiro, C. (2001). Control of Product Quality in Polymerization Processes, *in* J. B. Rawlings, B. A. Ogunnaike and J. W. Eaton (eds), *AIChE Symposium Series: Chemical Process Control-VI*, Vol. 98 of *326*, pp. 290–306.

Evans, D. F. and Wennerstrom, H. (1999). *THE COLLOIDAL DOMAIN Where Physics, Chemistry, Biology, and Technology Meet*, Second edn, Wiley-VCH.

Falk, L. and Schaer, E. (2001). A PDF modeling of precipitation reactors, *Chem. Eng. Sci.* **56**: 2445–2457.

Finlayson, B. A. (1980). *Nonlinear Analysis in Chemical Engineering*, McGraw-Hill, New York.

Flores-Cerrillo, J. and MacGregor, J. F. (2002). Control of Particle Size Distribution in Emulsion Semi-batch Polymerization using Mid-course Correction Policies, *Ind. Eng. Chem. Res.* **41**: 1805–1814.

Forcada, J. and Asua, J. M. (1990). Modeling of Unseeded Emulsion Copolymerization of Styrene and Methyl Methacrylate, *Journal of Polymer Science, Part A: Polymer Chemistry Edition* **28**: 987–1009.

Fredrickson, A. G. and Tsuchiya, H. M. (1963). Continuous Propagation of Microorganisms, *AIChE J.* **9**(4): 459–468.

Fritz, G., Schadler, V., Willenbacher, N. and Wagner, N. J. (2002). Electrosteric Stabilization of Colloidal Dispersions (To appear), *Langmuir*.

Garcia, C. E. and Morari, M. (1982). Internal Model Control 1. A Unifying Review and Some New Results, *IEC Process Design and Development* **21**: 308–323.

Garcia, C. E. and Morshedi, A. M. (1986). Quadratic Programming Solution of Dynamic Matrix Control, *Chem. Eng. Commun.* **46**: 73–87.

Gatzke, E. P. and Doyle III, F. J. (2001). Model predictive control of a granulation system using soft output contstraints and prioritized control objectives, *Powd. Tech.* **121**: 149–158.

Gerstlauer, A., Mitrovic, A., Motz, S. and Gilles, E.-D. (2001). A population model for crystallization processes using two independent particle properties, *Chem. Eng. Sci.* **56**: 2553–2565.

Gilbert, R. G. (1995). *Emulsion Polymerization: A Mechanistic Approach*, Academic Press, San Diego.

Giona, M., Adrover, A., Pagnanelli, F. and Toro, L. (2002). A closed-form solution of population-balance models for the dissolution of polydisperse mixtures, *Chem. Eng. Journal* **87**: 275–284.

Godin, F. B., Cooper, D. G. and Rey, A. D. (1999). Numerical Methods for a Population-Balance Model of a Periodic Fermentation Process, *AIChE J.* **45**(6): 1359–1364.

Goldberg, D. E. (1989). *Genetic Algorithm in Search, Optimization, and Machine Learning*, Addison-Wesley Publishing Company, Inc., Reading, MA.

Gupta, S. K. (1995). *Numerical Methods for Engineers*, Wiley Eastern.

Holland, C. D. and Liapis, A. I. (1983). *Computer Methods for Solving Dynamic Separation Problems*, McGraw-Hill Book Company.

Hollander, E. D., Derksen, J. J., Bruinsma, O. S. L., van den Akker, H. E. A. and van Rosmalen, G. M. (2001). A numerical study on the coupling of hydrodynamics and orthokinetic agglomeration, *Chem. Eng. Sci.* **56**: 2531–2541.

Hounslow, M. J., Ryall, R. L. and Marshall, V. R. (1988). A discretized population balance for nucleation, growth and aggregation, *AIChE J.* **34**: 1821–1832.

Israelachvili, J. (1998). *Intermolecular and Surface Forces*, Second edn, Academic Press.

Jazwinsky, A. H. (1970). *Stochastic Processes and Filtering Theory*, Academic Press, NY.

Kammona, O., Chatzi, E. G. and Kiparissides, C. (1999). Recent Developments in Hardware Sensors for the On-Line Monitoring of Polymerization Reactions, *J. M. S.-Rev. Macromol. Chem. Phy.* **C39**(1): 57–134.

Kauchali, S., Rooney, W. C., Beigler, L. T., Glasser, D. and Hildebrandt, D. (2002). Linear programming formulations for attainable region analysis, *Chem. Eng. Sci.* **57**: 2015–2028.

Kiparissides, C., MacGregor, J. F. and Hamielec, A. E. (1979). Continuous emulsion polymerization. modeling oscillations in vinyl acetate polymerization, *Journal of Applied Polymer Science* **23**: 401–418.

Kiparissides, C., Moustakis, I. and Hamielec, A. (1993). Electrostatic and Steric Stabilization of PVC Primary Particles, *J. Appl. Polym. Sci.* **49**: 445–459.

Kozub, D. J. and MacGregor, J. F. (1992a). Feedback Control of Polymer Quality in Semibatch Copolymerization Reactors, *Chem. Eng. Sci.* **47**: 929–942.

Kozub, D. J. and MacGregor, J. F. (1992b). State Estimation for Semi-Batch Polymerization Reactors, *Chem. Eng. Sci.* **47**: 1047–1062.

Kumar, S. and Ramkrishna, D. (1996a). On the Solution of Population Balance Equations by Discretization - II. A Moving Pivot Technique, *Chem. Eng. Sci.* **51**(8): 1333–1342.

Kumar, S. and Ramkrishna, D. (1996b). On the Solution of Population Balance Equations by Discretization-I. A Fixed Pivot Technique, *Chem. Eng. Sci.* **51**(8): 1311–1332.

Lee, K., Lee, J. H., Yang, D. R. and Mahoney, A. W. (2002). Integrated run-to-run and on-line model-based control of particle size distribution in semi-batch precipitation reactor, *Comp. Chem. Engng.* **26**(7-8): 1117–1131.

Liotta, V. (1996). *Control of Relative Particle Growth in Emulsion Polymerization*, PhD thesis, Lehigh University, Bethlehem, Pennsylvania.

Liotta, V., Georgakis, C. and El-Aasser, M. (1997). Real-time Estimation and Control of Particle Size in Semi-Batch Emulsion Polymerization, *Proc. American Control Conf.*, Albuquerque, NM, pp. 1172–1176.

Liotta, V., Georgakis, C., Sudol, E. D. and El-Aasser, M. S. (1997). Manipulation of Competitive Growth for Particle Size Control in Emulsion Polymerization, *Ind. Eng. Chem. Res.* **36**: 3252–3263.

Liu, Y. and Cameron, I. T. (2001). A new wavelet-based method for the solution of the population balance equation, *Chem. Eng. Sci.* **56**: 5283–5294.

Luyben, M. L. and Floudas, C. A. (1994). Analyzing the Interaction of Design and Control - 1. A Multiobjective Framework and Application to Binary Distillation Systhesis, *Comp. Chem. Engng.* **18**(10): 933–969.

Ma, D. L., Chung, S. H. and Braatz, R. D. (1999). Worst-Case Performance Analysis of Optimal Batch Control Trajectories, *AIChE J.* **45**(7): 1469–1476.

Ma, D. L., Tafti, D. K. and Braatz, R. D. (2002). High resolution simulation of multi-dimensional crystallization, *Ind. Eng. Chem. Res.*

Maas, U. and Pope, S. B. (1992). Simplifying Chemical Kinetics: Intrinsic Low-Dimensional Manifolds in Composition Space, *Combustion and Flame* **88**: 239–264.

Mahoney, A. W. (2001). *Inverse Problem Modeling of Particulate Systems*, PhD thesis, Purdue University.

Mahoney, A. W. and Ramkrishna, D. (2002). Efficient solution of population balance equations with discontinuities by finite elements, *Chem. Eng. Sci.* **57**: 1107–1119.

McKenna, T. F., Fevotte, G., Graillat, C. and Guillot, J. (1996). Joint Use of Calorimetry, Densimetry and Mathematical Modelling for Multiple Component Polymerizations, *Trans. IChemE.* **74**: 340–348.

Mead, R. N. and Poehlein, G. W. (1988). Emulsion copolymerization of styrene-methyl acrylate in continuous stirred tank reactors, *Ind. Eng. Chem. Res.* **27**: 2283–2293.

Meadows, E. S., Crowley, T. J., Immanuel, C. D. and Doyle III, F. J. (2002). Non-isothermal Modeling and Sensitivity Studies for Batch and Semi-batch Emulsion Polymerization of Styrene, *Ind. Eng. Chem. Res. (Accepted).*

Melis, S., Kemmere, M., Meuldijk, J., Storti, G. and Morbidelli, M. (2000). A model for the coagulation of polyvinyl acetate particles in emulsion, *Chem. Eng. Sci.* **55**: 3101–3111.

Min, K. W. and Ray, W. H. (1974). On the mathematical modelling of emulsion polymerization reactors, *J.M.S.-Rev. Macromol. Chem.* **C11**(2): 177–255.

Mitra, K., Deb, K. and Gupta, S. K. (1998). Multiobjective dynamic optimization of an industrial nylon 6 semibatch reactor using genetic algorithm, *J. Applied Polym. Sci.* **69**: 69–87.

Na, J., Chang, Y. K. and Chung, B. H. (2001). Optimization of Fed-batch Culture of Recombinant Yeast by using Genetic Algorithm, *Proc. IFAC Conf. Dynamics and Control of Process Systems*, Korea, pp. 714–717.

Noel, L. F. J., Brouwer, E. C. P., vanHerk, A. M. and German, A. L. (1995). On-Line Gas Chromatography and Densimetry to Obtain Partial Conversions of Both Monomers in Emulsion Copolymerization, *J. Appl. Polym. Sci.* **57**: 245–254.

Nomura, M., Yamamoto, K., Horie, I. and Fujita, K. (1982). Kinetics of emulsion copolymerization. ii. effect of free radical desorption on the rate of emulsion copolymerization of styrene and methyl methacrylate, *Journal of Applied Polymer Science* **27**: 2483–2501.

O'Toole, J. T. (1965). Kinetics of emulsion polymerization, *Journal of Applied Polymer Science* **9**: 1291–1297.

Ozdeger, E., Sudol, E. D., El-Aasser, M. S. and Klein, A. (1997a). Role of Nonionic Surfactant Triton X-405 in Emulsion Polymerization. I. Homopolymerization of Styrene, *J. of Polym. Sci.: Part A: Polym. Chem.* **35**: 3813–3825.

Ozdeger, E., Sudol, E. D., El-Aasser, M. S. and Klein, A. (1997b). Role of Nonionic Surfactant Triton X-405 in Emulsion Polymerization. III. Copolymerization of Styrene and n-Butyl Acrylate, *J. of Polym. Sci.: Part A: Polym. Chem.* **35**: 3837–3846.

Penlidis, A., MacGregor, J. F. and Hamielec, A. E. (1985). Dynamic modeling of emulsion polymerization reactors: A review, *AIChE Journal* **31**(6): 881–889.

Perry, R. H. and Green, D. (eds) (1984). *Perry's Chemical Engineers' Handbook*, sixth edn, McGraw-Hill International Edition.

Piirma, I. and Chang, M. (1982). Emulsion Polymerization of Styrene: Nucleation Studies with Nonionic Emulsifier, *J. of Polym. Sci.: Polym. Chem. Ed.* **20**: 489–498.

Pope, S. B. (1997). Computationally efficient implementation of combustion chemistry using in situ adaptive tabulation, *Combust. Theory Modelling* **1**: 41–63.

Prasetya, A., Liu, L., Litster, J., Watanabe, F., Mitsutani, K. and Ko, G. H. (1999). Dynamic model development for residence time distribution control in high-impact polypropylene copolymer process, *Chem. Eng. Sci.* **54**: 3263–3271.

Press, W. H., Teukolsky, S. A., Vetterling, W. T. and Flannery, B. P. (1992). *Numerical Recipes in Fortran 77: The Art of Scientific Computing*, Second edn, Cambridge University Press.

Rajesh, J. K., Gupta, S. K., Rangaiah, G. P. and Ray, A. K. (2001). Multi-objective Optimization of an Industrial Hydrogen Plant, *Chem. Eng. Sci.* **56**(3): 999–1010.

Ramkrishna, D. (1985). The Status of Population Balances, *Rev. Chem. Eng.* **3**(1): 49–95.

Ramkrishna, D. (2000). *Population Balances*, Academic Press, San Diego.

Ramkrishna, D. and Mahoney, A. W. (2002). Population balance modeling. Promise for the future, *Chem. Eng. Sci.* **57**: 595–606.

Randolph, A. D. (1964). A Population Balance for Countable Entities, *Can. J. Chem. Engg.* pp. 280–281.

Randolph, A. D. and Larson, M. A. (1962). Transient and Steady State Size Distributions in Continuous Mixed Suspension Crystallizers, *AIChE J.* **8**(5): 639–645.

Rawlings, J. and Ray, W. (1988a). The Modeling of Batch and Continuous Emulsion Polymerization Reactors. Part I: Model Formulation and Sensitivity to Parameters, *Poly. Eng. Sci.* **28**: 237–256.

Rawlings, J. and Ray, W. (1988b). The Modeling of Batch and Continuous Emulsion Polymerization Reactors. Part II: Comparison With Experimental Data From Continuous Stirred Tank Reactors, *Poly. Eng. Sci.* **28**: 257–274.

Rhodes, C. and Morari, M. (1997). A Computational Algorithm for Nonlinear Model Reduction, *Presented at the AIChE Annual Meeting.*

Richards, J. R., Congalidis, J. P. and Gilbert, R. G. (1989). Mathematical modeling of emulsion copolymerization reactors, *Journal of Applied Polymer Science* pp. 2727–2756.

Russel, B. M., Henriksen, J. P., Jorgensen, S. B. and Gani, R. (2002). Integration of design and control through model analysis, *Comp. Chem. Engng.* **26**: 213–225.

Sajjadi, S. and Brooks, B. W. (2000). Unseeded Semibatch Emulsion Polymerization of Butyl Acrylate: Bimodal Particle Size Distribution, *J. Polym. Sci., Polym. Chem. Ed.* **38**: 528–545.

Saldivar, E. (1996). *Modeling and Control of Emulsion Copolymerization Reactors*, PhD thesis, University of Wisconsin-Madison.

Saldivar, E., Dafniotis, P. and Ray, W. H. (1998). Mathematical Modeling of Emulsion Copolymerization Reactors. I. Model Formulation and Application to Reactors Operating with Micellar Nucleation, *J.M.S.-Rev. Macromol. Chem. Phys.* **C38**(2): 207–325.

Saldivar, E. and Ray, W. (1997). Control of Semicontinuous Emulsion Copolymerization Reactors, *AIChE J.* **43**(8): 2021–2033.

Semino, D. and Ray, W. (1995a). Control of Systems Described by Population Balance Equations - I. Controllabity Analysis, *Chem. Eng. Sci.* **50**(11): 1805–1824.

Semino, D. and Ray, W. (1995b). Control of Systems Described by Population Balance Equations - II. Emulsion Polymerization with Constrained Control Action, *Chem. Eng. Sci.* **50**(11): 1825–1839.

Siani, A., Storti, G. and Morbidelli, M. (1999). Procedure for Calibrating an Ultrasonic Sensor for Online Monitoring of Conversion in Latex Reactors, *J. Appl. Polym. Sci.* **72**: 1451–1477.

Silva, C. M. and Biscaia Jr., E. C. (2001). Genetic algorithm development for multiobjective optimization of polymerization reactors, *Second Pan American Workshop on Process Systems Engineering*, Guaruja, Brazil.

Skogestad, S. and Postlethwaite, I. (1996). *Multivariable Feedback Control*, John Wiley & Sons, New York, NY.

Storti, G., Carra, S., Morbidelli, M. and Vita, G. (1989). Kinetics of Multimonomer Emulsion Polymerization. The Pseudo-Homopolymerization Approach, *J. Appl. Polym. Sci.* **37**: 2443–2467.

Tsoukas, A., Tirrell, M. and Stephanopoulos, G. (1982). Multiobjective dynamic optimization of semibatch copolymerization reactors, *Chem. Eng. Sci.* **37**(12): 1785–1795.

Urretabizkaia, A., Arzamendi, G. and Asua, J. M. (1992). Modeling semicontinuous emulsion terpolymerization, *Chemical Engineering Science* **47**(9-11): 2579–2584.

Urretabizkaia, A., Arzamendi, G., Unzue, M. J. and Asua, J. M. (1994). High Solids Content Emulsion Terpolymerization of Vinyl Acetate, Methyl Methacrylate and Butyl Acrylate. II. Open Loop Composition Control, *J. Polym. Sci.: Part A: Polym. Chem.* **32**: 1779–1788.

Urretabizkaia, A., Sudol, E. D., El-Aasser, M. S. and Asua, J. M. (1993). Calorimetric monitoring of emulsion copolymerization reactions, *Journal of Polymer Science: Part A: Polymer Chemistry* **31**: 2907–2913.

Wang, C.-C., Kuo, J.-F. and Chen, C.-Y. (2000). Polymerization of styrene initiated by a novel initiator sodium formaldehyde sulfoxylate and sodium lauryl sulfate, *Eur. Poly. J.* **36**: 965–974.

Wang, Y. and Doyle III, F. J. (2002). Reachability Studies for Particle Size Distribution in Emulsion Polymerization, *Under Preparation.*

Yiannoulakis, H., Yiagopoulos, A. and Kiparissides, C. (2001). Recent developments in the particle size distribution modeling of fluidized-bed olefin polymerization reactors, *Chem. Eng. Sci.* **56**: 917–925.